SPECTROSCOPIC STUDIES ON INTERACTIONS OF IONS, WATER AND BIOMOLECULES AND APPLICATIONS

By

MOHAMMED AHMED

CHEM01200904022

Bhabha Atomic Research Centre, Mumbai

A thesis submitted to the Board of Studies in Chemical Sciences

In partial fulfillment of requirements For the Degree of

DOCTOR OF PHILOSOPHY

OF

HOMI BHABHA NATIONAL INSTITUTE

May, 2015

Homi Bhabha National Institute

Recommendations of the Viva Voce Committee

As members of the Viva Voce Committee, we certify that we have read the dissertation prepared by **Mohammed Ahmed** entitled **"Spectroscopic Studies on Interactions of Ions, Water and Biomolecules and Applications"** and recommend that it may be accepted as fulfilling the thesis requirement for the award of Degree of Doctor of Philosophy.

Chairman – Dr. D. K. Palit	**Date:** 19/05/2015
External Examiner – Dr. Arindam Chowdhury	**Date:** 19/5/2015
Guide/Convener – Dr. Ajay K. Singh	**Date:** 19/05/2015
External Member – Dr. Kaustuv Das	**Date:**
Member 1 – Dr. H. Pal	**Date:** 19-05-2015
Member 2 – Dr. S. Adhikari	**Date:** 19-05-2015

Final approval and acceptance of this thesis is contingent upon the candidate's submission of the final copies of the thesis to HBNI.

I/We hereby certify that I/we have read this thesis prepared under my/our direction and recommend that it may be accepted as fulfilling the thesis requirement.

Date: 19/05/2015

Place: Mumbai

Dr. Ajay K. Singh

(Guide)

STATEMENT BY AUTHOR

This dissertation has been submitted in partial fulfillment of requirements for an advanced degree at Homi Bhabha National Institute (HBNI) and is deposited in the Library to be made available to borrowers under rules of the HBNI.

Brief quotations from this dissertation are allowable without special permission, provided that accurate acknowledgement of source is made. Requests for permission for extended quotation from or reproduction of this manuscript in whole or in part may be granted by the Competent Authority of HBNI when in his or her judgment the proposed use of the material is in the interests of scholarship. In all other instances, however, permission must be obtained from the author.

Mohammed Ahmed

DECLARATION

I, hereby declare that the investigation presented in the thesis has been carried out by me. The work is original and has not been submitted earlier as a whole or in part for a degree/diploma at this or any other Institution / University.

Mohammed Ahmed

List of Publications arising from the thesis

1 Deciphering the Binding modes of Hematoporphyrin to Bovine serum albumin
Mohammed Ahmed, Apurav Guleria, Ajay K Singh, Tusar Bandyopadhyay, and Sisir K Sarkar
Indian Journal of Biochemistry and Biophysics **2014**, *51(3)*, 175-182.

2 Facile and Green Synthesis of CdSe quantum dots in Protein matrix: Tuning of morphology and optical properties,
Mohammed Ahmed, Apurav Guleria, Madhab C. Rath, Ajay K. Singh, Soumyakanti Adhikari and Sisir K. Sarkar
Journal of Nanoscience and Nanotechnology, **2014**, *14(8)*, 5730-5742.

3 Water in the Hydration Shell of Halide Ions Has Significantly Reduced Fermi Resonance and Moderately Enhanced Raman Cross-Section in the OH Stretch Regions
Mohammed Ahmed, Ajay K. Singh, Jahur A. Mondal, and Sisir K. Sarkar,
J. Phys. Chem. B, **2013**, *117*, 9728-9733.

4 How Ions Affect the Structure of Water: A Combined Raman Spectroscopy and Multivariate Curve Resolution Study
Mohammed Ahmed, Vinu V. Namboodiri, Ajay K. Singh, Jahur A. Mondal, and Sisir K. Sarkar
J. Phys. Chem. B, **2013**,*117,* 16479-16485.

5 On the Intermolecular Vibrational Coupling, Hydrogen Bonding and Librational freedom of water in the hydration shell of mono and bivalent ions
Mohammed Ahmed, Vinu V. Namboodiri, Ajay K. Singh, Jahur A. Mondal
J. Chem. Phys, **2014**,*141*, 164708-164715.

6 Vibrational Coupling and Hydrogen-bonding of Water at Charged and Neutral Molecular Hydrophobic Interfaces
Mohammed Ahmed, Ajay K. Singh, Jahur A. Mondal (communicated)

7 The Methyl groups Attached with Quaternary Nitrogen: Do They Behave Like a Polar Hydrophilic Group? *(Manuscript under preparation)*

Conferences

1 Hydrogen Bonding and Intermolecular Coupling of Water in Hydrophobic Hydration Shell

The 5th International Conference on Perspectives in Vibrational Spectroscopy (ICOPVS-2014), Thiruvananthapuram, Kerala, July 2014.

2 Raman Spectroscopic Investigation of the Liberational, Bend, and Stretch modes of Water in the Hydration Shell of Ions

Trombay Symposium on Radiation and Photochemistry (TSRP-2014), January 2014, BARC, Mumbai, January 2014.

3 Structure and Properties of Water in the Hydration Shell of Halide Ions as Revealed by Raman Spectroscopy

National Symposium on Radiation and Photochemistry (NSRP-2013), NEHU, Shillong, March 2013.

4 Intra and Intermolecular Coupling in Hydration Shell of Halide Ions Investigated by Raman Spectroscopy

National Laser Symposium (NLS-2013), NPCIL, Mumbai, February 2013.

5 Bio-Compatible CdSe Quantum Dots in Aqueous Solutions through Green Chemistry Route

Interdisciplinary Symposium on Material Chemistry (ISMC-2012), TSH, BARC, Mumbai, December 2012.

6 Exploring the Mechanism of Hematoporphyrin Induced Fluorescence Quenching of a Plasma Protein

Trombay Symposium on Radiation and Photochemistry (TSRP-2012), TSH, BARC, Anushaktinagar, Mumbai, January, 2012.

Others

1. Structural Transformation of Water in the Hydration Shell of Ions and Molecules:
   A Raman-MCR Study
   Research Scholars Meet (RSM-2014), Mumbai.

Mohammed Ahmed

In memory of my loving father

Mohammed Khaseem

Acknowledgement

During the course of this work many people have supported and contributed to the work described in this thesis. On this occasion, it gives me an immense pleasure to acknowledge all the people who have helped me in one way or the other, in preparing this little contribution to science. I have done my best in compiling the list of people all of whom have made important contributions to my journey in obtaining PhD and I apologize for omissions, if any.

First and foremost, I must acknowledge and thank The Almighty Allah for blessing, protecting and guiding me throughout this period. I could never have accomplished this without the faith I have in the Almighty.

I would like to express my deep and sincere gratitude to my guide, Dr. Ajay K. Singh for his invaluable guidance, constant encouragement, unstinted inspiration, keen interest and good wishes. Above all and the most needed, he provided me unflinching encouragement and support during many difficult situations and I am indebted to him more than he knows.

This thesis would not have been possible without the guidance, help, support, critical analysis and valuable suggestions from Dr. Jahur Alam Mondal who has been truly invaluable to me both on an academic and a personal level, for which I am extremely grateful. I am also thankful to him for sharing his excellent knowledge and scientific understanding with me throughout the work. His enthusiasm, deep engagement in research and critical analysis strategy of experimental data has made a deep impression on me. He has been great company and sources of inspiration and advice whenever I found myself in doubt. I thank him a lot for being patient with me on many occasions in particular, while reviewing this thesis.

I would like to give heartfelt special thanks to Dr. Sisir K. Sarkar for his excellent supervision, incredible support, ceaseless encouragement and enthusiastic about my research. Your most trenchant comments with always very good suggestions and positive compliments shaped my work better.

I take the opportunity to express my heart full thanks to Dr. M. C. Rath for his support, encouragement and sharing his valuable experiences in nanomaterials synthesis. I am privileged to thank Dr. T. Bandyopadhyay, who helped me in Docking and MD simulation studies.

My special thanks go to my dear friend Mr. Apurav Guleria for his moral support, diversified help, and several funs which will always be remembered. I also offer my thanks to Dr.Vinu Namboodiri and Dr. P. Mathi for their support, encouragement and constructive criticism, particularly related to my review presentations.

It gives me immense pleasure to thank the members of the doctoral committee Dr. D. K. Palit (Chairman), Dr. H. Pal (Member), Dr. S. Adhikari (Member), Dr. Kaustuv Das (External member) and Dr. T. Mukherjee (Former Chairman) for their critical review and suggestions during the progress review and pre-synopsis viva-voce.

I also gratefully acknowledge the help rendered by Dr. B. N. Jagatap, Director, Chemistry group and all the members of RPCD. I am grateful to DAE for giving me this opportunity, providing funding and fellowship during this course of work.

I am immensely indebted and express my deep sense of gratitude and heart full thanks to all my teachers, who have added different dimensions to my life at different stages.

I also extend many thanks to Arun, Sunil, Rammohan, Ganesh, Shalini, Chandralekha, Shashi shukla, Snehal, Sushanth, Hari, Sughosh, Bhavana, Mhejabeen, Farheen, Juby, Laboni, KK,, Abhishek, Ashmita, Mohini, Pallavi, Tusar, Partha, Jayantha, and Srinivas for their support during the period of my doctoral work.

Words fail me to express my appreciation to my roommates, Dilip, Suresh, Venky, Khaiser, Kamal, Gangaprasad, Nagaraju, Sushanth, Rajmurthy, Abdullah, GM and Suma, Yusuf and Jasna, Vivek and Anju, Satish and Anusha and Naresh and Vani for their unwavering support during my difficult time and homely feeling at Mumbai. I always cherish the time spent with all of you during these years. I also extend thanks to my batch mates Avishek, Jerina, Vasundhara, Suman, Monika, Shikha and Debashree.

It gives me a great pleasure in thanking my dear friends Shashi, Wahid khan, Prasad, Bhaskar, Jali, Sridhar, Jagan, Srikanth, Shefeek and Ahmed hussain for their support and cooperation in various aspects and cheered me up during difficult times. I also thank all my university friends especially Pullaiah, Suresh chary, Balaji, and Jagadish who have always encouraged me in all aspects.

Most importantly, none of this would have been possible without the love and patience of my family. My great and lovely mother, I really don't want to through a piece of word 'thanks' for you because it never expresses my feeling for you; I just simply wish you to be with me and rest of the family healthier and happier ever. I am indebted to my younger brother and sister for their support, encouragement and consolation through times of happiness and sorrow. I also want to thank elder sisters and brother-in-laws for their support and pride in me.

This last word of acknowledgment I have saved for my dear father. Without his inspiration, sacrifices, unending support and love from childhood, I never would have made it through this process or any of the tough times in my life. I dedicate this thesis to my late father. Abba, this is for you.

December, 2014 *Mohammed Ahmed*

CONTENTS

Synopsis

Physicochemical processes in chemical, biological, and environmental systems are governed by a myriad of non-covalent interactions involving ions, water, and uncharged solutes. In biology, for instance; non-covalent interactions, such as hydrogen-bonding, electrostatic (ion-ion, ion-dipole), and hydrophilic/hydrophobic interactions are crucial for the formation of lipid bilayer-the most important biological border, transport of ions/molecules across lipid membrane, cell signalling, protein conformation change, enzymes activation, ligand-binding, etc.[1-4] Fundamental elementary chemical reactions, for example acid-base equilibrium and electron transfer are directly related with ion-water interaction through the hydration of the conjugate acid-base pairs or the charged species produced during electron transfer.[5-8] Therefore, a molecular level understanding of the interactions involving ions, water, and hydrophobic/hydrophilic solutes are essential for the elucidation of complex chemical processes occurring in various chemical, biological, and applied fields.

A water molecule, because of its small size, dipolar character, and hydrogen-bond donating and accepting abilities, can participate in diverse interactions with the variety of ions and molecules, which enable water to act as a universal solvent and an active constituent in living organisms. Nevertheless, a slight variation of such interactions (between water and a solute say a protein) can lead to a conformational change of the solute. It is believed that the conformational change of a protein in presence of ions is associated with the structural transformation of water in presence of ions. Accordingly, the ions were categorized as 'structure makers' (kosmotrope; e.g. CO_3^{2-}, PO_4^{3-}, SO_4^{2-})

and ‘structure breakers’ (chaotrope; I^-, Br^-, NO_3^-, SCN^-, ClO_4^-) depending on whether they increase or decrease the hydrogen bond net-work of liquid water.[9-13] In pure liquid however, the water molecules are strongly coupled (intra- and intermolecular vibrational coupling that provides a collective nature to liquid water) with each other and in dynamic equilibrium of breaking and making of hydrogen-bond with neighbours. These features which are crucial for the energy relaxation in water are important for aqueous reactions in chemical and biological systems.[14-17] Recently, X-ray and neutron diffraction as well as ultrafast IR pump-probe studies[18,19] have suggested that the hydrogen-bonding and vibrational/orientational relaxations of water are mainly affected within the hydration shell of ions. Therefore, it is essential to understand hydrogen-bonding and collective properties of water in the ‘*hydration shell*’ of solute.

The present thesis deals extensively with the hydrogen-bonding and vibrational coupling of water in the hydration shell of the so-called ‘kosmotropic’ and ‘chaotropic’ anions by using Raman multivariate cruve resolution (Raman-MCR) spectroscopy.[20] Raman-MCR spectroscopy provides the selective vibrational characteristics of water in the hydration shell of a fully hydrated solute/ion, which is difficult to obtain otherwise. This is because, to probe a fully hydrated hydration shell (free from ion-pairing/hydration shell sharing), it is necessary to use diluted solution; and in diluted solution, the weaker signal of hydration water gets buried into the stronger signal of bulk water. As a result, understanding the hydration water is difficult from the experimentally recorded IR/Raman spectra of diluted salt solutions (raw spectra). We have overcome this problem by

applying multivariate curve resolution analysis[21,22] on the experimental Raman spectra of diluted salt solution.

Unlike the hydration shell of anions, the water molecules in the hydration shell of an uncharged hydrophobic solute cannot participate in strong hydrogen-bond interaction with the solute, and hence, reorganize to optimize the hydrogen-bonding with neighbouring water molecules. Thermodynamic measurements have reveled an increase in heat capacity and decrease in entropy of water in presence of hydrophobic solutes. These observations were explained by proposing more ordered and tetrahedral structure of water at the vicinity of a hydrophobic solute.[23] However, a more ordered and tetrahedral structure of water in hydrophobic hydration shell was later challenged by neutron scattering and MD simulations, which showed that the water structure in the vicinity of the hydrophobic groups is analogous to bulk water.[24,25] We investigated the structural transformation of water in the hydration shell of charged as well as uncharged hydrophobic molecular groups by using Raman-MCR spectrsocopy.

Secondary structure of protein is a consequence of intermolecular forces including ionic and hydrophobic interactions. The perturbations of ionic and hydrophobic interactions (interaction between charged amino acid residues and between nonpolar groups of protein residues) lead to folding and unfolding of proteins which are related with its functions. For instance, the electrostatic interactions between charged amino acid groups of the protein and a dipolar/charged ligand determine the binding location of the later in the protein and the hydrophobic interaction between the protein and the ligand decide the overall stability of protein-ligand complex.[26] The second part of this thesis is a

continuation of the endeavour to understand these fundamental interactions involved in the binding of serum albumin with hematoporphyrin. Serum albumin is the major soluble protein in the circulatory system and plays important role in the distribution and metabolism of many metabolites/drugs whereas hematoporphyrin is the drug used as a marker in diagnostics and imaging and as a photosensitizer in photodynamic therapy (PDT) treatment of malignancies and other diseases. In this part, we have studied the binding interaction between serum albumin and hematoporphyrin by using combined experimental and computational methods. Furthermore, to address the role of electrostatic and hydrogen bonding interactions of protein amino acid groups in controlling the morphology and dimensions of nanoparticles, we have synthesized CdSe nanoparticles in the serum albumin protein matrix at different experimental conditions.

The results obtained for different systems investigated in the present research program have been presented and discussed in this thesis. Based on the theme of the work, different aspects of the present work have been discussed in a systematic manner in eight different chapters of the thesis. A brief account of each chapter is given below.

Chapter 1

Chapter 1 deals with general introduction to various non-covalent interactions (for example, hydrogen-bonding, electrostatic (ion-ion, ion-dipole), and hydrophobic interactions) that are encountered in various chemical and biological processes. After presenting basic aspects of these interactions, this chapter describes in detail the ion-water and hydrophobe-water interactions. In particular, an elaborate account has given on the

current understanding of ion-water and hydrophobe-water interactions and the structural changes of water in presence of ion/hydrophobic molecules. A brief description on role of various interactions in protein-drug binding has also been presented in this chapter. The aspects of protein based synthesis of nanomaterial have been discussed. Towards the end of the chapter, the objective and motivation of the present thesis work has also been discussed.

Chapter 2

Chapter 2 contains the details of experimental techniques and data analysis methods employed in this research work. To investigate ion-water and hydrophobe-water interactions, we have mainly used Raman spectroscopy and multivariate curve resolution (MCR) analysis method. The basic principles of Raman spectroscopy and MCR analysis have been discussed. Raman spectroscopy in combination with MCR-analysis allows one to selectively obtain the vibrational characteristics of a solvent in the solvation shell of a solute. Additionally, a brief outline of steady state UV-Vis absorption, fluorescence, and time-resolved fluorescence spectroscopy techniques, which were used for protein-drug interaction and protein-nanoparticle synthesis, has been presented.

Chapter 3

Chapter 3 deals with change in spectroscopic properties of water (e.g. Raman cross-section, σ) and the coupling among different vibrational modes of water (e.g. coupling between OH stretch fundamental (ν_1) and HOH bend overtone ($2\nu_2$) which is known as Fermi resonance (FR)) in concentrated alkali halide (NaX) solution. In this

study, we have compared the Raman spectral changes in OD (OH) stretch regions by the addition of alkali halides in D_2O (H_2O) and in the isotopically diluted water. It has been observed that the σ of water changes significantly in presence of alkali halides (NaX; X = F, Cl, Br, and I). Moreover, the modification of σ–values depends upon the physicochemical properties of the halide ions. For example, the relative Raman cross-section, σ_H/σ_b (i.e. with respect to bulk water) increases as 0.6, 1.1, 1.5, and 1.9 for F^-, Cl^-, Br^-, and I^- anions. We have assigned the increased Raman cross-section to pre-resonance enhancement mediated by the charge transfer from halide ions to the hydrating water. Moreover, it has been observed that the changes in the OH stretch band, by the addition of NaX (X= Cl, Br, I) in H_2O, are similar to those obtained by the addition of D_2O in H_2O. These spectral changes have been discussed in detail, and a picture that emerges from the discussion is the following: the vibration of water has reduced stretch-bend coupling at the vicinity of halide ions.

Chapter 4

In chapter 4, we have addressed more extensively the issue of vibrational coupling of water in the hydration shell of ions. As discussed in Chapter 3, Raman spectroscopy of concentrated (~ 5-6 mol dm^{-3}) aqueous salt solution provides vibrational characteristics of water that are assignable mostly to the hydration water. Nevertheless, in concentrated salt solutions, ion-pairing and overlapping/sharing of individual hydration shells may complicate the vibrational band shape and dynamics of water in the so called 'hydration shell of a fully hydrated ion'. In this chapter, we have combined multivariate curve resolution (MCR) analysis with the Raman spectra of diluted (<1.0 mol dm^{-3}) aqueous

salt solution (Raman-MCR spectroscopy) that provided the vibrational response selective to the hydration water. We have applied the Raman-MCR approach to the OH stretch, HOH bend, and [bend+librational] combination band regions of water in the hydration shell of a variety of ions such as the so-called 'structures breakers' (e.g. Cl^-, Br^-, I^-) and 'structure makes' (e.g. CO_3^{2-}, SO_4^{2-}). The MCR-retrieved vibrational spectra of water demonstrates that the hydrogen-bond strength hydration water decreases as $CO_3^{2-} > SO_4^{2-} \approx$ bulk water > Cl^-.> > I^- and the librational mobility of hydration water increases as $CO_3^{2-} \approx SO_4^{2-}$ < bulk water < Cl^- < I^-. Moreover, the water molecules are vibrationally decoupled with neighboring water molecules in the hydration shell. In other words, the collective nature of liquid water is compromised in the hydration shell.

Chapter 5

As discussed in Chapter 4, the Raman-MCR analysis can selectively provide the vibrational spectrum of water in the hydration shell of a solute. Therefore, in this chapter, the Raman-MCR analysis was extended to understand the structure of water in the hydration shell of uncharged (*tert*-butanol, TBA) and charged (tetramethylammonium cation, TMA^+) hydrophobic molecular groups. The results show that the hydrophobic hydration shell has increased population of strongly H-bonded water and a depletion of weakly H-bonded water compared to that of bulk water. The emergence of a distinct narrow band at ~ 3660 cm^{-1} give clear indication about existence of dangling OH bonds at the surface of hydrophobic molecular groups. Quantitative analysis of the MCR-retrieved vibrational spectra of water in the hydration shell of TBA and TMA^+ in isotopically diluted water of varying composition ($[H_2O]/[D_2O+H_2O]$ = 1, 0.75, 0.5, 0.25; v/v)

revealed that the water in the hydration shell of TBA or TMA^+ are vibrationally decoupled from neighbouring water molecules like that in the hydration shell of halide ions, as observed in Chapter 4. Nevertheless, the dangling OH is intramolecularly coupled with the H-bonded OH stretch vibration.

Chapter 6

In Chapter 4 and 5, it has been discussed that the solute (ions and hydrophobic molecules) strongly affect the structure and properties of surrounding solvent (water). It is likely that the solvent (water or ion-water mixture) also affects the properties of a solute (hydrophobic molecule). In Chapter 6, we have addressed this issue by monitoring the vibrational response of the methyl groups of model hydrophobes (*tert*-butanol (TBA), trimethylamine-N-oxide (TMAO) and tetra-methyl ammonium (TMA)-cation) in water and [water + electrolyte] mixtures as well as in relatively less polar/nonpolar solvents (CD_3OH, $CDCl_3$). It has been observed that vibrational band position of typical hydrophobic methyl's, such as that of TBA, shifts toward higher frequency with increasing dipolar and hydrogen bonding ability of the solvent. This is known as blue-shifted H-bonding which indicates the apolar character of the C-H bonds in TBA. Similar spectral changes have been observed for the CH stretch band of TMAO and TMA^+. Moreover, the effect of halide ion (F^-, Cl^-, Br^-, I^-) on the CH stretch bands TBA is comparable to that of TMAO and TMA^+. These results suggest that regardless of the positive change the methyl's in TMAO and TMA^+, interact with water by blue-shifted H-bonding and that halide ion adsorb at the surface of their methyl groups.

Chapter 7

Chapter 7 deals with the molecular level interaction between bovine serum albumin (BSA) and hematoporphyrin (HP), a well known photosensitizer used in photodynamic therapy. This study has been carried out in aqueous buffer solution using steady state and time-resolved emission techniques. The results have been further substantiated by molecular docking and molecular dynamics (MD) simulation. It has been observed that the fluorescence of BSA is dominantly quenched by the ground-state complex formation with HP accompanied by the minor contribution from electronic energy transfer (EET) to the later. Molecular docking analysis suggested that HP bound to the two well-separated sites located in the sub domain IB and IIA, where the sub domain IB (primary binding site) was distinctly more occupied than IIA (secondary binding site). Based on the detail docking analysis and experimental thermodynamic parameters, it was confirmed that hydrogen-bonding and Vander Waals forces were the driving forces for the BSA-HP complexation. Such studies are essential and could be beneficial in understanding the transport and delivery of different therapeutic agents including drugs.

Chapter 8

In Chapter 8, protein-ion interaction driven synthesis of cadmium selenide (CdSe) quantum dots (QDs) was carried out. The process was mediated by bovine serum albumin (BSA), which played a dual role of reducing and stabilizing agent for CdSe QDs. Furthermore, we have altered the type of interaction between protein functional groups and surface atoms of QDs by changing the experimental condition such as varying molar

ratio of the precursors, which enable us to tune the morphology and optical properties of the QDs. This aspect can provide details about role of protein-inorganic ion interactions on controlling the shape of CdSe nanoparticles. The possible mechanism of the formation as well as for the shape variation of these nanoparticles with the molar ratios of precursors has been proposed. On the whole, the methodology of protein assisted synthesis is relatively new, especially for semiconducting nanomaterials and may provide some unique and interesting aspects to control and tune the morphology *vis-à-vis,* their optical properties.

References

(1) Dill, K. A. *Biochemistry* **1990**, 29, 7133.

(2) Ruply, J.; Careri, G. *Adv*. *Protein Chem*. **1991**, 41, 37.

(3) Sussman, F.; Weinstein, H. *Proc. Natl. Acad. Sci. U.S.A.* **1989**, 86, 7880.

(4) Jordan, P. C. *Biophys. J*. **1990**, 58, 1133.

(5) Franks, F., Ed. *The physics and physical chemistry of water*, Plenum Press: New York, 1972; Vol. 1.

(6) Maroncelli, M.; Maclnnins, J.; Fleming, G. R. *Science* **1989**, 243, 1674.

(7) Kropman, M. F.; Bakker, H. J. *Science* **2001**, 291, 2118.

(8) Habuchi, S.; Kim, H. B.; Kitamura, N. *Anal*.*Chem*. **2001**, 73, 366.

(9) Kunz, W.; Henle, J.; Ninham, B. W. *Curr. Opin. Colloid Interface Sci.* **2004**, 9, 19.

(10) Chen, Y.; Zhang, Y. H.; Zhao, L. J. *Phys. Chem. Chem. Phys.* **2004**, 6, 537.

(11) Yonehama, K.; Yoshimura, Y.; Takekiyo, T.; Kanno, H. *Bull. Chem. Soc. Jpn.* **2009**, 82, 563.

(12) Samoilov, O. Y. *Discuss. Faraday Soc.* **1957**, 24, 141.

(13) Frank, H. S.; Wen, W.-Y. *Discuss. Faraday Soc.* **1957**, 24, 133.

(14) Yang, M.; Skinner, J. L. *Phys. Chem. Chem. Phys*. **2010**, 12, 982.

(15) Auer, B. M.; Skinner, J. L. *J. Chem. Phys*. **2007**, 127, 104105.

(16) Hare, D. E.; Sorensen, C. M. *J. Chem. Phys*.**1992**, 96, 13.

(17) Ramasesha, K.; De Marco, L.; Mandal, A.; Tokmakoff, A. *Nature chem*. **2013**, 5, 935.

(18) Soper, A. K.; Weckstrom, K. *Biophys. Chem*. **2006**, *124, 180.*

(19) Omta, A. W.; Kropman, M. F.; Woutersen, S.; Bakker, H. J. *Science* **2003**, *301*, *347*.

(20) Ahmed, M.; V. Namboodiri, A. K.; Mondal, J. A., *J. Phys. Chem. B* **2013**, 117, 16479.

(21) Perera, P. N.; Browder, B.; Ben-Amotz, D. *J. Phys. Chem. B* **2009**, 113, 1805.

(22) Fega, K. R.; Wilcox, D. S.; Ben-Amotz, D. *Appl. Spectrosc.* **2012**, 66, 282.

(23) Frank, H. S.; Evans, M. W., *J. chem. phys.* **1945**, 13, 507.

(24) Soper, A. K.; Finney, J. L. *Phys. Rev. Lett.* **1993**, 71, 4346.

(25) Stirnemann, G.; Hynes, J. T.; Laage, D. J. *J. Phys. Chem. B* **2010**, 114, 3052.

(26) Tanford, C. *Science* **1978**, 200, 1012.

LIST OF FIGURES

LIST OF TABLES

Chapter 1

Introduction

Interactions involving ions, water, and hydrophilic/hydrophobic solutes play important roles in chemical, biological, environmental, and industrial processes. In chemistry, for instance, several processes including solubility of a solute, acid-base equilibria, electron transfer, ion-pairing, etc. are dependent on the solvation/hydration of the chemical constituents. Important biological processes, such as formation of lipid bilayer, secondary structures of DNA, replication of DNA, transport of ions/molecules across lipid membrane, cell signaling, protein conformational change, enzyme activation, binding between proteins and drugs, etc. are strongly influenced by the interactions between water and hydrophilic/hydrophobic molecular groups.[1,2] Therefore, a molecular level understanding of the interactions involving ions, water, and hydrophobic/hydrophilic groups and the associated change in the properties of water around a solute is important for the elucidation of complex chemical processes occurring in various chemical, biological, and applied fields.

1.1. Water: A Universal Solvent and Active Constituent of Biological systems

Water is a small molecule with two hydrogen's attached with central sp^3-hybridized oxygen. Due to its bent structure and an unequal sharing of electrons between oxygen and hydrogen ('O' is more electronegative than 'H') the O-H bonds are dipolar and that water possesses a permanent dipole moment (Scheme 1.1). Because of the permanent dipole moment, water molecules can engage in dipole-dipole interaction with each other. Moreover, the polar O-H groups can participate as hydrogen-bond donor as well as an acceptor. Thus, each water molecule can form up to four hydrogen-bonds with neighboring water molecules, and hence, can have an extended three dimensional H-bond network. In liquid state, the water molecules are in dynamic equilibrium of breaking and

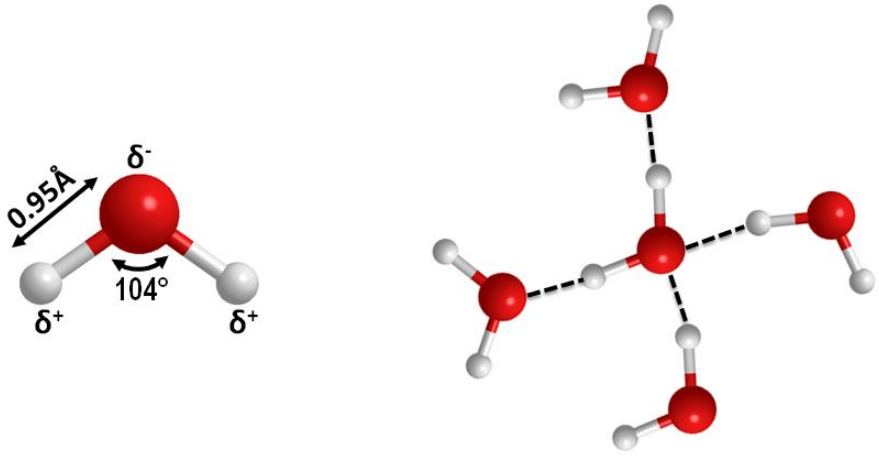

Scheme 1.1. *Left: The water molecule. The red sphere represents the oxygen atom and the grey spheres are the hydrogen atoms. The δ+ and δ− signs indicate the relative charge. Right: The tetrahedral arrangement of the hydrogen-bonded water network. Hydrogen bonds are indicated with the dashed lines.*

making of these H-bonds on a picosecond time scale.[3,4] These interactions lead to strong intra- and intermolecular vibrational coupling among water molecules, which provides a collective nature to liquid water. However, the electrostatic (dipole-dipole) and H-bond interaction in water are not only confined among water molecules, but also occur with several charged and dipolar solutes dissolved in water. In fact, this is why water can act as a universal solvent.

In a biological system, the structure, stability and folding of proteins crucially depends on the hydration of individual amino acids and their H-boding with water.[5-8] Similarly, the stability of nucleic acids depends on the hydration of phosphate groups that diminish repulsive phosphate-phosphate interactions.[9-13] The binding of drugs/ligand to the protein receptors occurs via the interaction of water with the functional groups of protein binding sites.[14-16] The various electron and proton transfer reactions in the biological processes are facilitated by water.[17,18] DNA-protein binding also depends on the structural arrangement of water around the base pairs of DNA.[19] The formation of lipid bilayer - the most important biological border is also crucially dependent on hydrophilic/hydrophobic interaction between phospholipid and water.[20] Thus, water is an active matrix for biological system and is essential for biological activities.

Presence of ions or other solutes do affect the H-bonding, dipolar interaction, and vibrational coupling of water at the immediate vicinity of the ion/solutes. The perturbation of these properties of water in the hydration shells of ions and hydrophobic molecular groups are the major focus of the thesis.

1.2. Ion Hydration

An electrolyte dissolves into water due to the hydration of its constituent cations and anions. H-bonding and ion-dipole interactions between the ions and water are the major interactions that dislocate the cations and anions from their crystal lattice of the electrolyte and produce the hydrated ions. It is likely that these ions in turn would affect the properties of water. In other words, the structure and properties water in the vicinity of an ion is expected to be different from that of bulk water.[21,22] It is intuitive that the electric field of an ion tends to reorient the water at its vicinity. The reorientation of water dipole may affect the water-water H-bond interaction, which is directional in nature.[23] Earlier studies suggest that the ions profoundly affect the secondary and tertiary structures of proteins (Hofmeister effect), which has some bearings with the change in the water structure in presence of ions. When different ions are arranged in order of their ability of precipitating (favoring the folded state) certain proteins, the following series (Hofmeister series) is obtained:[21,24,25]

$CO_3^{2-} > SO_4^{2-} > HPO_4^{2-} > CH_3COO^- > F^- > Cl^- > Br^- > NO_3^- > I^- > ClO_4^- > SCN^-$.

Here, the anions on the left hand side of Cl^- favor the folded state of protein (precipitation/salting-out) and those on the right side promote the unfolded state (denaturation/salting-in). These specific ion effects are ubiquitous in chemistry and biology, and similar ordering of ions is observed for numerous microscopic properties including surface tension, chromatographic selectivity, colloidal stability, and protein-denaturation temperatures.[26]

To explain the macroscopic properties in the ionic solution, Frank and Wen[27] proposed the ionic hydration model in 1957, in which they proposed that an ion is surrounded by three concentric regions characterized by different interactions between water and ion. According to this model, the water molecules in the inner most region (first hydration shell) are tightly bound to the ion and exhibit lower mobility than those in pure water. In the second region (surrounding the first hydration shell), ions disrupt the hydrogen bonding structure of water and induces a "structure breaking effect".[28] The third region, which is far from the ion, contains the water molecules normally polarized by the ionic field. In the same year, Samoilov[29] classified ion hydration in terms of the activation energy of the exchange of water molecules around the ion. He classified ion hydration as positive or negative based on the activation energy and proposed that the ions which induce the positive hydration (positive activation energy) act as the structure maker and negative hydration (negative activation energy) act as the structure breaker.

Based on the above models, it was proposed that the ions on the left side of the Hofmeister series (*i.e.* Br^-,NO_3^-,I^-,ClO_4^-, SCN^-) enhance the water structure ('structure maker' or 'kosmotrope') and the ions on the right side of the series (*i.e.* CO_3^{2-}, SO_4^{2-}, HPO_4^{2-}) reduce the water structure ('structure breakers' or 'chaotrope'). It was believed that kosmotropes interact strongly with water and makes it less aggressive to a protein (solute) thus helps the protein to retain its native/folded structure (stabilization). On the contrary, chaotropes interact weakly with water and makes water more aggressive to a solute (protein) and promotes denaturation (destabilization).[27,29-31] These "structure maker" and "structure breaker" concept is supported by the influence of ions on the

viscosity of water. The Jones-Dole expression for the viscosity of aqueous ionic solutions for concentrations up to~1M is given by

$$\frac{\eta-\eta_0}{\eta_0} \approx A\sqrt{c} + BC \quad (1.1)$$

Where η and η_0 are the viscosities of the solution and pure water; c is the concentration of ion; A and B are empirical constants. The 'first term' on the right-hand side is assigned to the electrostatic interaction between the ions. The 'second term' is attributed to the influence of ions on the hydrogen bond structure of water. It has been found that the so called 'kosmotropic' anions increases the viscosity of water (positive Jones-Dole viscosity coefficient, B) whereas the chaotropic anions decreases the same (negative B coefficient) and the ordering of ions on the basis of their B-coefficient values: PO_4^{3-} (0.495) > CO_3^{2-} (0.294) > CH_3COO^- (0.25) > SO_4^{2-} (0.206) > F^- (0.107) > Cl^- (-0.005) > Br^- (-0.033) > NO_3^- (-0.043) > I^- (-0.073) which are in agreement with their order in Hofmeister series.[30,32-35] However, changing the viscosity of water in presence of certain ions does not necessarily indicate that these ions affect the H-bond network of bulk water in the long range like that of temperature.[36,37]

Several experimental and computational methods[38-45] have been used to probe the H-bonding, vibrational and orientational relaxation of water in aqueous salt and hydrophilic/hydrophobic solutions. These studies showed that the rotational dynamics of water molecules in the hydration shells of multivalent ions are slower than that in bulk water. In contrast, the rotational motions of water in the hydration shell of large monovalent ions are faster than those in bulk water.[46] The orientational dynamics of water

in the hydration shells of ions have also been studied with depolarized Rayleigh scattering. However, the intrinsic measuring times in the NMR and depolarized Rayleigh scattering studies are long compared to that of the exchange time of water between the hydration shells and the bulk (picosecond). Therefore, these measurements only provided an ensemble average dynamics and could not distinguish the dynamics of water in the hydration shell of ions from the bulk water. Recently, ultrafast spectroscopy techniques were used to probe the dynamics of water molecules on a sub-picosecond time scale, which is shorter than the exchange time of water molecules in bulk and in hydration shell. The OH stretching frequency of water is very sensitive to the length and strength of hydrogen bonds and provides clear information on the structural changes of water in presence of various ions. As water molecules are in dynamic equilibrium of breaking and making of H-bonds with each other on a picosecond time scale, the vibrational OH stretching frequencies also fluctuate on the picosecond timescale depending upon the strength of H-bond and local environment of water. Time dependence of these frequency fluctuations is known as vibrational spectral diffusion. Bakker and coworkers[47,48] carried out femtosecond mid-infrared spectroscopic studies of the dynamics of vibrational spectral diffusion in aqueous alkali halide solutions and found that, apart from the characteristic time (~100 fs) of spectral diffusion in pure water, there is additional slow long time (12 - 25 ps) decay of spectral diffusion pertinent to the hydration shell water of ions. These authors suggested that in aqueous solutions, the strength of hydrogen bonding in hydration shell is different compared to the water-water hydrogen bonds in the bulk. In addition to the vibrational spectral diffusion experiments, femtosecond mid-infrared

pump-probe spectroscopy studies, that measured the rate of vibrational energy transfer or orientational relaxation of water, have revealed that the orientational and energy relaxation components of hydration shell water are different from that of the bulk water.[49-52] Dielectric relaxation spectroscopy, which detects the polarization response (*i.e.* the reorientation of dipolar water molecules) to an applied electric field of the light in aqueous solutions, revealed that the ions have very little effect on the structural dynamics of the water molecules outside the first hydration shells. X-ray and neutron diffraction studies[39,41,53-56] which provide a relative distribution of the number density of H and O atoms of water, as a function of distance, from the ion/solute, revealed that the static structure of water is significantly perturbed only in the immediate vicinity of ions/solute. In agreement with these experimental observations, MD-simulations[36,43,49,57-63] found that the hydrogen bonding and the structural motifs of water of the first hydration shell strongly differ from that of bulk water and beyond this shell, water rapidly acquires the similar structure like bulk water (Scheme 1.2) .

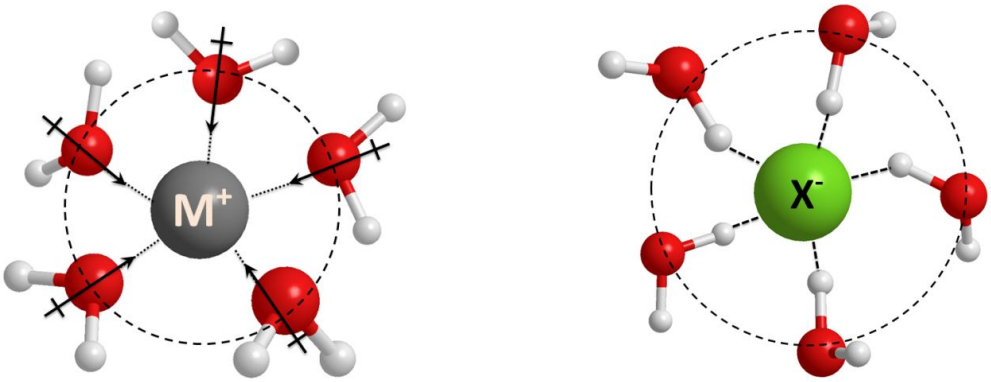

Scheme 1.2. *Preferential orientation of water in the hydration shells of ions.*

1.3. Hydrophobic Hydration

Hydrophobic solutes (e.g. alkane and alcohols with long alkyl chain) because of their nonpolar nature, cannot participate in strong interactions with dipolar water.[64] As a result, hydrophobic solutes aggregate in water to minimize the contact surface with water. The water on the other hand, reorganizes at the surface of a molecular hydrophobe, to optimize the hydrogen-bonding and dipolar interaction with neighboring water molecules. These structural changes of a hydrophobic solute and the water at the surface of the solute are the driving force for the hydrophobic effect, which is the key to many biological processes, like protein folding, formation of various self-assemblies (like lipid bilayers), molecular recognition, etc.[65] Thermodynamic investigations have revealed that the introduction of hydrophobic solute in water increases the heat capacity and decreases the entropy of water. These observations were explained by Frank and Evans in 1945 on the basis of 'iceberg' model.[66] According to this model, water in hydrophobic hydration shell has stronger H-bonding and enhanced ordering in comparison to that in bulk.

Based on the 'iceberg' model, Kauzmann's proposed entropic origin for the hydrophobic interaction.[67] He pointed out that due to the formation of cage (relatively ordered structure) around the hydrophobic solutes, the rotational and translational freedom of the water molecules are compromised and leads to an entropy decrease. But if two "caged" hydrophobic solutes come together, the "ordered" water around the solutes is returned to the bulk, leading to an entropy increase (Scheme 1.3). Thus, there is an entropically based force of attraction between these solute particles (hydrophobic interaction). In contrast to Kauzmann's mechanism, Blokzijl and Engberts[68] suggested

that hydrophobic interaction results due to the limited capacity of liquid water to accommodate the apolar solute and maintain its original network of hydrogen bonds.

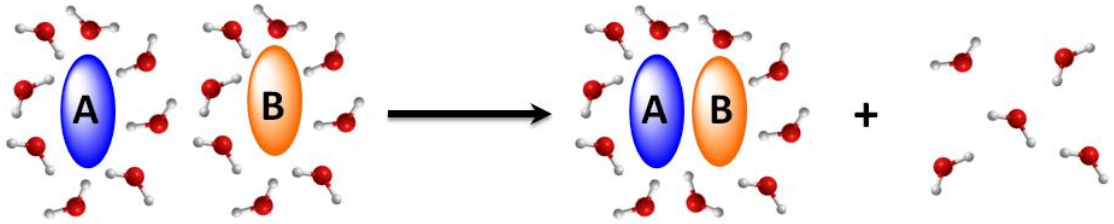

Scheme 1.3. *Aggregation of non-polar solutes (say A and B) in water releases some of their hydration water that adds to the increased entropy of the system.*

The 'iceberg' concept of hydrophobic hydration was disputed later by several experimental and theoretical results.[54,69-73] Neutron diffraction studies[58,74] revealed that the structure of the water around hydrophobic groups is comparable to that of bulk liquid and alternatively suggested that the anomalous properties upon dissolution of hydrophobic solutes arise from the incomplete mixing in the molecular level. Recent polarization-resolved mid-infrared pump-probe spectroscopy experiments,[71,74] that probe the dynamics of water molecules on a sub picosecond time scale, which is shorter than the exchange time of water molecules in bulk and in hydration shell, revealed that the water molecules in the hydration shell of hydrophobic groups show different orientational and hydrogen bond dynamics than bulk water. It was suggested that the presence of hydrophobic moieties sterically hinders the formation of the five coordinated water molecules, which is believed to be responsible for the high rotational mobility of water. In the absence of five coordinated molecules the rotational and translation dynamics of

water are retarded and lead to decrease in entropy.[75-77] These studies also revealed that the orientational and vibrational relaxations of water are slowed down in the hydration shell of hydrophobic solute and there is hardly any effect in the long range. Moreover, recent MD-simulation studies also suggested that the water molecules surrounding small hydrophobic solutes form fewer but stronger H-bonds. These simulations also suggested that geometric excluded volume effects account for the retardation in rotational orientation of water in the hydrophobic hydration shell.[75]

It is being increasingly evident from the experimental and computational studies that the static and dynamic properties of water are affected by an ion/hydrophobic solute and are mainly confined within the hydration shell of an ion/solute and the role of water in various chemical and biological processes are largely fulfilled those water molecules that reside within the hydration shell. Therefore, it is important to understand the structure and properties of water in the hydration shell of an ion/hydrophobic molecular group. Recently, extensive experimental[65,78-82] and computational efforts[43,83] have been devoted to understand the properties of water in the hydration shell of ions/solutes. However, one of the greatest obstacles to study the structure of hydration shell water is that one has to selectively monitor the response of hydration water, which is technically challenging.

1.4. Vibrational Spectroscopy of Water

Vibrational spectroscopy is a promising technique to study the effect of ions/hydrophobic solutes on water structure, since the frequencies of intra/intermolecular vibrational modes

of water are sensitive to the H-bond strength and local environment.[84] Figure 1.1 shows the various intra and intermolecular vibrational modes of liquid water.

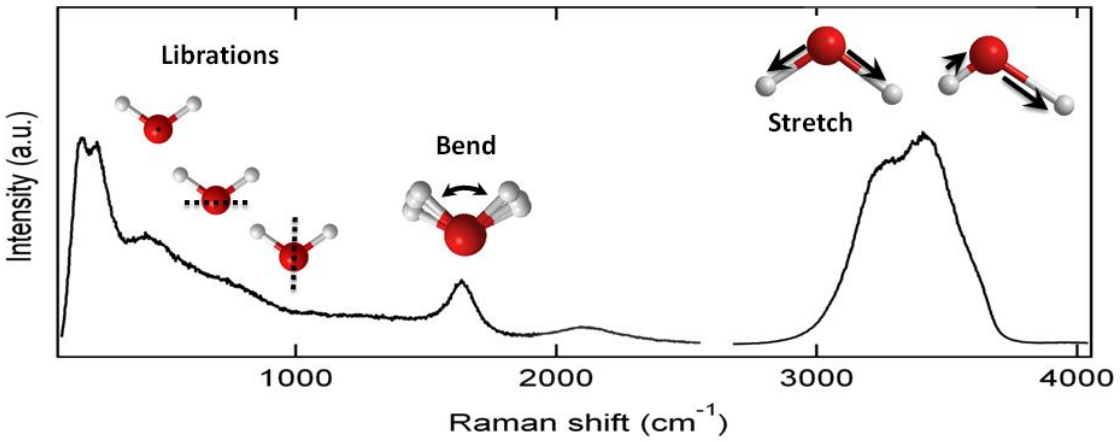

Figure 1.1. *Raman spectrum of water. The water molecules depict the intra (OH stretch (3000 – 3700 cm^{-1}) and HOH bend (1600 – 1700 cm^{-1})) and intermolecular (librational band below 1000 cm^{-1}) and combination ([bend +librational] band 1950 - 2200 cm^{-1}) vibrational modes of water.*

The vibrational frequencies of OH stretch vibrations are very sensitive to molecular environment, for instance, strongly (weakly) H-bonded water has weaker (stronger) O-H bond and that its OH stretch vibration appears in the low (high) frequency region of the OH stretch band. Liquid water has a continuous structure of varying H-bond strength such that at any instant liquid water has a wide range of H-bond distances and angles.[77] The wide variations of H-bond strengths/configurations lead to a distribution of OH stretch frequencies, which is reflected in the large spectral width of OH stretch band of water.

1.5. Intra/inter molecular Vibrational Coupling

Apart from H-bonding, vibrational coupling also contributes to the spectral width of the OH stretch and HOH bend modes. Intramolecular coupling, for example the coupling between the OH stretch fundamental (~3400 cm^{-1}) and HOH bend overtone ($2 \times 1645 = 3290$ cm^{-1}) (Fermi resonance, FR), leads to energy delocalization among 'stretch' and 'bend' modes of the same water molecule and deforms the OH stretch band by increased response at ~3250 cm^{-1} [85,86], whereas, the intermolecular vibrational coupling leads to vibrational delocalization among several water molecules. [87-90] As a result of these couplings, the vibration of water is extended among different vibrational modes as well as among several water molecules, and hence, represents a collective vibration of an ensemble of mutually interacting water molecules. Thus, the OH stretch band contains the combined response of both H-bond strength and/or the coupling effects (intermolecular coupling and FR) in liquid water.

Solutes in water (e.g. ions, hydrophobic/hydrophilic molecules) are likely to affect the H-bonding as well as vibrational coupling in liquid water. A vibrational probing of water, selective to the hydration shell of a solute, can shed light into the perturbation of these interactions. Interactions between ions/hydrophobic solute and water have been extensively studied by using vibrational (IR/Raman) spectroscopy.[91-95] Most of these studies have monitored the global changes in the IR/Raman spectrum, which were then used to understand the effects of ions/hydrophobic groups on the hydrogen bonding network of water. Nevertheless, the IR/Raman spectra of ions/hydrophobic groups in aqueous solutions contain the responses of both hydration shell and bulk water. In diluted

conditions, because of the larger concentration of bulk water than that of hydration water, the weaker hydration water signal gets buried into the stronger bulk water signal. As a result, understanding the hydration water is difficult from the experimentally recorded IR/Raman spectra of diluted salt/hydrophobic aqueous solutions. Moreover, as mentioned earlier the role of water in aqueous physicochemical processes is mainly governed by the properties of water in the hydration shell of the solutes. Therefore, it is important to elucidate the vibrational coupling of water in the hydration shell of a solute. However, because of the coherent character, and hence, inherently fast (<100 fs)[96] nature of delocalization via vibrational coupling, time-resolved IR spectroscopy techniques have not been applied successfully to understand the perturbation of vibrational coupling of water in the hydration shell of ion/hydrophobic molecular group.

We have combined Raman spectroscopy with multivariate curve resolution spectroscopy (Raman-MCR) to retrieve the response of hydration water from a combined response of hydration and bulk water. More specifically, the MCR-retrieved spectra (can be called as solute-correlated spectra, SC-spectra) contain the vibrational features of water that are perturbed by the solute as well as the vibrational bands of the solute itself.[78,97,98] This allows us to selectively extract the vibrational spectrum of water at the vicinity of ion/hydrophobic groups, which are often, buried in large bulk water signal in conventional IR/Raman measurements. An analysis of the band shapes of the MCR-retrieved spectra (OH stretch and HOH bend) with isotopic dilution has been used to elucidate the vibrational coupling (collective motion) and H-bonding of water in the hydration shell of ions and hydrophobic solutes. The first part of this thesis discusses the

structural perturbation of water in the hydration shell of ions and the hydrophobic molecular groups by using Raman-MCR in combination with isotopic dilution spectroscopy.

1.6. Protein-Drug Interaction

The secondary structure of protein is a consequence of the intermolecular forces including electrostatic, H-bonding, and hydrophobic interactions. The electrostatic interactions between charged amino acid residues and hydrophobic interaction between non-polar groups of amino acids lead to the folding of protein into a particular conformation. The delicate balance of these interactions provides stability and addresses the function of the protein structures. For instance, the electrostatic interactions between charged amino acid groups of the protein and ligand determine the binding location of the latter in the protein whereas optimization of hydrophobic interaction ultimately decides the overall stability of the protein-ligand complex. Therefore, understanding these elementary interactions are essential to elucidate protein-drug interaction and hence the bio-distribution, metabolism, elimination, and pharmacological effect of drugs in the body.

Protein-drug binding, depends on several factors such as intermolecular interactions of protein, ligand and the surrounding solvent, relative conformations of binding partners and the thermodynamics of molecular association.[99] Binding of a drug with protein in an aqueous environment is driven by the decrease in the free energy of the protein-drug complex compared to the free energy of both the drug and the protein existing independently in solution and can be represented by following equation 1.2.

$$Protein\ (P)_{aq} + Drug\ (D)_{aq} \overset{\Delta G}{\Leftrightarrow} Protein{:}Drug\ (PD)_{aq} \quad (1.2)$$

The Gibbs free energy change (ΔG) for interaction of the protein-drug complex is related to the standard Gibbs free energy change (ΔG^0_{bind}), under defined conditions (25 ºC and 1 M of both protein and drug) and can be represented as:

$$\Delta G = \Delta G^0_{bind} - RTln\frac{[Protein{:}Drug]}{[Protein][Drug]} \quad (1.3)$$

Where R is the universal gas constant ($J.mol^{-1}.K^{-1}$) and T denotes the absolute temperature (in K).

The change in free energy of protein-drug complex is associated with changes in enthalpy (ΔH) and entropy (ΔS) of the system according to the following relationship

$$\Delta G = \Delta H - T\Delta S \quad (1.4)$$

The change in enthalpy (ΔH) and entropy (ΔS) of protein-drug binding processes depends on the several factors such as the nature of interaction, conformational changes and role of solvent. For example, change in enthalpy (ΔH) is associated with breaking and making of various non-covalent interactions such as electrostatic, hydrogen bonding and hydrophobic contacts between protein-drug, protein-solvent and drug-solvent. The delicate balance of these interactions and their relative strength ultimately determines the overall binding process. Similarly, change in entropy (ΔS) of protein-drug binding is related to solvent displacement during binding process. As protein-drug complex formation takes place, the solvent molecules initially bound to the protein and drug detaches and leads to increase in entropy (ΔS).[100,101] However, formation of specific

interactions between protein and drug causes structural rigidity and decreases the entropy. Therefore, for spontaneous protein-drug complex formation, enthalpy-entropy compensation should be such that the free energy change (ΔG) is negative.[102-104]

The binding affinity of the protein-drug complex is depicted in terms of binding constant (K), which is related to the free energy change (ΔG) by the following equation:

$$\Delta G = -RTlnK \quad (1.5)$$

Where $K = \frac{[Protein{:}Drug]}{[Protein][Drug]}$

Different spectroscopic techniques such as absorption, fluorescence, NMR, and mass spectrometry are used to determine the binding affinity (K) of the protein-drug complex. Isothermal titration calorimetry (ITC) is the direct method to obtain the thermodynamic and binding affinity parameters. However, most of these experimental techniques provide binding affinity (K) parameter, which gives the macroscopic understanding about strength of interaction between protein-drug.[105]

Computational methods such as docking and molecular dynamic (MD) simulations have been developed over past few years for modeling and prediction of protein-drug interactions at molecular level.[106,107] Docking method generates the possible relative conformations of the ligand and protein in the protein-drug complex based on binding energy calculations. The binding energy calculations include contribution from different types of interactions such as hydrogen bonds, hydrophobic interactions and ionic interactions and also entropic contributions to the binding of drug with protein.[108]

Molecular docking provides residue specific information on the type of interaction between different groups of protein and drug that stabilizes the protein-drug complex. Additionally, MD simulations provide the stability and conformational dynamics of the protein-drug complex in aqueous environment. Therefore, the combination of experimental and computational methods may provide unique molecular level information about protein-drug binding interactions.

In recent years, there has been a growing interest in the use of tetrapyrrole based molecules, such as porphyrins and their derivatives as photosensitizing drugs in medicine, due to their characteristic properties, such as high quantum yield of singlet oxygen production, significant absorption at longer wave lengths, preferential tumor location, and minimal dark toxicity.[109-111] Porphyrin IX species such as protoporphyrin IX (PP), heamatoporphyrin IX (HP), heamatoporphyrin derivative (HPD), etc. are widely used photosensitizers in photodynamic therapy (PDT). Compared to current treatments including surgery, radiation therapy and chemotherapy, PDT offers the advantage of an effective and selective method of destroying diseased tissues without damaging surrounding healthy tissues.[112,113] Moreover, because of its intrinsic fluorescence and selective accumulation in the neoplastic tissues, HP-derivatives are used as marker in cancer detection (fluorescence diagnostics and imaging).[114,115]

One of the important limiting factors, which decide the efficiency of PDT is the preferential localization of porphyrin drug in the target tissues. As distribution of drug crucially depends on the interaction with plasma proteins, the knowledge of binding interaction between porphyrin drugs and plasma proteins is important to rationalize their

uptake and passive transport through the circulatory system. Serum albumin is one of the most abundant plasma protein and is used frequently to understand protein-drug interactions due to its high capability to bind and transport many endogenous and exogenous substances including amino acids, hormones, fatty acids, metals and foreign molecules such as drugs.[116-118]

Earlier studies on binding interaction of porphyrin derivatives with serum albumins, particularly related to HP and its derivatives were mainly based on the determination of the binding constant by utilizing the intrinsic fluorescence of either tryptophan of serum albumin or HP derivative, without further characterizing the mode of interaction and location and nature of binding sites at the molecular level. Most of the experimental studies provided only macroscopic understanding on the strength of interaction between serum albumin and HP.[115,119-124] From the experimental results of these studies, it is difficult to decipher the nature of interaction and the exact binding location of the drug in the protein. As mentioned earlier, computational methods such as molecular docking and MD simulations helps in studying the interactions between protein and drugs by identifying the possible binding sites in protein, obtaining the best geometry of drug-protein complex and calculating the energetic contribution of different non-covalent interaction in protein-drug complex.[125,126] In this perspective, the work in the chapter 7 of this thesis is carried out to understand the fundamental interactions involved in the binding of serum albumin with hematoporphyrin by using combined experimental and computational methods.

1.7. Protein-Quantum dot (QD) Interaction

A material which is size-restricted in three dimensions such that the electron wave functions are confined within its volume is called a quantum dot (QD). Due to this confinement the electronic properties of quantum dots depend on their size in the nanometer regime. The consequence of this confinement is quantization of the energy levels according to Pauli's exclusion principle (Figure 1.2). Accordingly, the energy gap between highest valence band and the lowest conduction band (band gap E_g) depends on the size of the QD. As the size of the QD decreases, the band gap (E_g) increases resulting in shift from red to blue in the emitted light. Therefore, QDs can emit at different regions of the spectrum depending on their size.[127-129] Furthermore, compared to organic fluorophores, QDs show high luminescence stability under excitation and significantly

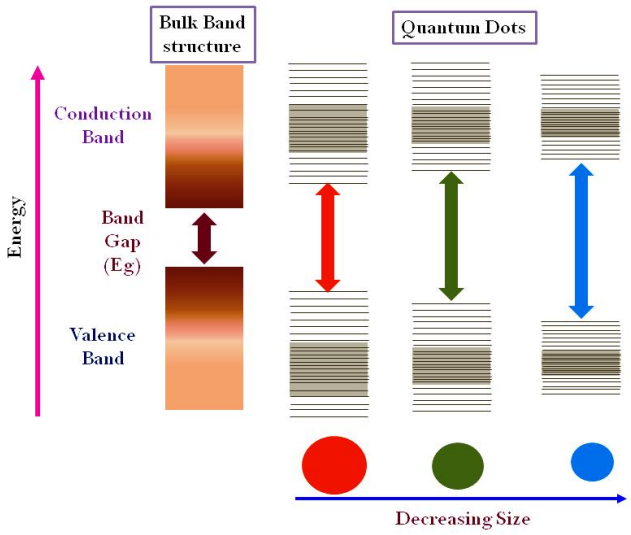

Figure 1.2. *Splitting of energy levels in quantum dots due to the quantum confinement effect, semiconductor band gap increases with decrease in size of the nanocrystals.*

lower photobleaching rates.[130] Moreover, the broad absorption spectra of QDs allow for the excitation of multiple QDs of different size with a single excitation wavelength. These fascinating optical properties make QDs suitable for different applications like light-emitting diodes, thin-film transistors, optoelectronics, sensors, solar cells, superionic materials, laser materials and especially in bio-medical applications like medical imaging, biosensors, etc.[128,131-137]

Semiconductor QDs are synthesized by various methods including chemical route, electrochemical, photochemical, radiation-chemical, etc. with fine tuning of their size and optical properties using surfactants, amines, thiols, and phosphates as surface passivating agents in condensed phase.[138,139] However, most of these methodologies involve stringent conditions, such as high temperature, pressure, inert atmosphere, use of toxic reducing agents and so on. Moreover, QDs synthesized by above chemical routes are not suitable for *in vivo* biological applications since the additional foreign toxic reagents are mostly incompatible with biological systems and/or might even induce reactions in them. Since most of the passivating agents are toxic in nature it is desirable to find capping agents that are biocompatible as well as provide nanomaterials with the desired aqueous solubility. In this perspective, extensive research has been directed toward synthesis of QDs conjugated with biomolecules such as amino acid, protein, and antibodies. Such conjugated biomolecules on the surface QDs impart biocompatibility and efficient use in various biological applications.[140] Several synthesis methods for linking proteins to QDs have been explored. However, it is observed that preparation of protein-conjugated QDs using linking ligands is a complex process that usually consist of several steps and leads to

difficulty in obtaining chemically stable protein-conjugated QDs with desired properties.[140,141]

Alternatively, researchers are now developing new synthesis methods inspired by biomineralization.[142] Biomineralization is a natural process in which biological organism's intake inorganic species to subsequently form natural inorganic materials, such as bone, dental structures, shells, and silica skeletons.[143-146] In this process, different organisms use specific interactions between the peptide or protein and inorganic species to collect and transport raw materials and nucleate them steadily and uniformly into ordered composites. This natural phenomena motivated scientists to use biomolecules such as proteins, DNA, and RNA as templates/building blocks for semiconductor QDs synthesis and named them as "Bio-inspired" or "Biomimetic" methods. This biomimetic synthesis approach of semi conductor QDs is attractive for a number of reasons. First, peptides and proteins make the bioenabled syntheses of semiconductor QDs inherently "green" process due to mild reaction conditions, aqueous solution chemistry, and absence of strong reducing agents. Secondly, proteins and peptides can exquisitely control the size, shape, optical properties, and crystal structure of the QDs. Due to specific interactions between inorganic ions and biomolecules, the surface of semiconductor QDs is effectively capped by different functional groups of biomolecules and provide bioactive functionalities throughout the QD surface for application in luminescence tagging, drug delivery, and many other applications.[142]

In recent times, studies on the synthesis of QDs by biomimetic route using biological macromolecules, such as amino acids, proteins, DNA and RNA have gained

momentum.[136,147-154] However, most of these studies report the use of external reducing agents at stringent conditions. Such conditions are expected to damage the inherent native structure of biomolecules and eventually making the QDs inappropriate for the bio-related applications. Moreover, as the optical properties of the QDs strongly depend on their size and shape due to quantum size effects, controlling the shape and morphology of QDs is one of the most important aspects in any synthesis method. Thus, Chapter 8 of this thesis presents room temperature green synthesis of CdSe nanoparticles in the serum albumin protein matrix.

1.8. Outline of the Thesis

As discussed in the previous sections, the central theme of this thesis is the study of structural changes of water in the hydration shell of ion/hydrophobic molecular groups. We study the effect of ion/hydrophobic groups on the structure of water (H-bonding and intermolecular vibrational coupling) by combining Raman spectroscopy with multivariate curve resolution (MCR) analysis. Raman-MCR enables us to decompose experimental Raman spectra into solute correlated (SC) and bulk water components. The SC component spectra contain features from the water molecules perturbed by the ions/hydrophobic solute as well as the vibrational bands of ions/solute. This allows us to selectively extract the true vibrational spectrum of hydration water at the vicinity of ion/hydrophobic groups and to obtain unique understanding about the structure of water (hydrogen bonding and intermolecular vibrational coupling) in the hydration shell.

In Chapter 2 we describe the experimental techniques and data analysis methods employed in this research work.

In Chapter 3, we investigated the changes in spectroscopic properties of water (e.g. Raman cross-section, σ) and the coupling among different vibrational modes of water (e.g. coupling between OH stretch fundamental (ν_1) and HOH bend overtone ($2\nu_2$) which is known as Fermi resonance (FR)) in concentrated alkali halide (NaX) solution.

Chapter 4 focuses on hydrogen bonding and vibrational coupling of water in the hydration shell of ions. In this chapter, we combine multivariate curve resolution (MCR) analysis with the Raman spectra of diluted (<1.0 mol dm^{-3}) aqueous salt solution (Raman-MCR spectroscopy) that provide the vibrational response selective to the hydration water.

In chapter 5 we discussed the structure of water in the hydration shell of uncharged (tert-butanol, TBA) and charged (tetramethylammonium cation, TMA^+) hydrophobic molecular groups. In this chapter, we combined Raman-MCR with isotopic dilution spectroscopy to investigate the intra-/intermolecular vibrational coupling and H-bonding of water at uncharged and charged molecular hydrophobic interfaces.

Chapter 6 deals with the interaction of ions and water with the methyl groups that are attached to positively charged nitrogen. In this study, we directly compare the vibrational response of methyl groups attached to positively charged nitrogen (in TMAO and PC-head group) with that of a typical non-polar methyl and polar carbonyl groups for the unambiguous assignment of their polar/non-polar nature.

The last two chapters are concerned with the role of molecular interactions in protein-ligand binding and nanoparticle synthesis. Chapter 7 deals with the molecular level interaction between bovine serum albumin (BSA) and hematoporphyrin (HP), a well known photosensitizer used in photodynamic therapy. This study has been carried out in

aqueous buffer solution using steady state and time-resolved emission techniques. The results have been further substantiated by molecular docking and molecular dynamics (MD) simulation.

Chapter 8 describe the room temperature green synthesis of CdSe nanoparticles in the serum albumin protein matrix. This chapter extensively discusses the role of interactions between protein amino acid groups and inorganic ions in controlling the morphology and optical properties of CdSe QDs.

Chapter 2

Experimental Techniques

2.1 Introduction

This chapter gives an overview of the various experimental techniques employed for the research work described in this thesis. Raman spectroscopy has been used extensively to understand structure and properties of water in the hydration shell of ions and hydrophobic solutes. Therefore, a detailed theoretical background of Raman spectroscopy is described, along with an overview of Raman instrumentation that has been used for this work. In general, Raman spectroscopy does not provide the vibrational characteristics of water selective to the hydration shell; rather it gives the combined response of hydration shell water and bulk water for an aqueous solution of a solute. We have applied multivariate curve resolution analysis (MCR-analysis) on the experimentally recorded Raman spectra of aqueous electrolytes/hydrophobic solute solutions to retrieve the vibrational characteristics of hydration water from the combined response of hydration and bulk water. The basic principles and analysis methodology of MCR are also outlined. To understand the binding interaction between protein and porphyrin drug as well as the optical properties of CdSe QD's, both steady-state and time-resolved photophysical

measurements have been carried out using absorption and fluorescence techniques. Important aspects of different instrumental techniques are briefly described in this chapter.

2.2 Raman Spectroscopy

Raman Spectroscopy is a vibrational spectroscopy technique based on the phenomenon known as *Raman effect*, named after the Indian scientist Sir Chandrasekhara Venkata Raman who first discovered it in 1928 (Nobel prize in 1930).[155-157] Raman Effect arises when monochromatic light is incident on a molecule and interacts with the dipole moment of the molecule. Most commonly, when monochromatic light i.e. the incoming photons interact with the electron cloud of the molecule, it results in elastic scattering (Rayleigh scattering) in which the incident photons does not exchange energy with the interacting molecule and scattered with the same energy (frequency). However, a small fraction of the light (1 in 10 million photons) upon interaction with sample exchanges energy with the molecules and scattered at frequencies different from the incident light. During this scattering, the frequency of the scattered light is either higher or lower than the frequency of the incident light depending on the particular process. When a photon of energy $h\nu_0$ is absorbed by the molecule in the ground state, part of the photons energy is transferred to the Raman active mode with frequency ν_m and the resulting frequency of scattered light is lower to $\nu_0 - \nu_m$ and is termed Stokes Raman scattering as shown in Figure 2.1. At room temperature, the thermal population of vibrational excited state is low, although not zero. Therefore, for the majority of molecules, the initial state is the

ground vibrational state, and the scattered photon will have lower frequency (longer wavelength) than the exciting photon (Stokes shift). According to the Boltzmann population of states, a small fraction of the molecules are in vibrationally excited states. Thus, when a photon of energy $h\nu_0$ is absorbed by a Raman active molecule which at the time of interaction, is already in the excited vibrational state, excessive energy of the Raman active mode is released and the molecule returns to the ground vibrational state. [158] The resulting frequency of scattered light goes up to $\nu_0 + \nu_m$ and is termed Anti-stokes Raman scattering which is also shown in Figure 2.1.

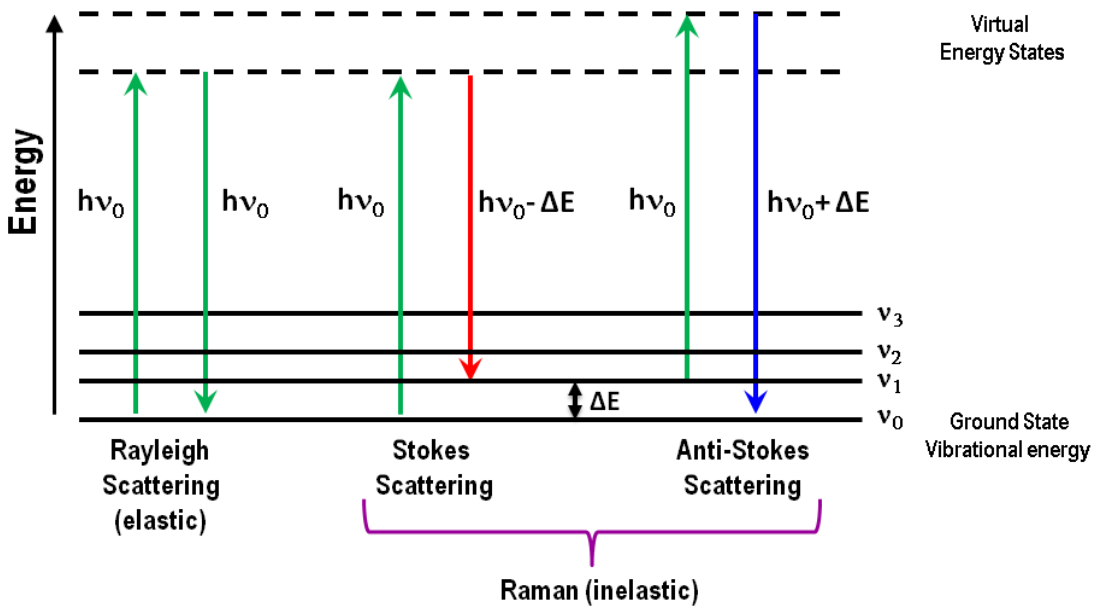

Figure 2.1. *Energy level diagram showing the states involved in the Rayleigh and Raman scattering. Green lines signify incident light, the red line signifies Stokes Raman scattering, and the blue line signify anti-Stokes Raman Scattering. The energy of the incident laser beam is denoted by* $h\nu_0$ *and* ΔE *represent the vibrational energy of the molecule (*$h\nu_m$*).*

The frequency shifts of the incident monochromatic light corresponds to the vibrational energy levels of a molecule, and hence, provides the vibrational signature of molecules. The vibration of a molecule, which is characteristics of the molecule, also depends upon its interaction with neighboring molecules. Therefore, analysis of the Raman spectra (vibrational response) provides valuable insight about the structure of molecules and their interactions with the surroundings. As a scattering process, however, the Raman Effect is exceedingly weak: typical Raman cross sections per molecule range between 10^{-30}-10^{-25}cm^2 compared to fluorescence cross sections. (typically 10^{-17}-10^{-16}cm^2).[159] However, recent technological advances with efficient lasers, charge-coupled devices, optical fibers, and computers have transformed Raman spectroscopy as a versatile and extremely useful technique to study vibrational structures of molecules by overcoming the major impediments of low scattering efficiency, fluorescence interference, and inefficient light collection and detection.[159]

2.2.1 Theory of Raman Scattering

The physical origin of Raman scattering is the change in molecular optical properties due to the electric field ($\vec{E}$) of incident light. The interaction of light with molecular systems can be interpreted in terms of classical as well as quantum mechanical pictures. In classical interpretation, light is considered as electromagnetic radiation, with an oscillating electric field that induces a dipole moment (polarization) while interacting with molecules. The resulting oscillating induced dipole moment emits an EM radiation, thereby resulting in scattered light.[159,160]

Classical Theory of Raman Scattering

The classical theory of the Raman Effect is based upon polarizability of molecules, which reflects how easily the electron density distribution of a molecule/bond can be distorted by an electric field. According to classical theory, when the electric filed ($\vec{E}$) of the light interacts with a molecule, the equilibrium distribution of the negatively charged electron cloud of the molecule is perturbed, which gives rise to an induced dipole moment (μ_i). Thus, the induced dipole moment per unit volume (known as the polarization, P) of the macroscopic system is proportional to the incident electric filed $\vec{E}$ (assuming that the intensity of the incident light is not high enough to introduce nonlinear polarization).

$$N\,\overrightarrow{\mu_i} = \vec{P} \propto \vec{E}$$

$$\vec{P} = \alpha \vec{E} \tag{2.1}$$

Where, N is the number dipoles in unit volume and α is the proportionality constant, known as polarizability. The oscillating electric field of the incident light can be written as,

$$\vec{E} = E_0 \cos(2\pi\nu t) \tag{2.2}$$

Where E_0 is the amplitude of the electric field vector and ν is the frequency of the incident light, and t is time. Thus from eq. 2.1 and 2.2,

$$\vec{P} = \alpha E_0 \cos(2\pi\nu t) \tag{2.3}$$

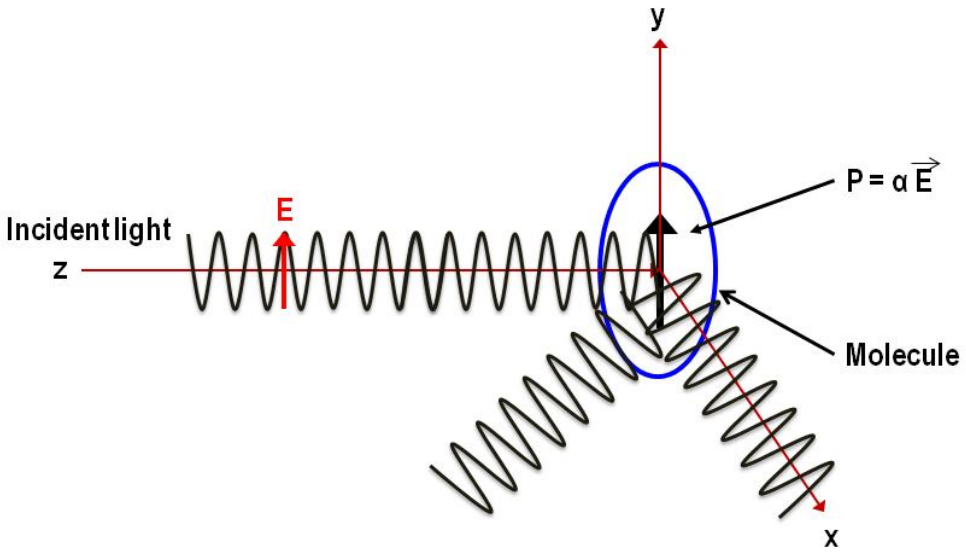

Figure 2.2. *Polarization (P) induced in a molecule's electron cloud by an incident optical electric field $\vec{E}$. Scattering may be in various directions.*

Thus, the polarization (dipole moment density) also oscillates at the frequency of the incident light (ν).This oscillating polarization becomes the source of scattered light at the frequency ν which is same as that of the incident light (Rayleigh scattering).

The polarizability of the molecule is a function of the instantaneous position of constituent atoms and depends on the molecular vibrations. Thus, the 'α' of a vibrating molecule can be described as a time varying quantity related to the frequency of the vibration of the molecule. For small atomic displacements, α can be expressed by a Taylor series expansion given by,

$$\alpha = \alpha_0 + \left(\frac{\delta\alpha}{\delta Q}\right)_0 Q + \cdots, \qquad (2.4)$$

where, α_0 is the polarizability of the molecule at its equilibrium position, Q is the vibrational coordinate and $\left(\frac{\delta\alpha}{\delta Q}\right)_0$ is the rate of change of the polarizability with the vibration at the equilibrium position of the molecule.

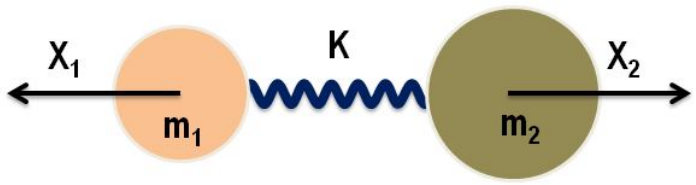

Figure 2.3. *Diatomic Molecule as a Spring –Mass System*

The classical interpretation of the vibration of a molecule, can be derived by considering a simple diatomic molecule as two masses connected by a spring (as shown in Figure 2.3) where *m* represents the atomic mass, *x* represents the displacement, and *K* represents the bond strength (Spring Constant). By using this approximation, according to Hooke's law the displacement of the molecule can be expressed as

$$\frac{m_1 m_2}{m_1+m_2}\left(\frac{d^2x_1}{dt^2}+\frac{d^2x_2}{dt^2}\right) = -K(x_1 + x_2) \qquad (2.5)$$

By replacing the reduced mass $\left(\frac{m_1 m_2}{m_1+m_2}\right)$ with μ and the total displacement $(x_1 + x_2)$ with *Q*, the equation can be simplified to,

$$\mu\frac{d^2Q}{dt^2} = -KQ \qquad (2.6)$$

By solving this equation for *Q* we get,

$$Q = Q_0 \cos(2\pi\nu_m t) \quad (2.7)$$

Where Q_0 is the amplitude of the displacement and ν_m is its vibrational frequency and is defined as,

$$\nu_m = \frac{1}{2\pi}\sqrt{\frac{K}{\mu}} \quad (2.8)$$

Based on the vibrational displacement of Eq. (2.7), the polarizability may be given as

$$\alpha = \alpha_0 + \left(\frac{\delta\alpha}{\delta Q}\right)_0 Q_0 \cos(2\pi\nu_m t) \quad (2.9)$$

Using Eq. (2.9), Eq. (2.3) can now be written as:

$$\vec{P} = \alpha_0 E_0 \cos(2\pi\nu t) + \left(\frac{\delta\alpha}{\delta Q}\right)_0 E_0 Q_0 \cos(2\pi\nu_m t)\cos(2\pi\nu t) \quad (2.10)$$

Using the trigonometric formula $\cos A \cos B = \frac{1}{2}\{\cos(A-B) + \cos(A+B)\}$, the above Eq. can be written as

$$\vec{P} = \alpha_0 E_o \cos(2\pi\nu t) + \left(\left(\frac{\delta\alpha}{\delta Q}\right)_0 \frac{E_o Q_o}{2}\right)\{\cos 2\pi[(\nu - \nu_m)t] + \cos 2\pi[(\nu + \nu_m)t]\} \quad (2.11)$$

The first term in right hand side of equation 2.11, $\alpha_0 E_o \cos(2\pi\nu t)$, provides the mathematical expression of the elastic Rayleigh scattering, which is the dominant effect and results in no change in the frequency of the incident light (ν).The second term in right hand side of equation 2.11, $\left(\left(\frac{\delta\alpha}{\delta Q}\right)_0 \frac{E_o Q_o}{2}\right)\{\cos 2\pi[(\nu - \nu_m)t] + \cos 2\pi[(\nu + \nu_m)t]\}$, is

the Raman scattered component, which occurs only if vibrations change polarizability ($\frac{\delta\alpha}{\delta Q} \neq 0$). The change in the polarizability ($\frac{\delta\alpha}{\delta Q}$) of the molecules causes shift in the frequency of the incident light (v) by $\pm v_m$, the frequency of the molecular vibration. The increase in frequency ($v + v_m$) is known as the anti-Stokes shift and the decrease in frequency ($v - v_m$)) is known as the Stokes shift (Figure 2.1). Therefore, the vibrational frequency of a molecular bond can be analyzed by measuring the change in frequency from the incident light i.e. Stokes or anti-Stokes Raman shift.[159,161-163]

2.2.2. Micro-Raman Instrumentation

Experimental Raman spectra presented in this thesis have been collected using a micro-Raman spectrometer (STR-300, SEKI Technotron, Japan). The optical layout of the micro-Raman setup is shown in Figure 2.4. A fiber coupled 532 nm CW diode pumped solid state laser (50mW, DPSS, gem532, Laser Quantum) was initially passed through a band pass filter (532nm), which removes wavelengths other than 532nm. The laser is then passed through dichroic mirror (532nm) and 10/90 (R/T) beam splitter (BS). The light transmitted through the BS is directed into an objective lens of magnification 10X (Olympus, N.A. 0.30) and focused onto the sample contained in 2 mm spectroscopic quartz cell. The Raman scattered light was collected by the same objective lens and passed through a long pass filter (LPO3-532RU-25, Semrock). The long pass filter rejects the Rayleigh and anti-stokes scattered light and allows only stokes signal to pass through. The stokes signal after the long pass filter was focused by a lens onto a fiber and coupled to a 300 mm focal length imaging spectrograph (Action series SP2300i, 1200groove/mm)

and detected by a thermo-electric cooled (-75°C) charge coupled device (CCD) detector (Pixis 256 CCD camera, Princeton Instruments). The spectrograph was calibrated using the 520.5 cm^{-1} line from silicon wafer and was verified by measuring the Raman spectrum of naphthalene and sulphur. The spectral and spatial resolution of the Raman system was nearly 1.5cm^{-1} and 0.5µm (with 100X objective lens), respectively.

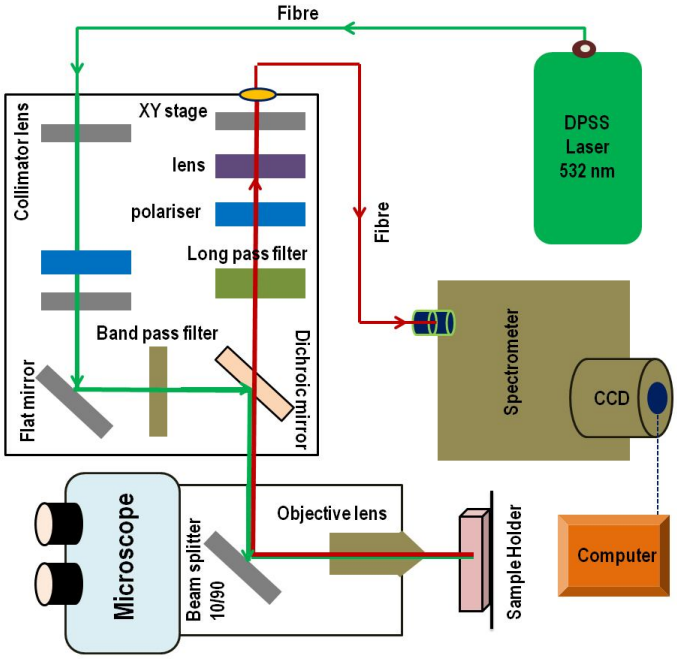

Figure 2.4. *Optical layout of the of Micro-Raman Instrumentation.*

2.3 Solvation Shell Spectroscopy

Raman (vibrational) spectroscopy provide a promising experimental technique for investigating solute-solvent interactions by monitoring changes in the vibrations of chemical bonds of solute and/or solvent molecules in solution. For instance, the changes in the vibrational frequencies of OH stretch band of water provide information about the

structural changes of water in presence of solute molecules. Conventional IR and Raman spectra of dilute solutions contain the responses of solvent, solute, and solvent molecules perturbed by solute. Because of larger concentration of bulk solvent than that of solvent molecules perturbed by solute (solvation shell), the weaker solvation shell signal gets buried into the stronger bulk solvent signal.[97] As a result, understanding the perturbation of solvent in presence of solute is difficult from the experimentally recorded IR and Raman spectra of dilute solutions.

Conventional data analysis techniques, such as difference spectroscopy, peak fitting are used to obtain information about the perturbations of solvent by solute.[164-166] In difference spectroscopy, the contribution of bulk solvent to the solution spectrum is separated by subtracting proportionate bulk solvent spectrum from the solution spectrum.[91,94,167] However, this method does not produce the true spectral features of perturbed solvent molecules. In peak fitting method, spectra are fitted with presumed functional forms and number of components.[168-170] Thus, the result of fitting analysis often depends on the assumed model and does not provide unique solution.

In the present thesis, we have applied a new approach known as multivariate curve resolution (MCR) to extract the vibrational response of solvent molecules perturbed by the solute from a combined response of solvation shell and bulk solvent. This approach differs from the conventional difference spectroscopy and peak fitting methods.[98] MCR method does not have any assumption regarding the fitting parameters, such as amplitude,

position, and width of either the bulk solvent or the solvent perturbed by solute. The basic principles and analysis methodology of MCR is outlined in the following sections.

2.4. Multivariate Curve Resolution (MCR)

Multivariate curve resolution (MCR) is a broad class of data analysis method that is widely used in the quantitative analysis of multi-component mixtures in chromatographic, kinetic, environmental, and biochemical studies[171-175]. The main goal of these methods is to perform a mathematical decomposition of instrumentally unresolved spectral response of mixtures to extract the number of individual components, their spectral response and the concentration profiles. MCR methods have been successfully used to analyze data from infrared spectroscopy, chromatography, nuclear magnetic resonance, hyper spectral imaging, and mass spectrometry.[176-180]

MCR method is based on a bilinear model, which decomposes the experimental data matrix D (m x n) into product of two matrices C (m x k) and S^T (k x n), each of them containing concentration and spectral profiles of the k components in the mixture respectively, according to Eq. (2.12): [181-185]

$$D= CS^T+ E \qquad (2.12)$$

where E (m x n) is the error matrix.

2.4.1. Singular Value Decomposition (SVD)

MCR methods are known as model free (since they do not require any prior knowledge or assumption about the nature and composition of the system). However, the information

about the number of components present in the system is needed for MCR analysis. This number of pure components is estimated by rank analysis of the data matrix applying factor analysis methods. Singular value decomposition (SVD) is one of the most widely used factor analysis method to estimate chemical rank of a data matrix. SVD is the factorization of a matrix X of real or complex numbers.[186-188] Let X be an m x n matrix; mathematically SVD of X can be expressed as follows:

$$[X]_{m\times n} = [U]_{m\times r}[\Sigma]_{r\times r}[V^T]_{r\times n} \quad (2.13)$$

Besides, U and V are orthogonal so that

$$U^T U = I$$

and

$$V^T V = I$$

Where, I is the identity matrix.

The columns of U are the left singular vectors of the matrix X, and the columns of V (or the rows of V^T) are the right singular vectors. The matrix Σ is a diagonal matrix, whose diagonal values are the singular values of the matrix X.

Mathematical calculation of SVD is to find the eigen vectors and the eigen values of XX^T and X^TX. The eigen vectors of XX^T are the columns of U and the eigen vectors of X^TX are the columns of V. The singular values of X, in the diagonal matrix Σ, are the square root of the eigen values of XX^T and X^TX. The number of singular values of a

matrix is the rank of that matrix, which is the number of linearly independent columns or rows of a matrix and represents the number of pure components present in the system.

2.4.2. Ambiguities in MCR

The main limiting issue that affects the resolution of the component concentration and spectral profiles in MCR analysis is the non-unicity of the solution, the so called ambiguities of the solution.[98,189] Ambiguities means many pairs of C and S^T type matrices can be reproduce the original data matrix with the same fit quality as true solutions. In other words, the correct reproduction of the original data matrix can be achieved by using component profiles differing in shape (rotational ambiguity) or in magnitude (intensity ambiguity) from the original profiles. Mathematically these MCR ambiguities can be explained as follows:

The basic equation associated with MCR bilinear model, $D = CS^T$, can be rewritten as

$$D = C (T T^{-1}) S^T \quad (2.14)$$

$$T T^{-1} = 1$$

$$D = (CT) (T^{-1}S^T) \quad (2.15)$$

$$D = C' S'^T$$

Where $C' = C T$ and $S'^T = T^{-1}S^T$ are rotationally equivalent to the real C and S^T and describe the D matrix as correctly as the true C and S^T matrices do, though C′ and S'^T are not sought solutions. Due to rotational ambiguity, MCR method can potentially give as

many solutions as T matrices can exist. Often this may provide an infinite set of solutions, unless C and S^T are forced to obey certain conditions.

Similarly, intensity ambiguity arises from the following mathematical expression, as shown in equation 2.16.

$$D = \sum_{i=1}^{n} \left(\frac{1}{k_i} c_i\right)\left(k_i S_i^T\right) \quad (2.16)$$

Where k_i are scalars and *n* refers to the number of pure components. Each concentration profile of new C′ matrix would have the same shape as the real one, but it would be k_i times smaller, whereas the related spectra of the new S'^T matrix would be equal to the real spectra, though k_i times more intense. Different approaches have been proposed to overcome these ambiguity problems. Rotational ambiguity may be resolved by including extra information during the MCR analysis, such as known reference spectra. Alternatively, imposing certain constraints such as non-negativity and unimodality can improve the analysis procedure further to obtain true spectral or concentration profiles.[190,191]

2.4.3. Alternative Least Square (ALS) Method

The initial estimates of C′ and S′, obtained from the SVD, were further improved by alternating least square fitting (ALS) method. This method uses alternative approach to find the matrices of C′ and S′ by optimizing both at each iterative cycle.

Under appropriately chosen constraints, the ALS method involves solving of following two least square problems:

Given the spectra matrix S, the concentration matrix C can be estimated as:

$$C = DS(S^TS)^{-1} \quad (2.17)$$

And, given the concentration matrix, the spectra matrix can be estimated as:

$$S = D^TC(C^TC)^{-1} \quad (2.18)$$

Equation 2.17 and 2.18 are solved sequentially, i.e., in each iterative cycle, the concentration matrix C is calculated and this new C is used to get the spectral matrix S^T and similarly we use S^T to calculate C. The convergence criterion in the alternating least-squares optimization is based on the comparison of the fit obtained in two consecutive iterations. When the relative difference $||X - CS^T|| = E$ in a fit is below a threshold value, the optimization is achieved.

2.5. Raman-MCR: Hydration Shell Spectroscopy

We combined Raman spectroscopy with MCR analysis (Raman-MCR) [98,192-195] to study the structural changes of water in the hydration shell of ion / hydrophobic groups. In dilute aqueous solutions, solute-solute interactions are negligible. Under such condition, we can state that the solution spectrum (S_T) is a linear combination of the response of solute (R_S), bulk water (R_{BW}), and solute-perturbed water (*i.e.* hydration shell water R_{HW}).

$S_T = R_{S+} R_{BW +} R_{HW}$

Or, $S_T = C_{BW}S_{BW+} C_SS_{S+} C_{HW}S_{HW}$ (2.19)

Where C_{BW} and S_{BW} are the concentration and the spectrum of the bulk water, C_S and S_S are the concentration and the spectrum of the solute, and C_{HW} and S_{HW} are the concentration and the spectrum of water molecules in the solute hydration shell.

Both $C_S S_S$ and $C_{HW} S_{HW}$ terms in the above equation are linearly correlated with the solute concentration *i.e.* $C_{HW} = kC_S$. Therefore, we can combine these two terms and collectively represent with one term as:

$$S_T = C_{BW} S_{BW+} C_S S_{S+} kC_S S_{HW} \quad (2.20)$$

$$S_T = C_{BW} S_{BW+} C_S [S_{S+} kS_{HW}]$$

$$C_S [S_{S+} kS_{HW}] = C_{SC} S_{SC} \quad (2.21)$$

$$S_T = C_{BW} S_{BW+} C_{SC} S_{SC} \quad (2.22)$$

C_{SC} and S_{SC} are the solute-correlated concentration and spectrum, respectively. To extract the solute-correlated spectrum (S_{SC}) *i.e.* Raman spectrum of water perturbed by solute, we record a series of Raman spectra of water in presence of different concentration of solute. Then the area normalized Raman spectra were arranged in to the rows of a matrix, X. The first row corresponds to the spectrum of bulk water and the other rows contain the spectra of solutions with varying concentration of solute. The data matrix X of size $m \times n$ can be written as

$$[X]_{m\times n} = \begin{bmatrix} x_{11} & x_{12} & \cdots & x_{1n} \\ x_{21} & x_{22} & \cdots & x_{2n} \\ \vdots & \vdots & \ddots & \vdots \\ x_{m1} & x_{m2} & \cdots & x_{mn} \end{bmatrix}$$

As a result, the columns of X can be regarded as vectors in the space of concentration profiles; and the rows can be thought of as vectors in the space of spectral profiles. As mentioned earlier, the main objective of multivariate curve resolution (MCR) analysis is to extract the linearly independent spectral components from the data matrix X. In order to do so, the data matrix is decomposed by singular value decomposition (SVD) as discussed in section 2.4.1.

$$[X]_{m\times n} = [U]_{m\times r}[\Sigma]_{\mathrm{r}\times\mathrm{r}}[V^T]_{r\times n} \tag{2.23}$$

The singular value decomposition gives two sets of singular vectors $\boldsymbol{u}$'s (columns of the matrix U) and $\boldsymbol{v}$'s (columns of the matrix V) which are eigen vectors of the matrices XX^T and X^TX respectively. Since both these matrices are symmetric $(A^T = A)$, their eigen vectors can be chosen orthonormal. Since $\boldsymbol{u}$'s and $\boldsymbol{v}$'s constitute the columns U and V, orthogonality gives $V^TV = I = U^TU$. The singular vectors $v_1, v_2, \dots, v_r$ are in the row space of X and the singular vectors $u_1, u_2, \dots, u_r$ are in the column space of X. Since the row space of X contains information about the spectral profile, $\boldsymbol{v}$'s constitute the basis vectors for the spectral profile. Similarly $\boldsymbol{u}$'s constitute the basis vectors for the column space, i.e., the concentration profile. The rank (r) of the data matrix X gives the number of independent spectral components contained in X so that there will be r significant singular values (σ's) in the diagonal matrix Σ. Accordingly, the singular value decomposition can be expanded as:

$$[X]_{m\times n} = [U]_{m\times r}[\Sigma]_{\mathrm{r}\times\mathrm{r}}[V^T]_{r\times n} = [u_1 \quad \cdots \quad u_r]\begin{bmatrix}\sigma_1 & & \\ & \ddots & \\ & & \sigma_r\end{bmatrix}\begin{bmatrix}v_1^T \\ \vdots \\ v_r^T\end{bmatrix}$$

or

$$X = u_1\sigma_1 v_1^T + u_2\sigma_2 v_2^T + \cdots + u_r\sigma_r v_r^T \quad (2.24)$$

Arranging the singular values in descending order $\sigma_1 \geq \sigma_2 \geq \cdots \geq \sigma_r > 0$, the SVD gives the rank-one (component wise) pieces of the data matrix X in the order of importance. The expansion in equation (2.24) can be rearranged as

$$X = c_1 s_1^T + c_2 s_2^T + \cdots + c_r s_r^T = CS^T \quad (2.25)$$

Where, $c_i = u_i$ are the concentration components; and $s_i^T = \sigma_i v_i^T$ are the spectral components. C is the matrix with the concentration profile vectors (c_i) as columns and S is the matrix with component spectra (s_i) as columns.

In the case of diluted solutions, it is likely that the data matrix X contains two independent spectral components: (i) bulk water and (ii) the water molecules around the solute as well as the intramolecular vibrational bands (if any) of the solute. Hence, the number of significant singular values (σ's) is expected to be two. Thus after SVD, two most prominent singular values are retained and the rest of the singular values, usually very small, are assumed to be due to experimental noise. Thus, the equation (2.24) can be rewritten as

$$X = u_1\sigma_1 v_1^T + u_2\sigma_2 v_2^T + E = c_{BW} s_{BW}^T + c_{SC} s_{SC}^T + E = C`S`^T + E \quad (2.26)$$

Where, E is the experimental noise matrix. The initial estimates of C` and S`, obtained from the SVD, were further improved by alternating least square fitting (ALS) method as discussed in section 2.4.3. The resulted s_{SC}^T spectrum known as solute correlated spectrum (SC) and contain vibrational spectral feature arising from water molecules around the

solute and solute itself.[98,195,196] In the case of salt solutions, where there is no intramolecular vibrational feature of ions, SC spectrum essentially represents the vibrational spectrum water molecules in the hydration shell of ions (Ion-correlated spectrum).

2.6. Steady-State Absorption Measurements

Optical absorption (Ultraviolet-visible; UV-vis) spectroscopy is a widely used technique to obtain the information about the ground state of the chemical system (wavelength of absorption and extinction coefficients of the absorbing molecules at different wavelengths). It provides information about electronic transitions from ground state to excited state, which allows the characterization or identification of the molecules.[197-199]

The absorbance of a sample is given by "Beer-Lambert's law"[200,201]

$$A = log\left(\frac{I_0}{I}\right) = \varepsilon_\lambda Cl \tag{2.27}$$

Where, C and l corresponds to concentration of chromophore in a solution and optical path length of the light beam passing through the sample (typically 1cm, quartz cell), respectively. The molecular extinction coefficient (ε_λ) is a wavelength dependent property and vary for different "type of electronic transitions". It allows quantitative and qualitative measurements such as solvent polarity, hydrogen bonding, charge transfer effects on electronic transitions of molecule. Hence, this simple photochemical technique gives preliminary information regarding the nature of interactions between a chromophoric molecule and its surrounding environment.[202,203] In this work, absorbance

measurements were carried out on a JASCO V650 UV-visible spectrophotometer. Typical wavelength range is 200-900 nm. As the light sources, spectrophotometer use W-lamp for the 900 to 350 nm region and a D_2 lamp for the 350-200 nm region. Si-photodiodes are used as the light detectors. The minimum wavelength resolution for the spectrophotometer is 0.2 nm and lowest absorbance measurable is ~0.005.

2.7. Steady-State Fluorescence Measurements

Fluorescence spectroscopy is the most sensitive and extremely powerful technique to investigate various photochemical processes that occur in the excited state of the chromophoric molecules. Fluorescence generally occurs when a molecule absorbs light photons from the UV/visible (200-900 nm) light spectrum, known as excitation, and then rapidly emits light photons of a longer wavelength as it returns to the ground state. All chemical compounds absorb energy which causes transition of molecules from initial electronic energy state to higher energy electronic state. The absorbed energy is equivalent to the difference between the initial and higher electronic energy states. This value is constant and characteristic of the molecular structure. This value termed as the excitation wavelength, is characteristic of the molecule involved. The excited molecule returns to ground state by releasing the energy through heat and/or emission of photons. The emission wavelength equivalent to the difference between two discrete energy states is also characteristic of the molecular structure. Thus, fluorescence spectroscopy establishes the relationship between absorbed and emitted photons at specified wavelengths. The characteristic properties of the fluorescence photons such as energy (wavelength), lifetime, polarization and intensity (number of photons at a given

wavelength) are very sensitive to the local environment surrounding the fluorophore under investigation.[203] Therefore, analysis of these properties of the fluorescence provide information about the local environment of the fluorophore.

In the present study steady-state fluorescence measurements were carried out using a Hitachi model F-4500 fluorescence spectrometer. The instrument uses a 150 watt continuous powered high pressure xenon lamp as the excitation source and R-928F (Hamamatsu) photomultiplier tube (PMT) as the photo detector. Sample is taken in a 1 cm x 1 cm suprasil quartz cuvette is excited and the fluorescence is collected and measured in a perpendicular direction with respect to the direction of the excitation beam. The wavelength range covered in the present instrument is 220 to 800 nm.

Fluorescence quantum yield of sample (Φ_{Sample}) is calculated with respect to known quantum yield of a standard ($\Phi_{Standard}$) by using the eq. 2.28[203]

$$\Phi_{sample} = \Phi_{standard} \times \frac{F_{sample}}{F_{standard}} \times \frac{A_{standard}}{A_{sample}} * \left(\frac{n_{sample}}{n_{standard}}\right)^2 \quad (2.28)$$

Where $A_{standard}$ and A_{sample} are the absorbance values of standard and sample at the excitation wavelength, $F_{Standard}$ and F_{sample} are the integrated fluorescence intensities and $n_{standard}$ and n_{sample} are the refractive indices for the standard and the sample solutions, respectively.

2.7 Time-Resolved Fluorescence Measurements

Time resolved fluorescence measurements illustrate the variation of fluorescence intensity as a function of time after the creation of the excited state. It monitors the

temporal evolution of the excited state and the mechanism by which the excited state relaxes to the ground state. Time-Correlated Single Photon Counting (TCSPC) technique is the most widely used experimental method to measure the time-dependent fluorescence of a sample in the nanosecond to picoseconds time scales. The working principle and operation of TCSPC spectrometer can be described as follows. The TCSPC technique involves the excitation of the sample with pulses from a laser or a flash lamp and the detection system monitors the time difference between the excitation pulse and the first fluorescence photon from the sample. The prerequisite for this measurement is that only one photon is observed for a large number of excitation pulses. In other words, an extremely low count rate must be ensured such that the system operates in single photon counting mode. In such a situation, the statistics follows the Poisson distribution and a

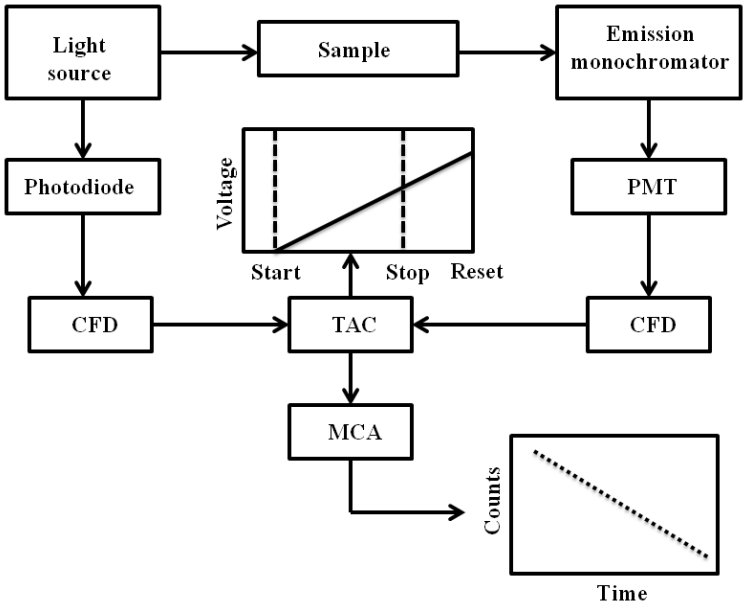

Figure 2.7. *Schematic diagram of TCSPC setup*

true time resolved emission profile is obtained.[203,204] The schematic diagram of a typical TCSPC set up is shown in Figure 2.7.

As shown in Figure 2.7, an excitation pulse (optical pulse) from the pulsed excitation source is split into two parts, one part is used to excite the sample kept in the sample chamber and the other part of the light pulse is directed to a start PMT. The optical signal at the start PMT generates an electrical START pulse, which is then routed through a Constant Fraction Discriminator (CFD) to the START input of the Time to Amplitude Converter (TAC) unit to initiate its charging operation. On receiving the start pulse, the TAC continues to undergo charging linearly with time. The part of the optical pulse, which excites the sample, effectively gives rise to the emission photons. These photons are then detected one by one by the stop PMT (at the right angle to the direction of excitation) to generate electrical STOP pulses for each of the individual photons received. The STOP pulses thus generated in the stop PMT are also routed through a CFD and a variable delay line to the STOP input of the same TAC unit. On receiving the first STOP pulse, the TAC unit stops it's charging operation and subsequently generates an electrical output pulse (TAC-output), having amplitude proportional to the time difference (Δt) between the START and the STOP pulses reaching the TAC unit. The TAC output pulse is then fed to the input of a Multichannel Analyzer (MCA) through an Analog-to-Digital Converter (ADC). The ADC generates a numerical value proportional to the height of the TAC output pulse and thus selects the corresponding memory address (channel) in the MCA, where a single count is added up. The above cycle (from the triggering of the pulsed excitation light source to the data storage in the MCA) is repeated

for a large number of times and thus a histogram of counts is collected in the MCA channels. The distribution of the counts against the channel number in the MCA then represents the fluorescence decay curve of the sample, provided the collection rate of the emission photons by the stop PMT is kept very low, only about 2% or less, compared to the repetition rate of the excitation pulses. This experimental condition effectively means that following an excitation pulse, in no circumstances more than one emission photon can be detected by the stop PMT. Thus, in the TCSPC measurement, for about 98% cases of the excitation pulses, though the sample is excited, there is effectively no emission photon that is directed to the stop PMT. Only about 2% cases of the sample excitations by the pulsed light source there is an effective emission of photon that is directed to the stop PMT and detected by the TCSPC setup. Such a low count rate is essential to maintain the time-dependent probability distribution of the photon emission from a single excited molecule following its excitation process.[204]

For the measurements carried out in the present thesis, TCSPC instrumental set up from Horiba Jobin Yvon IBH, UK, Model Data station Hub. is used. Both diode laser and LED are used as excitation source. The full width at half maximum (FWHM) of the instrument response function (IRF) is typically about ~ 100 ps for the 450 nm diode laser used in the case of CdSe samples and it is 800 ps in the case of 292 nm LED used for BSA life time measurements. An emission polarizer is used before collection optics and fluorescence is recorded at magic angle (54.7°) polarization with respect to excitation light. The fluorescence collected at the magic angle with respect to the excitation polarization is free from any anisotropy components and represents the actual total

fluorescence intensity decay. All the measurements are done such that the counts at the peak of the time resolved fluorescence is 5000 to 10000. The obtained decay curves are fit to either a single exponential or multi exponential functions as described by Equation 2.28 with non-linear least square analysis supported by instrument fitting program of IBH DAS 6.2 software.

$$I(t) = \sum_i^n \alpha_i \, e^{-t/\tau_i} \qquad (2.28)$$

Where τ_i is the fluorescence lifetime and α_i is the pre-exponential factor of the i^{th} component of the sample. The goodness of the fit was judged by the reduced χ^2 value, which should be close to 1 and weighted residuals should be randomly distributed about the zero line for the whole range of the data channels used in the decay analysis.

Chapter 3

Fermi Resonance and Raman Cross-section of Water in the Hydration Shell of Halide Ions

3.1. Introduction

Interactions between ions and water have and play important roles in biological, chemical, environmental, and industrial processes.[21,22,25,205,206] In chemistry, several processes including acid-base equilibrium, solubility, energy, and electron transfer processes dependent on ion solvation. Important biological processes such as activation of enzymes/proteins, trans membrane ion transport, cell signaling, and ligand binding are strongly influenced by interactions between water and charged molecular groups and ions.[2,62,207,208] As a result the molecular level understanding of ion- water interactions has been an important endeavor for physicists, chemists, and biologists. Vibrational spectroscopy is widely used to understand these interactions since the vibrational transitions of a molecule are highly sensitive to its local environments.[84] For example, the position and width of OH stretch and HOH bend modes of water provide information about the H-bond strength and inhomogeneous/heterogeneous nature of water. Therefore, in principle, a comparison of spectral width, position, and intensity of the vibrational

spectrum of neat water with those of aqueous electrolytes solutions would reveal the interactions between ions and water.

Earlier IR and Raman studies[27,91,92,95]of aqueous alkali halide solutions showed that the alkali cations have negligible effect on the OH stretch band of water, but the halide ions reduce the band width and shifts the band position toward blue, which were described as the 'structure breaking' properties of halide ions. Moreover unlike the IR absorption in the OH stretch regions, the Raman intensity (in the blue region of the OH stretch band) increases with increasing concentration of alkali halides in water, which was qualitatively explained by the change in polarizability of the OH bonds in presence of halide ions.[209,210] However, these straightforward spectral analysis may not be fully accountable the observed spectral changes. This is because; the band shape and the intensity of the OH stretch band are heavily affected by coupling effects in liquid water. In fact, the OH stretch band of liquid water is not the response of individual water molecules but the collective response of a number of water molecules whose OH stretch vibrations are in phase with each other.[87,211] This is referred as intermolecular vibrational coupling which leads to larger width and reduced Raman intensity of the OH stretch band. Similarly the coupling between OH symmetric stretch and bend overtone is known as Fermi resonance (FR), which further deforms the OH stretch band of liquid water.[85,212,213]Therefore, it is important to understand the perturbation of intermolecular vibrational coupling and FR of water in presence of ions for the correct interpretation of vibrational spectrum of water in presence of electrolytes.

In this chapter, we address the intermolecular vibrational coupling, FR, and the Raman cross-section of water in the hydration shell of halide ions by comparing the Raman spectra of water and isotopically diluted water ($D_2O/HOD/H_2O$ = 1/18/81 and 81/18/1) in presence of varying concentration of alkali halides (NaX). On isotopic dilution (addition of H_2O in D_2O), the OD stretch band width (FWHM) decreases and the integrated Raman intensity increases due to reduced intermolecular coupling and FR. Addition of NaX in D_2O leads to similar spectral changes. In isotopically diluted water, addition of NaX leads to smaller change in FWHM and intensity in the OD (OH) stretch bands compared to those in D_2O (H_2O). More specifically, our quantitative estimation revealed that the relative Raman cross-section, σ_H/σ_b (σ_H and σ_b are the Raman cross-section of water in the first hydration shell and in bulk) in D_2O (H_2O) is higher than that in isotopically diluted water. These results suggested that the hydrating water has reduced FR and intermolecular coupling than those in bulk water. In alkali halide solutions of isotopically diluted water, the experimentally determined relative Raman cross-sections were smaller than the calculated values based on the energy of the charge transfer excited state of water. The smaller values of σ_H/σ_b suggest that the charge transfer from halide ions did not significantly change in the OD (OH) bond lengths of hydrating water.

3.2. Experiments and Methods

Salts, such as NaX (X = Cl, Br, I) and KF (≥ 99.0 %) and heavy water (D_2O, > 99.9 atom %) were purchased from Sigma Aldrich. Milli-Q water (18.2 MΩ cm resistivity) was used for all measurements. The spontaneous Raman spectra of the samples were recorded using a STR-300 micro-Raman spectrometer (SEKI Technotron,

Japan) which has been described in detail in Chapter 2. Small concentration of acetonitrile was used as the internal standard, to account for the laser fluctuations during the acquisition. The small concentration of acetonitrile was found not to affect the integrated intensity in the OD (OH) stretch band and reproducible spectra were acquired by measuring at the same experimental conditions. Background subtracted spectra were obtained using Peakfit v4.12 software.

3.3. Results and Discussion

3.3.1. Effect of NaBr on H_2O and D_2O

The concentration normalized Raman spectra of D_2O and H_2O in presence of different mole fractions of NaBr are shown in Figure 3.1. The concentration normalized Raman spectra (I_{norm}) of NaBr solutions were calculated as follows

$$I_{norm} = I \times (C_0/C_1) \quad (3.1)$$

where, I was the measured spectra of NaBr solutions, C_0 and C_1 were the concentrations

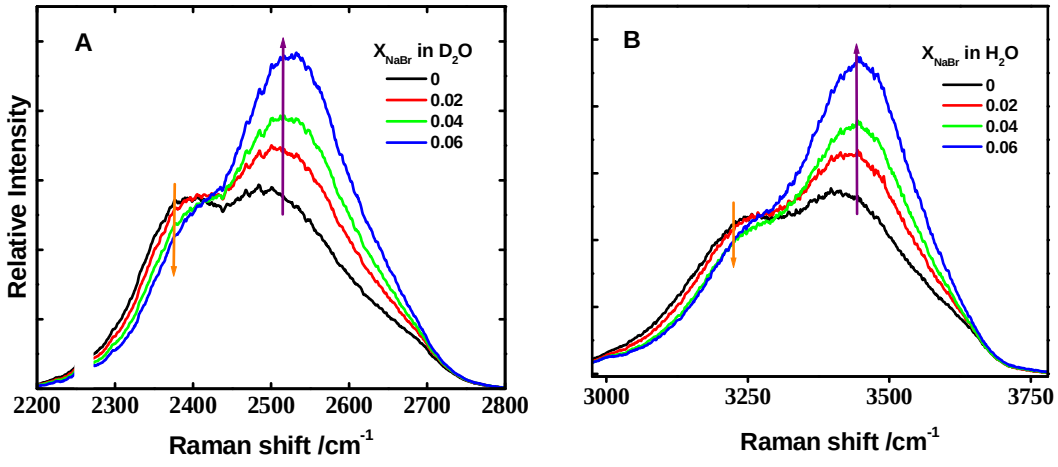

Figure 3.1. *Concentration normalized Raman spectra of (**A**) D_2O in the OD stretch regions (**B**) H_2O in the OH stretch regions with different mole fractions of NaBr as mentioned in the panel.*

of D_2O (H_2O) in neat D_2O (H_2O) and in NaBr solutions respectively. On increasing the concentration of NaBr, the intensity in the red regions of the OD (OH) stretch band (strongly H-bonded water) decreases and that in the blue regions (weakly H-bonded water) increases (Figure 3.1A and B), which is quite similar to the effect of increasing temperature on the IR or Raman spectra of water.[84,209,213] These spectral changes apparently indicate that the population of strongly H-bonded water decreases and that of the weakly H-bonded water increases in presence of NaBr.

Previous IR and Raman studies[169,210,214-218] have shown that the spectral change in the OD (OH) stretch band is primarily due to the halide ion (X^-) and the alkali cation (Na^+) has negligible effect on the OD (OH) stretch band of water. Moreover, time-resolved IR studies[47,50,219,220]have also shown that the halide ions affect the water only in the (first) hydration shell and do not influence the H-bond network in the bulk of liquid water. Therefore, the spectral changes in Figure 3.1 A and B were assignable primarily to the H-bond strength of water in the hydration shell of Br^-.

3.3.2. Effect of Intra-/intermolecular coupling and Fermi Resonance on the OD stretch band of D_2O

Figure 3.2 show the concentration normalized Raman spectra of isotopically diluted water in the OD stretch regions with different mole ratios of D_2O, HOD and H_2O. Interestingly, the spectral changes similar to that in Figure 3.1A (NaBr in D_2O) were observed with gradual addition of H_2O in D_2O (Figure 3.2).

The normalized spectra (I_{norm}) in Figure 3.2 were calculated by equation 3.2,

$$I_{norm} = I \times \{C_0/(C_{D_2O} + C_{HOD}/2)\} \quad (3.2)$$

Here, I was the measured spectrum in D_2O-H_2O mixtures, C_{D_2O} and C_{HOD} were the concentrations of D_2O and HOD in the D_2O-H_2O mixtures. The concentration of HOD was divided by 2, since unlike the two OD bonds in D_2O; each HOD molecule has one OD bond. Like the addition of NaBr in D_2O, on increasing isotopic dilution (gradual addition of H_2O in D_2O), the intensity in the red regions decreases and that in the blue regions increases and the integrated Raman intensity also increases. On isotopic dilution, the intra-/intermolecular vibrational coupling and Fermi Resonance (FR) of water decrease but the H-bond strength of water does not change.[89,213,221] Thus, the similarities between the spectral changes in Figure 3.1 and 3.2 suggested that the water in the hydration shell of Br^- might also have reduced intermolecular vibrational coupling and FR compared to that of bulk water.

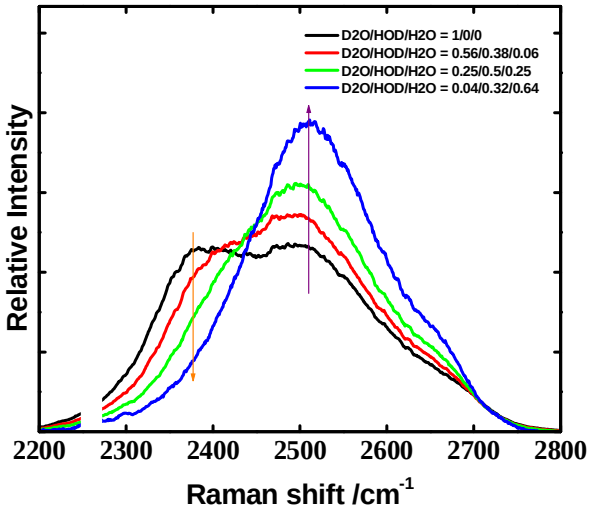

Figure 3.2. *Concentration normalized Raman spectra of D_2O-H_2O mixtures in the OD stretch regions with different mole ratios as mentioned in the panel.*

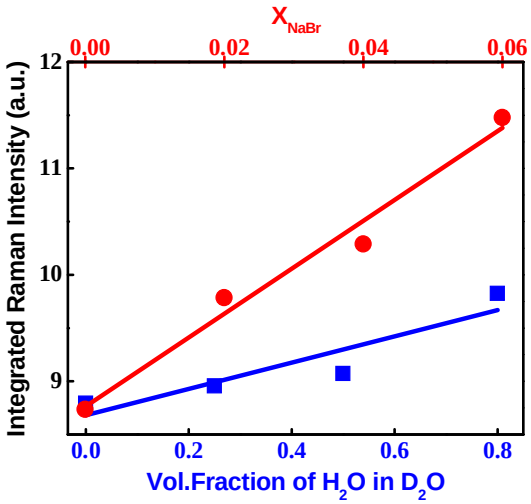

Figure 3.3. *Plot of integrated Raman intensity (OD stretch band) against the mole fraction of NaBr in D_2O (red) or the volume fraction of H_2O in D_2O (blue).*

Moreover, It could be seen in Figure 3.1A and B that the increase in intensity in the blue region of the OD (OH) band (weakly H-bonded water) was significantly higher than the decrease in the red regions (strongly H-bonded water)[209], which leads to an increase in integrated Raman intensity with the concentration of NaBr (red line in Figure 3.3). The increase in Raman intensity suggests that the water that was perturbed by Br^- has higher Raman cross-section (σ) than that of bulk water. Raman studies[210,222,223]of aqueous alkali halide solution qualitatively suggested that the average Raman cross-section of water increases due to change in polarizability of the OD (OH) bonds by charge transfer from the halide ions. To investigate this effects, the Raman spectra of isotopically diluted water, $D_2O/HOD/H_2O$ = 1/18/81(OD) or 81/18/1(OH), which was free from intermolecular coupling and FR (at atmospheric pressure[224]) in the OD (OH) stretch regions[89,225] were measured in presence of different concentrations of NaBr.

3.3.3. Effect of NaBr on the OD and OH stretch band of isotopically diluted water

Raman spectra of isotopically diluted water, ($D_2O/HOD/H_2O$ = 1/18/81 for the OD stretch band and $D_2O/HOD/H_2O$ = 81/18/1 for the OH stretch band) were recorded in the OD and OH stretch regions with different concentrations of NaBr, which are shown in Figure 3.4. It is observed that on increasing salt concentration, the intensity in the red regions of the OD (OH) stretch band decreases and that in the blue region increases with an isobestic point at ~ 2490 (3350) cm^{-1}. This shows that the hydrating water whose population increases with increasing concentration of Br^- scatters in the higher frequency regions of the OD (OH) stretch band compared to that of the bulk water. Moreover, comparing Figure 3.1 and 3.4, it could be seen that the spectral width (FWHM) of the OD (OH) stretch band decreased significantly in D_2O (H_2O) than that in the isotopically diluted water (see Figure 3.5) with increasing intermolecular coupling and FR, the larger

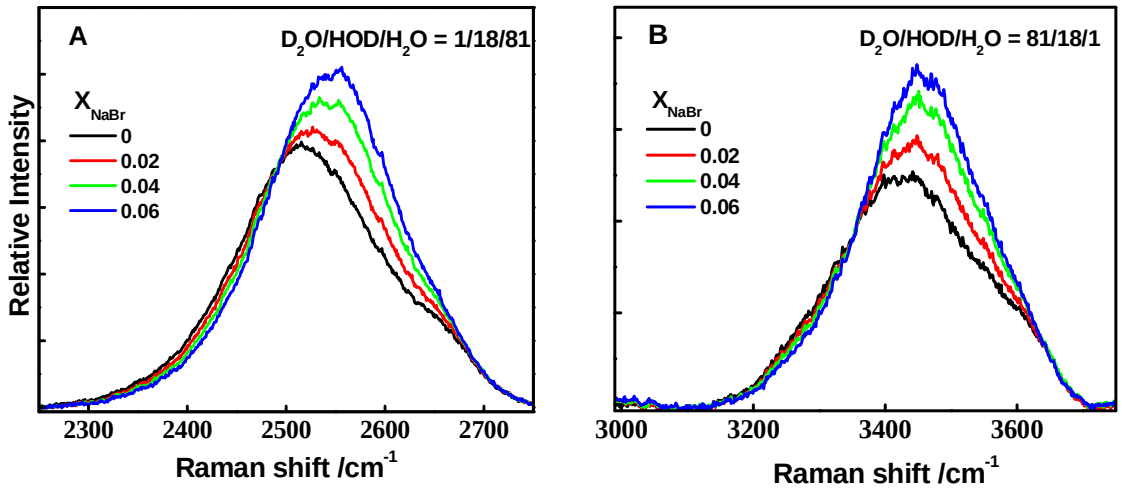

Figure 3.4. *Raman spectra of isotopically diluted water (**A**) ($D_2O/HOD/H_2O$ = 1/18/81) in the OD stretching regions (**B**) ($D_2O/HOD/H_2O$ = 81/18/1) in the OH stretching regions with different mole fractions of NaBr. The spectra were normalized according to Eq.3.2.*

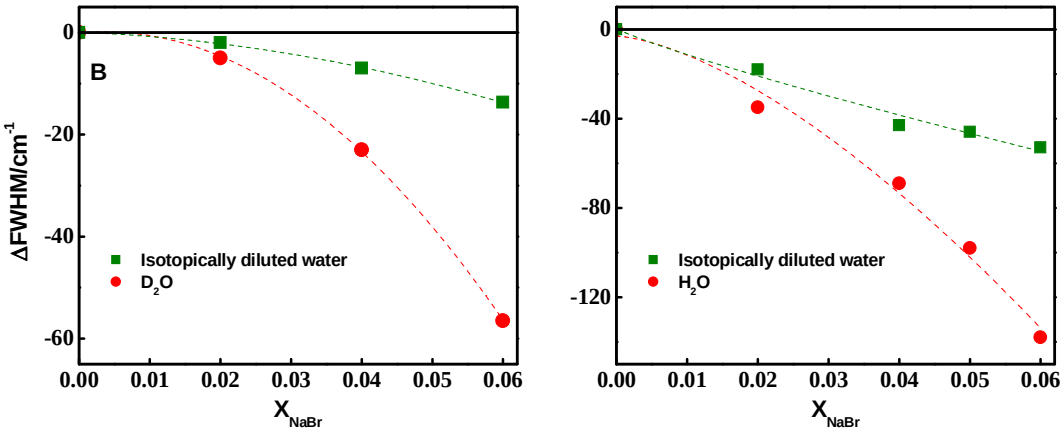

Figure 3.5. *(A) Change in FWHM of the OD stretch band with increasing concentration of NaBr in D_2O (red circle) and in isotopically diluted water (D_2O/HOD/H_2O = 1/18/81) (green square) (B) Change in FWHM of the OH stretch band with increasing concentration of NaBr in H_2O (red circle) and in isotopically diluted water (D_2O/HOD/H_2O = 81/18/1) (green square). The dashed lines are guides for the eye.*

decrease in ΔFWHM in D_2O (H_2O) than that in the isotopically diluted water reveal the significant reduction of intermolecular coupling and FR in the hydrating D_2O (H_2O).[91,226]

In the isotopically diluted water, a small decrease in ΔFWHM with a blue shift of the OD (OH) stretch band could be assigned to decreased H-bond strength of water with increasing concentration of NaBr. Recently, Perera et al.[78] have reported that ion correlated Raman spectrum of water obtained by multivariate Raman curve resolution shows significant reduction of intensity in the red regions of the OH stretch band (~ 3250 cm^{-1}), which was assigned to the reduced FR of hydrating water. It could be seen from Figure 3.4 that even in the isotopically diluted water the magnitude of the increase (in intensity) in the blue region of the OD band was larger than the magnitude of the decrease (in intensity) in the red regions. This suggested larger average Raman cross-section of hydrating water than that of the bulk water.[43,78] To elucidate the intermolecular coupling

and FR in the hydration shell of Br^-, a quantitative analysis of the relative Raman cross-section in isotopically diluted water and in D_2O was performed in the following section.

3.3.4. Relative Raman cross-section of water in the hydration shell of Br^- in D_2O and in isotopically diluted water

The area under the Raman spectrum of D_2O recorded at constant excitation intensity is proportional to the average Raman cross-section per D_2O molecule and the number density of D_2O.

$$\int I_0(\nu)\, d\nu \propto \sigma_b\, N_A\, C_{D_2O} \tag{3.3}$$

Here σ_b is the average Raman cross-section of D_2O in bulk, N_A and C_{D_2O} are the Avogadro number and concentration of D_2O respectively. In aqueous NaBr solution, the integrated intensity could be approximated as the sum of the responses of water in the first hydration shell of Br^- and in the bulk.[91] Assuming that there is no significant effect of Br^- beyond its first hydration shell,[219,220] equation 3.3 takes the following form in presence of NaBr.

$$\int I_{norm}(\nu)\, d\nu \propto \{\sigma_H\, n\, N_A\, C_{Br^-} + \sigma_b\, N_A(C_{D_2O} - n\, C_{Br^-})\} \tag{3.4}$$

where 'n' and σ_H were the average number of D_2O molecules and the Raman cross-section of D_2O in the first hydration shell of Br^- respectively. Now,

$$\frac{\int I_{norm}(\nu)\, d\nu}{\int I_0(\nu)\, d\nu} \propto 1 + \left(\frac{\sigma_H}{\sigma_b} - 1\right)\left(\frac{n}{C_{D_2O}}\right) C_{Br^-} \tag{3.5}$$

Here, σ_H/σ_b was the relative Raman cross-section of D_2O in the first hydration shell of Br^-. The relative Raman cross-section, σ_H/σ_b provides a quantitative idea about the variation of the average Raman cross-section in the hydration shell of halide ions.

In case of NaBr in isotopically diluted water, equation (3.5) was reduced to

$$\frac{\int I_{norm}(\nu)\, d\nu}{\int I_0(\nu)\, d\nu} \propto 1 + \left(\frac{\grave{\sigma_H}}{\grave{\sigma_b}} - 1\right)\left(\frac{0.19n}{C_{HOD}}\right) C_{Br^-} \qquad (3.6)$$

σ'_H/σ'_b was the relative Raman cross-section of the isotopically diluted water. On the basis of relative populations of D_2O and HOD in the isotopically diluted water (D_2O/HOD/H_2O = 1/18/81), the 'n' in equation (3.5) is replaced by '0.19 n' in equation (3.6).

Figure 3.6A shows a plot of the ratio of integrated intensity vs. the concentration of NaBr in D_2O and in the isotopically diluted water (D_2O/HOD/H_2O = 1/18/81). In both cases, the ratio of integrated intensity was found to increase with increase in concentration of NaBr. However, the slope was higher in case of D_2O than that in the isotopically diluted water. In the OH stretch region as well, the plot of the ratio of integrated intensity vs. concentration of NaBr (Figure 3.6B) shows larger slope for H_2O

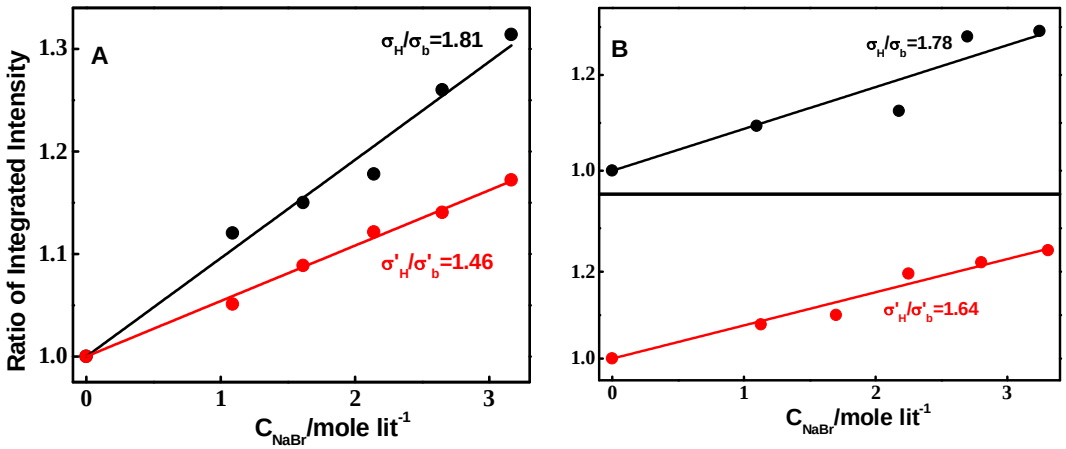

Figure 3.6. *Plot of relative integrated intensity vs. the concentration of NaBr in (A) D_2O (black circles) and isotopically diluted water (D_2O/HOD/H_2O = 1/18/81) (red circles) (B) H_2O (black circles) and isotopically diluted water (D_2O/HOD/H_2O = 81/18/1) (red circles). The solid lines are the fitted functions as mentioned in the text.*

than that in the isotopically diluted water ($D_2O/HOD/H_2O$ = 81/18/1). The data points for D_2O (H_2O) (black circles in Figure 3.6) were fitted with equation (3.5) and those for the isotopically diluted water with equation (3.6) and the fitted functions were shown by the solid lines.

In the isotopically diluted water ($D_2O/HOD/H_2O$ = 1/18/81), the relative Raman cross-section, $\sigma_H`/\sigma_b`$ is 1.46 for Br^-. Since the isotopically diluted water was free from intermolecular coupling and FR,[89,225] the higher value of $\sigma_H`$ than that of $\sigma_b`$ was assignable to the preresonance enhancement of the Raman cross-section by charge transfer from Br^- to the combined anti-bonding orbital of hydrating water[210,222,227] (vide infra). Similarly, if there was no change in the intermolecular coupling and FR of D_2O by the addition of NaBr, the σ_H/σ_b for D_2O was expected to be 1.46. However, as shown in Figure 3.6A, the σ_H/σ_b for D_2O was higher (1.81) than that of the isotopically diluted water. This means, the intermolecular couplings and FR in D_2O were perturbed in the hydration shell. It was reported that the intramolecular coupling has lesser effect on the intensity and the position/width of the OD (OH) stretch band than the FR and intermolecular coupling in water[87,89,212,213]Raman cross-section of water increases either due a reduction in FR[228] or due to an increase in intermolecular coupling.[89,90] On average, a water molecule in the first hydration shell of Br^- interacts with lesser number of neighboring water molecules compared to those in the bulk, and experiences a rapidly varying electric field.[43,226] In a sense, the water in the first hydration shell experiences an anisotropic environment with lower probability of interaction with neighboring water and the intermolecular interaction was expected to be weaker i.e. σ_H/σ_b was expected to be

< 1.46. On the contrary, the experimentally determined σ_H/σ_b (1.81) was higher than that in the isotopically diluted water. The large enhancement of σ_H was assignable to the significant decrease in FR of D_2O in the hydration shell of Br^-. The decrease in FR could be explained by the perturbation of the stretching and bending vibrations of water in the hydration shell of halide ions. As shown in Figure 3.4, the maximum of the OD stretch band (ν_{OD}) shifted toward higher frequency with increasing concentration of NaX which mean that the water in the hydration shell has weaker H-bonding than that of the bulk.[50,220,229] In the case of bending vibration of water (δ_{OD}), the maximum of δ_{OD} shifts toward lower frequency with decreasing interaction with neighboring molecule[229-231]and so is the overtone band ($2\delta_{OD}$). Therefore, in the hydration shell of Br^-, the weakly interacting water has larger energy gap between ν_{OD} and $2\delta_{OD}$ (bending overtone) than that of the neat water, which result in weaker Fermi Resonance coupling.

3.3.5. Relative Raman cross-section of water in the hydration shell of different halide ions in isotopically diluted water

Figure 3.7 shows a plot of relative integrated intensity vs. the concentration of alkali halide (MX; M =Na/K and X = F, Cl, Br, I) in the isotopically diluted water ($D_2O/HOD/H_2O$ = 1/18/81). The data points for different halide ion solutions were fitted with equation (3.6) with 'n' = 5, 5.8, 6.2, and 6.6 for F^-, Cl^-, Br^-, and I^-,[232-234]and the fitted functions were shown as solid lines in Figure 3.7. It was observed that except for F^-, the $\sigma_H^{'}/\sigma_b^{'} > 1$ and increases as the size of the halide ions increased ($\sigma_H^{`}/\sigma_b^{`}$ = 1.11 for Cl^-, 1.46 for Br^-, and 1.86 for I^-). With increasing size, the charge transfer ability of the halide ions to the combined antibonding orbital's of hydrating water increases and the

energy of the lowest excited electronic state of hydrating water decreases.[210,222] So, the energy gap between the electronic excited state (UV region) and the virtual state (the excited state created by the 532 nm laser excitation in the present experiment) decreased, which caused an increase of the Raman cross-section according to equation (3.7).[235,236]

$$\sigma \propto k\,\nu_0(\nu_0 - \nu_j)^3 \left[\frac{\nu_e^2+\nu_0^2}{(\nu_e^2-\nu_0^2)^2}\right]^2 \qquad (3.7)$$

Here, ν_e and ν_0 were the electronic absorption and excitation frequencies, ν_j is the frequency of the j^{th} vibrational transition, and k is a scaling constant. With decreasing energy gap between the electronic excited state (ν_e) and the virtual state (ν_0), the denominator in equation 3.7 decreased, which lead to an increase of σ. In this case, σ increases not by the resonant excitation, but due to closeness of the virtual state to the resonant excited state, and hence the increase of the Raman cross-section is known as

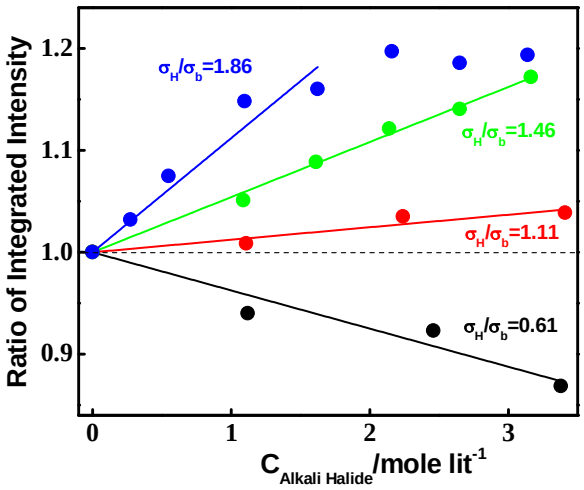

Figure 3.7. *Plot of the relative integrated intensity vs. the concentration of MX: NaI (blue), NaBr (green), NaCl (red), and KF (black) in the isotopically diluted water, $D_2O/HOD/H_2O$ = 1/18/81. The solid lines are the fitted functions according to equation 3.6 with R^2 values 0.97(NaI), 0.99(NaBr) 0.957 (NaCl) and 0.969 (KF).*

preresonance enhancement. Raman measurements[78,210,222,223,237] and computational studies[43,238] suggested the increase in Raman intensity with increasing size of halide ions, which qualitatively agrees with our results in isotopically diluted water. In the following section, we modeled the increase in relative Rama cross-section with equation 3.7.

3.3.6. Variation of relative Raman cross-section with the energies of lowest excited electronic states

For the hydrating water, equation 3.7 takes the form,

$$\sigma_H \propto k` \nu_0 \left(\nu_0 - \nu`_j\right)^3 \left[\frac{\nu_{e(H)}^2 + \nu_0^2}{\left(\nu_{e(H)}^2 - \nu_0^2\right)^2}\right]^2 \quad (3.8)$$

Here $\nu_{e(H)}$ was the frequency of lowest energy electronic absorption of hydrating water. In aqueous halide ion solutions, the lowest energy electronic transition arises due to the transfer of electron from the halide ion to linear combination of antibonding orbitals of hydrating water.[210,227,239,240] Assuming a comparable scaling constant (k` ≈ k) and neglecting the small spectral shift in the OD stretch band in presence of alkali halide ($\nu`_j \approx \nu_j$), the relative Raman cross-section of the isotopically diluted water takes the form,

$$\frac{\sigma`_H}{\sigma`_b} \approx \left[\frac{\nu_{e(H)}^2 + \nu_0^2}{\nu_{e(b)}^2 + \nu_0^2}\right]^2 \left[\frac{\nu_{e(b)}^2 - \nu_0^2}{\nu_{e(H)}^2 - \nu_0^2}\right]^4 \quad (3.9)$$

Where $\nu_{e(b)}$ is the frequency of lowest energy electronic absorption of bulk water (60240 cm^{-1}). In aqueous NaX (X= Cl, Br, I) solutions, the lowest energy electronic excited state of water (λ_{max} ~ 166 nm) shifts toward lower energy as the size of the halide ions increases λ_{max} (Cl^-) ~ 173 nm, λ_{max} (Br^-) ~ 200 nm, and λ_{max} (I^-) ~ 227 nm).[210,222] Figure 3.8 shows a plot of the σ'_H / σ'_b *vs.* the energy of the lowest energy absorptions band

for different NaX solutions (red circles). As expected, the relative Raman cross-section increases with decreasing the energy of the lowest excited electronic state of water (i.e., with decreasing the energy gap between $\nu_{e(H)}$ and ν_0).

However, the experimental $\sigma_H`/\sigma_b`$ (red circles) is lower than the calculated values (blue line) corresponding to the preresonance enhancement by the lowest energy electronic state. This shows that the preresonance enhancement of the Raman cross-section of the hydrating water was only weakly mediated by the lowest energy excited state of water. In other words, the charge transfer in hydrating water causes little change in their O-H bond lengths of hydrating water. Simulation studies[229,241] revealed that halide ions do not directly increase the OD (OH) bond lengths of water but the mean water-water H-bond angle in the first hydration shell increase, which shifts the OD (OH) stretching mode of water to higher frequency. The results in Figure 3.8 could be modeled

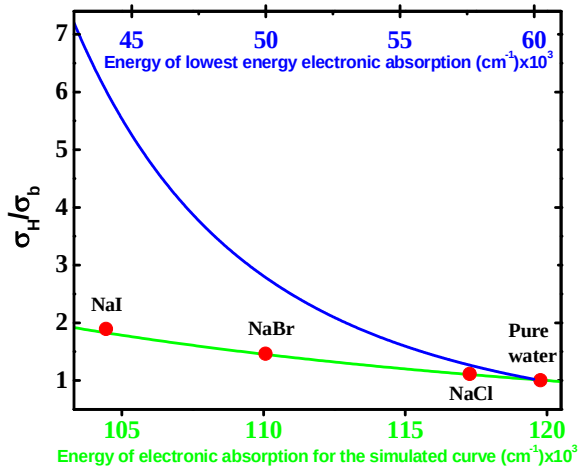

Figure 3.8. *Plot of relative Raman cross-section vs. the energy of electronic absorption of water (red circle) for different alkali halide solutions. Blue and green lines are the simulated curves corresponding to the lowest energy (60240 cm^{-1}, top horizontal axis) and higher energy (120000 cm^{-1}, bottom horizontal axis) electronic excited states of water.*

by the simulated curve (green line in Fig. 3.8) corresponding to the preresonance enhancement by a higher energy excited electronic state ($\nu_{e(b)}$ = 120000 cm^{-1}) of water. Recently, Xiong et al.[214] measured the excitation wavelength dependence of the Raman cross-section for the OH stretch band of water and predicted that the electronic state responsible for the preresonance enhancement lies in far UV regions (either 150000 cm^{-1} or 91000 cm^{-1}), which is consistent with the present results.

3.4. Conclusions

This chapter deals with investigation of Fermi-Resonance (FR) and the Raman cross-section of neat and isotopically diluted water in presence of halide ions (F^-, Cl^-, Br^-, and I^-) by measuring the Raman spectra in the OD and OH stretch regions. Except for F^-, all the halide ions cause blue-shift and enhancement of intensity in OD stretch regions, which were also observed by the isotopic dilution of D_2O (H_2O). Comparison of the spectral changes by the addition of alkali halides in D_2O (H_2O) and in the isotopically diluted water reveals that the magnitude of ΔFWHM of the OD (OH) stretch band and the relative Raman cross-section (σ_H/σ_b) in D_2O (H_2O) were higher than that in the respective isotopically diluted water. These results suggested that water has reduced FR and intermolecular coupling in the hydration shell of halide ions compared to those in bulk. In the isotopically diluted water, increase in relative Raman cross-section with the size of the halide ions (σ_H/σ_b = 0.6, 1.1, 1.5, and 1.9 for F^-, Cl^-, Br^-, and I^-) shows that the charge transfer from halide ions to the hydrating water leads to preresonance enhancement of the Raman cross-section of hydrating water. Quantitative analysis, however, revealed that the

Raman cross-section of hydrating water was only weakly enhanced by the lowest energy charge transfer electronic excited state of water.

Chapter 4

Hydrogen-Bonding and Vibrational Coupling of Water in the Hydration Shell of Ions

4.1. Introduction

Ion hydration has long been a subject of great interest due to its important implications in chemical, biological, environmental, industrial, and geological processes[1-5]. Fundamental chemical processes, such as acid-base equilibrium, electron transfer, ion-exchange are related to ion hydration. Biological processes including activation of enzymes, trans-membrane ion transport, cell signaling and ligand-binding are crucially dependent on the hydration of charged groups/ions.[6-9]. To elucidate chemistry associated with the above processes, it is important to understand the structural perturbation of water at the hydration shell of ion.

Water molecules because of their small size, dipolar nature and hydrogen-bond donating-accepting ability can exist as a highly structured liquid with collective vibrational properties. For example, the normal vibrational modes of water (symmetric and antisymmetric OH stretching and HOH bend) are coupled with the vibrations of neighboring water molecules. These vibrational couplings (collective nature) do affect the

vibrational energy relaxation of water, and hence the aqueous reactions.[87-90] Hence, it is of important to understand the structural and dynamical perturbations of water in presence of ions and molecules.

As early as 1888, Franz Hofmeister observed that different ions influence solubility of protein in differently.[24] For example, some ions favor the folded state of proteins (precipitation/salting-out) and others promote the unfolded state (denaturation/salting-in). When these ions are arranged in order of their ability to precipitate proteins in aqueous solution, then the following series (known as Hofmeister series) is obtained: $CO_3^{2-} > SO_4^{2-} > HPO_4^{2-} > CH_3COO^- > F^- > Cl^- > Br^- > NO_3^- > I^- > ClO_4^- > SCN^-$.[21] The anions on the left hand side of Cl^- favor the folded state of protein and are known as kosmotrope (structure-maker).[27,30,31,242] On the contrary, the ions on the right side of Cl^- favor the unfolded state and are known as chaotrope (structure-breaker). It was believed that the ions on the left side of the series bind more strongly with water (than water binds with itself in bulk solution), which makes water less aggressive to a protein (solute). These ions, thus, help the protein to retain its native/folded structure (stabilization). The ions on the right side of the series interacts weakly with water (*i.e.* weaker than water binds with itself in bulk), which make water more aggressive to a solute (protein) and promotes denaturation (destabilization).

In agreement with this view, it has been found that the so called kosmotropic anions increase the viscosity of water (positive Jones-Dole viscosity coefficient, B) whereas, the chaotropic anions decrease the same (negative B coefficient).[30,35] When some of the anions are arranged on the basis of their B-coefficient values, the following

series is obtained: PO_4^{3-} (B = 0.495) > CO_3^{2-} (0.294) > CH_3COO^- (0.25) > SO_4^{2-} (0.206) > F^- (0.107) > Cl^- (-0.005) > Br^- (-0.033) > NO_3^- (-0.043) > I^- (-0.073); which is in conformity with their order in Hofmeister series. Because of this conformity, it was believed that the Hofmeister effect and the change in viscosity of water have a common origin. The common origin is the modification of H-bond network of liquid water in presence of anions. Nevertheless, unlike the effect of temperature, the change of viscosity in presence of ions does not necessarily mean that these ions affect the H-bond network of bulk water in long-range.[36,37] With increasing temperature the average H-bond strength of water decreases and so does the viscosity.

In recent years, as discussed in Chapter 1, the classification of ions as structure makers/breakers and their long-range effect on water structure have been disputed by several experimental and theoretical results.[44,45,219,243-246] X-ray and neutron diffraction studies[39,41,53-56] which provide relative distribution of number density of H and O atoms of water, as a function of distance from the ion/solute, revealed that the static structure of water is significantly perturbed only in the immediate vicinity of ion/solute. Time-resolved infrared (IR) studies of aqueous solutions,[50,51,247] that measure the rate of vibrational energy transfer or orientational relaxation of water, showed that in aqueous salt solution, apart from the dynamical components of bulk water, there is additional relaxation component pertinent to the hydration water of ion/solute. In agreement with these experimental observations, MD-simulation[43,49,58,60,62,63] suggested that the H-bonding and other structural motifs of water are mainly affected within the hydration shell of ions.

Conventional IR/Raman spectra of aqueous electrolyte solutions contain the responses of both, hydration shell and bulk water. In diluted salt solutions, because of larger concentration of bulk water than that of hydration water, the weaker hydration water signal gets buried into the stronger bulk water signal. As a result, understanding the hydration water is difficult from the experimentally recorded IR/Raman spectra of diluted salt solutions. This problem was partially overcome either by analyzing the vibrational spectrum of concentrated salt solutions[50,51,248] (in concentrated salt solution, say ~5 mol dm^{-3} aqueous NaCl solution, it is assumed that the vibrational response is dominated by hydration water since there is hardly any bulk water) or by subtracting proportionate bulk water spectrum from the salt solution spectrum.[91,94,167] However, in concentrated salt solutions, ion-pairing and overlapping/sharing of individual hydration shells may complicate the vibrational band shape and dynamics of water in the so called 'hydration shell of a fully hydrated ion'.[249,250]

We have applied multivariate curve resolution (MCR) method[78,195] (*vide infra*) to retrieve the vibrational response of hydration water from the conventional Raman spectra of diluted aqueous salt solutions. The MCR-analysis of the OH stretch band, for example, provides two component spectra. One of the component spectra corresponds to the vibrational spectrum of ion-perturbed water (ion-correlated spectrum; IC-spectrum), which is assignable to hydration shell water,[98] and the other corresponds to the spectrum of unperturbed water, i.e. bulk water. It is observed that the band shapes of the IC-spectra are quite different from bulk water, which means that the vibrational characteristics of hydration water are different from the bulk water. In this chapter, we will discuss about

the structural perturbation of water in the hydration shell of different ions by selectively measuring the vibrational response of hydration water using Raman-MCR approach.

4.2. Experiments and Methods

Heavy water (D_2O, > 99.9 atom % D) and the Na-salts (≥ 99.0 %; NaCl, NaI, NaBr, $NaNO_3$, Na_2SO_4, Na_2CO_3 and Na_3PO_4) were purchased from Sigma Aldrich. Milli-Q water (18.2 MΩ cm resistivity) was used for all the measurements. The spontaneous Raman spectra of the samples were recorded using a STR-300 micro-Raman spectrometer (SEKI Technotron, Japan). The details about Raman spectrometer discussed in Chapter 2. We used low concentration of salts (≤ 1.0 mole dm^{-3}) to ensure that the ions are fully hydrated without significant ion-pairing. To obtain reproducible results, the spectra were acquired at the same experimental conditions.

A constant background signal was subtracted from the experimentally recorded Raman spectra, and the background subtracted spectra were area normalized to nullify the effect of intensity variation (either due to laser fluctuation or due to the change in Raman cross-section of water in presence of ions) in subsequent multivariate analysis. The area normalized Raman spectra were arranged into the rows of a matrix (data matrix X; the first row of X is the spectrum of neat water) for MCR analysis[78,98,251,252] using Igor pro 6.22A software. The details of the MCR analysis have been described in Chapter 2. Briefly, the data matrix, containing mixed spectral response of hydration and bulk water, is decomposed by singular value decomposition (SVD) that provides an initial estimate of the number of components and their spectral responses. Then, the initial estimates were optimized by alternating least square (ALS) fitting method, while incorporating certain

restrictions, such as non-negative intensity of the component spectra, concentrations of salt (known from the experiments), number of components (two in the present case). One of the two spectral components, obtained after SVD-ALS operations, represents the bulk water response, and the other component corresponds to the response of water molecules that are perturbed by ions (ion-correlated spectra, IC-spectra).

In the case of bend and [bend + librational] combination band regions, the IC-spectra were obtained by restricting the MCR analysis within the frequency regions of the bend and combinations bands. Because of low Raman cross-section of water in the HOH-bend and combination (bend + librational) band regions, the IC-spectra of these bands exhibit low S/N ratio. The IC-spectra in these regions were smoothened for better presentation by Savitzky-Golay algorithm using 25 points. It is noted that the smoothening operation did not change the band shape of the IC-spectra. To compare the IC-spectra with the Raman spectrum of isotopically diluted water, which is free from intra-/intermolecular coupling and FR, we used largely diluted H_2O-D_2O mixture (H_2O/D_2O = 1/19 (v/v) i.e., $H_2O/HOD/D_2O$ = 0.25/90.25/9.5). The H_2O-D_2O mixture (described as diluted water (HOD)) and the neat water (as undiluted water (H_2O)), in this chapter.

4.4. Results and Discussion

4.4.1. Raman spectra of water in the OH stretch region

Figure 4.1(A to F) shows the area normalized Raman spectra (OH stretch) of water in presence of different concentrations of Na-salts ($\leq$ 1 mol.dm^{-3}). Except for NaI (Fig.4.1A), the Raman spectra of the salt solutions are not very different from that of neat

water, especially at low concentration, e.g. at 0.3 mol.dm^{-3}. In the case of NaI solution, on increasing concentration of NaI, the intensity in the red regions of the OH stretch band decreases and that in the blue regions increases. This effect is less pronounced in the case of NaBr, $NaNO_3$, and Na_2SO_4 salt solutions (Fig.4.1 B-D). In contrast, the Raman spectra of Na_2CO_3 and Na_3PO_4 solutions (Fig.4.1 E-F) show a slight increase in intensity below 3100 cm^{-1}, with a concomitant decrease in intensity around 3300 cm^{-1} region. From such small changes in spectral features, one can guess the trend in the structural perturbation of water in presence of these ions. However, the precise understanding of water structure at the immediate vicinity of these ions is difficult.

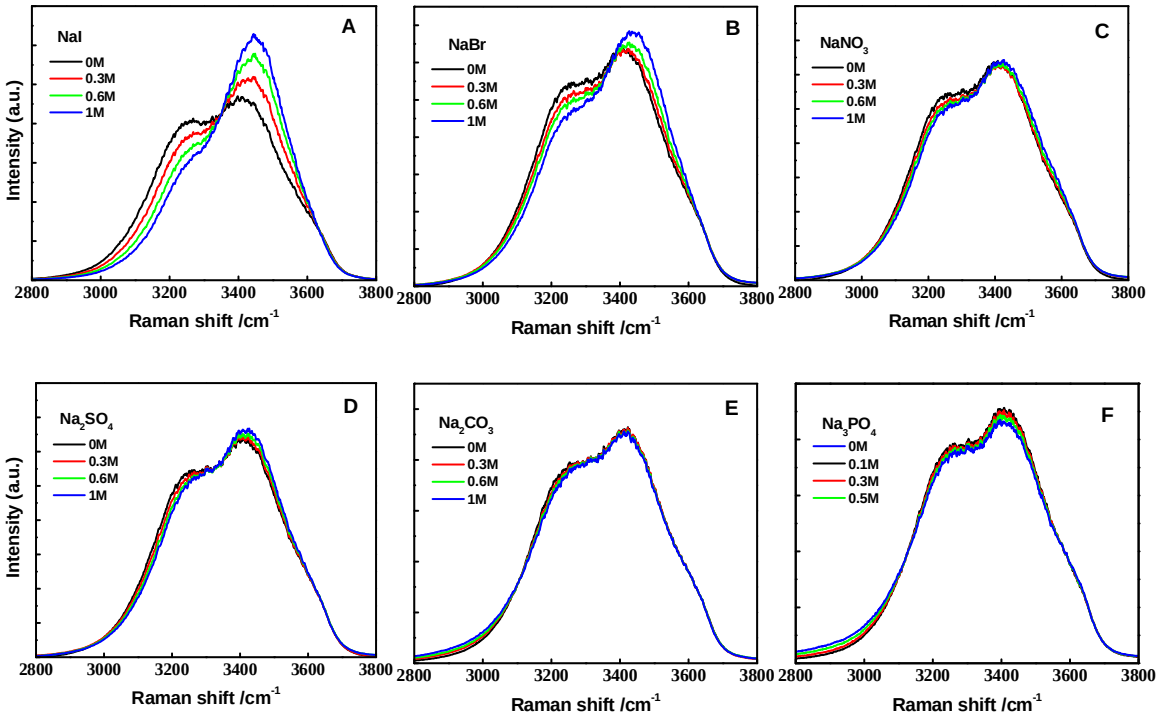

Figure 4.1. *Area normalized Raman spectrum of water with different concentration of (A) NaBr (B) NaI (C) $NaNO_3$ (D) Na_2SO_4 (E) Na_2CO_3, and (F) Na_3PO_4.*

Application of multivariate curve resolution (MCR) on these experimental Raman spectra, however, shows that the salt-correlated spectrum of water, the vibrational response of water in the hydration shell of the ions produced by the dissociation of salt, is significantly different from that of neat water (Fig. 4.2 A and B). The salt-correlated spectra for NaI, NaBr, and $NaNO_3$ show a large decrease in intensity in the red-region of the OH stretch band (below 3400cm^{-1}). Furthermore, the maximum of the salt-correlated spectra are blue-shifted compared to that of neat water (Fig. 4.2A). Similar decrease in intensity (in the red region) has been observed in the case of Na_2SO_4. However, in the case of Na_3PO_4, the salt-correlated spectrum looks almost similar to neat water above 3100 cm^{-1} (slight higher intensity below 3100 $cm^{-}1$, Fig. 4.2B). The higher intensity in the red- region (below 3100 cm^{-1}) becomes more prominent in the case of Na_3CO_3. In fact the

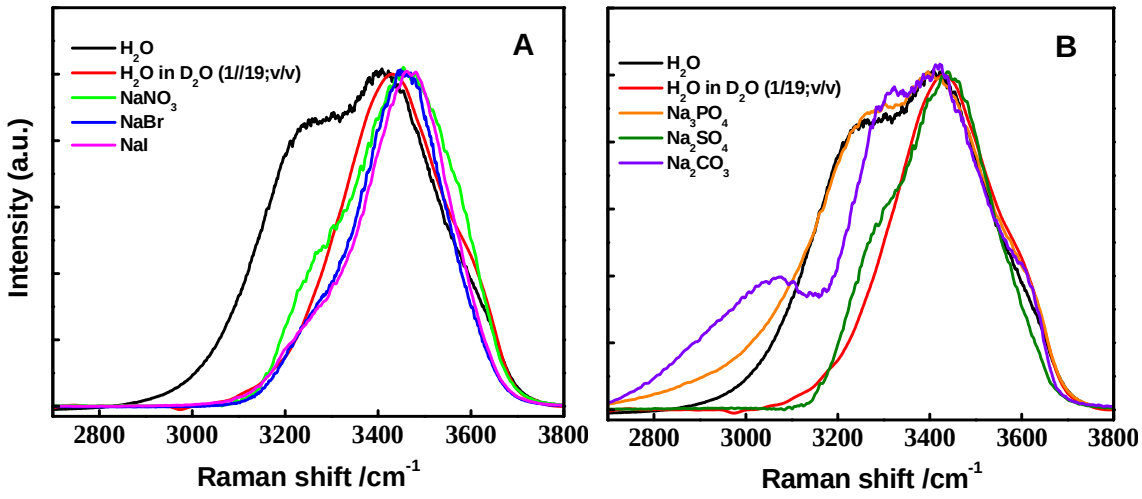

Figure 4.2. *Salt-correlated Raman spectra of water in the OH stretch regions for various Na-salts of chaotropic (A) and kosmotropic (B) anions as mentioned in the graph panel. Raman spectra of H_2O (black), HOD (red; H_2O/D_2O = 1/19; v/v), $NaNO_3$ (green), NaBr (blue), NaI (magenta), Na_3PO_4 (orange), Na_2SO_4 (olive), and Na_2CO_3(violet).*

salt-correlated spectrum for Na_3CO_3 shows a separate band at 3050 cm^{-1} and a dip feature at 3200 cm^{-1}.

In the present study, we used Na-salts of different mono-, bi-, and tri- valent anions such that the salt-correlated spectra contain the spectral response of both, the hydration water of Na^+-cation and that of the corresponding anions. It has been observed that the effect of Na^+-cation on the OH stretch band of water is negligible compared to that of the anions (e.g. Br^-, I^-, NO_3^-, etc.).[78,216,253,254] This means that salt-correlated spectra are largely the anion-correlated spectra which contain the vibrational response of water in the hydration shell of the respective anions. Thus, the MCR-retrieved spectra (Figure 4.2) suggest that the OH stretch band of water is significantly affected in the hydration shell of anions. However, interpretation of these spectral changes is nontrivial, since the band shape and peak position of the OH stretch band of water depends, not only upon the H-bond strength, but also on the intra- and intermolecular vibrational coupling of water.[87-90] This is quite evident from the OH stretch band of vibrationally decoupled water (isotopically diluted water, HOD; red curve in Figure 4.2 A & B), which is very different, especially in the red-region (<3400 cm^{-1}) of the OH stretch band, from that of vibrationally coupled water (bulk H_2O; black curve in Figure 4.2 A & B), even though the H-bond strength of HOD and H_2O are comparable. In HOD (HOD, H_2O/D_2O = 1/19; v/v), the OH oscillator (~3420 cm^{-1}) is energetically separated with its crowded neighbors, OD oscillators (~2500 cm^{-1}), and hence, the OH stretch mode is intermolecularly decoupled. Similarly, the Fermi resonance (FR: intramolecular coupling between the OH stretch fundamental and HOH bend overtone)[86,212,248] is also turned off

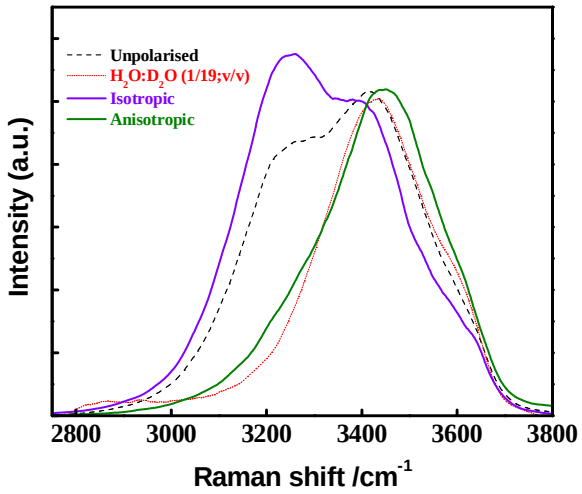

Figure 4.3. *Polarized Raman spectra of water (isotropic (violet), anisotropic (olive) and unpolarized (black dashed line)).Raman spectra of HOD (red dotted line; H_2O/D_2O = 1/19; v/v) is shown for comparison.*

by energy mismatch of OH stretch fundamental with the bend overtone of HOD (2 × 1445 = 2890 cm^{-1}).[255] Therefore, on isotopic dilution, even though the H-bond strength does not change appreciably, the reduction of intermolecular vibrational coupling and FR lead to significant decrease in intensity in red region of the OH stretch band (compare black and red spectra in Figure 4.2 A & B). Thus, a comparison of the OH stretch band of HOD and H_2O suggests that the vibrational response in the red-region of the OH stretch (<3400 cm^{-1}) band is dominated by intra- and intermolecular vibrational coupling.

Now, as can be seen from Fig. 4.2, the anion-correlated spectra of the chaotropic anions (NO_3^-, Br^-, and I^-) look like the Raman spectrum of isotopically diluted water (HOD). The similarity of the OH stretch band of H_2O in the hydration shell of NO_3^-, Br^-, and I^- anions (anion-correlated spectra) with the Raman spectrum of HOD suggests that the H_2O molecules in the hydration shell of chaotropic anions behave more like HOD

than H_2O. This means hydration shell water is decoupled from the neighboring H_2O molecules and has reduced FR.[78,248] This is evident from the polarized Raman spectrum of water. Figure 4.3 shows the polarized (isotropic and anisotropic) and unpolarised Raman spectrum of water in the OH stretch region.[256-258] The symmetric OH stretch vibrations that are coupled in-phase with neighboring symmetric OH oscillators oscillate at lower frequency (maximum ~3230 cm^{-1}) and appears mainly in isotropic Raman spectrum; whereas, the antisymmetric OH stretch vibrations that coupled in-phase with neighboring antisymmetric OH stretches oscillate at higher energy (maximum ~3430 cm^{-1}) and become prominent in the anisotropic Raman spectrum (Figure. 4.3). As can be seen in Fig. 4.2 and 4.3, anion-correlated spectra of the chaotropic anions (NO_3^-, Br^-, and I^-) are more similar to the anisotropic Raman spectrum of water. This observation suggests that the OH stretch vibration of water in the hydration shell of these anions are decoupled (out-of-phase vibrations) with neighboring water molecules. Nevertheless, the maximum of the anion-correlated spectra are blue-shifted compared to that of HOD. The blue-shift indicates that water forms weaker H-bond in the hydration shell of the chaotropic anions than that in bulk.

Unlike the chaotropic anions, the anion-correlated spectrum of kosmotropic PO_4^{3-} anion shows significant intensity at ~3250 cm^{-1}, and the relative intensity below 3100 cm^{-1} is higher than that of bulk H_2O. These features suggest that the water in the hydration shell of PO_4^{3-} is strongly H-bonded. The anion-correlated spectrum for CO_3^{2-} is neither similar to the Raman spectra of bulk H_2O nor to that of HOD. The CO_3^{2-}-correlated spectrum shows a separate band at 3050 cm^{-1} and a dip feature at 3200 cm^{-1}.

The dip feature is presumably due to the intensity reduction by intermolecular decoupling (localization vibrational mode) and/or modification of FR and the appearance of new band at the extreme red region of the OH stretch band (~3050 cm^{-1}) corresponds to the strongly H-bonded water molecule in the hydration shell of bivalent CO_3^{2-} anion (*vide infra*). In contrast to $PO_4^{3-}$and CO_3^{2-}, the anion-correlated spectrum for SO_4^{2-} which is also a strong kosmotropic anion (positioned in extreme left side of Hofmeister series) shows significantly reduced intensity at ~3250 cm^{-1} regions. In other words, the anion-correlated spectrum of SO_4^{2-} ion resembles that of the Raman spectrum of HOD or the anion-correlated spectrum of the chaotropic NO_3^-, Br^-, and I^- anions (Figure 4.2 A and B). The maximum of the anion-correlated spectrum for SO_4^{2-} was very close to peak position of the Raman spectrum of HOD. These results indicate that the H-bond strength of H_2O in the hydration shell of SO_4^{2-} is comparable to that of bulk HOD, which is in sharp contrast to the belief that water forms stronger H-bond (than bulk HOD) with SO_4^{2-} anion.[259,260]

As mentioned earlier, the OH stretch band of water contains the combined response of H-bonding and coupling effects (Intermolecular vibrational coupling and FR). To obtain more meaningful and quantitative information about the H-bond strength and intermolecular vibrational coupling of water in the hydration shell of various kosmotropic and chaotropic anions, we have fitted the Raman/IC-spectra with multiple Gaussian bands as described in the following section.

4.4.2. Component analysis of the anion-correlated spectra in the OH stretch region

Figure 4.4 shows three component Gaussian fits of the area normalized Raman spectra of H_2O, HOD, and the anion-correlated spectra of the salt solutions (minimum three components are required to fit the experimental spectra[261]). The fitted spectra (dashed curves) and the component bands (dotted curves) are shown in respective Graph panels. The fitting parameters and the relative integrated area of the component bands are summarized in Table 4.1. From the relative integrated areas (Table 4.1), it is obvious that on isotopic dilution, the relative contribution of the 3250 cm^{-1} band (component-1) decreases and that of the 3450 cm^{-1} band (component-2) increases. A similar trend has been observed in the anion-correlated spectra of SO_4^{2-}, NO_3^-, Br^-, and I^- ions. However, in presence of PO_4^{3-}, the relative contribution of component-1 increases from that of bulk H_2O. The contribution of component-3 which is a minor component even in bulk H_2O does not change significantly with the addition of D_2O or Na-salts in H_2O.

In presence of SO_4^{2-}, NO_3^-, Br^-, and I^- ions, the spectral width (fwhm) of component-2 and component-3 does not change much, but that of component-1 is much lower than that of H_2O (Figure 4.4B). The integrated areas of the three bands (centered at ~3250, 3450, and 3600 cm^{-1}) are plotted against the Na-salts in Figure 4.5A. It is observed that in the case of SO_4^{2-}, NO_3^-, Br^-, and I^- anions, the relative contribution of component-1 is significantly lower, and that of component-2 is higher than those in H_2O. However, the relative areas of the three components do not change significantly in

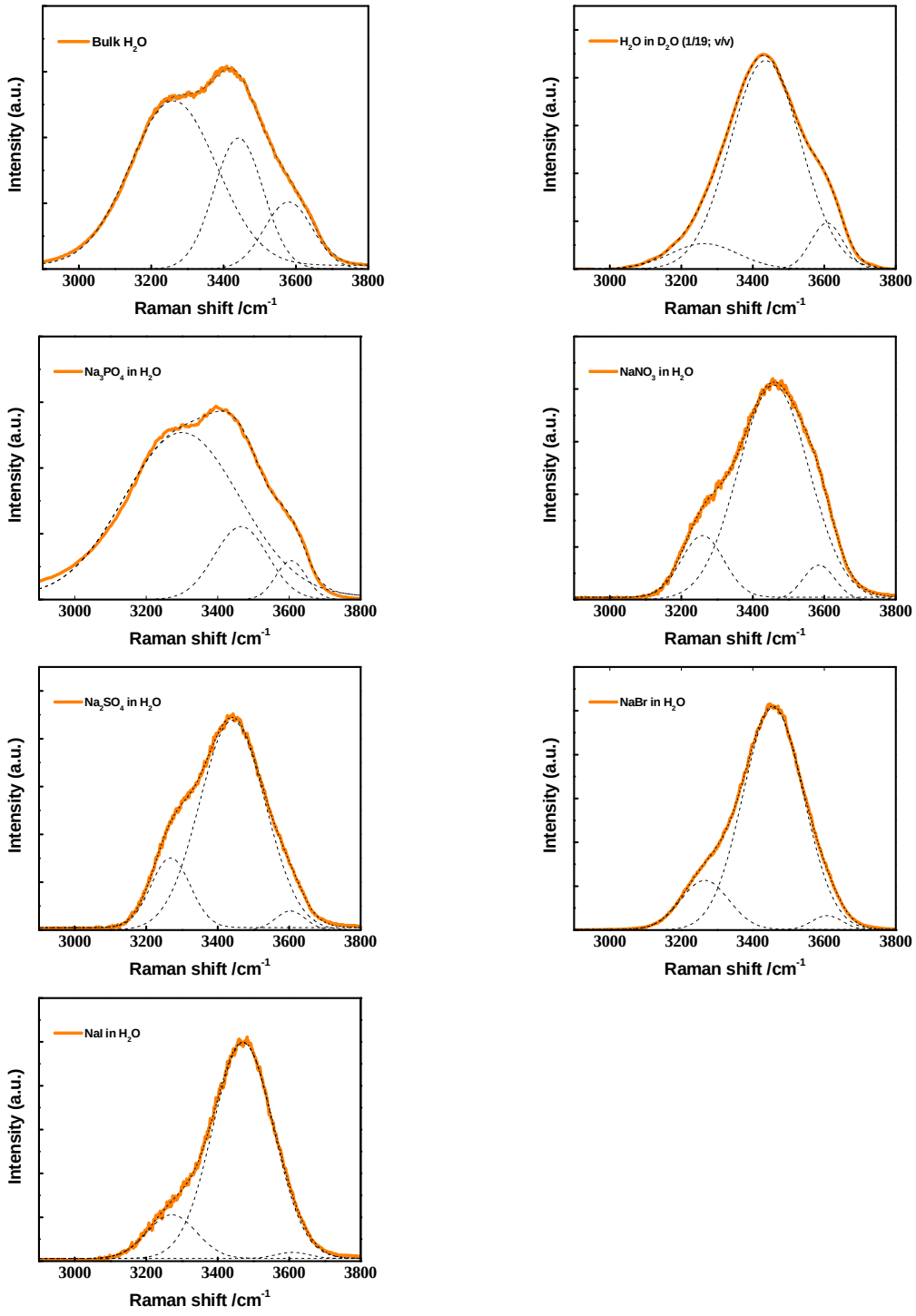

Figure 4.4. *Multiple Gaussian peak fits of the Raman spectra of H_2O, HOD (H_2O/D_2O = 1/19; v/v), and the anion-correlated spectra of Na-salt solutions. The fitted spectra and the corresponding component bands are shown by dashed and dotted lines, respectively.*

Table 4.1. ***Fitting parameters: centre wave number (ν_c), fwhm (Γ), and relative integrated area of different component bands***

Raman/SC-spectra	ν_c , cm^{-1}	Γ, cm^{-1}	Relative integrated area
H_2O	3261	283	0.599
	3441	160	0.254
	3579	156.5	0.1266
HOD (H_2O/D_2O = 1/19; v/v)	3264	221.5	0.096
	3435	233	0.821
	3608	106	0.082
Na_3PO_4	3300	379.3	0.793
	3465	176.5	0.158
	3605	100	0.0478
Na_2SO_4	3268	128	0.1858
	3441	216.5	0.764
	3603	98	0.0310
$NaNO_3$	3260	140	0.1617
	3458	233	0.7678
	3585	105	0.055
NaBr	3265	158	0.1554
	3457	200	0.8171
	3608	116.5	0.0268
NaI	3271	161.5	0.171
	3471	200	0.762
	3610	111.5	0.067

presence of PO_4^{3-}. These integrated areas of the component bands (Figure 4.5 and Table 4.1) enable one to estimate relative coupling effects (intermolecular vibrational coupling and FR) of water in the hydration shell of anions. The basic concept is, the OH stretch mode in HOD is vibrationally decoupled so that the component-1 is mainly due to the contribution of strongly H-bonded water. In other words, for diluted water (H_2O/D_2O =

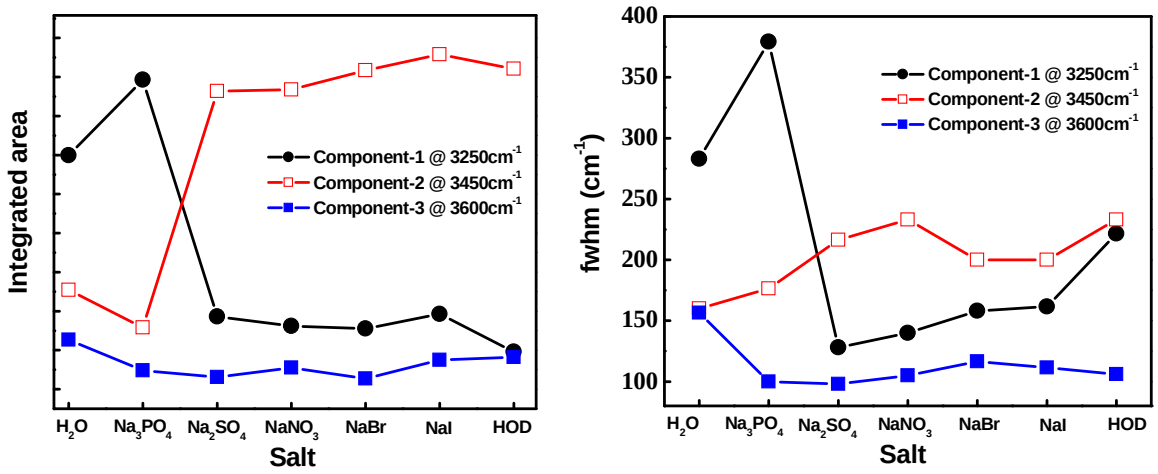

Figure 4.5. *Variation of (A) Integrated area (B) spectral width (fwhm) of the component bands in the OH stretch regions.*

1/19; v/v), the integrated area of component-1 (0.096) is an estimation of the relative population of strongly H-bonded (maximum 3264 cm^{-1}) water. Whereas, in the case of neat H_2O (undiluted water), the corresponding area (0.599) is an estimation of the contribution of strongly H-bonded (maximum 3261 cm^{-1}) as well as strongly coupled water. Assuming the percentage contribution of intermolecular coupling and FR in bulk H_2O as 100, the percentage of the combined intermolecular vibrational coupling and FR in the hydration shell of an ion/solute (PC(S)) can be calculated by equation 4.1.

$$PC(S) = \frac{A_1(S) - A_1(HOD)}{A_1(H_2O) - A_1(HOD)} \times 100 \qquad (4.1)$$

Where, $A_1(i)$ is the relative integrated area of component-1 for the respective area normalized Raman/anion-correlated spectra; S stands for the solute (ion). A plot of PC(S) vs. Na-salts of various chaotropic and kosmotropic anions is shown in Figure 4.6. It is

observed that there is more than 80% reduction of PC(S) in the hydration shell of SO_4^{2-}, NO_3^-, Br^-, and I^- anions.

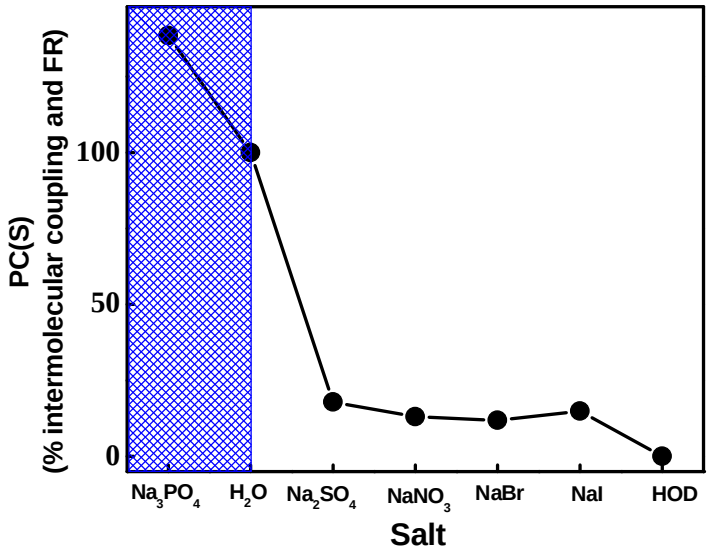

Figure 4.6. *Variation of percentage coupling (intermolecular vibrational coupling and FR) of water in the hydration shells of kosmotropic and chaotropic anions. The coupling in H_2O (undiluted) is assumed as 100 %.*

For further understanding of the H-bond strength of water in the hydration shell of different anions, the peak area averaged wavenumber (ν_a) of the anion-correlated spectrum, which is defined as $\nu_a = \sum A_i \nu_i$ (A_i and ν_i are the relative integrated area and centre wavenumber of the i^{th} component band) are evaluated. The peak area averaged wavenumber (ν_a) reflects the average O-H bond strength, and inversely, that of the H-bond strength (i.e., when ν_a increases, O-H bond strength increases and consequently the H-bond strength decreases) of water in the hydration shell of the anions. As shown in Figure 4.7, the ν_a value for PO_4^{3-} is lowest among all the anions studied ($PO_4^{3-} < SO_4^{2-}$

≈ bulk HOD < NO_3^- < Br^- < I^-), which indicates stronger H-bonding of water in the hydration shell of PO_4^{3-}. Thus, the anion-correlated spectra in the OH stretch region provide important insights into the H-bond strength and collective vibrations (intermolecular vibrational coupling) of water in the hydration shell of different kinds of anions.

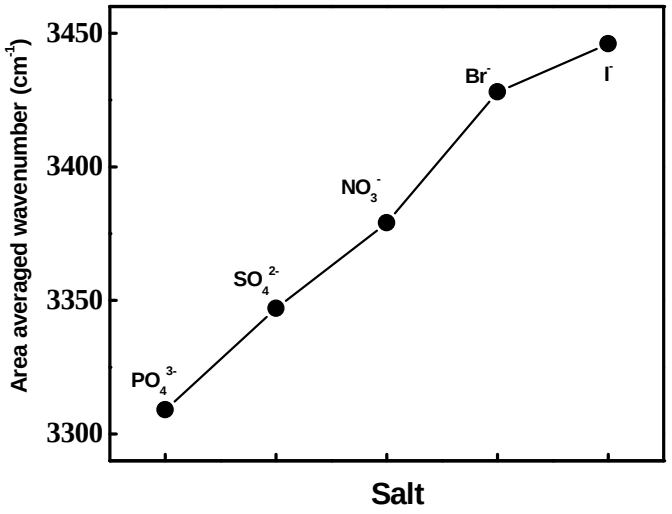

Figure 4.7. *Peak area-averaged wavenumber (ν_a) of anion-correlated spectra in the OH stretch regions.*

We will now discuss on the origin of the observed decrease in intermolecular vibrational coupling and FR in the hydration shell of different kinds of anions. As shown by component analysis, the peak area averaged wave number (Figure 4.7 and Table 4.1) of the anion-correlated spectra shifts toward higher frequency for chaotropic anions, which reveals weaker H-bonding of H_2O in the hydration shell of those anions. Consequently, the energy difference between the OH stretch fundamental and bend-overtone increases in the hydration shell than that in bulk water. The increased energy

difference is expected to reduce the coupling between stretch fundamental and bend overtone (FR) of H_2O. Moreover, because of the weaker H-bonding in the hydration shell, the frequency of the OH stretch vibration of water in the hydration shell mismatches with that of the neighboring bulk-like water. The frequency mismatch discourages the delocalization of vibrational mode (collective vibration).

However, unlike in the hydration shell of chaotropic anions, water in the hydration shell of kosmotropic SO_4^{2-} has comparable H-bond strength to that of bulk water, which means that SO_4^{2-} does not make stronger H-bond with water than water does with bulk water. This means for SO_4^{2-} anion, the energy mismatch between the OH stretch fundamental and bend overtone as well as that between OH stretch fundamentals of neighboring water molecules in the hydration shell are not as large as those for NO_3^-, Br^-, and I^- anions. Nevertheless, the comparable PC(S) value for SO_4^{2-} with those of the $NO_3^-/Br^-/I^-$ suggests that there is almost equal (~80%) reduction of coupling effects in the hydration shell of all these anions. The reduction of intermolecular vibrational coupling of H_2O in the hydration shell of SO_4^{2-} ion is assignable to the stronger electric field at the vicinity of the divalent SO_4^{2-} anion (higher charge density than the monovalent chaotropic NO_3^-, Br^-, and I^- anions). The strong electric field at the immediate vicinity of an anion leads to a time averaged preferential orientation of water at the surface of the anion, and with increasing charge density (of the anion) the water in the hydration shell approaches closer to the anion.[36,43,262] It follows that the water in the (first) hydration shell is polarized by the ion's electric field and experience a significant spatial patterning (orientations and intermolecular distances) and dynamical

perturbations[29,244,263-265] which are likely to promote localization of vibrational modes in the hydration shell. Finally, due to excluded volume, on average, the water molecules in the first hydration shell that directly interacts with the anion has less number of accessible H_2O molecules than that in the bulk, which leads to decreased intermolecular vibrational coupling in the hydration shell.

Accordingly, the ions with even higher charge density (like trivalent PO_4^{3-}) are expected to have even stronger electric field, and hence, weaker coupling (lower PC(S) than that of SO_4^{2-}). In contrast, the PC(S) value for PO_4^{3-} is much larger than that of SO_4^{2-}; as if the water in the hydration shell of PO_4^{3-} has efficient intermolecular coupling and FR (Figure 4.6). This apparent anomaly can be rationalized on the basis of the contribution of strongly H-bonded water species (~3250 cm^{-1}) in the hydration shell of trivalent PO_4^{3-} anion. The strongly H-bonded water in the hydration shell of PO_4^{3-} enhances the relative Raman intensity in the red region (~3250 cm^{-1}) of the OH stretch band. In fact, the anion-correlated spectrum for PO_4^{3-} shows larger intensity in the red region of the OH stretch band (< 3100 cm^{-1}) than the Raman spectrum of H_2O (Figure 4.2B). The intensity enhancement in red region is compensated to some extent by the reduction of intermolecular coupling of water due to strong electric field and excluded volume effect in the hydration shell. As a result, the anion-correlated spectrum for PO_4^{3-} apparently looks similar to the Raman spectrum of bulk H_2O and the PC(S) value is even little larger than that of bulk H_2O (blue shaded region in Figure 4.6). Thus, the large PC(S) value for PO_4^{3-} signifies that the vibrational response due to collective OH

oscillators (~3250 cm^{-1}) is replaced by the response of strongly H-bonded isolated OH oscillators in the hydration shell.

Although the anion-correlated spectra in the OH stretch band region provide valuable information about H-bonding and intermolecular vibrational coupling of water in the hydration shell of different anions, their interpretation has been complicated by FR and intramolecular coupling that deformed the OH stretch band. For the clear-cut understanding of H-bonding and intermolecular vibrational coupling in the hydration shell, we extended the MCR-analysis to the HOH bend (ν_B) mode of water, which is neither deformed by FR nor by intramolecular coupling. We can expect that, the position and width of the ν_B band will provide unambiguous information about the H-bond strength and intermolecular vibrational coupling of water. Unlike the OH stretch band which shifts to lower frequency due to stronger H-bonding, the HOH bend mode of strongly H-bonded water behaves like a constrained oscillator and oscillates at a frequency higher than that of the free oscillator. As a result, stronger H-bonding is indicated by a blue-shift of the HOH bend maximum[229] and the perturbation of intermolecular coupling is reflected in the band width (fwhm) of ν_B band.[256,257]

4.4.3. Anion-correlated Raman spectra of water in the HOH bend region

Figure 4.8 shows the anion-correlated Raman spectrum of the salt solutions as well as the Raman spectrum of neat water (i.e. intermolecularly coupled H_2O) and decoupled water (i.e. H_2O in D_2O) in the HOH bend region. The effect of intermolecular vibrational coupling on the position and width of the HOH bend mode is obvious from a comparison

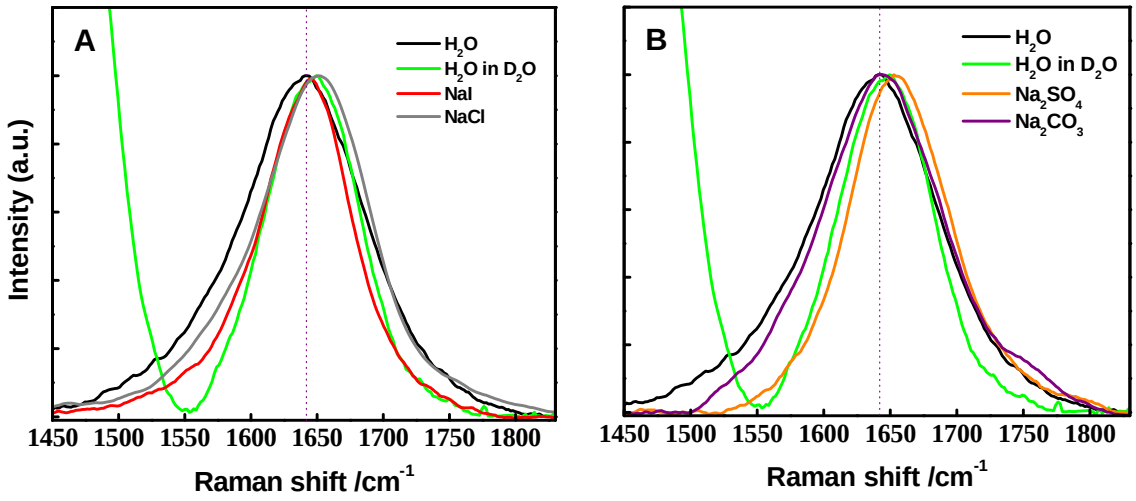

Figure 4.8. *IC-Raman spectra of H_2O in presence of (A) NaCl (gray), NaI (red), (B) Na_2SO_4 (orange), and Na_2CO_3 (purple). The Raman spectrum of bulk H_2O (black line) and MCR-retrieved spectrum of H_2O in D_2O (green line) that bears the Raman response of decoupled H_2O (around 1650 cm^{-1}) are shown in both panels.*

of HOH bend spectra of coupled (H_2O, black line) and decoupled (H_2O in D_2O, green line) water. We obtained the HOH bend spectrum of decoupled H_2O by MCR-analysis of the Raman spectra of H_2O-D_2O mixture. In H_2O-D_2O mixture (H_2O/HOD/D_2O = 11.1:44.4:44.4), the HOH bend mode (~1642 cm^{-1}) is energetically well separated from the bend modes of D_2O (~1210 cm^{-1}) and HOD (1450 cm^{-1}). Therefore, the H_2O molecule in D_2O (at low dilution) is vibrationally decoupled with neighboring molecules. As shown in Figure 4.8, in contrast to the bend mode of vibrationally coupled H_2O (neat H_2O) that appears at 1642 cm^{-1} with an fwhm of ~110 cm^{-1}, the bend mode of decoupled H_2O appears at 1651 cm^{-1} with a fwhm of ~68 cm^{-1} (peak positions and band widths are summarized in Table 4.2). The blue-shift of the bend maximum (~10 cm^{-1}) and the

decrease of spectral width (~40%) is a bench mark of intermolecular decoupling of the bend mode of H_2O.

Now from a comparison of the anion-correlated spectra with the HOH bend spectra of coupled and decoupled water (MCR-retrieved spectrum of H_2O in D_2O), one can clearly identify the perturbation of intermolecular vibrational coupling in the hydration shell of ions. For example, very similar to that of decoupled water, the anion-correlated spectra for Cl^- and I^- ions are blue-shifted and have lower fwhm than that of neat H_2O, which indicates the bend mode of water in the hydration shell of Cl^- and I^- ions are decoupled from neighboring water molecules. This observation is in qualitative agreement isotropic and anisotropic Raman measurements of aqueous electrolyte solutions in HOH bend region.[256,258] The band shape of the isotropic/anisotropic Raman spectra of water are sensitive to the symmetry of intermolecular coupling and it has been observed that the difference between isotropic and anisotropic Raman spectra of water

Table 4.2. ***Centre wavenumber (ν_c) and fwhm (Γ) of the ν_B and combination ($\nu_B + \nu_{L1}$) band of water in different environments. The frequency difference between the combination band and bend fundamental i.e. $\Delta\nu = [(\nu_B + \nu_{L1}) - \nu_B]$ is equivalent to the librational band position of water.***

Raman/IC-spectra	ν_c (ν_B), cm^{-1}	ν_c ($\nu_B+\nu_{L1}$), cm^{-1}	$\Delta\nu$ = (ν_B + ν_{L1}) - ν_B	$\Gamma(\nu_B)$, cm^{-1}	$\Gamma(\nu_B+\nu_{L1})$, cm^{-1}
H_2O	1642	2114	472	109	236
H_2O in D_2O	1651	-	-	82	-
NaI in H_2O	1646	2063	417	79	226
Na_2SO_4 in H_2O	1654	2142	499	87	258
Na_2CO_3 in H_2O	1648, 1760	2137	489	106	243

decreases with increasing concentration of electrolytes (conc. 2 - 3 mole dm^{-3}), which was explained by the reduced vibrational coupling of water in presence of electrolytes. Moreover, the maximum of the anion-correlated spectrum for Cl^- (1651 cm^{-1}) matches with decoupled H_2O, whereas that for I^- (1646 cm^{-1}) is ~5 cm^{-1} red-shifted from decoupled H_2O. The red-shift reflects weaker H-bonding of water in the hydration shell of I^-, which is consistent with the results in OH stretch region.

In the case of bivalent SO_4^{2-}, the anion-correlated spectrum shows a lower band width and a blue-shifted (~12 cm^{-1}) maximum than bulk water. These results indicate intermolecular vibrational decoupling of water in the hydration shell of SO_4^{2-} as well. The peak frequency for SO_4^{2-} is even blue-shifted than that of decoupled H_2O (MCR-retrieved spectrum of H_2O in D_2O), which reveals stronger H-bonding of water with SO_4^{2-} anion. The strong H-bonding of water in hydration shell of SO_4^{2-} is not very evident in the anion-correlated spectrum in OH stretch region (Figure 4.2). This is due to the interplay of other processes in the OH stretch region (e.g. modification of FR and intramolecular vibrational coupling) that masked moderate spectral changes of the OH stretch band due to H-bonding.

Similar to the Cl^-, I^- and SO_4^{2-} anions, it is likely that the bend mode of water is also decoupled in the hydration shell of CO_3^{2-}. The anion-correlated spectrum for CO_3^{2-} is moderately blue-shift (~6 cm^{-1}), but the fwhm of the IC-spectrum is close to that of bulk H_2O (Table 4.2). The large width (more than that of IC-spectrum for SO_4^{2-}) is assignable to greater distribution of H-bond strength in the hydration shell of CO_3^{2-}, which is also reflected by the broad IC-spectrum in OH stretch region (violet line in

Figure 4.2). In addition to the large width and moderate blue-shift of the main band, there is a shoulder in the high frequency region (around 1760 cm^{-1}) of the IC-spectrum for CO_3^{2-} anion. Such a largely blue-shifted bend mode is likely to originate from strongly H-bonded water species. Previous IR study[266] suggested that the frequencies of OH stretch (ν_{str}) and HOH bend (ν_B) vibrations and their dependence on H-bond strength can be correlated by the following empirical relation,

$$\nu_B = 1590 + 0.26(3706 - \nu_{str}) \quad (4.2)$$

Accordingly, the blue-shifted bend mode (1760 cm^{-1}) corresponds to the water species whose OH stretch frequency appears at 3052 cm^{-1}. In fact, the MCR-analysis in the OH stretch region (for CO_3^{2-} anion) showed a new band at ~3050 cm^{-1} (violet line in Figure 4.2). Thus, the present results suggest that the hydration shell of bivalent CO_3^{2-} anion contains two types of water molecules: water in the first hydration shell that is directly interacting with CO_3^{2-}-oxygens is very strongly H-bonded, and that in the second hydration shell has the H-bond strength stronger than bulk water but weaker than the first hydration shell water. It is intuitive that the bivalent CO_3^{2-} anion because of its high charge density can affect water even beyond the first hydration shell. Infrared photo dissociation (IRPD) study[267] of mono- and bivalent anion containing aqueous nanodrops suggested that the effect of bivalent anion propagates beyond the first hydration shell.

The Raman-MCR results in the HOH bend region show that all the anions (Cl^-, I^-, SO_4^{2-}, and CO_3^{2-}) lead to a blue-shifted (~5-10 cm^{-1}) maxima of HOH bend mode of water, which is largely due to intermolecular vibrational decoupling in the hydration shell. Previous IR study,[91] however showed that the HOH band maximum shifts toward

lower energy at high concentration of salts (~5 mol dm^{-3} NaI). To understand these seemingly contradicting observations, we reinvestigated the variation of fwhm and position of the ν_B band in presence of low and high concentrations of Na-salts. As shown in Figure 4.9A, in the case of SO_4^{2-} and CO_3^{2-} anions, the peak position gradually shifts toward higher energy with increasing concentration (up to 2 mol dm^{-3}). But, in the case of I^-, the band position shifts toward higher energy with increasing concentration up to ~ 0.8 mol dm^{-3}, and then decreases for a concentration up to 6.0 mol dm^{-3}. The spectral width also decreases marginally for SO_4^{2-} and CO_3^{2-}, but that in the case of I^- has decreased significantly within 0.8 mol dm^{-3}, and then decreases slowly up to a concentration of 6.0 mole lit^{-1} (Figure 4.9B). The non-monotonic variations of peak position and width (for I^-) imply that there are two opposing factors which switch at a concentration of

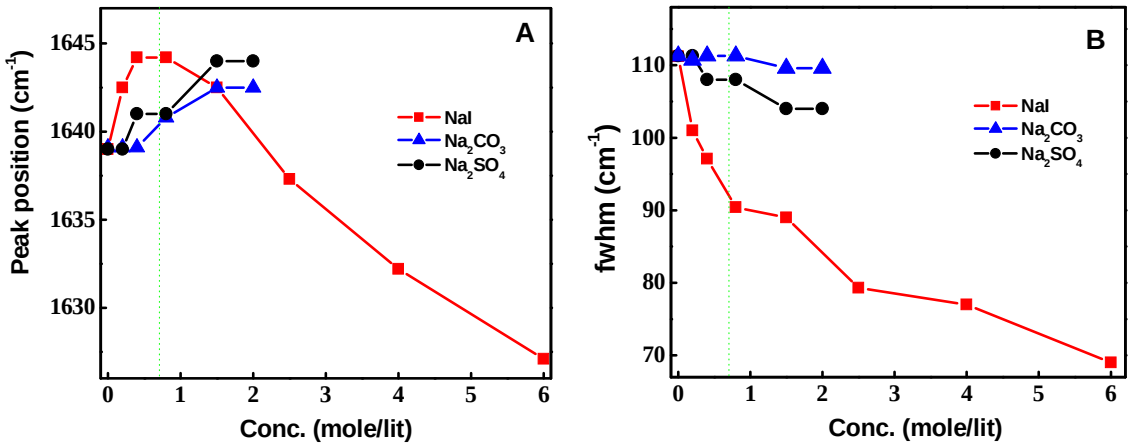

Figure 4.9. *Variation of (A) peak position and (B) width (fwhm) of the HOH bend mode of water with the concentration of Na-salts (salts are mentioned in the graph panel).*

~ 0.8 mol dm^{-3}. The anion-correlated spectrum for I^-, whose maximum is blue-shifted than that of bulk H_2O, but red-shifted than that of decoupled H_2O, also hints at the presence of two opposing factors, such as (i) intermolecular decoupling which causes blue-shift the ν_B band and (ii) weakening of H-bond strength that red-shifts the ν_B band. In the low concentration limit (< 0.8 mol dm^{-3}), with increasing concentration of I^-, the population of weakly H-bonded as well as vibrationally decoupled water increases which leads to a net blue shift of the ν_B band. At higher concentrations (>0.8 mol dm^{-3}), with increasing concentrations of I^-, the population of weakly H-bonded water increases but not that of decoupled water, since at high concentration there is not enough bulk water to be decoupled. As a result, in the high concentration limit, the position of ν_B band is solely governed by the H-bond strength of hydrating water and shifts toward lower frequency with increasing concentration of I^-.

4.4.4. Librational band region of water

In liquid water, intermolecular interactions give rise to low frequency vibrational modes (hindered translation and Libration (hindered rotation)) that appears <1000 cm^{-1}.[254,268,269] Libration, for example, appears at 470 (ν_{L1}) and 670 cm^{-1} (ν_{L2}) as shown by the deconvolution of the low frequency Raman spectrum of water (Figure 4.10). The frequency positions of these librational bands reveal the strength of intermolecular interactions (e.g. H-bonding) and rotational freedom of water. However, because of the strong mutual overlap of these two low frequency bands and large background signal, it is cumbersome to precisely analyze the small changes of the librational bands due to the added salts.

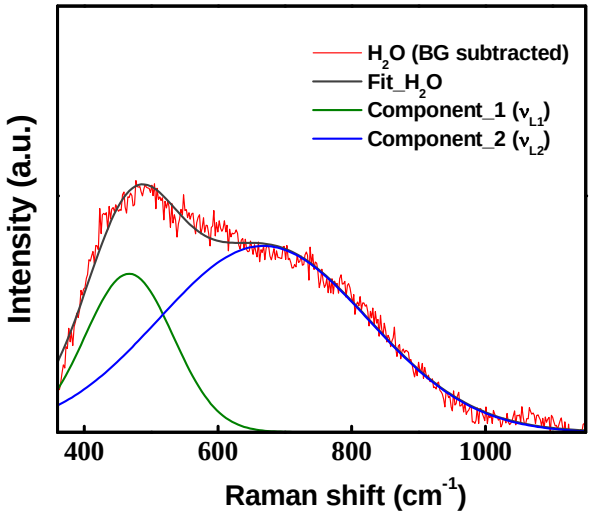

Figure 4.10. *Background subtracted Raman spectrum (red) of H_2O in hindered rotational band regions (400 – 1000 cm^{-1}). Gray line is the fitted spectrum, olive and blue lines are the Gaussian component bands.*

We have applied an alternative approach to obtain the frequency position of the ν_{L1} band of water in the hydration shell of anions. First, the anion-correlated (AC) spectra of water were obtained in the bend fundamental (ν_B) and combination ($\nu_B + \nu_{L1}$) band regions. Then, the frequency difference between the combination band and the bend fundamental ($\Delta\nu_{AC} = [(\nu_B+\nu_{L1})_{AC} - (\nu_B)_{AC}]$) is calculated, which corresponds to the librational band position of water in the hydration shell. The anion-correlated spectra of water in combination ($\nu_B + \nu_{L1}$) band regions and the modification of librational band positions in the hydration shell of different anions are discussed in the following section.

4.4.5. Anion-correlated Raman spectra of water in the combination (bend + librational) band region

Peak normalized Raman spectrum of bulk H_2O and the anion-correlated spectra for the mono- and bivalent anions in the combination band region are shown in Figure 4.11. The

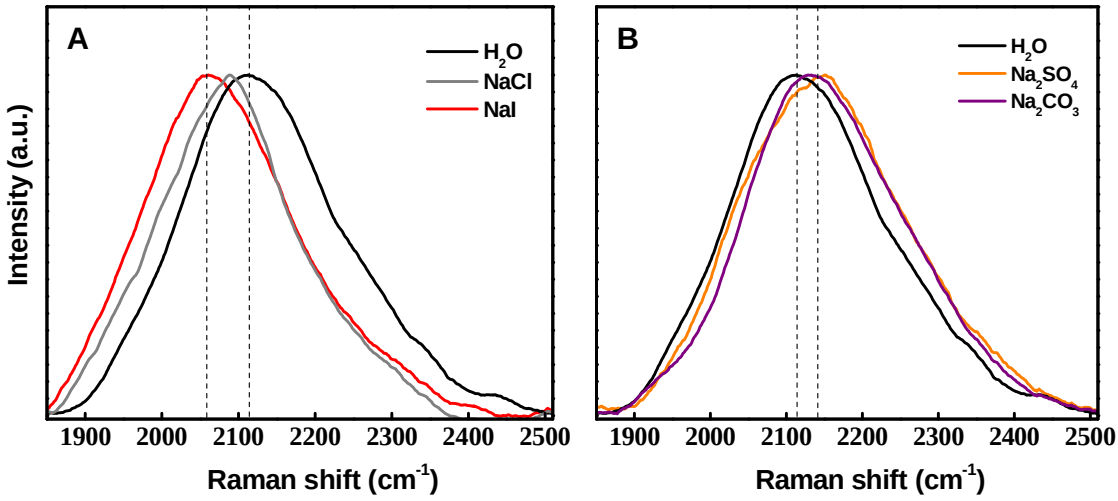

Figure 4.11. *Peak normalized IC-Raman spectra for (A) NaI and NaCl (B) Na_2SO_4 and Na_2CO_3 in the combination ($\nu_B + \nu_{L1}$) band regions. The Raman spectrum of neat H_2O (black) is shown in each panel for comparison with the IC-spectra.*

frequency positions of the combination bands are governed by the band position of librational and bend motions of water. Therefore, as mentioned in previous section, one can obtain the librational band position of hydration water ($\Delta\nu_{AC}$) for different anions (summarized in Table 4.1). It is observed that the librational band position in the hydration shell varies differently for different anions. For Cl^- and I^- anions, the band maximum is red-shifted, whereas for SO_4^{2-} and CO_3^{2-} anions, the band maximum is blue-shifted than that of bulk water. The red-shift of the librational band reflects weaker interaction (H-bonding and electrostatic) of hydration water with the anion and/or with neighboring water molecules (or, conversely, blue-shift of librational band indicates stronger interaction of water with the anion and/or with neighboring molecules in hydration shell). Thus, the hydration shells of monovalent Cl^- and I^- anions are composed of weakly interacting water molecules. Because of weak interactions, such water

molecules have higher librational freedom than bulk water. On the other hand, the hydration shell of bivalent SO_4^{2-} and CO_3^{2-} anions are formed of strongly interacting water molecules of lower librational freedom.

It is likely that the librational mobility of hydration water depends upon the strength of ion-water (e.g. ion-dipole interaction and ion-water H-bond) and water-water interactions in the hydration shell. Therefore, we can expect that the weaker H-bonding of water in the hydration shell of I^- is responsible for the higher librational freedom of water at the vicinity of I^- anion. However, as can be seen from Figure 4.11A and 4.11B, the librational position of hydration water of bivalent SO_4^{2-} and CO_3^{2-} anions has comparable librational band position even though the H-bond strength in their hydration shells varies significantly. These results suggest that the librational freedom of hydration water not only depends upon the H-bond strength, but also on the ion-water electrostatic interactions, especially for the high charge density anions. This is consistent with the Monte Carlo simulation result[262] which implied that the water structure around high charge density ions are governed largely by ion-water electrostatic interaction, whereas, the same for low charge density ions are governed by the H-bond strength of surrounding water. In case of high charge density anions, along with the H-bond strength, the preferential orientation of water dipole or the OH vector increases in the hydration shell.[27,29,76,83,244,263,270,271] Such an orientational preference is expected to decrease the librational freedom of water at the immediate vicinity of a multivalent anion.

The dynamics of vibrational and reorientation relaxation of water, which are important for stabilization of reactive intermediates in aqueous phase,[272,273] depend upon

the interactions with neighboring molecules and the coupling among vibrational modes of water.[51,52,96,274,275] The bend overtone of water, for example, acts as receptor for the OH stretch vibration relaxation. Therefore, a perturbation of coupling between bend overtone and OH stretch fundamental (FR) in the hydration shell, as observed in the present as well as in previous studies,[78,248] is likely to affect the OH stretch vibrational relaxation. It is anticipated that the modification of H-bond strength and librational energy of water in the hydration shell of ions will affect the vibrational as well as short (sub-100fs librational reorientation) and long time orientational relaxation of water.

4.4. Conclusion

In this chapter, Raman spectroscopy in combination with multivariate curve resolution (Raman-MCR) is used to extract the different vibrational bands (OH stretch, HOH bend, and combination (bend + librational)) of water in the hydration shell of different anions (anion-correlated spectrum). The frequency positions and width of the anion-correlated spectra in the OH stretch and HOH bend regions reveal two important aspects: (1) the hydrogen-bond (H-bond) strength of hydration water decreases as $CO_3^{2-} > PO_4^{3-} > SO_4^{2-} >$ bulk water ~ $Cl^- > I^-$ (2) water in the hydration shell of all the anions studied is vibrationally decoupled from neighboring water molecules. Comparison of integrated areas of component bands of the anion-correlated spectra (OH stretch region) with that of the Raman spectrum of H_2O and HOD enables to quantify the modification of intermolecular vibrational coupling (collective OH stretch) of water at the immediate vicinity of different kinds of anions. It is observed that there is ~80% reduction of coupling effects (intermolecular coupling and FR) in the hydration shell of I^-, Br^-, NO_3^-,

and SO_4^{2-}ions. In the case of PO_4^{3-}, the water is strongly hydrogen bonded with reduced intermolecular vibrational coupling. Moreover, the librational band position, as obtained by the frequency difference of the combination and bend fundamental bands, shows that the librational mobility of hydration water increases as $CO_3^{2-} \approx SO_4^{2-}$ < bulk water < I^-. Larger librational freedom of water in the hydration shell of I^- is assignable to weaker H-bonding of water whereas, the lower rotational freedom in the hydration shell of CO_3^{2-} and SO_4^{2-} anions is presumably due to strong H-bonding and ion-dipole interaction in the hydration shell.

Chapter 5

Structure and Properties of Water at Charged and Neutral Hydrophobic Hydration Shells

5.1. Introduction

Hydrophobic effect is a manifestation of the segregation of nonpolar molecules in water, which plays important role in various chemical and biological processes.[276-280] The example includes the formation of micelle, microemulsion, lipid bilayer membrane, folding-unfolding of proteins, activation of enzymes, etc.[1,2,64,281-284] The hydrophobic effect crucially dependents on the interaction between hydrophobic molecular groups and water. For the aqueous solution of a solute, it has been observed that a solute affects water only at its immediate vicinity. Therefore, the hydrophobic effect is intimately related with the structure and properties of water around a hydrophobic solute (Hydrophobic hydration shell).

Hydration of hydrophobic molecules/molecualr groups has been studied using numerous techniques, such as thermodynamics measurements, NMR, neutron diffraction, Infrared and Raman, THz-spectroscopy, photoelectron spectroscopy and molecular dynamic simulation.[131-152] Thermodynamic measurements revealed that the introduction of hydrophobic solute in water increases the heat capacity and decreases the entropy.[285-

[287] These observations were explained on the basis of 'iceberg' model by Frank and Evans in 1945. According to this model, water in a hydrophobic hydration shell undergo structural enhancement (either stronger or more hydrogen bonds per volume unit and more ordered structure) in comparison to that in the bulk, which would account for the entropy loss and increase in heat capacity of the system.[66,288] The iceberg model was disputed later by several experimental and theoretical results.[54,69] Neutron diffraction experiments which provide the water-water radial distribution function (RDF) around the solute, reveals that the structure of water around hydrophobic groups is comparable to that of bulk water.[100,289,290] It has been proposed that the anomalous properties upon dissolution of hydrophobic solutes arise from incomplete mixing of the solute and water at the molecular level. In contrast, NMR[291-294] and dielectric relaxation studies[295-297], that measure the orientational dynamics of water molecules, show that the average mobility of water molecules in solutions containing hydrophobic solutes is decreased. However, as these methods measure a response that is averaged over all water molecules (bulk and hydration shell), these techniques cannot provide selective information of water in the hydration shell. Therefore, many of the hydration shell specific information are obtained by MD-simulations,[298-302] which suggest that the water molecules surrounding small hydrophobic solutes form fewer but stronger H-bonds. These simulations furthermore suggested that geometric excluded volume effects are account for the retardation in rotational orientation of water in the hydrophobic hydration shell.[303]

For an unambiguous understanding of the water structure in the vicinity of the hydrophobic groups, it is essential to selectively probe the water molecules in the

hydration shell of hydrophobic groups. We have used Raman spectroscopy in combination with multivariate curve resolution (Raman-MCR) to selectively map the vibrational features of water in the hydration shell of hydrophobic groups such as, tert-butanol (TBA) and tetramethyl ammonium cation (TMA^+).

4.2. Experiments and Methods

The chemicals, tetramethylammonium chloride (TMA) (≥ 98.0 %), Heavy water (D_2O, > 99.9 atom % D) and the NaCl (≥ 99.0 %) were purchased from Sigma Aldrich. *tert*-Butanol (TBA) is from Spectrochem India. Milli-Q water (18.2 MΩ cm resistivity) was used for all the measurements. The unpolarized Raman spectra of the samples were recorded at 23°C using a micro-Raman spectrometer (STR-300, SEKI Technotron, Japan). We used low concentration of solutes (≤ 1.0 mole dm^{-3}) to ensure that the solutes are fully hydrated without significant solute-solute interactions (aggregation or ion pairing). Aqueous solution of the solutes were taken in quartz cell of 2 mm optical path length and were excited at 532 nm (power ~20 mW at sample position, continuous wave (CW) YAG laser) using a 10X objective lens (Olympus). The scattered light was collected by the same objective lens and passed through an edge filter (LPO3-532RU-25) to filter Rayleigh and anti-Stokes scattered signals. The Stokes signal after the edge filter was passed through a fiber-coupled spectrograph (Acton series SP 2300i, 1200 groove/mm) and detected by a thermo-electric cooled (-75°C) charge-coupled device (CCD, Model no PIXIS:256). The spectrograph was calibrated using the 520.5 cm^{-1} line from silicon wafer and was verified by measuring the Raman spectrum of naphthalene. The Raman spectra of all solutions were acquired at the same experimental conditions

(acquisition time for each spectrum was 300 sec (60 sec × 5), slit width 80 μm). For polarization studies, the stokes signal after long pass filter was passed through a polarizer allowing the selection of either its parallel (VV) or perpendicular (VH) polarization component with respect to the excitation light. The isotropic and anisotropic Raman components were calculated in the usual way, Isotropic = VV-(4/3) VH; Anisotropic = (4/3) VH.

A constant background signal was subtracted from the experimentally recorded Raman spectra, and the background subtracted spectra were area normalized to nullify the effect of intensity variation (either due to laser fluctuation) in subsequent multivariate analysis. The area normalized Raman spectra were arranged into the columns of a matrix (data matrix, DM; the first column of the DM is neat water spectrum) for multivariate analysis, the details of which have been described in chapter 2. Briefly, the data matrix, containing mixed spectral response of hydration and bulk water, is decomposed by singular value decomposition (SVD) that provides an initial estimate of the number of components and their spectral responses. Then, the initial estimates were optimized by alternating least square (ALS) fitting method, while incorporating certain restrictions, such as non-negative intensity of the component spectra, concentrations of solute (known from the experiments), number of components (two in the present case). One of the two spectral components, obtained after SVD-ALS operations, represents the bulk water response, and the other component corresponds to the response of water molecules that are perturbed by solute and the response of the solute itself (if any), which is designated as solute-correlated spectra (SC-spectra).

As mentioned earlier, in aqueous electrolyte solution, say NaCl, there are Na^+ cation and Cl^- anion; therefore, the IC spectrum of NaCl solution contains vibrational response of water that are perturbed by both, Na^+ and Cl^-. It is has been observed, in previous IR and Raman-MCR studies, that Na^+-cation has relatively negligible effect on the OH stretch band of water compared to that of halide anions. Thus, the IC-spectra of aqueous Na-salt solutions predominantly bear the vibrational characteristics of water in the hydration shell of the anions. In the case of TMACl (1M), the TMA^+-correlated spectrum was obtained by considering 1M NaCl solution as the pure solvent spectrum for MCR analysis. The SC-spectra are compared with the OH stretch band of bulk H_2O and isotopically diluted water of different compositions (HOD75 (H_2O/D_2O = 75/25, v/v); HOD50 (H_2O/D_2O = 50/50, v/v), and HOD25 (H_2O/D_2O = 25/75, v/v)).

5.3. Results and Discussion

5.3.1. OH stretch response of water in the hydration shell of TBA

Figure 5.1 shows the normalized Raman spectra of neat water (black line) and aqueous TBA solution (1.0 mol dm^{-3}, blue line) in 2900 – 3750 cm^{-1} region. The Raman spectrum of aqueous TBA solution contains the combined response of hydration water, bulk water, and TBA. The contribution of TBA, as shown by the spectrum of TBA (1.0 mol dm^{-3}) in D_2O (red dotted line), is mainly the CH_3 stretch bands below 3050 cm^{-1}, since the alcoholic OH band (around 3365 cm^{-1}) is very weak for such low concentration of TBA. Thus, in the region above 3050 cm^{-1}, the spectrum of aqueous TBA solution is largely due to the combined response of hydration and bulk water. Nevertheless, the spectrum of

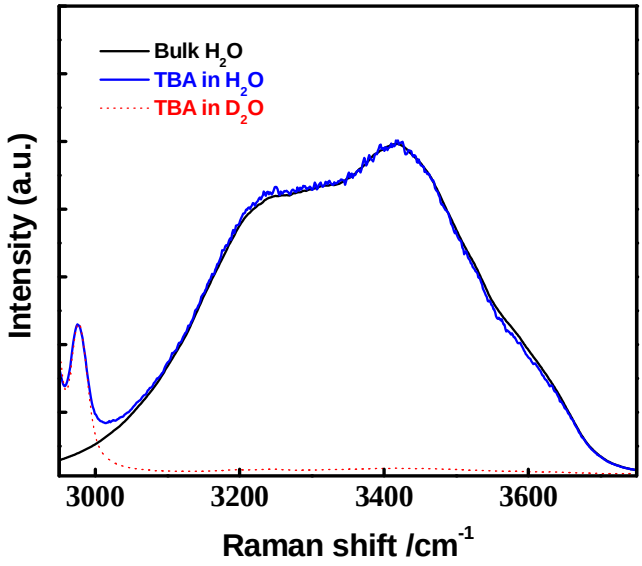

Figure 5.1. *Raman spectra of neat water (black line), TBA (1.0 mole dm^{-3}) in H_2O (blue line) and in D_2O (red dashed line) in 2900 – 3750 cm^{-1} region.*

aqueous TBA solution is very similar to that of neat H_2O. The subtle difference of the OH stretch band in presence of TBA, however, does not mean that the vibrational spectrum of water in the hydration shell of TBA is comparable to that of bulk water. The population of hydration water in diluted TBA solution (1.0 mole dm^{-3}) is much lower than that of bulk water, and the total Raman signal is a cumulative sum of weak signal of hydration water and a strong signal of bulk water. As result, even if the vibrational response of hydration water differs from that of bulk water, the combined response may resemble to that of neat water.

Multivariate curve resolution (MCR) analysis[97,98] of the Raman spectra of neat water and aqueous TBA solution enable us to retrieve the weak signal of hydration water, which is buried in a large signal of bulk water. As shown in Figure 5.2, the MCR-

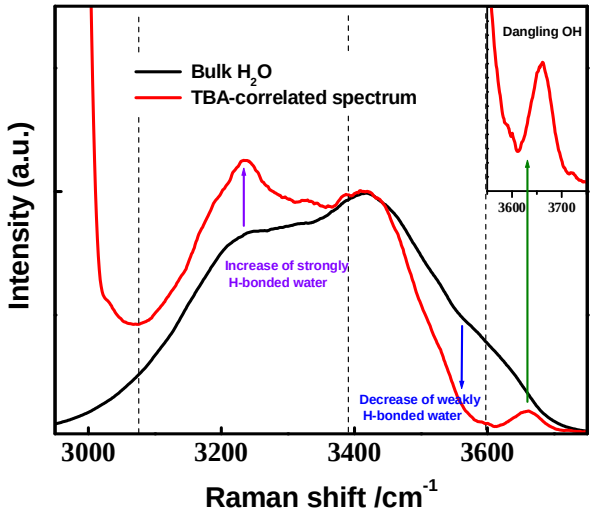

Figure 5.2. *TBA-correlated Raman spectrum of water (red) in 2900 – 3750 cm^{-1} region. Raman spectrum of neat water (black) is shown for reference.* ***Inset:*** *expanded view of the TBA-correlated spectrum in the high frequency region that shows the dangling OH at the surface of TBA.*

retrieved hydration water spectrum (TBA-correlated spectrum; red line) is substantially different from the Raman spectrum of bulk water. A qualitative comparison between these spectra reveals three distinct features: first, in the extreme blue region (3600 - 3700 cm^{-1}), the TBA-correlated spectrum shows a narrow band (fwhm ~45 cm^{-1}) with maximum at ~3660 cm^{-1}. Such an OH stretch band is a typical signature of very weakly interacting OH group, which is prevalent at macroscopic hydrophobe/water (e.g. lipid monolayer/water) interfaces as observed by vibrational sum frequency generation (VSFG) spectroscopy.[304] Moreover, the heterodyne–detected vibrational sum frequency generation (HD-VSFG) study of lipid monolayer/water interfaces showed that such weakly interacting OH is pointed toward the hydrophobic lipid phase, quite similar to the dangling OH at air/water interface.[80]

Thus, the 3660 cm^{-1} band is assigned to the very weakly interacting dangling OH which is pointed toward the hydrophobic alkyl group of TBA in the hydration shell. The dangling OH band at TBA surface is ~ 50 cm^{-1} red-shifted than that at the air/water interface. This is due to the van der Waals interaction of the dangling OH with the methyl groups of TBA. Secondly, in the 3400 – 3600 cm^{-1} region of the OH band, the intensity of TBA-correlated spectrum is weaker than that of bulk water. Weaker intensity in the blue region has also been observed in FTIR study[93] of the hydration of tetrabutylammonium cation (Bu_4N^+) in HOD (D_2O/H_2O = 4/96; w/w). The weaker intensity in this region, suggests a decrease of relative population of weakly H-bonded water in the hydration shell of TBA. Finally, in the red region of the OH stretch band (below 3400 cm^{-1}), the TBA-correlated spectrum is more intense than that of bulk water. Apparently, higher intensity in the red region of the OH stretch band indicates an increase of relative population of strongly H-bond of water in the hydration shell.

Nevertheless, as shown in Figure 5.3, the TBA-correlated spectrum of water is quite similar to the isotropic Raman spectrum of bulk water. As mentioned in chapter 4, the band shapes of the polarized (isotropic/anisotropic) Raman spectra of water are sensitive to the symmetry of intermolecular coupling. The symmetric OH stretch vibrations that are coupled in-phase with neighboring symmetric OH oscillators oscillate at lower frequency (maximum ~3230 cm^{-1}) and appears mainly in isotropic Raman spectrum; whereas, the antisymmetric OH stretch vibrations that coupled in-phase with neighboring antisymmetric OH stretches oscillate at higher energy (maximum ~3430 cm^{-1}) and become prominent in the anisotropic Raman spectrum.

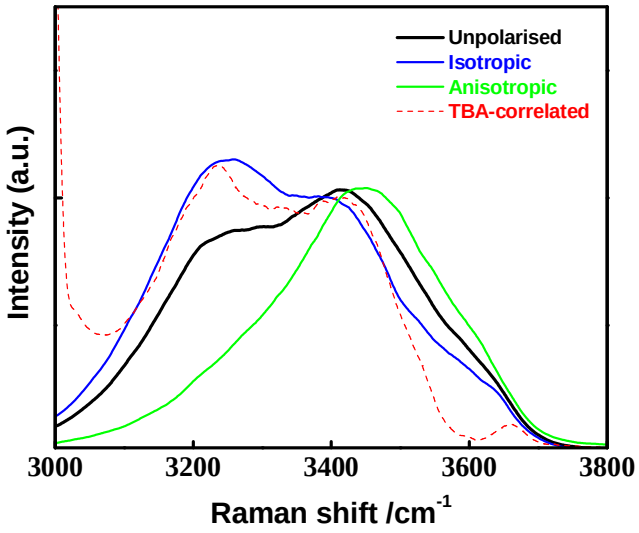

Figure 5.3. *TBA-correlated spectrum (red dashed curve) and polarized Raman spectra of bulk water (isotropic (blue), anisotropic (green) and unpolarized (black)) in 3000 - 3800 cm^{-1} region.*

Because of the similarity of the TBA-correlated spectrum with the isotropic Raman spectrum of bulk water, we can also expect that the OH stretch vibration of water at the surface of TBA is more strongly coupled with neighboring water molecules than that in bulk water. In the following sections, we have elucidated the vibrational coupling and H-bonding of water in the hydration shell of uncharged (TBA) and charged (tetra-methyl ammonium cation, TMA^+) hydrophobic groups, by using Raman-MCR in combined with isotopic dilution spectroscopy.

5.3.2 Variation of the OH stretch band with isotopic dilution of water

To gain a better understanding of the modification of vibrational coupling and H-bonding at the surface of hydrophobic solute, we have compared the MCR-retrieved spectra for different isotopic dilution of water. Isotopic dilution (addition of D_2O in H_2O) diminishes

the vibration coupling without affecting the H-bond strength of water, and hence, isotopic dilution spectroscopy in combination with Raman-MCR can shed light on the modification of vibrational coupling in the hydration shell of a solute. Figure 5.4A shows the normalized Raman spectra of neat H_2O and isotopically diluted water with varying percentage of D_2O in H_2O (HOD75 (H_2O/D_2O = 75/25, v/v); HOD50 (H_2O/D_2O = 50/50, v/v), and HOD25 (H_2O/D_2O = 25/75, v/v)). As mentioned in Chapter 4, the broad OH stretch band (2900 - 3700 cm^{-1}) of liquid H_2O has at least three component bands that are centered around ~ 3200, 3400 and 3600 cm^{-1}, respectively. The 3200 cm^{-1} band, along

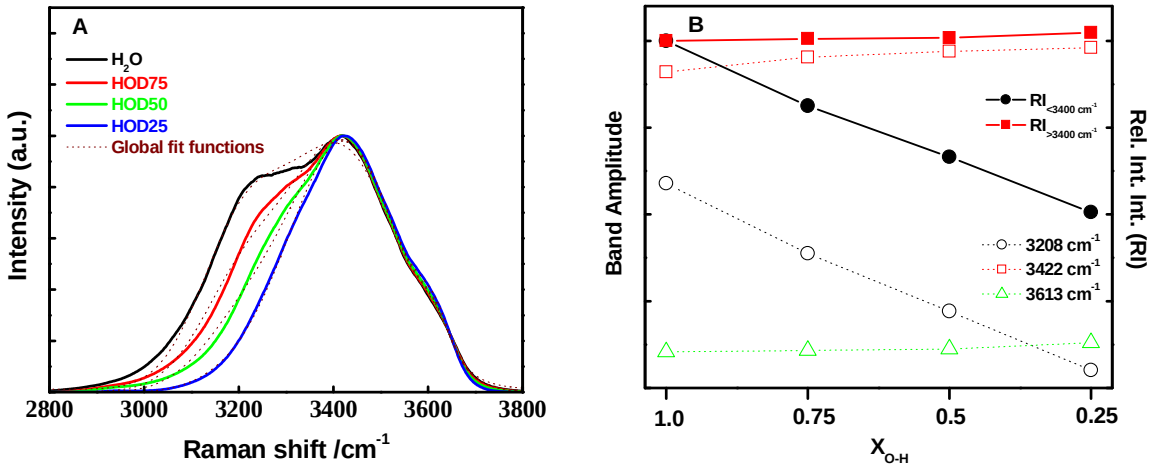

Figure 5.4. *(A) Global fitting of the normalized Raman spectra of neat H_2O and isotopically diluted water (HOD75 [H_2O/D_2O = 75/25]; HOD50 [H_2O/D_2O = 50/50], and HOD25 [H_2O/D_2O = 25/75]) with three component Gaussian fitting functions. Dotted lines represent the fitting functions. (B) Plot of amplitude of the component bands (dashed lines: black (3208 cm^{-1}), red (3422 cm^{-1}), and green (3613 cm^{-1})) vs. the mole fraction of O-H oscillators in water. Variations of relative integrated intensity above 3400 cm^{-1} (red solid line) and below 3400 cm^{-1} (black solid line) vs. the mole fraction of O-H oscillators are shown in the same panel.*

with the response of strongly H-bonded water, also contains the represents the coupled vibration of water molecules (intermolecular vibrational coupling and Fermi resonance (FR)). On increasing isotopic dilution, the intermolecular vibrational coupling and FR decrease, but the H-bond strength does not appreciably. Therefore, a global analysis of the OH stretch bands of different isotopically diluted water with a three component Gaussian fit function can elucidate the vibrational coupling and H-bonding in water. As shown in Figure 5.4A, the dashed lines are the global fit-functions of the experimentally recorded spectra of different isotopically diluted water (fitting parameters are summarized in Table 5.1). The variation of amplitude of the component bands (centre frequencies: 3208, 3422, 3613 cm^{-1}) with the mole fraction of OH oscillator (X_{OH}) is shown in Figure 5.4B.

Table 5.1. ***Global fitting parameters of normalized Raman spectra of neat and isotopically diluted water***

Water with different isotopic dilution	Component band amplitudes obtained by global fitting		
	Band-1 (ν_c = 3208 cm^{-1}, Γ = 217.2 cm^{-1}	Band-2 (ν_c = 3422 cm^{-1}, Γ = 271.35 cm^{-1}	Band-3 ν_c = 3613 cm^{-1}, Γ = 78.6 cm^{-1}
H_2O	0.586	0.91	0.1
HOD75	0.387	0.953	0.11
HOD50	0.221	0.97	0.11
HOD25	0.051	0.98	0.13

The amplitudes of band-2 (3422 cm^{-1}) and band-3 (3613 cm^{-1}) do not change on decreasing $X_{OH,}$ which confirms the previous understanding that the H-bond strength of water does not change on isotopic dilution.[89,213,221] However, the amplitude of band-1

(3208 cm^{-1}) band decreases on decreasing X_{OH}, which is assignable to the reduction of intermolecular coupling and FR of water.

These observations clearly reveal that the decrease of intermolecular coupling and FR on isotopic dilution is mainly manifested in the band-1, whereas the band-2 and band-3 are unaffected by these coupling effects. In other words, the red region of the OH stretch band (<3400 cm^{-1}) contains information about the intermolecular coupling, FR, as well as the H-bond strength of liquid water, whereas the blue region (>3400 cm^{-1}) is sensitive only to the H-bond strength of liquid water. Accordingly, *the* relative integrated intensity of isotopically diluted water in the red region of the OH stretch band ($RI_{<3400} = [\int_{2800}^{3400} I_\nu \, d\nu]_{HOD} / [\int_{2800}^{3400} I_\nu \, d\nu]_{H2O}$) is expected to decrease on decreasing X_{OH} . Similarly, *the* relative integrated intensity in the blue region of the OH stretch band ($RI_{>3400} = [\int_{3400}^{3800} I_\nu \, d\nu]_{HOD} / [\int_{3400}^{3800} I_\nu \, d\nu]_{H2O}$) is expected not to change noticeably on decreasing X_{OH}. The variation of relative integrated intensity against X_{OH} in fact goes parallel to the amplitude plot of band-1 and band-3 (Figure 5.4B). Thus the relative integrated intensity above and below the centre frequency (3400 cm^{-1}) of the OH stretch band is a straightforward measure of the perturbation of coupling effects and H-bond strength in water. In the following section, we applied the relative integrated intensity approach to elucidate the perturbation of coupling effects and H-bond strength of water in the hydration shell of hydrophobic molecular groups.

5.3.3. Variation of OH stretch response with isotopic dilution in the hydration shells of atomic anion and hydrophobic molecular groups

Figure 5.5 shows the solute correlated spectra (SC-spectra) for Cl^- (atomic anion), TBA (uncharged hydrophobe), and TMA^+ (positively charged hydrophobe) in neat H_2O as well as in isotopically diluted water of different compositions (H_2O (75%) i.e. $H_2O/HOD/D_2O$=56.25/37.5/6.25; H_2O (50%), $H_2O/HOD/D_2O$=25/50/25; and H_2O (25%), $H_2O/HOD/D_2O$=6.25/37.5/56.25). As a first step, let us discuss the variation of the OH stretch band with isotopic dilution in the hydration shell of Cl^- anion, and then those in the hydration shell of TBA and TMA^+ cation. The Cl^--correlated spectrum of H_2O shows lower intensity than bulk H_2O in the red region (< 3400 cm^{-1}), but that in the blue region (> 3400 cm^{-1}) is only slightly higher than bulk H_2O. The global analysis of the OH stretch band with isotopic dilution, as discussed in section 5.3.2, shows that the relative intensity in the blue region of the OH stretch band (>3400 cm^{-1}) does not depend on the intra-/intermolecular vibrational coupling of water. Therefore, the little higher intensity in the blue region (>3400 cm^{-1}) indicates that the relative population of weakly H-bonded water (~3580 cm^{-1}) is increased marginally in the hydration shell of Cl^-. However, as has been observed in previous Raman-MCR studies,[78,305] the large reduction of intensity in the red region of the OH stretch band (<3400 cm^{-1}) is due to vibrational decoupling of water in the hydration shell of Cl^- anion. It follows that, on increasing isotopic dilution, the effect of Cl^- anion on the vibrational decoupling of its hydration water will be less pronounced, since the hydration water progressively becomes decoupled (OH stretch) due to isotopic dilution. This has indeed been observed (Graph A1-A4 in Figure 5.5). With increasing

isotopic dilution (H_2O (100%) to H_2O (25%)), the intensity difference between the Cl^--correlated spectrum and the corresponding bulk water decreases in the red (<3400 cm^{-1}).

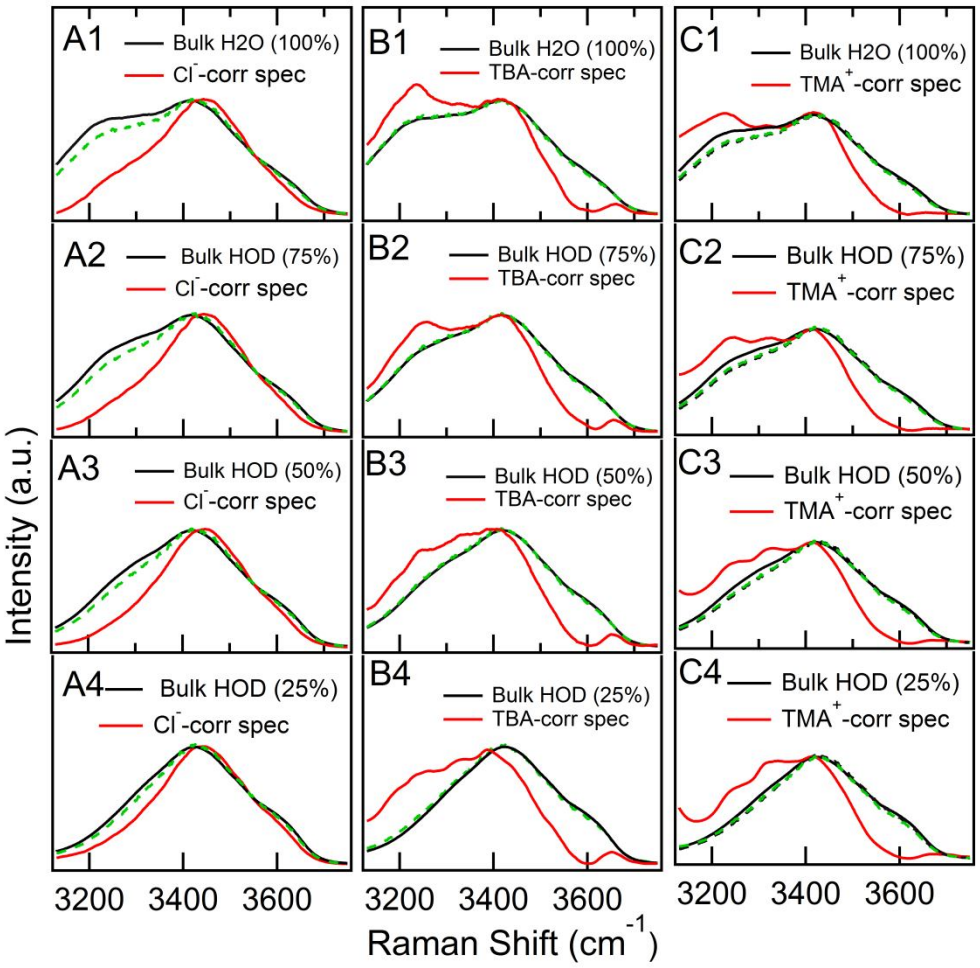

Figure 5.5. *SC-Raman spectra of water (red solid line) in the OH stretch regions for H_2O and H_2O-D_2O mixtures as mentioned in the graph panels. Experimentally recorded Raman spectra (green dashed line) of 1.0 mol dm^{-3} aqueous solutions of NaCl (left panel, A1-A4), TBA (middle panel, B1-B4), and TMACl (right panel, C1-C4) and that of bulk water (black solid line) are shown in respective panels for references. The dashed black line in the right panel is the experimental Raman spectra of 1.0 mol dm^{-3} aqueous NaCl solution.*

Therefore, the relative intensity of Cl^--correlated spectrum with respect to that of corresponding bulk water increases with increasing dilution of H_2O with D_2O. Thus, in general, the variation of relative intensity of SC-spectrum (in red region <3400 cm^{-1}) with isotopic dilution can provide information about the perturbation of intermolecular vibrational coupling of water in the hydration shell of an ion/solute. This issue has been discussed in more detail in the next section.

In contrast to Cl^- anion, the TBA-correlated spectra have lower intensity in the blue region (>3400 cm^{-1}) than those of the respective bulk water spectra (Graphs B1-B4 in Figure 5.5). The reduced intensity of TBA-correlated spectrum (>3400 cm^{-1}) from that of bulk water is due to a decrease of relative population of weakly H-bonded water (whose OH stretch response appear around 3580 cm^{-1}) in the hydration shell of TBA.[194] Similar depletion of weakly H-bonded water has also been observed in the hydration shell of positively charged hydrophobe, TMA^+ (right panels in Figure 5.5). These results suggest that unlike in the hydration shell of halide ion, there is a depletion of weakly H-bonded water in hydrophobic hydration shell. Moreover, the comparable reduction of intensity (>3400 cm^{-1}) for TBA and TMA^+ indicates that the positive charge on the hydrophobe does not affect the depletion of such weakly H-bonded water. Comparison of the dangling OH band (>3600 cm^{-1}) for TBA and TMA^+, however, shows that the dangling OH band is more prominent at the surface of uncharged TBA than that of positively charged TMA^+. The dangling OH is pointed toward the centre of the hydrophobic group,[196] and hence, it is intuitive that the orientation of the positive pole of dangling OH ($^{\delta-}O—H^{\delta+}$) toward the centre of the positively charged hydrophobe (TMA^+)

is energetically unfavorable by electrostatics and hence, there is a depletion of dangling OH in the hydration shell of a positively charged hydrophobe compared to that of an uncharged hydrophobe. Thus, the solute charge does influence dangling OH formation.

In the red region of the OH stretch band (<3400 cm^{-1}), the TBA and TMA^+-correlated spectra have higher intensity than those of respective bulk water. Moreover, on increasing the percentage of D_2O in H_2O (H_2O (100%) to H_2O (25%)), the intensity difference between the solute-correlated spectrum and the corresponding bulk water spectrum increases (Graph B1-B4 and C1-C4 in Figure 5.5). Higher intensity in the red region of the OH stretch band could be either due to increased population of strongly H-bonded water and/or due to stronger intermolecular vibrational coupling of water at the surface of the hydrophobes. We have addressed these issues in the following section by disintegrating the intermolecular vibrational coupling and H-bonding effects in the hydration shell of Cl^-, TBA, and TMA^+.

5.3.3. Disintegration of intermolecular vibrational coupling and H-bonding in hydration shells

As discussed in the previous paragraph, on isotopic dilution, the relative intensity of the SC-spectra above and below the centre frequency (3400 cm^{-1}) of the OH stretch band evolves differently for atomic anion (Cl^-) and hydrophobic molecular groups (TBA and TMA^+). Integrated area analysis of the OH stretch band of isotopically diluted water shows that, in the red region of the OH stretch band (<3400 cm^{-1}), the relative intensity is reduced due to vibrational decoupling (reduction of intermolecular coupling and FR) of water; whereas, that in the blue region (> 3400 cm^{-1}), which mainly depends upon the H-bond strength of water, does not change noticeably (section 5.3.2). A similar analysis of

relative integrated intensity of the SC-spectra can shed light into the vibrational coupling and H-bonding of water in the hydration shell of a solute.

Figure 5.6 shows a plot of the relative integrated intensity of water in the hydration shell of Cl^-, TBA, and TMA^+ against the mole fraction of OH oscillator in bulk. In the case of Cl^- hydration shell, the relative intensity in the red region ($RI_{<3400} = [\int_{3130}^{3400} I_\nu \, d\nu]_{HS} / [\int_{3130}^{3400} I_\nu \, d\nu]_B$; HS: hydration shell, B: bulk) is less than unity in isotopically pure H_2O (X_{OH} = 1) and increases on increasing dilution with D_2O (decreasing X_{OH}). Because of the spectral overlap of the CH_3 stretch band (TBA, TMA^+) with the OH stretch band of water below 3100 cm^{-1}, the lower limit of $RI_{<3400}$ has been restricted to 3130 cm^{-1}. The increase of $RI_{<3400}$ with decreasing X_{OH} is a manifestation

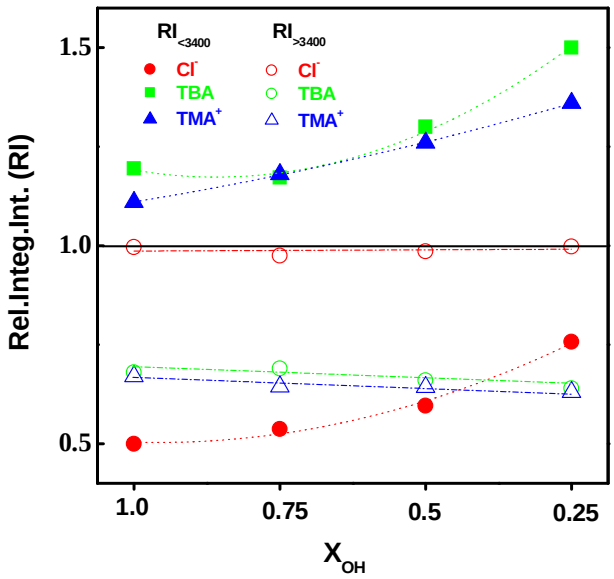

Figure 5.6. *Plot of Relative integrated intensity (RI) of the SC-spectra against the mole fraction of OH oscillator (X_{OH}) in bulk H_2O-D_2O mixtures. $RI_{>3400}$ and $RI_{<3400}$ are the relative integrated intensity of the OH stretch band above and below 3400 cm^{-1}. Dotted and dashed-dotted lines are visual guide to the variations of $RI_{<3400}$ and $RI_{>3400}$ respectively.*

of decoupling of water in the hydration shell Cl^-. In the case of TBA and TMA^+, $RI_{<3400}$ is more than unity in isotopically pure water (X_{OH} = 1) and increases on decreasing X_{OH}. The increase of $RI_{<3400}$ with decreasing X_{OH} suggest that the water in the hydration shell of TBA and TMA^+ is also vibrationally decoupled like that in the hydration shell of Cl^-. Had the water been vibrationally decoupled without significant change in average H-bond strength, $RI_{<3400}$ is expected to be less than unity, at least in isotopically pure water (X_{OH} = 1). However, in the case of TBA and TMA^+, $RI_{<3400}$(X_{OH} = 1) is more than unity, which clearly shows the increased H-bond strength of water in the hydration shell of TBA/TMA^+. Thus, the intensity reduction due to vibrational decoupling is over compensated by increased H-bond strength of water in the hydration shell of TBA/TMA^+. Similar analysis of relative integrated intensity in the blue region of the OH stretch band ($RI_{>3400} = [\int_{3400}^{3600} I_\nu \, d\nu]_{HS} / [\int_{3400}^{3600} I_\nu \, d\nu]_B$) shows that $RI_{>3400}$ for Cl^- anion is close to unity and almost invariant with X_{OH} (red dash-dotted line in Figure 5.7). This means that the blue region of the OH stretch band is almost free from vibrational coupling effects and that the H-bond strength of water does not change significantly in the hydration shell of Cl^-. $RI_{>3400}$ for TBA and TMA^+ also do not vary with X_{OH}, but is less than unity, which suggest a decrease of relative population of weakly H-bonded water in the hydration shell of TBA/TMA^+ compared to that in bulk.

Monte Carlo simulation[306] suggested that the mean water H-bond angle (i.e. O(1)—H----O(2) angle between two neighboring water molecules (1) and (2) that are H-bonded with each other, which is 0° for linear H-bond) in the first hydration shell of hydrophobic TMA^+-cation is lower than that of bulk water. Water with less bent H-bonds

is more strongly H-bonded, which has also been reflected by radial distribution function of water (oxygen-oxygen and hydrogen-hydrogen) in the first hydration shell. Thus, the present experimental results in consistent with theoretical studies suggest that water adopts stronger H-bonding in the hydration shell of uncharged/cationic hydrophobic molecular group. Nevertheless, the OH stretch vibration of such strongly H-boned water is rather weakly coupled with neighboring OH oscillators than that in bulk water. Apparently, this is counter intuitive in the sense that stronger H-bonding between water molecules is expected to induce stronger coupling between vibrations of those water molecules. In fact, in bulk water, it has been observed that decreasing temperature (which increase the average H-bond strength of water) enhances intermolecular coupling and FR.[213] In hydrophobic hydration shell, the structural perturbation of water is grossly equivalent to ~10 - 20°C decrease of temperature of bulk water. However, unlike in bulk water, the surface of a hydrophobic solute, especially the region of the first hydration shell, is highly anisotropic in nature which promotes more ordered water structure in the hydration shell. Experimentally, it has been observed that water is indeed preferentially oriented at macroscopic oil/water interfaces.[307,308] This ordered arrangement of water gives rise to negative entropy of hydration ($\Delta S_H < 0$) for hydrophobic solute; and also in conformity with the reduced water-water H-bond angle in hydrophobic hydration shell. The constraints imposed by such ordered orientation may force water to adopt a configuration that is no longer optimal for the vibrational delocalization with neighbors. In fact, it has been suggested that with decreasing water H-bond cone angle (O(1)—H----O(2)) the librational freedom of water decreases.[76] Moreover, because of the exclude

volume, a water molecule in the first hydration shell has access to less number of neighbors to couple with, compared to that in the bulk.[309] Finally, the presence of dangling OH clearly indicates that the vibrational degeneracy of the two OH oscillators is lifted in the hydration shell, at least for a fraction of water molecules. Therefore, the water with dangling OH, whose neighbors are mostly water molecules with H-bonded OH are coupled weakly with the latter.

5.3.4. Variation of dangling OH band with isotopic dilution: Intramolecular coupling of dangling OH in hydrophobic hydration shell

The intramolecular vibrational (OH stretch) coupling of water decreases progressively from gas (coupling constant, Λ ~50 cm^{-1}), to liquid (Λ ~23 cm^{-1}), to solid (ice; Λ ~14 cm^{-1}) phases.[85] Moreover, in liquid water, the intramolecular coupling (Λ ~23 cm^{-1}) is weaker than the intermolecular coupling (coupling constant, Σ ~100 cm^{-1}). The dangling OH in hydrophobic hydration shell, as observed for TBA, is well separated from the red-shifted H-bonded OH stretch, and also spectrally narrow (fwhm ~45 cm^{-1}). Therefore, the position and width of dangling OH band are sensitive to even weak interactions (e.g. intramolecular vibrational coupling of dangling OH with the H-bonded OH of the same molecule, van der Waals interaction with the methyl's of TBA).

As shown in the left panel of Figure 5.7, the dangling OH band in the hydration shell of TBA shifts toward lower frequency with increasing isotopic dilution (H_2O(100%) to H_2O(25%)). On increasing isotopic dilution, the dangling OH (H_2O) on TBA surface is progressively replaced by dangling OH (HOD). In the case of H_2O, the dangling OH (H_2O) is coupled with the H-bonded OH stretch (~3430 cm^{-1}) in the same molecule, as

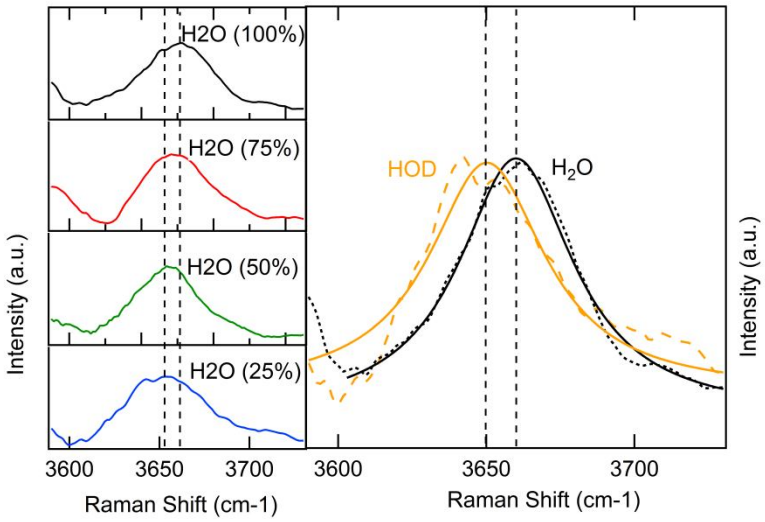

Figure 5.7. *Left panel: Variation of dangling OH band with isotopic dilution in the hydration shell of TBA. Right panel: Dangling OH band of HOD (orange dashed line; orange solid line is the Lorentz fitting function) and H2O (black dashed line; black solid line is the Lorentz fit function) in the hydration shell of TBA. The dangling OH band of HOD is obtained by a second MCR analysis of the TBA-correlated spectra in H_2O (100%) and H2O (25%).*

has been observed for the topmost layer of water at air/water interfaces.[310] However, in the case of HOD, such kind of intramolecular coupling (coupling between dangling OH (HOD) and H-bonded OD stretch (2510 cm^{-1})) is weaker than that in H_2O. This is because, the energy difference between the dangling OH and H-bonded OD stretch ($\Delta E \approx$ 1150 cm^{-1}; (3650 cm^{-1} – 2510 cm^{-1})) is larger than that between dangling OH and H-bonded OH stretch ($\Delta E \approx$ 220 cm^{-1}; (3650 cm^{-1} – 3430 cm^{-1})) and the large energy mismatch reduces the strength of coupling (Scheme 5.1). Moreover, it has been observed that dangling OH is hardly affected by intermolecular coupling at air/water interface.[310] This is because the number density of dangling OH at TBA surface is negligibly small as

well as the dangling OH is well separated in energy from the H-bonded OH stretch for efficient intermolecular coupling.

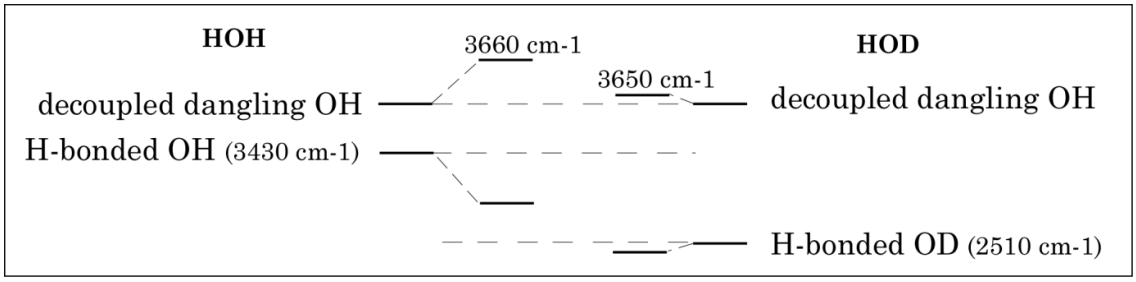

Scheme 5.1. *Model diagram showing the intramolecular vibrational coupling and the dangling OH band positions of H_2O and HOD in hydrophobic hydration shell. In H_2O, the dangling OH (H_2O) is shifted to higher frequency (blue-shift) from that of decoupled dangling OH, due to strong intramolecular coupling with H-bonded OH stretch (~ 3430 cm^{-1}). In HOD, because of the large energy gap between the dangling OH (HOD) and the H-bonded OD stretch (~2510 cm^{-1}), the intramolecular coupling is weak, and the dangling OH (HOD) band is close to that of decoupled dangling OH.*

Thus, we can expect that the red-shift of the dangling OH band on isotopic dilution is due to decoupling of dangling OH from the H-boned OH of the same molecule (intramolecular). In other words, the dangling OH bond of H_2O (isotopically pure) is intramolecularly coupled in the hydration shell of TBA. To elucidate the strength of intramolecular vibrational coupling of dangling OH in the hydration shell, we have retrieved the dangling OH (HOD) band by a second MCR-analysis of the TBA-correlated spectra. In the second MCR-analysis, the TBA-correlated spectrum in H_2O (100%) was considered as the spectrum of pure component (dangling OH (H_2O)) and that in isotopically diluted water (H_2O (25%)) was considered as the mixed spectrum, which contains two kinds of dangling OHs (OH (H_2O) and OH (HOD)). The right panel in Figure 5.7 shows the dangling OH (HOD) (orange dashed line) which is red-shifted

(δ ~10 cm^{-1}) in comparison to the dangling OH (H_2O) (black dashed line). The magnitude of red-shift (δ) of dangling OH (HOD), whose frequency position is comparable to that of decoupled dangling OH, can provide quantitative information about the strength of intramolecular coupling (Λ_s) in the hydration shell, since δ and Λ_s are related with the frequency difference (Δ) between dangling OH and H-bonded OH stretches as follows.[310]

$$\delta = \sqrt{\frac{\Delta^2}{4} + \Lambda_s^2} - \frac{\Delta}{2} \qquad (5.1)$$

Where, δ is the frequency shift of the dangling OH from H_2O to HOD (in the present case it is 10 cm^{-1}), Δ is the energy difference between the dangling OH in hydrophobic hydration shell and H-bonded OH stretch (~200 cm^{-1}), and Λ_s is the intramolecular coupling constant for interfacial water. As obtained from equation (5.1), Λ_s is ~45 cm^{-1} for the water at TBA surface, which is almost double to that of bulk water (Λ ~23 cm^{-1}).[85] This means that the intramolecular vibration coupling (OH stretch) of the first layer of water in hydrophobic hydration shell is stronger than that in bulk water. Interestingly, the magnitude of the red-shift (10 cm^{-1}) of the dangling OH(HOD) band is almost equal to that observed at macroscopic hydrophobe (e.g. air/water interface).[311] Therefore, it is expected that intramolecular vibrational coupling of water at molecular hydrophobic interface (the first layer of water in hydrophobic hydration shell) is comparable to that of the topmost water at macroscopic hydrophobe (air)/water interface. In that sense, it is likely that the intramolecular energy transfer, which is the dominant relaxation mechanism of dangling OH at air/water interface,[312,313] is also prominent at molecular hydrophobe interface.

5.4. Conclusion

In this chapter, we have carried out a joint investigation of isotopic dilution spectroscopy and multivariate curve resolution (MCR) analysis to understand the structure of water in the hydration shell of uncharged (*tert*-butanol, TBA) and positively charged (tetramethylammonium cation, TMA^+) hydrophobic molecular groups. The results show that the hydrophobic hydration shell has increased population of strongly H-bonded water and a depletion of weakly H-bonded water compared to that of bulk water. The emergence of a distinct narrow band at ~ 3660 cm^{-1} give clear indication of dangling OH bonds at the surface of hydrophobic molecular groups. Integrated area analysis of the MCR-retrieved spectra of water in the hydration shell of TBA and TMA^+ in isotopically diluted water of varying composition ($[H_2O]/[D_2O+H_2O]$ = 1, 0.75, 0.5, 0.25; v/v) revealed that the water in the hydration shell of TBA or TMA^+ are also vibrationally decoupled from neighboring water molecules like that in the hydration shell of halide ions, as observed in Chapter 4. Nevertheless, the dangling OH in hydrophobic hydration shell is coupled with the H-bonded OH stretch vibration of the same water molecule.

Chapter 6

Interaction of Ions and Water with the Methyl groups that are Attached to Positively Charged Nitrogen

6.1. Introduction

The previous chapters (Chapter 3-5) describe the structural changes of water (solvent) at the surface of a solute (ions, hydrophobic alkyl groups, etc.). The results suggest that ions and hydrophobic groups strongly affect the H-bonding and vibrational coupling of water such that the collective nature of liquid water is largely reduced in the hydration shell. In this Chapter, we will discuss about the effect of solvent and electrolytes on alkyl groups that are present in different chemical environments. For example, the three methyl groups in *tert*-butanol (TBA) are attached with a neutral central carbon atom, and behave like a typical hydrophobic alky group. In other words, the C-H bonds of the methyl groups of TBA interact very differently with water from that of a polar hydrophilic group such as the alcoholic O-H group of TBA. It is in fact, the molecular level interaction between the constituent molecules groups and water that determines the macroscopic hydrophilic/hydrophobic property of material.

However, unlike in TBA, the nonpolar and hydrophobic nature of a methyl group

is not that obvious when it is attached with a strongly electron withdrawing atom, such as a positively charged nitrogen. The positively charged nitrogen, by drawing electron density may polarize the apolar C-H bonds of the methyl group. Such kind of methyl groups that are attached with positively charged quaternary nitrogen are quite common in biological molecules, such as the headgroup of phosphatidylcholine (PC) lipid − the principal structural component of biological membrane and trimethylamine-N-oxide (TMAO) − a protecting osmolyte and protein stabilizer (Figure 6.1A).

Previous IR study and theoretical calculation indicated that, at the low hydration level, the choline-methyls (methyls with quaternary nitrogen) of phosphatidylcholine (PC-headgroup) participates in conventional hydrogen-bond interaction (similar to that of

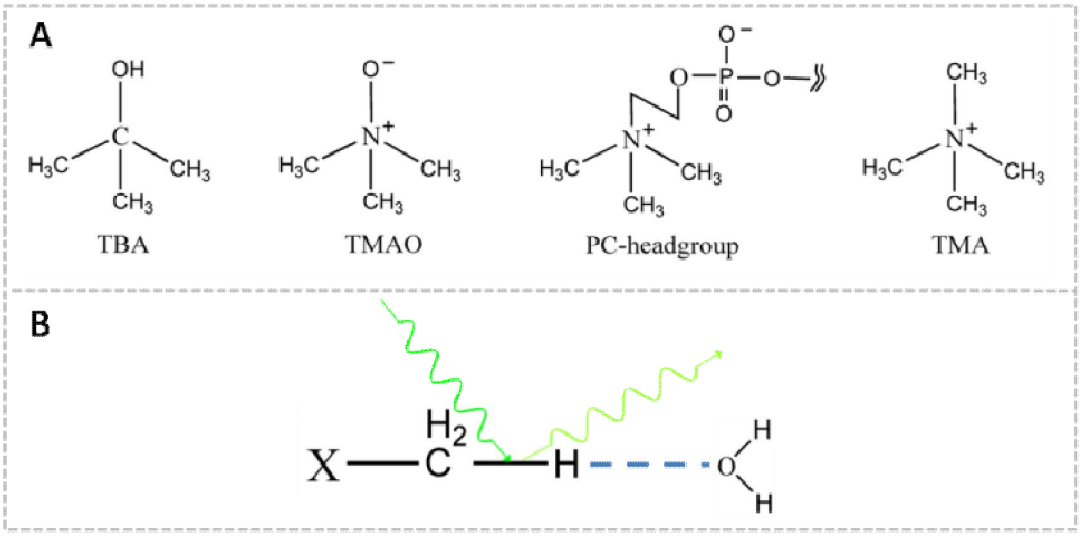

Figure 6.1. *(A) Chemical structure of the molecules with methyl groups attached with different neighboring atoms/groups of varying charge. The counter ion (Cl^-) in TMA is omitted for simplicity. (B) Motivation (schematic): Interaction of a methyl group and water can be probed by measuring the CH_3 stretch vibration (Raman band). X is the atom/group attached with the methyl group.*

polar group) with the phosphate group.[314] The conventional hydrogen-bond interaction (red-shifted H-bond), C—H-----O(phosphate), implies that the C-H bonds of the methyl groups of choline are quite polar (unlike the apolar methyl group in TBA).[315] Therefore, it is reasonable to expect that the positively charged nitrogen polarize the methyl C-H bonds by pulling the electrons from the methyl group, which makes the choline-methyls polar. Thermodynamic studies suggested that the N-methyl groups do not show hydrophobicity rather promote hydrophilicity.[316] A recent vibrational sum frequency generation (VSFG) study[317] of TMAO at the octadecyltrichlorosilane (OTS)/water interface also pointed out that the methyl groups of TMAO, because of their interaction with water, prefer the aqueous phase than the hydrophobic alkyl phase of OTS. Clearly, the above mentioned IR and VSFG studies give an impression that the methyl groups when attached with a quaternary nitrogen (e.g., in TMAO and choline of the PC-headgroup) behave like a polar group. On the otherhand, another VSFG (heterodyne-detected; HD-VSFG) study[80] at the phosphatidylcholine lipid/water interfaces, in consistent with several theoretical studies,[318-320] proposed that the choline-methyls provide a hydrophobic enviroment to the neighbouring water molecules. This follows that the methyl groups are nonpolar even if they are attached with positively charged nitrogen.

The hydrophilic nature of the methyl's in TMAO as indicated by the VSFG study[317] or the hydrophobic nature of the methyl's in PC-head group as suggested by the HD-VSFG study[80] was indirectly inferred either from the preferential orientation of TMAO-methyl's at the OTS/water interface or from the structure of water at the vicinity of the choline at the PC/water interface. Here, we have directly compared the vibrational

response of these methyl groups (in TMAO and PC-head group) with that of a typical nonpolar methyl and polar carbonyl groups for the unambiguous assignment of their polar/nonpolar nature.

6.2. Experiments and Methods

The chemicals, trimethylamine-N-oxide dihydrate (TMAO) (≥ 99.0%) and tetramethylammonium chloride (TMA) (≥ 98.0 %) were purchased from Sigma Aldrich. *tert*-Butanol and acetone (99.5%, HPLC grade) were from Spectrochem India. The chemicals were used as received. Solvents, such as CCl_4 (99.7 %,), $CDCl_3$, CD_3OD (99.8 %, NMR grade), and potassium halide salts (≥ 99.0 %) were from Merck. We used deuterated chloroform and methanol while measured the Raman spectra of the samples in the CH stretch regions. Milli-Q water (18.2 MΩ cm resistivity) was used for all measurements. Low concentrations (0.01 mole fraction) of the samples were used for the Raman measurements, if not mentioned otherwise.

Spontaneous Raman spectra of the samples were recorded using a STR-300 micro-Raman spectrometer (SEKI Technotron, Japan). The total acquisition time was 500 sec. or more for a single spectral measurement. The recorded spectra were baseline corrected by subtracting the corresponding solvent spectra recorded under identical conditions. At least, two such background subtracted spectra were averaged. The averaged spectrum was smoothened by 2^{nd} order Savitzky–Golay algorithm with 19 points. We note that the smoothening operation did not produce any noticeable change in the Raman bands while reducing noise in the spectrum.

6.3 Results and Discussion

6.3.1 CH stretch bands of *tert*-butanol and TMAO in $CDCl_3$ and H_2O

Figure 6.2A shows the Raman spectra of TBA (CH stretch regions) in nonpolar CCl_4 and $CDCl_3$ as well as in polar H_2O. The position of the CH_3 symmetric and anti-symmetric stretch bands (CH_3 $^{(SS)}$ 2942 cm^{-1} and CH_3 $^{(AS)}$: 2975 cm^{-1}) do not change noticeably on changing the solvent from CCl_4 to $CDCl_3$. This quite obvious, since CCl_4 and $CDCl_3$ provide comparable nonpolar environment to the methyl groups of TBA. The positions of these CH_3-stretch bands are ~ 7 cm^{-1} blue-shifted in water (polar solvent) compared to those in nonpolar CCl_4/$CDCl_3$.

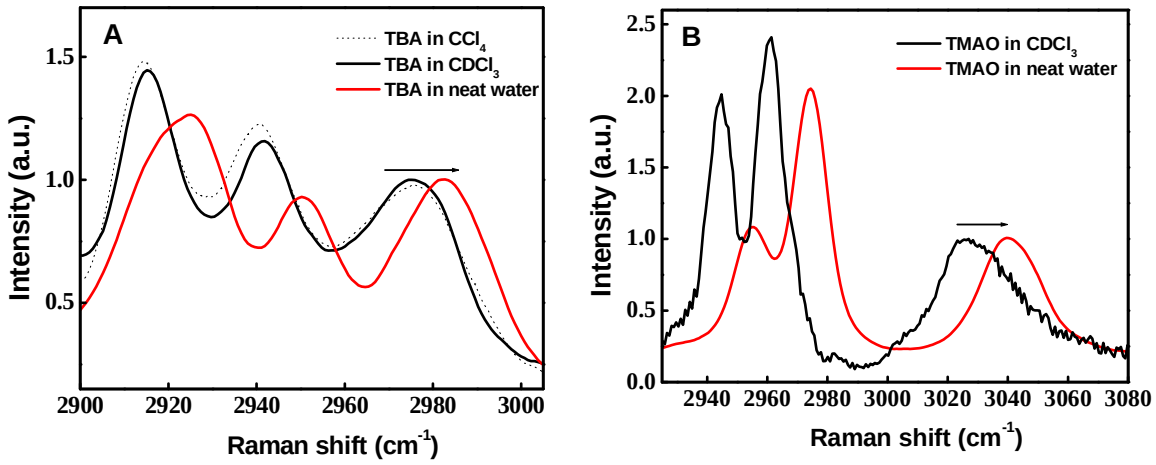

Figure 6.2. *Vibrational (Raman) spectra of (A) TBA (0.01 mole fraction) and (B) TMAO (0.01 mole fraction in water but less in $CDCl_3$) in the CH stretch regions, in $CDCl_3$ (black) and neat water (red). Dotted line in the panel A is the Raman spectrum of TBA in CCl_4. The spectra are normalized at the high frequency CH stretch band. The low S/N in the black spectrum in the bottom panel is due to poor solubility of TMAO in $CDCl_3$. The spectrum of TMAO in CCl_4 could not be recorded because of insolubility of TMAO.*

The blue-shift suggests that the methyls of TBA experience a different environment in polar protic solvent than that in nonpolar solvent. The blue-shift of CH vibrational frequency results from the shortening (strengthening) of the C-H bonds due to H-bonding interaction with water.[321,322] In conventional H-bonding interaction, A—H---B (A and B being electronegative atoms) the A—H bond becomes weaker (longer) due to H-bonding with B; and shifts toward lower frequency (red- shifted). In other words, the A—H bond is red-shift by H-bond interaction when the A—H bond is polar. The C-H bonds of the methyl groups of TBA are nonpolar and a nonpolar bond is blue-shifted in vibrational frequency when interacts with H-bond accepting group.[315,321-330]

Very similar to that of TBA, the CH stretch bands of the methyl groups of TMAO are blue-shifted in H_2O compared to those in $CDCl_3$ (Figure 6.2B). The $CH_3^{(SS)}$ and $CH_3^{(AS)}$ bands of TMAO are at 2961 and 3027 cm^{-1} in $CDCl_3$ and at 2974 and 3040 cm^{-1} in water. Clearly, the vibrational response of the methyl groups in TMAO is similar to that in TBA while the solvents are changed from nonpolar $CDCl_3$ to polar protic H_2O. This similarity in response suggests that the C-H bonds in TMAO are also nonpolar, like that in TBA, even though the TMAO-methyls are attached with the positively charged nitrogen. We note that the $CH_3^{(SS)}$ and $CH_3^{(AS)}$ stretch band of TMAO are shifted to higher frequency (~ 50 cm^{-1}) compared to that of TBA even in nonpolar $CDCl_3$. This means that the C-H bonds in TMAO are inherently stronger (shorter) than those in TBA. This is because the positively charged nitrogen in TMAO pulls the electron density from the C-H (methyl) bond and makes it shorter (stronger).[324] However, this withdrawal of

electron does not change the nonpolar character of the C-H bonds, as indicated by the blue-shift of the CH stretch band from $CDCl_3$ to H_2O.

6.3.2 Effect of concentration and ions on the CH stretch bands of *tert*-butanol in water

Figure 6.3A shows the Raman spectra of aqueous TBA solution, at different concentrations of TBA (mole fraction = 0.01, 0.1, 0.15). The maxima of the CH stretch bands shift to lower frequency (red-shift) as the concentration of TBA is increased. Previous Raman study[331] showed that TBA aggregates at higher concentrations (mole fraction > 0.025). In the aggregates, the nonpolar methyl groups of TBA are less exposed to water compared to those in non-aggregated dilute solution. Thus, the methyls of TBA

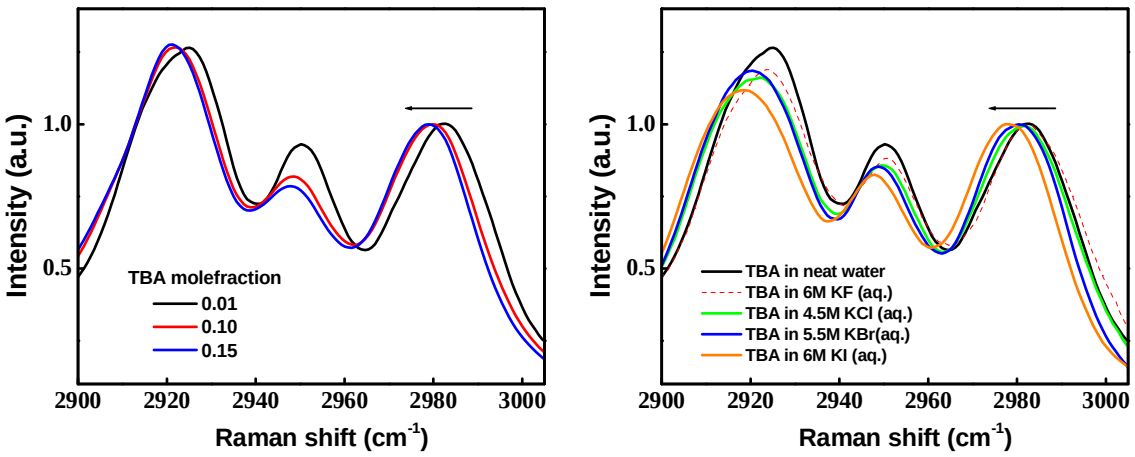

Figure 6.3. *Vibrational (Raman) spectra of TBA in the CH stretch regions (A) with varying concentration of TBA in water and (B) in different aqueous potassium halide solutions (0.01 mole fraction of TBA). Concentrations of potassium halides and TBA are mentioned in the graph panels. The spectra are normalized at the high frequency CH stretch band.*

experience nonpolar environment in the aggregated form, and hence, red-shifted from that of non-aggregated dilute solution. In diluted TBA solution, however, we observed a red-

shift of the CH stretch bands in presence of electrolyte water. Figure 6.3B shows the Raman spectra of diluted TBA solution in presence of potassium halide salts (KX; X = F, Cl, Br, I; conc. ≥ 4.5 mol dm^{-3}). The halide ions (except F^-), cause a red-shift of the CH stretch bands of TBA, as if, the TBA-methyls experience a nonpolar environment in presence of potassium halide in water.

Previous IR and Raman studies[78,216,219,319,332] suggested that the water in aqueous potassium halide solution is mainly affected by the halide ions (X^-) and the potassium ion (K^+) has negligible effect. Assuming that the addition of TBA (0.01 mole fraction) in the aqueous salt (KX) solution does not change the relative behaviour of K^+ and X^-, the TBA's methyls show a red-shift in their CH stretch band mainly because of the halide ions (X^-). It is well known that except the F^-, halide ions are surface active i.e., they prefer the less polar air/water interfacial region than the more polar aqueous bulk phase.[333,334] Therefore, it is likely that in a mixture of hydrophobic TBA and water, the halide ions would prefer the nonpolar surface of TBA. In fact, the adsorption of halide ions on the surface of hydrophobic solute has been suggested by Raman-multivariate curve resolution (Raman-MCR) spectroscopy and theoretical calculations.[193] Because of the adsorption of halide ions on TBA surface, the methyls of TBA are less exposed to water and hence red-shifted in band position. Thus, the red-shift of the CH stretch bands of TBA (in presence of halide ions) provides insight into the nature of the methyl groups and their interaction with halide ions.

6.3.3 CH stretch bands of TMAO in aqueous alkali halide solution

Figure 6.4A shows the Raman spectra of TMAO in the CH stretch regions, in different alkali halide (KX) solutions. Like that in TBA, the CH stretch bands of TMAO shift toward lower frequency (red-shift) in presence of halide ions, and the magnitude of the red-shift increase as the size of the halide ions increase. These results clearly show that the TMAO's methyls behave very similar to that of TBA's methyls and that both of them are nonpolar in nature, and halide ions are adsorbed at their surface.

In presence of fluoride ion, the CH stretch bands of TBA and TMAO are very close (or slightly blue-shifted) to those in neat water. Because of the smaller size, the fluoride ion (F^-, ionic radius = 1.19 A°) has higher charge density (~ 2.8 times higher than that of Cl^-) so that the water in the hydration shell of F^- is more strongly H-bonded compared to that in the neat (bulk) water.[50] The oxygen of strongly H-bonded water is a

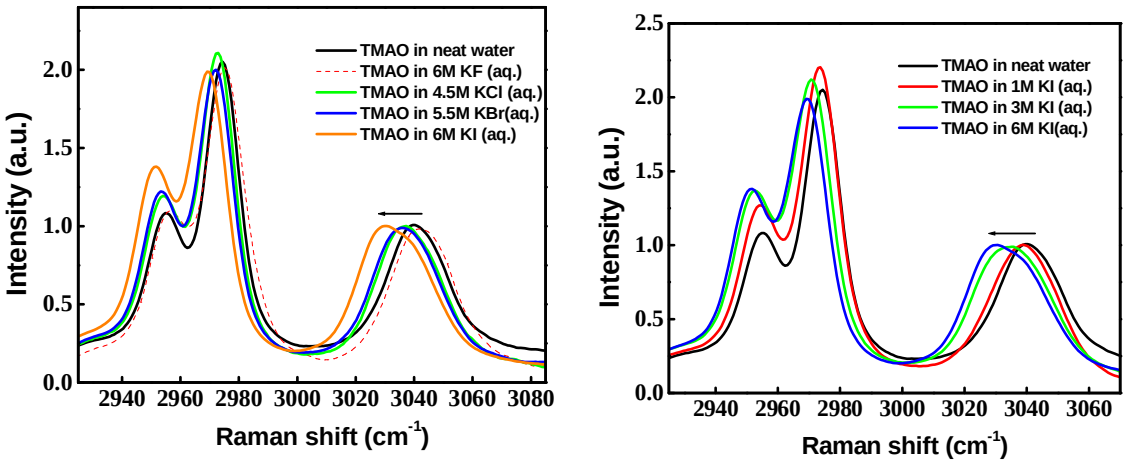

Figure 6.4. *Vibrational (Raman) spectra of TMAO (0.01 mole fraction) in the CH stretch regions, (A) in different aqueous media and (B) in aqueous solution with different concentrations of KI. The spectra are normalized at the high frequency CH stretch band.*

better electron donor,[335,336] and such water molecules when interact with methyl groups causes more contraction of an apolar C-H bond. Thus, the slight blue-shifted of CH band

in aqueous KF solution also suggest the apolar nature of the methyl groups in TMAO and TBA. It is noted that substantial change in the CH stretch band of TBA is observed only at high concentration of salts (≥ 4.5 mol dm^{-3}), whereas the CH stretch bands of TMAO show noticeable changes even at low salt concentration (e.g. 1.0 mol dm^{-3} of KI) and the spectral changes become more significant as the concentration of salt increases.

6.3.4 CH stretch bands of Tetramethylammonium cation (TMA+) in aqueous alkali halide solution

In the previous section, we have discussed that the methyl groups of TMAO behave like a nonpolar group even though they are attached with an electron withdrawing (positively charged) nitrogen. However, in TMAO the positively charged nitrogen is also attached with negatively charged oxygen. Whereas, in many biomolecules, for example, in phosphatidylcholine lipid, the head group contains positively charged ammonium group that is equivalent to the Tetramethylammonium cation (Figure 6.1). The positive charge on the nitrogen of phosphatidylcholine lipid is presumably higher than that of the nitrogen of TMAO. It is likely that the increased positively charged nitrogen on PC-headgroup would pull the CH (methyl) bond electrons more strongly than the nitrogen in TMAO. So, the question arises: do the choline-methyls in PC-headgroup interact differently with polar protic (water) and nonpolar (e.g. biomolecules) molecules and ions.

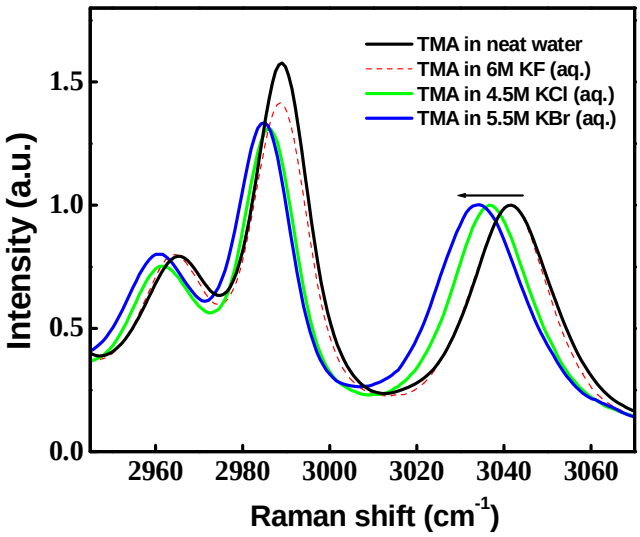

Figure 6.5. *Vibrational (Raman) spectra of TMA^+ (conc. = 0.01 mole fraction) in the CH_3 stretch regions, in different aqueous media. Concentrations of potassium halides are mentioned in the graph panels. The spectra are normalized at the $CH_3^{(AS)}$ stretch band.*

We have addressed this issue by analyzing the Raman spectra of tetramethylammonium (TMA) cation - the chemical analogue of choline-cation in PC-headgroup in different aqueous alkali halide solutions (Figure 6.5). The CH_3 $^{(SS)}$ and CH_3 $^{(AS)}$ bands of TMA^+-methyls shift toward red in presence of halide ions in water, which is caused by the adsorption of halide ions at the surface of TMA^+. As discussed in the case of TBA and TMAO- methyls, the red-shift of the CH (methyl) stretch bands, due to the adsorption of halide ions at the surface of a methyl group, indicates nonpolar nature of the methyl. Thus, the methyls in TMA-cation also behave like the nonpolar methyls in TBA. We note that TMA-cation precipitates in presence of I^- (conc. ~0.5 mol dm^{-3}) and therefore, the Raman spectra of TMA^+ in the presence of KI at a condition comparable to that used for recording other spectra (shown in Figure 6.5) could not recorded.

6.3.5 Comparison of the vibrational response of the methyl groups of TMAO with those of polar and nonpolar groups in solvents of varying polarity

The vibrational response of a molecule/group toward a changing environment can provide physicochemical insight about the polar/nonpolar nature of the molecule/group. As a model polar and nonpolar group we chose the >C=O and the -CH_3 groups of acetone, and measured their vibrational responses in different solvents. Figure 6.6 shows the relative position of the vibrational bands, ν/ν_0 (ν is the vibrational band position in respective solvents and ν_0 is the band position in nonpolar ($CDCl_3$) against E_T^N value (normalized $E_T(30)$ scale of polarity) of solvents. On increasing the E_T^N value, the ν/ν_0 of the

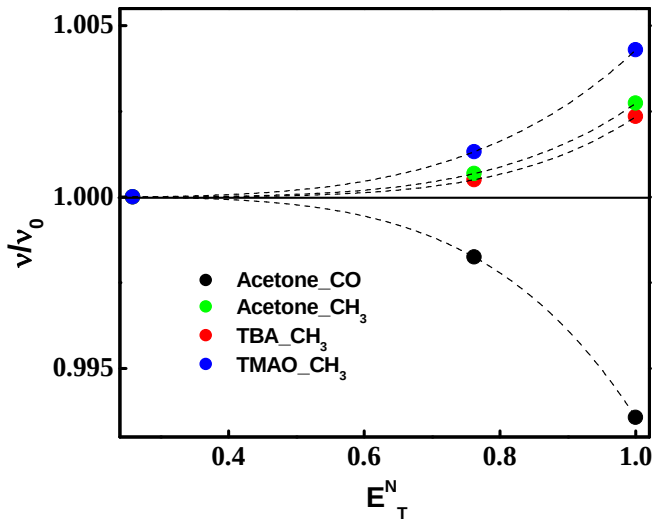

Figure 6.6. *Plot of relative position of Raman bands (ν/ν_0; ν is the vibrational band position in different solvents and ν_0 is the band position in apolar $CDCl_3$) vs. E_T^N values for the C=O stretch of acetone (black circle) and $CH_3^{(AS)}$ of acetone (green circle), TBA (red circle), and TMAO (blue circle). The dashed lines are guide to eye for the variation of ν/ν_0.*

polar >C=O decreases ($\nu/\nu_0 < 1$) i.e., the C=O bond becomes weaker on interaction with polar protic solvents compared to that in $CDCl_3$. On the other hand, ν/ν_0 of the nonpolar CH_3 group of acetone increases with increasing E_T^N, which means the C-H bonds become stronger on going from $CDCl_3$ to H_2O. Thus, as shown in Figure 6.6, with increasing E_T^N values of solvents, the relative position of the vibrational band shows a negative curvature ($\nu/\nu_0 < 1$) for the polar > C=O group, and a positive curvature ($\nu/\nu_0 > 1$) for the nonpolar CH_3 group. In other words, the sign of curvature of the ν/ν_0 vs. E_T^N plot is an indication of the polar/nonpolar nature of a group. Similar to the methyl groups of acetone, the methyls of TBA and TMAO show a positive curvature (Figure 6.6) which confirms the nonpolar nature of the mthyls of TBA and TMAO, respectively.

This result suggets that the positive charge on the nitrogen of TMAO could not make the C-H bonds of its methyl group polar enough so that they could interact with water in a fashion similar to a polar hydrophilic group. It is observed that the curvature of the ν/ν_0 vs. E_T^N plot for TMAO-methyls are more positive than that of the methyls of TBA or acetone. The larger positive curvature suggests that the nonpolar methyls of TMAO are more exposed to water (not more polar) than that of TBA or acetone. It is intutive that the positive charge on the nitrogen electrostatically attract the neighboring water molecules (dipoles) so that the water molecules approache closer to the methyls of TMAO compared to that of TBA.

6.3.6 Conclusions

In this chapter, we have examined the interaction between water and the methyl groups that are attached with quaternary nitrogen. Such kinds of methyl groups which are common in biological lipids (phosphatidylcholine) and osmolytes (trimethylamine-N-oxide) are believed to be more polar than the methyl group attached with an alkyl chain. It is observed that the vibrational response of the methyl groups in TMAO and TMA-cation are very similar to those of the typical nonpolar methyl groups in *tert*-butanol and acetone. The relative Raman band position vs. E_T^N plot of model molecules/groups shows a negative curvature for a polar >C=O group and a positive curvature for a nonpolar methyl group. In the case of TMAO, the relative Raman band position of the CH stretch bands varies with a positive curvature that signifies nonpolar nature of TMAO-methyls. Nevertheless, the positive charge on the quaternary nitrogen electrostatically attract the dipolar water molecules. As a result, water molecules approache closer to the methyl groups of TMAO/TMA^+ than that of a methyl group of an alkane chain.

Chapter 7

Interaction of a Photosensitizing Drug with Plasma Protein: Spectroscopic, Molecular Docking and Simulation Study

7.1. Introduction

The ionic and hydrophobic interactions play a key role in formation of secondary structure of protein, folding/unfolding, and ligand/drug binding. For example, the alterations of ionic and hydrophobic interactions (interaction between charged amino acid residues and between nonpolar groups of protein residues) lead to folding and unfolding of proteins which are related to its functions. Similarly, the electrostatic interactions between charged amino acid groups of the protein and a dipolar/charged ligand determine the binding location of the later in the protein and the hydrophobic interaction between the protein and the ligand/drug decide the overall stability of protein-ligand/drug complex. These interactions between proteins and ligands/drugs play crucial roles in the metabolism, efficacy and the overall distribution of the later in biological systems.

In mammals, Serum albumins (SA) are major soluble proteins in the circulatory system and play a crucial role in drug transportation and distribution. For instance, a weak

interaction between a soluble SA and a drug molecule will lead to increased free concentration of the drug in plasma (poor transport), whereas a strong interaction will decrease the free concentration, but may lead to poor distribution in target tissues.[116-118] Therefore, understanding the interactions between plasma protein and biologically active compounds is important in realizing their optimum transport and distribution at target tissues.

Tetrapyrrole based molecules, such as porphyrin and their derivatives have attracted much attention due to their extensive applications in medicine, namely as a marker in diagnostics and imaging and as a photosensitizer in photodynamic therapy (PDT) of malignancies and other diseases. Hematoporphyrin (HP, Fig. 7.1), for example is the main component of photofrin II, (the first generation photosensitizing drug for PDT). Because of its intrinsic fluorescence and selective accumulation in the neoplastic

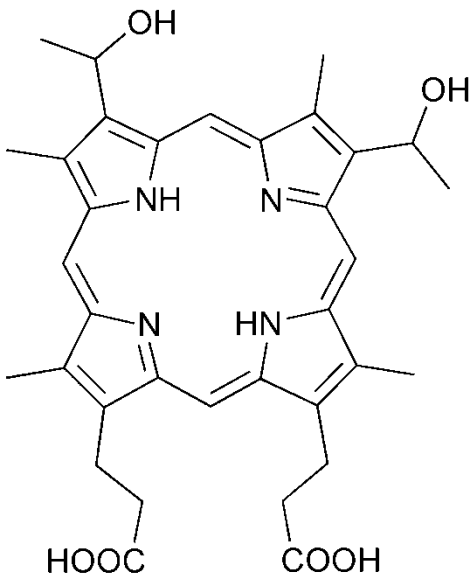

Figure 7.1. *Chemical structure of Hematoporphyrin (HP)*

tissues, HP-derivatives are used as marker in cancer detection (fluorescence diagnostics and imaging). Therefore, it is essential to investigate and gain the molecular level understanding of the interaction of HP with soluble proteins and other biomolecules for such applications.[109,110]

Not surprisingly, many research works have been carried out to understand the interaction of HP/HP-derivatives with soluble proteins, such as bovine serum albumin (BSA), human serum albumin (HSA), myoglobin, and hemoglobin.[337,338] In most of these studies, either the fluorescence of BSA/HSA is monitored in presence of different concentrations of HP-derivatives or the fluorescence of HP-derivatives is recorded in presence of different concentration of BSA/HSA. For example, Ehrenberg *et al.*[119] have investigated the fluorescence of HP-derivatives with varying length of hydrophobic alkyl chains in presence of increasing concentration of BSA and were found that the fluorescence is quenched and the position of the fluorescence maximum is red-shifted. Moreover, the rate of fluorescence quenching is enhanced as the hydrophobicity of the side chain of HP is increased. Based on these results, these authors have proposed that HP interacts with BSA by ground-state complex formation and that HP experiences a more apolar environment on complexation. A similar study with other HP derivatives has also revealed that HP experiences a more hydrophobic (apolar) environment in HSA-buffer solution compared to that in neat buffer and has suggested that hydrophobic forces play important role in HP-HSA interaction.[120]

Nevertheless, many other fluorescence quenching studies have indicated that the fluorescence of BSA/HSA is quenched by non-radiative deactivation of the excited

singlet state in presence of porphyrin derivatives. For instance, the Stern-Volmer plot of the fluorescence quenching of BSA in presence of N-confused porphyrins deviates from linearity at higher concentration of porphyrins, at 305 K.[121] The deviation from linearity is explained by two simultaneous quenching processes, involving ground state complex formation (static quenching) and non-radiative deactivation of the excited state (dynamic quenching). Feng *et al.*[122] have studied the quenching of BSA fluorescence in presence of monomethyl ether derivative of HP at different temperatures and have observed that the quenching constant (k_q) slightly increases with increasing temperature. Merely from the increasing trend of k_q with rise in temperature, it has been proposed that the HP interacts with the excited state of BSA (dynamic quenching). Surprisingly, the same experimental results modeled with a different form of the Stern-Volmer equation assuming ground-state complex formation suggest that hydrophobic forces are involved in the ground-state complex formation between BSA and HP. These premature analyses of quenching results have failed to provide further insight into the interactions between HP and BSA. Moreover, these studies[115,119-122,124,339]could not provide any information about the sites and domains in BSA/HSA, where HP binds.

Sylvester *et al.*[340] while studying the HP sensitized photo-oxidation of BSA have reported that oxidation takes place near the Cys-34 and Trp-residues in BSA and fluorescence competitive protein binding results indicated that HP binds in the subdomain IIA of BSA. The experimental results provide a macroscopic understanding of the binding interaction and the binding sites of HP-BSA/HSA interaction. Thus, further in depth studies are required in order to advance our understanding on how the structural

properties of porphyrins affect the mode of binding as well as detailed characterization of its binding locations in the proteins. Computational methods, such as molecular docking and molecular dynamic (MD) simulation can provide protein residue specific binding information and conformational changes.[125,126,341,342] These theoretical inputs in combination with experimental results may provide more insight into the sites/domains and nature of interaction in the protein.

In this chapter, we have investigated the interaction of HP with a typical plasma protein BSA in aqueous buffer solution by experimental (steady-state absorption, emission and fluorescence life-time measurement) and computational (molecular docking and MD-simulation) methods. We have found that the results of computational methods are in good agreement with the experimental observations. Our results have revealed that the fluorescence of BSA is quenched by the electronic energy transfer (EET) to HP and by the ground-state complex formation with HP. The molecular docking and MD-simulation in combination with experimental results suggest that hydrogen-bonding and Van der Waals interactions play important role in the complexation reaction and HP binds in the subdomains IB and IIA of BSA.

7.2. Experiments and Methods

7.2.1 Materials

Bovine serum albumin (BSA, ≥ 98%) hematoporphyrin dihydrochloride (HP) and 2-amino-2-hydroxymethyl-propane-1, 3-diol (Tris) were purchased from Sigma-Aldrich and used without any further purification. All other chemicals were purchased with spectroscopic grade available from sdfine chemicals, Mumbai. 10 mM Tris-HCl buffer

(pH = 7.4) and sample solutions were prepared by using nanopure water (conductivity 0.06 μS cm^{-1}). The pH of experimental solution was measured with a digital PICO pH meter (Lab India). 0.1 mM BSA stock solution was prepared in 10 mM Tris-HCl buffer for the quenching studies. In the case of HP solution, first 0.5 mM solution was prepared in aqueous Tris-HCl/methanol (9/1, v/v) and then diluted to required working concentration with Tris-HCl buffer. The concentration of BSA and HP were measured spectrophotometrically using the molar extinction coefficient values[343,344], ε_{BSA} (280 nm) = 4.38 x 10^4 lit $mole^{-1}cm^{-1}$ and ε_{HP} (396 nm) = 2.72 x 10^5 lit $mol^{-1}cm^{-1}$. Final concentrations of methanol in all studied solutions were less than 5%. Such low percentage of methanol induces no significant structural changes in BSA.[345]

7.2.2 Spectroscopic measurements

Steady-state absorption spectra were recorded with a JASCO-V650 spectrophotometer and the fluorescence spectra with a Hitachi F-4500 spectrofluorimeter, equipped with a temperature controlled accessory. The widths of excitation and emission slits were set to 5 nm. Fluorescence lifetime decays were recorded in a time-correlated single photon counting (TCSPC) instrument from IBH, with 292 nm LED as an excitation source having a pulse width of 800 ps and 1 MHz repetition rate. The instrument response function (IRF) was measured by collecting the scattered light from a TiO_2 suspension in water. The fluorescence decays were collected with the emission polarizer set at the magic angle, 54.7^o and analyzed by using IBH DAS 6.2 software.

7.2.3 Molecular docking

To predict the preferable binding orientation between HP and BSA, we performed molecular docking using the AutoDock 4.2[346] and the AutoDock Tools (ADT). The crystal structure of BSA (PDB ID 3V03) was obtained from the protein data bank with a resolution of 2.7Å. The crystal structure of BSA contains A and B polypeptides chains and we selected chain A for the present study. The X-ray crystal structure of BSA had several missing heavy atoms, which were added by the freeware molecular explorer programme NOC.[347] The completed crystal structures were then refined to fit the added atoms and subsequently the entire structure was energy minimized to remove any steric constraints by the AMBER 94 force field[348] based molecular dynamics module of NOC. The geometry of HP was optimized at HF/6-31G* level of theory using the GAMESS program[349] and the same was used for docking and simulation studies.

Autodock generates different ligand conformers using a Lamarkian genetic algorithm (LGA).[346] The genetic algorithm is implemented with an adaptive local search method. The energy based autodock scoring function includes terms accounting for short range *van der Waals* and electrostatic interactions, loss of entropy upon ligand binding, hydrogen bonding and solvation. Initially, the whole BSA protein was used to search the possible binding sites of HP by setting the grid size to 126, 126, 126 along X, Y, Z axes with a grid spacing 0.713 Å and then a more refined grid size of 40, 40, 40 along X, Y, Z axes with a grid spacing 0.352 Å was used at the binding site after assigning the BSA protein and HP with the Kollman charges. On the basis of the Lamarkian genetic algorithm (LGA), 100 runs were performed with 150 individuals in the population: the

maximum number of energy evaluations: 2500000, with number of generations 27000. The resulting docking conformers were subsequently clustered with a root-mean-square deviation (RMSD) tolerance of 2.0 Å and were ranked according to binding energy values.

7.2.4 Molecular dynamics (MD) simulations

All the simulations reported here were performed by the fully parallel version of the software GROMACS 4.5.5[350] using the Amber99SB force field[351] and the TIP3P water model.[352] For optimized docked geometry of the ligand molecule, we used general amber force field[353] and AM1-BCC charges.[354] The isothermal isobaric simulation protocol comprises of three major steps: energy minimization, position restrained run and finally the production run. To start with, the protein-ligand complex was put in a cuboid box having dimensions which kept the protein outer surface at least 10 Å away from the box wall. This was to ensure that no wall effect appeared in simulated results. The system was then solvated and required number of ions was added in each of the simulating systems (free BSA and BSA-HP complex) to attain electro neutrality.

In energy minimization step, flexible water model was used instead of rigid model that allowed steepest descent minimization technique to be followed and the energy minimization was thought to be converged when the maximum force in the system is smaller than 100 kJ mol^{-1} nm^{-1}. During the position restrained runs, linear constraint solver algorithm[355] was used to restrain the atom positions and a simulation time step of 2 fs was used to integrate the equation of motions of all atoms. The solvent and solute were separately coupled to temperature reservoirs of 300 K using Berendsen temperature

coupling method with coupling time of 0.1 ps. First the water molecules were heated to this temperature for 300 ps simulation run, while the protein-ligand complex was kept fixed. Then the simulation was restarted for heating the protein molecule to 300 K for 300 ps with the already equilibrated water molecules. And finally the ligand molecule was heated in a similar fashion for 100 ps. Pressure was restrained to 1 atm using Berendsen method with a coupling time of 0.5 ps.

The long-range electrostatic interactions were handled by Particle-Mesh Ewald electrostatics[356] with the real-space cut-off fixed at 12 Å and the highest magnitude of wave vectors used in reciprocal space was controlled by Fourier spacing parameter held at 1.2 Å. Grid dimensions were controlled with this Fourier spacing and the interpolation order 4. Finally, 10 ns production runs were performed for the corresponding systems comprising of ligand, protein, water and ions with same set of simulating conditions as in position restrained runs. MD simulation results were then used to investigate the functionally important protein residues responsible for binding the ligand and the binding free energies calculations.

7.3. Results and Discussion

7.3.1. Steady-state absorption and fluorescence characteristics of BSA and HP

Figure 7.2 shows the UV-visible absorption and fluorescence spectra of neat BSA and HP in aqueous buffer solution (pH = 7.4). The lower energy absorption band of BSA appeared in the UV-region with the maximum at 278 nm and the fluorescence spectrum had the maximum at 340 nm. The fluorescence of BSA originates from its two tryptophan

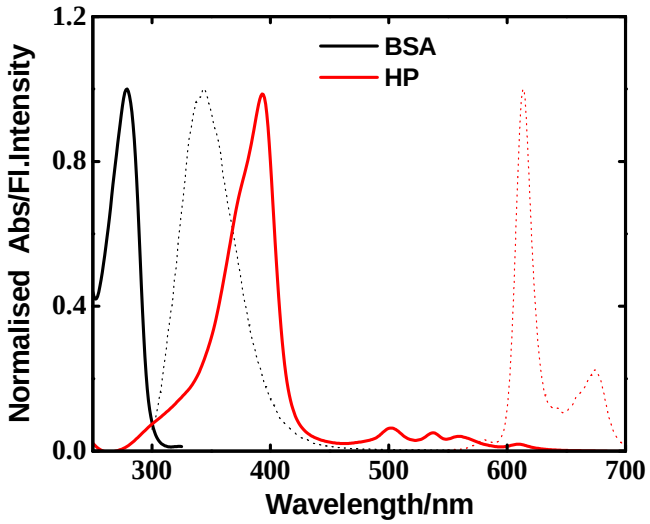

Figure 7.2. *Steady-state absorption (solid line) and fluorescence (dotted line) spectra of BSA (black) and HP (red) in Tris-HCl buffer (pH = 7.4).*

(Trp) residues (Trp-134 and Trp-213).[203] In the case of HP, there is a strong absorption band at 394 nm (soret band) and a few weak bands in 450-650 nm regions (Q-band). The fluorescence spectrum of HP recorded at 394 nm photoexcitation (soret band excitation) showed a sharp band at 614 nm and a relatively weak band at 675 nm. The absorption and emission characteristics of BSA and HP were in agreement with the previous reports[203,357]and might be useful in understanding the interaction between BSA and HP as discussed in the following sections.

7.3.2. Quenching of BSA fluorescence by HP

Figure 7.3A shows the corrected fluorescence spectra of BSA in the presence of different concentrations of HP. The fluorescence spectra were corrected to eliminate the inner-filter effect (caused by the absorption of HP) by the following equation:[203]

$$F_{cor} = F_{raw} \times \text{anti}\log\left(\frac{A_{ex} + A_{em}}{2}\right) \quad (7.1)$$

Here, F_{cor} and F_{raw} are the corrected and raw fluorescence spectra and A_{ex} and A_{em} the measured absorbance value at excitation and emission wavelength region, respectively caused by HP addition to BSA. As shown in Fig. 7.3A, the intensity of BSA fluorescence decreased with increasing concentration of HP, suggesting the interaction of HP with BSA either in the ground state, so that the photoexcited BSA becoming non-emissive (static quenching) and/or the emissive excited state of BSA found a way of dissipating its excitation energy by a non-radiative route (dynamic quenching). The quenching of BSA fluorescence had two more important features: (i) at high concentration of HP (~5μM), the BSA fluorescence reached to a residual intensity i.e., the fluorescence did not quench significantly on further increase in concentration of HP, and (ii) the maximum of the

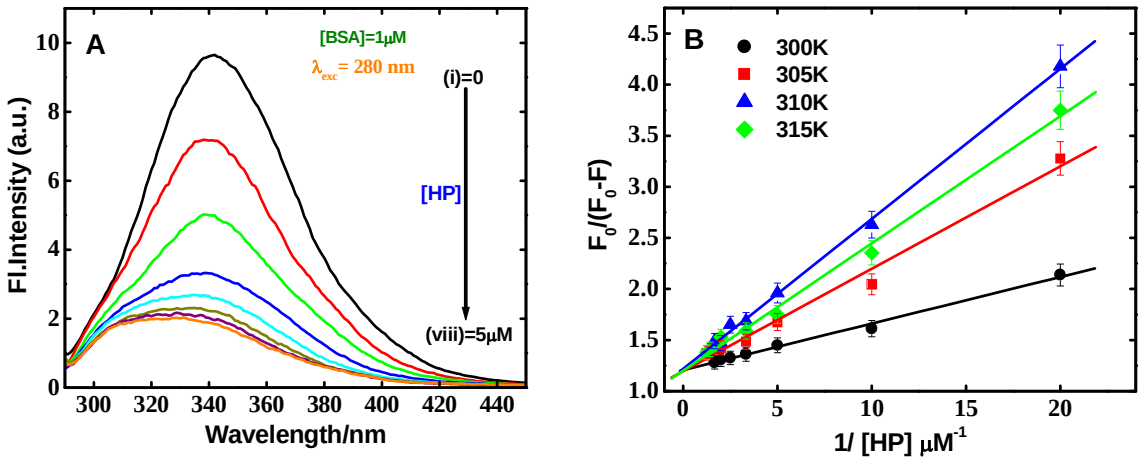

Figure 7.3. ***(A)*** *Fluorescence spectra of BSA (1.0 μM) in the absence and presence of HP in Tris-HCl buffer solution. Concentration of HP in μM: (i) 0, (ii) 0.25, (iii) 0.5,(iv) 1.0,(v) 2.0,(vi) 3.0,(vii) 4.0, and (viii) 5.0, respectively.* ***(B)*** *Plot of $F_0/(F_0-F)$ against 1/[HP]at three different temperatures as per the modified Stern-Volmer equation.*

residual fluorescence spectrum was about 15 nm blue-shifted, compared to that of neat BSA. Also, the band shape of residual fluorescence was broad compared to that of neat BSA.

The BSA fluorescence arises due to Trp residues, where Trp-134 is more exposed to solvent and emits at longer wavelength, while Trp-213 is buried in the hydrophobic region of protein, thereby emitting at slightly lower wavelength.[203] Consequently, the initial 15 nm blue shift of emission maximum is attributed to the more effective quenching of Trp 134 than that of Trp-213, as the later is difficult to access and gives residual fluorescence. The larger band width of the residual fluorescence suggests that inaccessible Trp-residues are placed in a more hydrophobic and inhomogeneous environment,[203] due to tightening of protein structure after addition of HP.

To get insight into the nature of interaction between HP and BSA with two kinds of Trp residues (accessible and inaccessible), we modeled the fluorescence quenching profile of BSA with the following Stern-Volmer equation (Eq. 7.2);[203,358-360]

$$\frac{F_0}{F_0 - F} = \frac{1}{f_a} + \frac{1}{f_a k_{sv}[HP]} \qquad (7.2)$$

where, F_0 and F are the integrated fluorescence intensity of BSA in absence and presence of HP. f_a is the accessible fraction of Trp-residue in BSA (fluorophore), $k_{SV} = k_q.\tau_0$ is the effective quenching constant or Stern-Volmer constant (k_q is the quenching constant, τ_0 is the fluorescence lifetime of BSA in absence of HP).

Table 7.1*: k_{SV}, k_q, and the fraction of accessible (f_a) Trp-residues in BSA and the thermodynamic parameters (ΔG^0, ΔH^0, ΔS^0) at different temperatures.*

T(K)	k_{SV} (M^{-1})	k_q (M^{-1} s^{-1})	f_a	ΔG^0 (kJ mol^{-1})	ΔH^0 (kJ mol^{-1})	ΔS^0 (kJ mol^{-1} K^{-1})
300	2.64×10^6	4.73×10^{14}	0.83	-36.8		
305	1.19×10^6	2.13×10^{14}	0.84	-35.5		
310	1.07×10^6	1.91×10^{14}	0.86	-35.8	-63.5	-0.07
315	0.83×10^6	1.49×10^{14}	0.82	-35.7		

Figure 7.3B shows a plot of $F_0/(F_0 - F)$ *vs.* 1/[HP] at four different temperatures. With increasing temperature, the slope of the plot ($1/f_a\ k_{SV}$) increases, indicating that the value of k_{SV} decreases with increasing temperature (assuming that f_a does not change in the temperature range studied). The plots in Fig. 3B are fitted with Eqn. (7.2) (solid lines) for a quantitative estimation of fraction of accessible fluorophore (f_a) and the quenching constants. The values of k_{SV}, k_q.(k_{SV}/τ_0) and 'f_a' are shown in Table 7.1. The value of 'f_a' is close to 0.8 and shows negligible dependence on the temperature range studied. Thus, ~80% of the Trp-residues (fluorophore) in BSA are accessible to HP and the remaining ~20% are buried in the hydrophobic regions of BSA and inaccessible to HP. The values of k_q are of the order of 10^{14} $M^{-1}s^{-1}$, which are at least four orders of magnitude higher than the bimolecular collisional quenching constant.[203] This higher value of k_q suggests that quenching of BSA fluorescence is not solely due to bimolecular collision of the excited state of BSA with HP. In other words, there may be ground-state complex

formation between BSA and HP or other ultrafast non-radiative relaxation processes caused by HP. In the following section, we determined the fluorescence life-time of BSA in presence of different concentrations of HP to understand the effect of HP on the non-radiative deactivation of BSA.

7.3.3. Fluorescence life-time of BSA in presence of HP

The interaction between HP and BSA is further explored by measuring the fluorescence lifetime of BSA in presence of different concentration of HP. The fluorescence decay profiles of BSA are shown in Fig. 7.4A and the corresponding life-time data are presented in Table 7.2. The obtained data clearly showed three life-time components of BSA even in the absence of HP. Of late, these life-time components have been attributed to the existence of different rotamers (rotational conformational isomers) of the Trp residues in

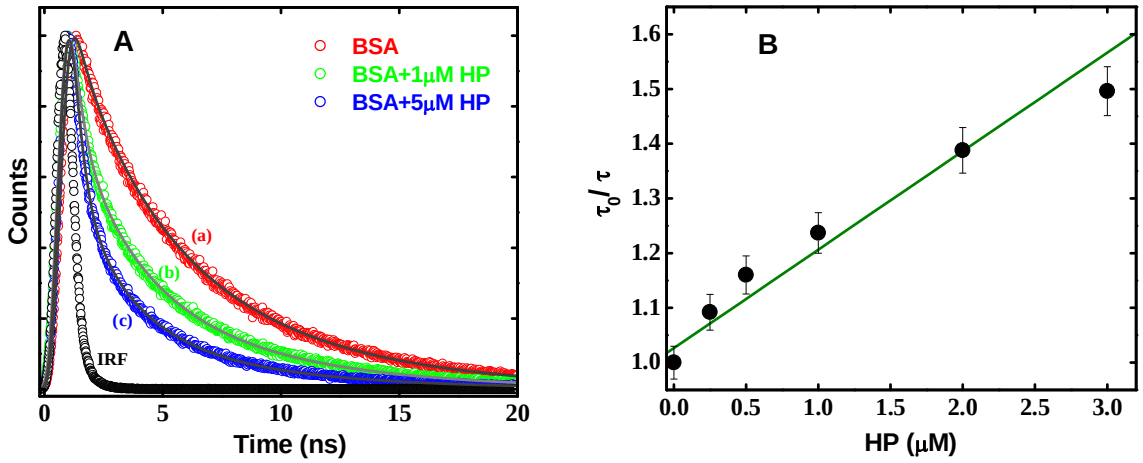

Figure 7.4. (*A) Fluorescence decay profiles (λ_{ex}=292 nm, λ_{em}=340 nm) of BSA in the absence (a) and presence of (b) 1μM and (c) 5μM HP. The scattered points represent actual decay profile while the solid dark yellow line represents a tri-exponential fit to that decay. (B) Plot of τ_0/τ vs. the concentration of HP.*

Table 7.2: ***Fluorescence lifetime parameters of BSA as a function of different concentration of HP in tris-HCl buffer (pH 7.4).***

HP / μM	τ_1(ns)	a_1	τ_2(ns)	a_2	τ_3(ns)	a_3	$<\tau>^a$ (ns)	$\chi^{2\,b}$
0	3.00	0.21	6.57	0.75	0.31	0.04	5.58	1.04
0.25	2.49	0.23	6.39	0.71	0.25	0.06	5.11	1.08
0.5	2.56	0.26	6.33	0.65	0.34	0.09	4.81	1.07
1.0	2.44	0.28	6.28	0.60	0.31	0.12	4.51	1.08
2.0	2.30	0.31	6.08	0.54	0.34	0.15	4.02	1.03
3.0	2.05	0.30	5.92	0.52	0.21	0.18	3.73	1.07
4.0	2.20	0.32	6.10	0.49	0.26	0.19	3.73	1.11
5.0	2.18	0.34	6.07	0.44	0.28	0.22	3.49	1.06

[a] $<\tau>=a_1\tau_1+a_2\tau_2+a_3\tau_3$ [b] The magnitude of χ^2 denotes the goodness of the fit.

BSA.[203,361,362] In the present case, however, it is difficult to analyze and interpret the effect of HP concentration on the fluorescence life-times of individual rotamers.

In order to obtain a semi-quantitative picture of the mechanism of interaction between HP and BSA, we simplified the situation by considering the average life-time and its variation with the concentration of HP. As shown in Table 7.2, the average fluorescence life-time of BSA decreases with increasing concentration of HP, due to non-radiative dissipation of excited BSA in presence of HP (dynamic quenching). To get a quantitative sense of quenching of the excited state by non-radiative deactivation, we plotted τ_0/τ *vs* [HP] as shown in Fig.7.4B and fitted the data points with the Stern-Volmer Eqn (7.3):

$$\frac{\tau^0}{\tau} = 1 + k'q\tau^0[\mathrm{HP}] \qquad (7.3)$$

Here, τ_0 and τ are the fluorescence lifetime of BSA in absence and presence of HP, k_q' is the dynamic quenching constant. The value of k_q' obtained from the plot in Figure.7.4B is 3.2 x 10^7 lit. mol^{-1} s^{-1}.

7.3.4. Fluorescence resonance energy transfer (FRET) from BSA to HP

In the previous section, we observed that fluorescence life-time of BSA decreased in presence of HP due to non-radiative deactivation of BSA by HP. This deactivation suggests the transfer of excitation energy from photoexcited BSA to the HP. In fact, while recording the fluorescence spectra of BSA (λ_{ex} = 280 nm) in presence of HP, we observed that with decrease in the BSA fluorescence, there is an increase in the fluorescence from HP in the region of 600-640 nm (Figure 7.5). As we can see in Figure 7.2, the emission

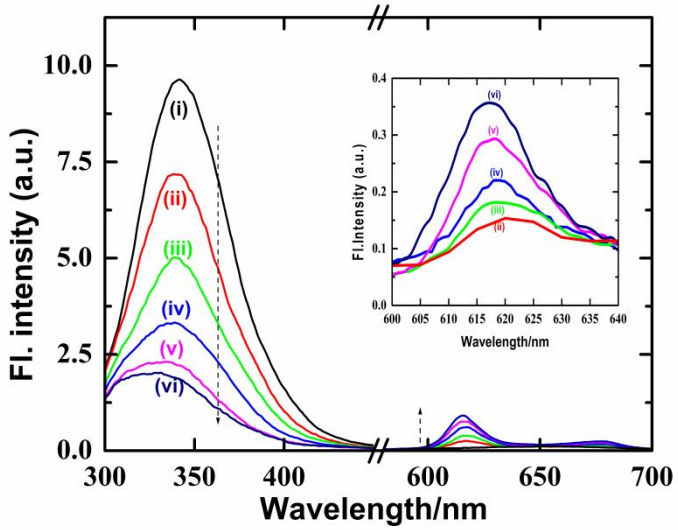

Figure 7.5. *Fluorescence spectra of BSA as a function of HP concentrations. Inset shows background subtracted fluorescence spectra of HP obtained by the 280 nm photoexcitation of BSA (1μM). Concentrations of HP in μM (i) 0.25 (ii) 0.5 (iii) 1.0 (iv) 3.0 and (v) 5.0.*

spectrum of BSA has significant overlap with the absorption spectrum of HP. Considering this, there could be two reasons for such increase in HP fluorescence. First, HP has weak absorption at 280 nm (excitation wavelength for BSA), so that HP molecules could be directly photoexcited along with BSA and the directly excited HP will have its own fluorescence. Therefore, as we increase the concentration of HP in BSA solution, it is likely that fluorescence of HP will increase due to direct excitation at 280 nm. Second, there could be an energetic interaction between excited BSA and unexcited HP, so as the excitation energy of BSA is transferred to the HP and then this indirectly excited HP could give rise to the fluorescence.

To identify these two possibilities, we recorded the fluorescence spectra of neat HP solution at different concentrations (same as that in BSA solution) on 280 nm excitation and compared with those observed in presence of BSA. It is noticed that fluorescence intensity of neat HP is weaker than the respective spectrum in presence of BSA. This indicates that during the fluorescence quenching of BSA the increase of HP fluorescence is due to both direct excitation, as well as indirect excitation (energy transfer from excited BSA to HP). To assess the enhancement in HP fluorescence due to energy transfer from BSA, we subtracted the fluorescence spectrum of neat HP from the respective spectrum of HP in presence of BSA and the subtracted spectra is shown in the inset of Figure. 7.5. Evidently, the quenching of BSA fluorescence by HP and the concomitant rise of HP fluorescence (Figure. 7.5) suggests an energetic interaction between excited BSA and unexcited HP, so that the electronic excitation energy of BSA is transferred to the HP.

The efficiency of energy transfer (Φ_E) can be expressed as[203]

$$\Phi_E = \frac{k_{EET}}{k_f + k_{nr} + k_{EET}} = 1 - \frac{\Phi_F}{\Phi_{FO}} = 1 - \frac{\tau}{\tau_o} \quad (7.4)$$

where k_{EET} is the rate constant of electronic energy transfer, k_f and k_{nr} are the decay rate constants of fluorescence and non-radiative processes in the absence of HP. Φ_{F0} and Φ_F are fluorescence quantum yields of BSA in the absence and presence of HP. From Eqn. (7.4), the energy transfer efficiency (Φ_E) between BSA and HP is obtained to be 0.37, while [BSA] = 1.0 μM and [HP] = 5.0 μM, respectively. According to the Förster energy transfer theory,[363,364] the energy transfer efficiency depends upon the distance between the donor and acceptor by Eqn (7.5).

$$\Phi_E = \frac{R_0^6}{R_0^6 + r^6} \quad (7.5)$$

where 'r' is the distance between the donor (Trp of BSA) and the acceptor (HP). While R_0 is called the Förster distance, which is the distance between the donor and acceptor at which electronic energy transfer efficiency is 50%. R_0 can be calculated by using Eqn 7.6[203,364]

$$R_6^0 = 8.8 \times 10^{25} [(k^2 n^4 \Phi_D J(\lambda)] \quad (7.6)$$

where κ^2 is the spatial orientation factor describing the relative orientations of the transition dipoles of donor and acceptor, n is the refractive index of the medium, Φ_D is the

donor quantum yield, J(λ) is the overlap integral of the normalized emission spectra of BSA and absorption spectra of the HP, which is calculated as follows:[203]

$$J(\lambda) = \frac{\sum F(\lambda)\varepsilon(\lambda)\lambda^4 \Delta\lambda}{\sum F(\lambda)\Delta\lambda} \qquad (7.7)$$

Here F (λ) is the fluorescence intensity of the donor in wavelength range of λ to λ + Δλ and ε(λ) is the extinction coefficient (in M^{-1} cm^{-1}) of the acceptor at λ. The values of κ^2, n and Φ_D are assumed as 2/3, 1.336 and 0.15, respectively. The value of J (λ) is calculated by integrating the overlap spectra in the 300 - 450 nm wavelength regions and is obtained as 2.55 x 10^{-15} M^{-1} cm^3. Subsequently, the value of R_0 is found to be 20.3 Å. Using the values of R_0 (20.3 Å.) and ϕ_E (0.37), the value of 'r' is determined to be 22.2 Å using Eqn. (7.5). Consequently, the estimated mean distance is found to be very close to the Forster energy transfer distance.

7.3.5. Thermodynamics of complexation between BSA and HP

In the previous sections, we found that rate of dynamic fluorescence quenching of BSA (k_q'= 3.2 x 10^7 $mole^{-1}$ s^{-1}) is seven orders of magnitude lower than the overall rate (k_q = 4.73 x 10^{14} $mole^{-1}$ s^{-1}) of fluorescence quenching of BSA by HP. This indicates complexation of HP in the ground state of BSA play a vital role in the quenching of BSA fluorescence. Further confirmatory evidence in favour of the ground state complex formation between BSA and HP is obtained from the UV-visible absorption measurements.

As shown in Fig. 7.6A, the maximum absorption wavelength of BSA around

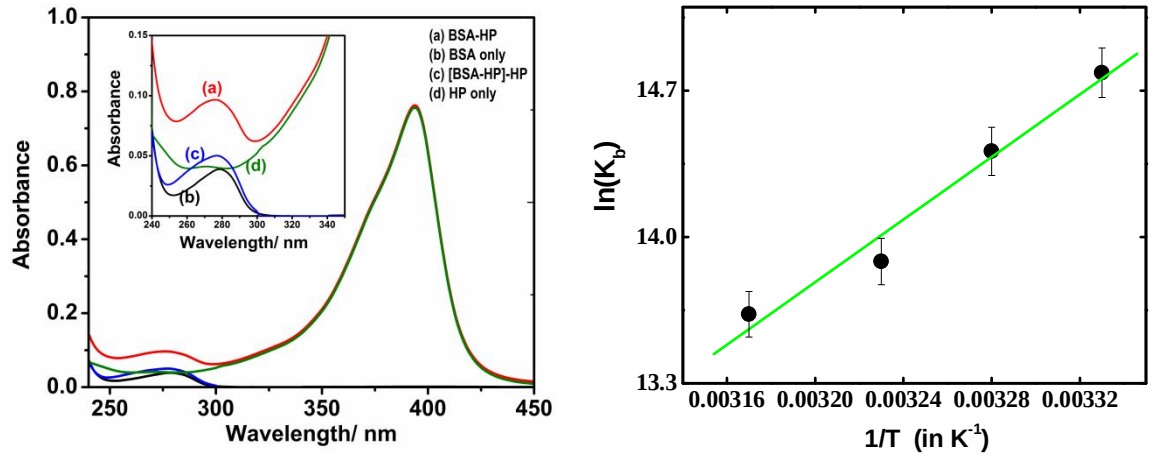

Figure 7.6. *(A)UV-visible absorption spectra of BSA in the presence of HP. (a) the absorption spectra of BSA-HP system; (b) the absorption spectra of BSA only; (c) the difference absorption spectra between BSA-HP and HP; (d) the absorption spectra of HP only. [BSA]=1μM and [HP]=3μM (B) van't Hoff plot for the interaction of BSA with HP in Tris-HCl buffer (pH=7.4).*

280 nm (black curve) shows little blue shift and the absorbance intensity obviously increased after addition of HP (blue curve), indicating that there is a ground state complex formation between BSA and HP. This observation further reconfirm that the HP induced quenching of BSA fluorescence is predominantly by static quenching process. Accordingly, the effective quenching constant (k_{SV}) which can be approximate as the binding constant (K_b) of BSA-HP complexation and could provide information about the thermodynamics of the complexation reaction.

$$K_{SV} \approx K_b = \exp\left(\frac{-\Delta G^0}{RT}\right)$$

$$In(K_b) = -\frac{\Delta H^0}{RT} + \frac{\Delta S^0}{R} \qquad (7.8)$$

Assuming that the enthalpy and entropy does not change appreciably in the temperature range 300-315 K, the ΔH^0 and ΔS^0 corresponding to the complexation between BSA and HP can be determined from Eqn (7.8). The plot of $\ln(K_b)$ against 1/T is a straight line as shown in Fig. 7.6B and the slope and intercept of the fitted line provides the enthalpy (ΔH^0 = -56.4 kJ mole^{-1}) and entropy (ΔS^0 = -0.06 kJ mole^{-1} K^{-1}) changes, as summarized in Table 7.1. According to the Ross and Subramanian,[365] the positive ΔH^0 and ΔS^0 values are taken as a typical evidence of hydrophobic interaction. Whereas, very low positive or negative values of ΔH^0 and positive ΔS^0 values are characteristic of electrostatic interactions and the negative ΔH^0 and ΔS^0 values are associated with hydrogen-bonding and Van der Waals interactions.[366] As can be seen from Table 7.1, the negative ΔH^0 and ΔS^0 values indicates that hydrogen bonding and Van der Waals interactions are the main driving forces in the binding of HP to BSA. More details on the nature of interactions are discussed in the following section on the basis of molecular docking and MD-simulations.

7.3.6. Molecular docking analysis

For recognition of possible binding sites in BSA, we performed a blind docking with a grid covering the whole protein and generated 100 distinct conformers of HP with an 'RMSD' tolerance of 2.0 Å. Out of these 100 conformers, 10 conformers are found to have significantly higher binding energies, as compared to the others (Table 7.3). Out of these ten conformations, seven are found in domain IB and three in domain IIA of BSA (Fig. 7.7). Then, we performed second round docking using a more refined grid covering in the subdomains IB and IIA and the corresponding energy minimized structures are shown in Fig.7.8 and the energies in Table 7.4. The free energy change (ΔG^0) for the

binding interaction between HP and BSA obtained from the docking studies (-31.3 kJ/mol) is close to the experimental value (-35.5 kJ/mol). Furthermore, the experimentally determined distance between Trp-residues and the bound HP (r = 22.2 Å) nicely matched with the distances determined from the lowest energy docked structure (~ 21 Å).

Table 7.3. ***Docking summary of BSA with HP by the Autodock program generating different ligand conformers using a lamaekian GA.***

Rank	Run	K_i (μM)	Binding energy (kcal mol^{-1})	Binding domain in BSA	Van der Waals-hydrogen bonding-desolvation energy (kcal mol^{-1})	Electrostatic Interaction energy (kcal mol^{-1})	Torsional energy (kcal. mol^{-1})
1	1	3.33	-7.47	IB	-9.57	-1.48	+3.58
2	53	11.06	-6.76	IIA	-8.74	-1.60	+3.58
3	7	16.30	-6.53	IB	-8.79	-1.33	+3.58
4	6	31.20	-6.15	IB	-8.92	-0.81	+3.58
5	21	43.55	-5.95	IB	-7.91	-1.61	+3.58
6	87	44.07	-5.94	IIA	-6.87	-2.65	+3.58
7	35	52.46	-5.84	IB	-9.03	-0.39	+3.58
8	86	59.43	-5.77	IIA	-6.58	-2.76	+3.58
9	78	59.80	-5.76	IIA	-7.44	-1.90	+3.58
10	32	60.45	-5.76	IB	-7.87	-1.46	+3.58

Table 7.4. ***Different interaction energies (kJ mol^{-1}) between HP and the BSA in the best docked structure obtained from Autodocking.***

Binding site	Binding energy (ΔG^0 / kJ mol^{-1})	Van der Waals-hydrogen bonding energy (kJ mol^{-1})	Electrostatic Interaction energy (kJ mol^{-1})	Torsional energy (kJ mol^{-1})
Subdomain IB	-31.26	-40.05	-6.19	+14.98
Subdomain IIA	-28.29	-36.58	-6.69	

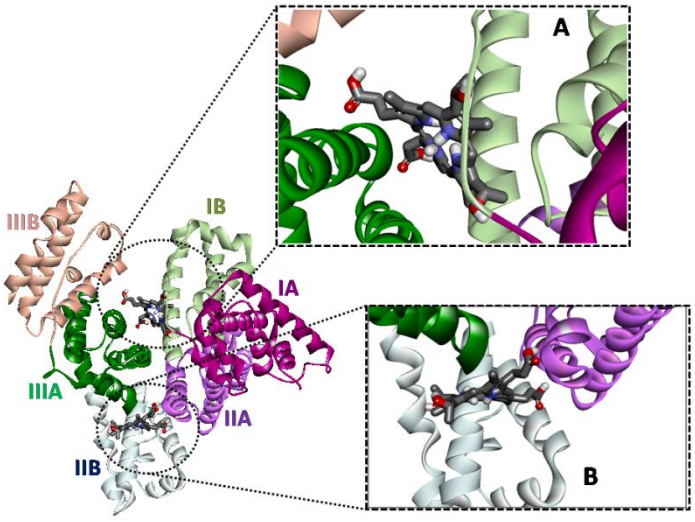

Figure 7.7. *Overview of the binding sites of HP in (A) subdomain IB and (B) IIA of BSA.*

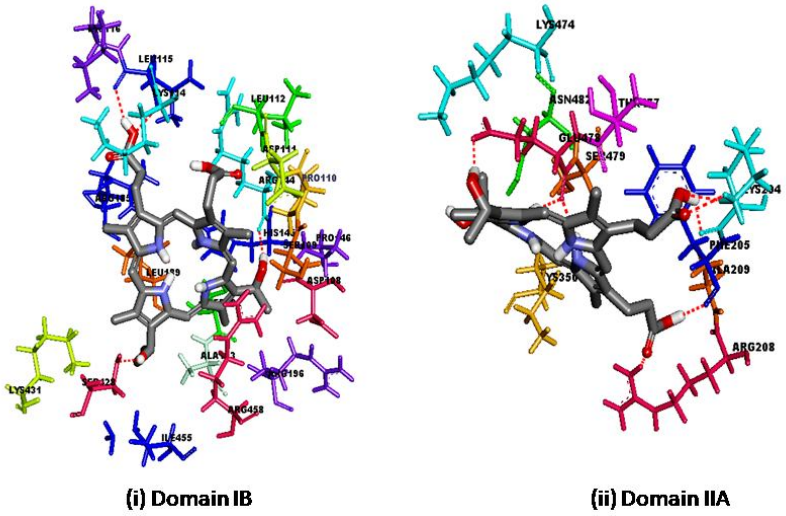

Figure. 7.8. *Stereo view of HP inside subdomain (i) IB and (ii) IIA of BSA obtained by using refined grid covering. The amino acid residues (in different colours) forming the binding cavity and H-bonds (as highlighted by the dashed lines in red color) formed between HP with BSA.*

Figure 7.8 shows that in subdomain IB, the hydroxyl groups of HP forms intermolecular hydrogen bonds with Ser-428, Arg-144 and Leu-115 of BSA with a distance of 2.14, 1.74

and 2.14 Å, respectively. Whereas in subdomain IIA, the propionic acid side groups of the HP forms intermolecular hydrogen bonds with Lys-204 and Glu-478. As shown in Table 7.4, the major contributions to the binding energies in subdomain IB and IIA are from the hydrogen-bonding and Van der Waals interactions.

7.3.7. Analysis of MD simulation trajectories

The MD simulation is carried out for 10 ns starting with the lowest energy structure of BSA-HP complex (HP in subdomain IB of BSA) in water. MD simulation results are analyzed on the basis of root mean square deviation (RMSD), root mean square fluctuation (RMSF) and radius of gyration (Rg) values for the free BSA and the HP bound BSA. The RMSD provides a direct measure of the structural changes from the initial coordinates, as well as the atomic fluctuations over the course of an MD simulation.[341,342]

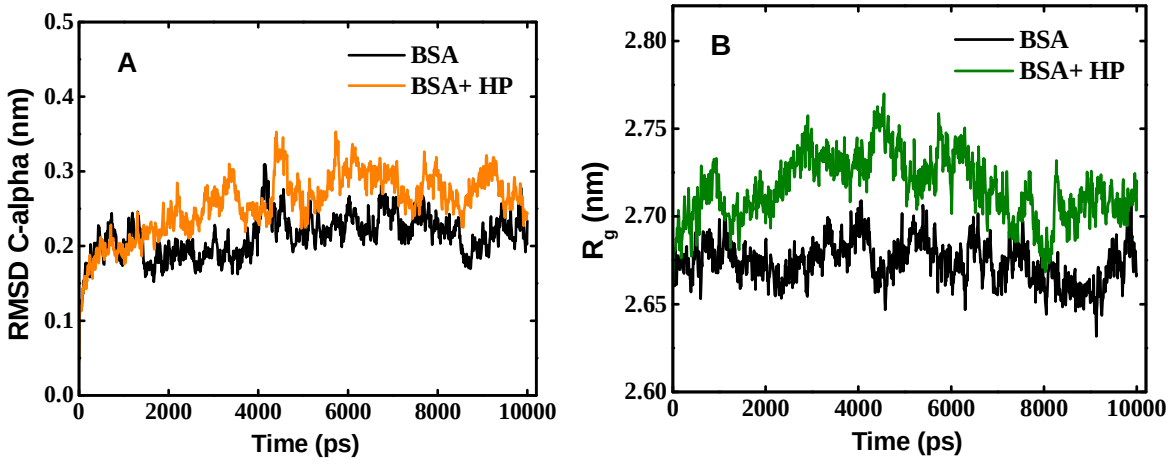

Figure 7.9. *(A) Plot of RMSD of C-Cα-N backbone against simulation time scale (ps) for solvated BSA and BSA-HP during10ns MD Simulation. (B) Plot of Rg during 10 ns MD simulation of BSA and BSA-HP complex.*

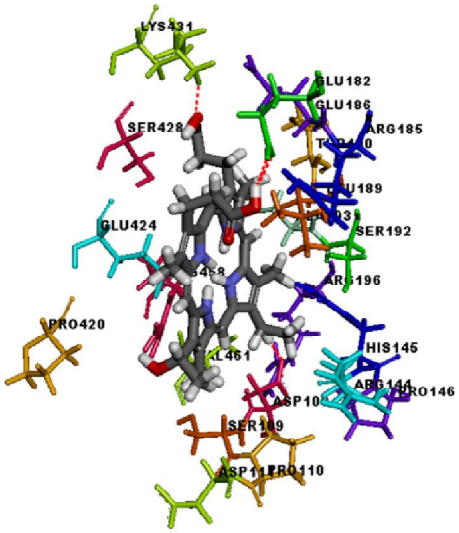

Figure 7.10. *HP bound to subdomain IB binding site after 10 ns of simulation. The H-bonds are depicted with red dash lines.*

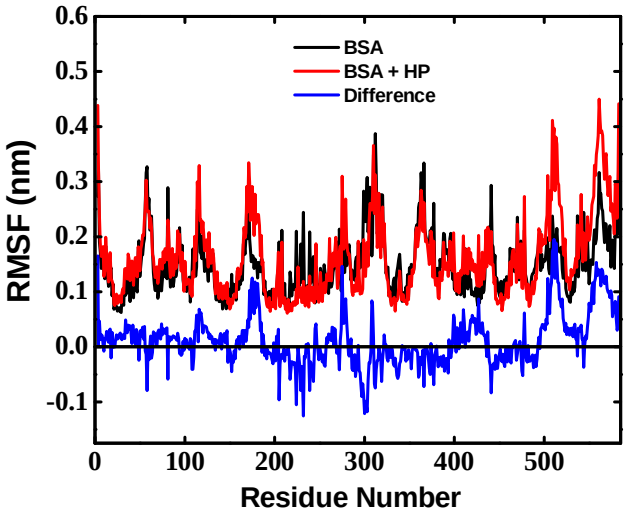

Figure 7.11. *Plot of RMSF values of BSA, its complex with HP and the difference (complex-BSA) against residue number.*

The RMSD values of protein backbone (C-Cα-N) in free BSA and BSA-HP complex presented in Fig. 7.9A shows that RMSD value reaches equilibration after 5 ns and then oscillates around an average value at longer time for both the free BSA and BSA-HP complex. However, magnitude of RMSD (after 5 ns) is slightly higher for the HP-BSA complex than in free BSA. The higher RMSD value suggests a structural change in HP-BSA complex, due to the flexible structure of BSA and presence of solvent. Indications of similar structural changes are obtained from the variation of radius of gyration of the protein. The radius of gyration (Rg) of the protein correlates with the size and compactness of the overall protein structure.[341] The Rg for both the solvated BSA and BSA in presence of HP are shown in Fig. 7.9B over the simulation time scale. During simulation time, the average Rg of BSA-HP complex (2.72 ± 0.05 nm) is slightly higher than that of free BSA (2.67 ± 0.03 nm). This higher Rg value of the BSA-HP complex clearly indicates a structural change that caused a little swelling of the BSA-HP complex.

Figure 7.10 shows the structure of BSA-HP complex obtained at the end of the 10 ns simulation, which is different from the minimum energy docked structure (subdomain IB in Fig.7.8). It is observed that the domain III experienced much more conformational changes in comparison to the subdomain IB, which results into a relatively different configuration with improved interactions between HP and domain III amino acid residues, in contrast to the lowest energy docked structure (demonstrated earlier). Local protein flexibility analyzed from the calculated time average RMSF values of all the residues over simulation time scale is presented in Fig. 7.11. Figure 7.11 suggests that the end of the helix and sub domain connecting loops is more flexible in comparison to the

other regions of the protein. Also, the HP binding site in subdomain IB shows little flexibility, suggesting the conformational adjustment upon HP binding.

7.3.8. Binding free energy calculation using solvated interaction energy method

From the 10 ns protein-ligand MD trajectories, 1000 snapshots are taken at regular intervals for the binding energy calculation using the solvated interaction energy (SIE) method.[367,368] The SIE function is given as,

$$\Delta G_{bind}(\rho, Din, \alpha, \gamma, C) = \alpha\left[E_c(D_{in}) + \Delta G^r_{bind}(\rho, D_{in}) + E_{vdw} + \gamma\Delta MSA(\rho)\right] + C \qquad (6.9)$$

The SIE function fitted on a set of protein-ligand complexes give absolute binding affinity predictions and when the predicted values are compared with experiments they often outsmarted estimations based on other methods, such as the molecular mechanics generalized born surface area (MM-GBSA). The definitions and values of the best fitted parameters in the SIE function are: AMBER van der Waals radii linear scaling coefficient, ρ = 1.1; the solute interior dielectric constant, D_{in} = 2.25; the global proportionality coefficient related to the loss of configurationally entropy upon binding α= 0.1048, the molecular surface area coefficient γ= 0.0129 kcal/ (mol Å^2) and a constant C= −2.89 kcal/mol. In SIE function for the binding free energy, E_C and E_{vdw} are the AMBER molecular mechanics force field based intermolecular Coulomb and van der Waals interaction energies in the bound state, respectively. ΔG^R_{bind} is the change in the reaction field energies between the bound and the free states and is calculated by solving the Poisson equation with the boundary element method program BRI BEM

and using a molecular surface generated with a variable-radius solvent probe. The ΔMSA term is the change in the molecular surface area upon binding.

From the 10 ns protein-ligand MD trajectories, 500 snapshots are taken at regular intervals in the last 5 ns of equilibration data and for each of them the binding energies analyses are performed using SIE function. Finally, a time series plot of the calculated snapshot ΔG_{bind} values is prepared to make sure that its average value could be extracted over a stable part of the MD trajectory with little drift in the mean value over time. The discovered average values of the SIE terms in the unit of kJ/mol were: $\langle E_C \rangle$ = -75.10, $\langle E_{vdw} \rangle$ = -232.34, ΔG^{R}_{bind} = 137.70, $\langle \Delta MSA \rangle$ = 47.45 and $\langle \Delta G_{bind} \rangle$ = -34.85. Clearly, the present MD ensemble averaged binding free energy (-34.85 kJ/mol) of the BSA-HP complex closely matches with our value (-35.5 kJ/mol), determined by fluorescence quenching experiments.

7.4. Conclusions

In this chapter, the binding interaction of HP to the protein BSA is examined in aqueous buffer solution by steady state absorption, emission and fluorescence life-time measurements in conjugation with molecular docking and MD simulation. On the basis of our experimental and theoretical findings, we conclude that the fluorescence of BSA is dominantly quenched by the ground-state complex formation with HP accompanied by the minor contribution from electronic energy transfer (EET) to the later. The critical energy transfer distance (R_0 = 20.3 Å) and the mean distance (r = 22.2 Å) between the BSA and HP are calculated using FRET. Molecular docking analysis suggests that HP bound to the two well-separated sites located in the sub domain IB and IIA, where the

sub domain IB (primary binding site) is distinctly more occupied than IIA (secondary binding site). Based on the detail docking analysis and experimental thermodynamic parameters, it is confirmed that hydrogen-bonding and Van der Waals forces are the driving forces for the BSA-HP complexation.

Additionally, with an intention to investigate the stability and conformational changes in the docked BSA-HP complex system in the aqueous environment, we carried out the MD simulation, which shows the stabilization and conformational flexibility of the protein upon HP binding. Further, the binding affinity energy values obtained from the post-MD free energy calculations using SIE method are in good correlation with the experimental results. Moreover, the experimental and computational results presented here demonstrated that the computational methods, such as molecular docking and MD simulations are the valuable tools for the investigation of interactions taking place between porphyrin based photosensitizing drugs and the proteins, especially when combined with experimental techniques. Essentially, the present report precisely explored the molecular level interactions occurring between the porphyrin and the protein.

Chapter 8

Protein-Ion Interaction driven Green Synthesis of CdSe Quantum Dots: Tuning of Morphology and Optical Properties

8.1. Introduction

II–VI group semiconductor quantum dots (QDs) are a class of fascinating nanocrystals owing to their size dependent physicochemical properties,[369-371] thereby posses numerous potential applications in various fields such as optoelectronics, sensors, solar cells, superionic materials, laser materials and biochemical field.[133-135] Recently, bioconjugated semiconductor QDs have added a new dimension to nanoparticle research due to their applications in drug delivery, biological labeling, luminescence tagging etc.[372-376] Cadmium selenide, (CdSe) with medium band gap energy of 1.74 eV at 300 K, is one of the most attractive member of II–VI semiconductor family due of its highly tunable optoelectronic properties.[377,378] Colloidal synthesis methods such as high temperature organometalic synthesis are the most followed route to obtain a variety of nanomaterials with the fine tuning of their morphologies. However, most of these methodologies involve stringent conditions, such as high temperature, pressure, inert atmosphere, use of

toxic reducing agents and so on. Further, various researchers have used different host matrix and stabilizing agents (surfactants, microemulsions, acids, organic or inorganic polymers, thiols, amines and polyphosphates) which cap the nanoparticle surface and provide charge and steric stabilization to get nanomaterials of desired morphologies.[379-387] However, selection of appropriate capping agents for biological applications demands dimensional stability, good solubility, environment friendly nature, minimum invasiveness and good biocompatibility.

In this perspective, there has been a recent upsurge of interest in synthesizing semiconductor QDs through environmental friendly biomimetic routes wherein the interaction between biomolecules (amino acids[147,148], proteins[150,151,388-390], DNA[136,152,153], RNA[391]) and inorganic ions were exploited to control the nucleation and growth of QDs to different degrees in aqueous solutions at biological pH and ambient temperatures. Bovine serum albumin (BSA) is a well characterized major soluble protein in the circulatory system thereby plays a crucial role in drug transportation and distribution. It has oblate ellipsoid shape and contains 583 amino acid residues with three α-helical domains I-III, which are further classified into two sub domains A and B. It is well established that each sub domain uniquely exhibits a certain degree of binding specificity depending on the molecular and physical properties of the ligand.[392-394] The binding site situated near the N-terminus in the domain III has strong affinity to a variety of inorganic ions and makes BSA as a host matrix or a template to synthesize various nanomaterials. In recent years there are many studies on synthesis of nanoparticles in a BSA matrix.[149,154,395] However, most of these reports involve the use of external reducing

agents accompanied by high temperature and inert atmosphere. Such conditions are highly expected to denature the inherent protein structure of BSA and eventually making the nanomaterials inappropriate for the bio-related applications.

In the present study, we have synthesized CdSe QDs in the host matrix of BSA at physiological pH. Besides, no external reducing agents were employed and the reaction was carried out at ambient conditions. Since, BSA is known to provide a micro cavity to various nanoparticles and able to catalyze certain processes in aqueous solutions. Considering this, we have utilized these properties of BSA to synthesize CdSe QDs in aqueous solutions. Most interestingly, by simply changing the molar ratios between Se and Cd precursors, different shaped CdSe nanocrystals have been synthesized, which provides a new direction to control the shape of CdSe nanocrystals. Further, our synthetic strategy also provides great potential for tuning of optical properties of as grown QDs across the visible spectrum just by varying molar ratios of the precursors due to their strong dependence on size and shape of the nanocrystals. Taking the advantage of such experimental conditions wherein the structure of BSA is supposed to remain intact, it would be interesting to perceive how the inherent structure of BSA and its interaction with precursor inorganic ions control the morphology and optical properties of the QDs. Thus, various such aspects regarding the role of BSA-ion interactions in the synthesis as well as in governing the morphology and optical properties of as grown CdSe QDs has been investigated and described in detail in this chapter.

8.2. Experiments and Methods

8.2.1. Materials

High purity chemicals, bovine serum albumin (BSA), cadmium sulfate ($CdSO_4$), selenium (Se) powder, sodium sulfite (Na_2SO_3), were obtained from Sigma-Aldrich and used as received. The reagent such as ethanol used for washing the precipitates was purchased with highest purity available from sdfine chemicals, Mumbai. Nanopure water (with a resistivity 18.2 MΩ cm) obtained from a Millipore water purifying system (Barnsted System, USA) was used for the preparation of the precursor solutions.

8.2.2. Synthesis

In a typical synthesis procedure, stock solution of Se precursor (250 mM Na_2SeSO_3) was prepared by refluxing the solution containing 1 g Se powder and 10 g Na_2SO_3 in 50 ml nanopure water at 70^0C for 7 hrs.[396] Stock solution of Cd precursor (BSA-Cd^{2+} complex) was prepared by mixing the desired concentrations of $CdSO_4$ (5 ml, 5 to 20 mM) and BSA (10 ml, 1mg/ml) aqueous solutions with continuous stirring at room temperature and kept under ambient conditions for 1 hr. An appropriate concentration of freshly prepared Na_2SeSO_3 (5 ml, 5 to 20 mM) was then added to the freshly prepared Cd precursor (BSA-Cd^{2+} complex, 15 ml) solution at room temperature. The pH of the reaction mixture was noted to be in the range of 7.0 to 8.0. The mixing of two aforesaid solutions was followed by stirring, which resulted in the evolution of color depending on the molar ratios of the Cd and the Se precursors. This emergence of color can be regarded as the primary signature for the formation of CdSe QDs. The molar ratio of the precursors were varied

and have been described in the following sections to investigate their impact on the morphology and the optical properties of the as-grown CdSe QDs. It is to be mentioned here that the concentration of the precursors solutions were very less such that no chemical reaction leading to the formation of CdSe QDs was observed in the absence of BSA. All the spectroscopic measurements were carried out 24 hrs after mixing the precursor solutions to ensure their complete reaction. The photoluminescence (PL) quantum efficiency (QE) of the QDs was determined based on the comparative method by using equation (8.1). The standard reference employed was Rhodamine 6G (Φ = 0.95) dissolved in ethanol.

$$\Phi_S = \Phi_R \frac{A_S}{A_R} * \frac{OD_R}{OD_S} * \left(\frac{n_S}{n_R}\right)^2 \quad (8.1)$$

Where, 'Φ' is the quantum yield, 'A' is the integrated PL intensity, 'OD' is the optical density, and 'n' is the refractive index. The subscript 'S' and 'R' refers to the sample and reference, respectively. The excitation wavelength was chosen on the basis, where the OD values of both the sample and the reference matched with each other.

8.2.3. Characterization

Optical absorption measurements were carried out by using a JASCO V-650 absorption spectrophotometer. Steady-state PL measurements were carried out at room temperature by using a Hitachi F-4500 spectrofluorimeter. X-ray diffraction (XRD) measurements were recorded on a Phillips X-ray diffractometer, model PW 1710 system, using a monochromatic Cu Kα source (λ = 1.54 Å). The instrument was well calibrated using standard samples before any measurements. The electron diffraction and transmission

electron microscopic (TEM) images were acquired on a TEM, Philips model number CM200 with operating voltages 20-200 kV and resolution: 2.4 Å. Samples for TEM measurements were prepared by depositing a drop of as prepared sol on thin carbon coated copper grid and consecutively, allowed the solvent to evaporate. The scanning electron microscope (SEM) images were recorded in an SEM model number AIS2100, SERON Technology, Korea. The compositional analysis for the samples was performed with energy dispersive X-ray spectrometer (EDX), an accessory of SEM (JEOL JSM-T330 SEM). The preparation of samples for SEM and EDX analysis was carried out by putting a drop of as obtained sols on the Silicon wafer, and subsequently allowing the solvent to evaporate. The FT-IR spectra were recorded using a diamond single reflectance ATR probe in an IR Affinity-1 FTIR spectrometer. Zeta potentials were determined with a Nanosizer Z (Malvern Instruments, Malvern, UK) by phase analysis light scattering. The light source was He-Ne laser operated at 633 nm operating at 4.0 mW. The zeta potential (ζ) values are calculated from the electrophoretic mobility data using Smoluchowsky approximation.

Raman spectral studies were carried out on Seki's STR 300 Raman spectrometer. For recording the Raman spectra, the precipitates of as grown CdSe nanoparticles were extracted and washed with water and ethanol for 5 to 6 times. The as obtained precipitates were taken on a glass slide and used for carrying out the Raman spectral studies. PL lifetime measurements were carried out by using a time correlated single photon counting (TCSPC) instrument (model: IBH, UK). The instrument response function (IRF) of the setup was measured by collecting the scattered light from a TiO_2 suspension in water. The

samples were excited by a diode laser of output wavelength, 450 nm with an IRF of less than 100 ps.

8.3. Results and Discussion

8.3.1. Morphology and structural characterization of as grown CdSe QDs

The structure, phase purity and size of as grown nanoparticles were determined from the XRD pattern. Following the synthesis of the nanoparticles, the precipitates were obtained by heating the solution to 40^0C for 5 to 10 minutes. Basically, the protein structure is highly vulnerable to pH and temperature.[397] Therefore, the heating resulted into the precipitation of the nanoparticles which were than centrifuged and washed 3 to 4 times with ethanol and nanopure water. The XRD of as obtained precipitates is shown in Figure 8.1. The diffraction pattern of the nanoparticles has been found to be in good agreement with the standard JCPDS card no. 19-0191, corresponding to the cubic structure of CdSe.

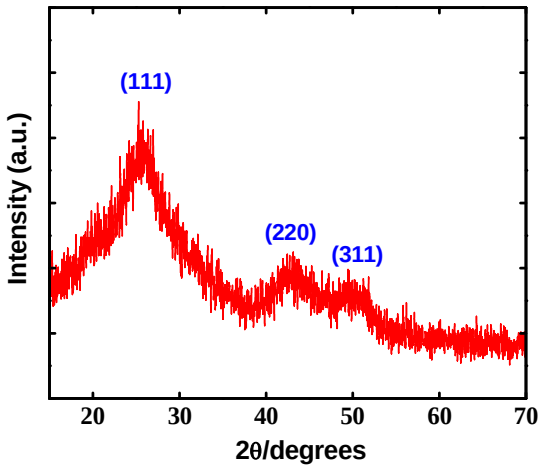

Figure 8.1. *XRD pattern for BSA-CdSe QDs synthesized with molar ratio ([Cd^{2+}]: [Se^{2-}], in mM) of 20:10. [BSA] = 1 mg/ml.*

The diffraction peaks of nanoparticles have been designated to their respective lattice planes i.e. (111), (220), (311). As can be seen, the diffraction peaks show considerable broadening, which indicates towards the nanoscale dimensions of as grown CdSe. However, the peak broadening in the XRD patterns may also arise due to the diffraction uncertainties originating due to reasons such as amorphous nature, small particle size and strain. To explore such possibilities, TEM measurements of as grown CdSe QDs were carried out. It is to be mentioned that the TEM images of the nanoparticles were recorded 24 hours after mixing of precursors. Figure 8.2 shows the TEM images of the QDs synthesized with various molar ratios of precursors. The size of the primary nanoparticles is within 3 nm as can be realised from Figure 8.2a. In fact, the size of the nanoparticles obtained from the UV-Vis absorption studies (discussed later) is found to be between 2 to 3 nm. However, there appear to be some sort of self aggregation occurring

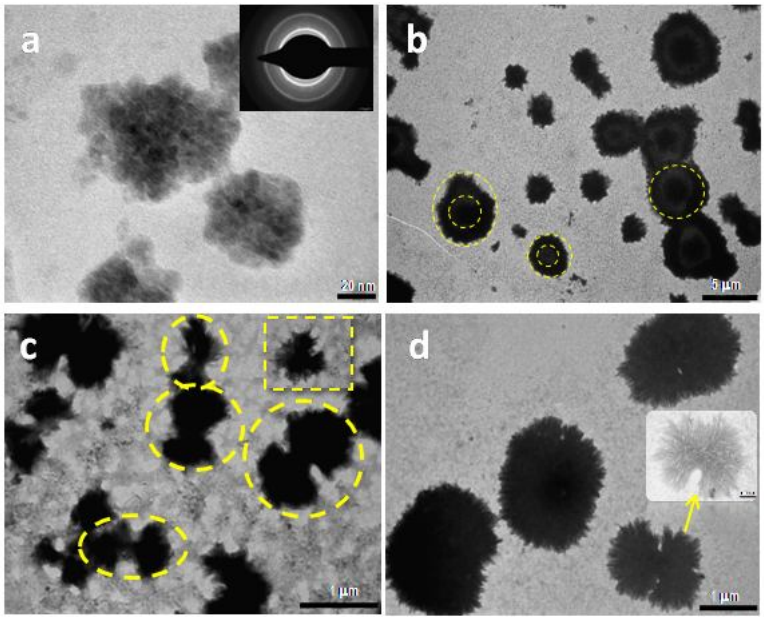

Figure 8.2. *TEM images of BSA-CdSe nanoparticles synthesized with molar ratio ([Cd^{2+}]: [Se^{2-}], in mM) of: (a) 20:10 (Inset: SAED pattern), (b) 20:10, (c) 10:10, (d) 10:20. [BSA] = 1 mg/ml.*

in these primary nanoparticles into a particular morphology, which is evident in the subsequent images of these nanoparticles

Figure 8.2b shows somewhat ring (mono and multi-centric) and core-shell like structures of the nanoparticles synthesized with molar ratio ($[Cd^{2+}]$: $[Se^{2-}]$, in mM) of 20:10. In other words, it seems that a patterned ring like structural formation might have taken place along with homocentric ring like features. Apparently, some nanorods like features are also present at the surface. While, no such specific pattern is noticed involving the molar ratio ($[Cd^{2+}]$: $[Se^{2-}]$, in mM) of 10:10 rather, a mixture of flower and dumbbell like shaped nanoparticles can be seen in Figure 8.2c. Likewise, Figure 8.2d illustrates some spherical sea urchin like shapes (with molar ratio ($[Cd^{2+}]$: $[Se^{2-}]$, in mM) of 10:20) trying to evolve into a dumbbell shaped morphology. From these images, it can be seen that these ensembles are composed of a few to thousands of hierarchically assembled nanoscaled primary unites and eventually organize themselves into a flower shaped or dumbbell like superstructures. Such superstructures are now receiving greater attention owing to their promising superior and more proficient applications ranging from light harvesting to sensing purposes.[398-400] Nevertheless, the formation of such superstructures has been plausibly ascribed to the hierarchical self-assembly of primary nanoparticles directed under the structural influence of BSA.[149] Besides that, the selected area electron diffraction (SAED) pattern shown in the inset of the Figure 8.2a clearly indicates towards the predominantly amorphous nature of as grown CdSe nanoparticles.

Raman spectroscopy is an important characterization tool for II-VI semiconducting nanomaterials with respect to their composition, crystal quality related to

orientation and symmetry and lattice stress/strain effects. To investigate the strain parameters in the CdSe QDs, we have recorded the Raman spectra of as grown CdSe QDs in the host matrix of BSA. Figure 8.3 shows the Room temperature Raman spectra of CdSe QDs synthesized with molar ratio ($[Cd^{2+}]$: $[Se^{2-}]$, in mM) of 20:10. As we can see in Figure 8.3, Raman spectra comprises of fundamental longitudinal optical (LO) phonon peak along with its overtone (2LO) peak at 206.9 cm^{-1} and 411 cm^{-1}, respectively. Furthermore, a shoulder near to 168 cm^{-1} can be noticed, which is attributed to the transverse optical (TO) phonon mode.[401] Moreover, the background in the Raman spectrum reveals the luminescent nature of as grown CdSe QDs (discussed later). The frequency position of the CdSe LO peak (206.9 cm^{-1}) is red shifted with compare to bulk CdSe (210 - 213 cm^{-1}). Earlier studies suggest that crystals with reduced dimensions experiences phonon confinement or tensile stress (strain effect) that leads to red shift in the optical phonon modes with respect to their bulk values.[402,403] However, the red shift

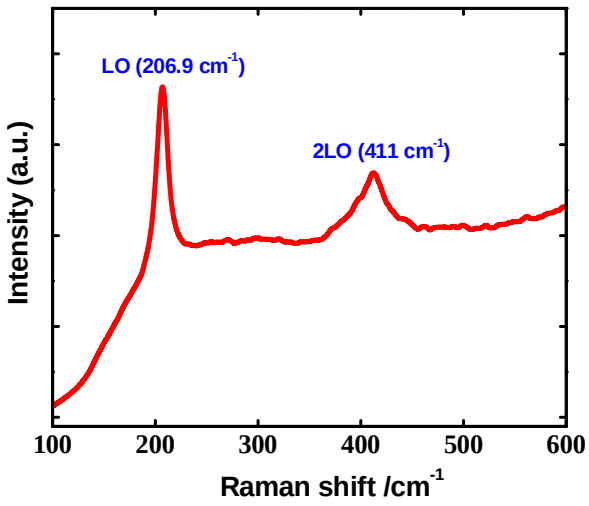

Figure 8.3. *Raman Spectra of BSA-CdSe nanoparticles synthesized with molar ratio ($[Cd^{2+}]$: $[Se^{2-}]$, in mM) of 20:10. [BSA] = 1 mg/ml.*

observed in our case has been mainly attributed due to the phonon confinement effect as the size of the primary nanoparticles was found to be between 2 to 3 nm (from TEM and absorption studies), which is less than the bulk Bohr exciton radius of CdSe (5.6 nm).[404] Mean while, the signatures of tensile stress leading to lattice contraction were also observed from the XRD analysis. The value of the lattice constant, 'a' was found to be 6.14 Å, which was approximately equivalent to that of the standard value of cubic CdSe (6.07 Å).[405] Therefore, the down shift in the LO peak relative to the bulk value appears to be solely due to the phonon confinement effect, while the possibility of any strain can be ruled out.

The surface morphological characterization of as grown nanoparticles is further carried out by using their SEM images, shown in Figure 8.4. Amazingly, the images indicate towards some of the very interesting morphological aspects, which varied with the precursor concentrations. Further, the SEM measurements reveal the close structural resemblance of the nanoparticles as observed in case of TEM images. As can be seen, the images in Figure 8.4a and b are of CdSe nanoparticles synthesized with molar ratio ($[Cd^{2+}]$: $[Se^{2-}]$, in mM) of 20:10. On carefully examining, the rings are a mixture of hexagonal and oval shapes; however, the later one is in majority. For convenience, the structures are marked according to their respective shapes in Figure 8.4b. Apparently, radial thorn-like branches growing outward their surfaces indicates their origin from the 1-D (dimensional) structures such as nanoneedles, nanowires or nanorods. Indeed such 1-D fragmented nanostructures are observed and shown in Figure 8.5. Therefore, it is beyond doubt that the self aggregation/assembly of the initially formed primary

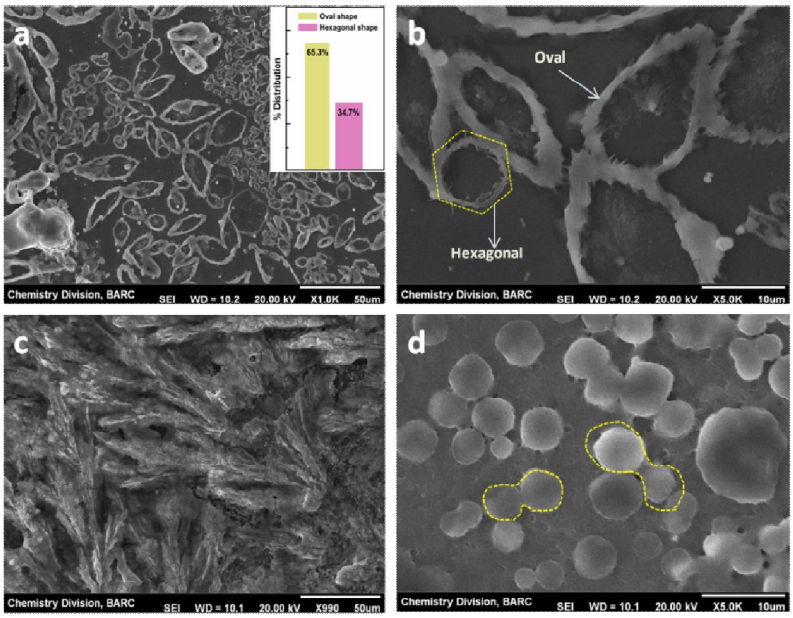

Figure 8.4. *SEM images of BSA-CdSe nanoparticles synthesized with molar ratio ([Cd^{2+}]: [Se^{2-}], in mM) of: (a) & (b) 20:10, (c) 10:10, (d) 10:20. [BSA] = 1 mg/ml. Inset of image (a) shows the % distribution plot of the oval and hexagonal shapes of CdSe.*

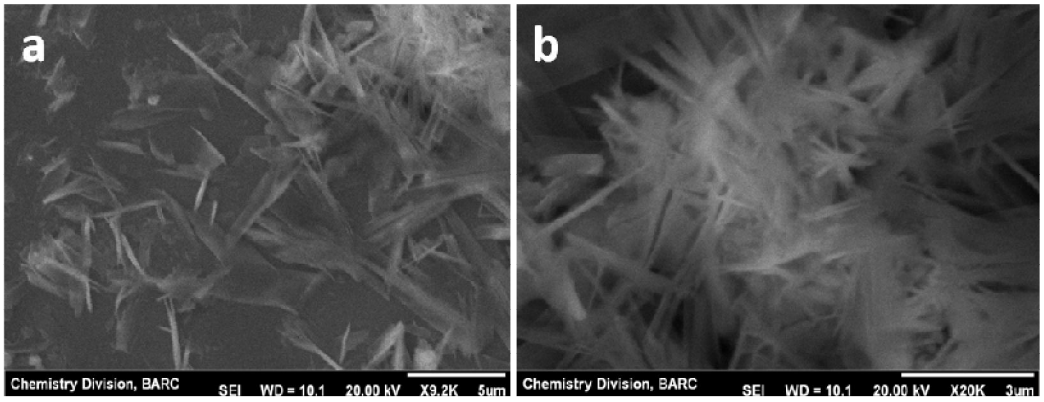

Figure 8.5. *SEM images showing the presence of the 1-D (nanorods) structures of CdSe with molar ratio ([Cd^{2+}]: [Se^{2-}], in mM) of 20:10. [BSA] = 1 mg/ml.*

nanoparticles led to the formation of first small scaled fragments of 1-D nanostructures (with small aspect ratios), which eventually fused together in a non-linear fashion to give

such meso/nanoscopic patterned ring-like morphologies. It is worth mentioning here that the precursor concentration of Cd was higher than that of Se. It is expected that the facets of 1-D nanostructures would be rich with Cd^{2+} cations and thereby, leading to the origin of polarization induced forces. In this context, the polar surfaces generally have facets or exhibit massive surface reconstruction to minimize the total energy. Considering this, it is believed that the as obtained nano-ring structures (hexagonal and oval) are driven under dipolar interactions. Therefore, a closed ring structure would lead to the neutralization of dipole moments, thus having lower electrostatic energy. This is also evidenced from the formation of hexagonal shaped structure, wherein the rotational symmetry is highest among the polygons.

Apart from dipolar interactions, BSA is playing a crucial role as a host matrix by stabilizing the as grown nanoparticles. Essentially, BSA comprises of various functional groups i.e. -OH, -NH, -COOH, which can act as strong binding sites for the precursor ions.[149] In addition to that, the BSA also contains 17 disulfide bonds with one free thiol group present in the cysteine residue. Apparently, BSA having a globular structure consists of hydrogen bonded α-helices and β-sheets.[150,151,390] Therefore, it is most likely that the strong conjugation between these inherent structures of BSA might be directing the 1-D growth of nanoparticles with particular precursor concentrations. In fact, Yang *et al.*[388] has reported the fabrication of silver sulfide nanorods in the host matrix of BSA and explained their formation mechanism on the basis of the strong conjugate bonds between the later and surfaces of the colloidal nanoparticles, wherein the β-sheet part was presumed to play the dominating role in directing the 1-D growth of the particles. Taking

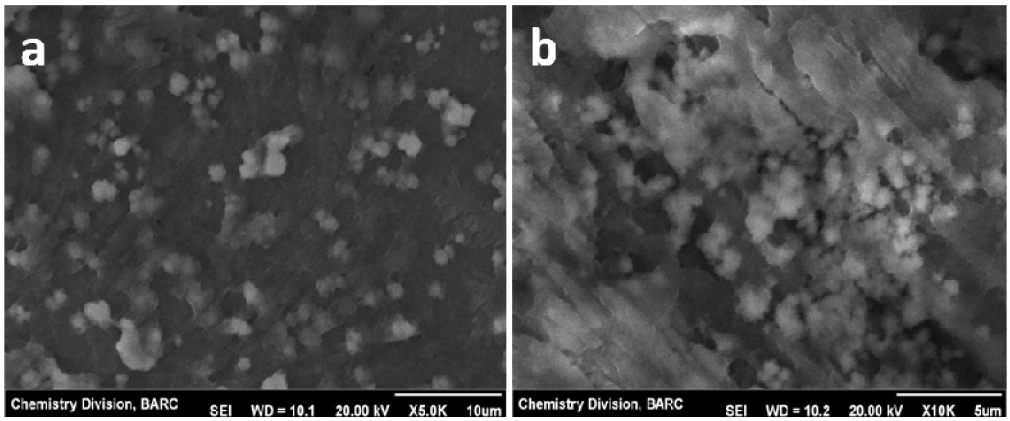

Figure 8.6. *SEM images showing the presence of the spherical globular like nanostructures of CdSe with molar ratio ([Cd^{2+}]: [Se^{2-}], in mM) of 10:10. [BSA] = 1 mg/ml.*

these facts into account, it is most likely that the initially formed 1-D nanostructures most plausibly self assembled and oriented in the specific manner under the influence of certain driving forces (explained earlier) to furnish aforementioned morphologies. Nevertheless, such ring like nanostructures have been reported recently by some of the researchers and their formation mechanism has been explained similarly, on the basis of dipolar interactions together with the symmetry related constraints.[406,407 408]

Furthermore, the molar ratio ([Cd^{2+}]: [Se^{2-}], in mM) of 10:10 led to the formation of a mixture of flower/leaflet and dumbbell like structures as can be observed from the TEM (Figure 8.2c) and the SEM images (Figure 8.4c). Basically, no specific orientation pattern is observed herein however, the aforementioned structures are found to undergo seeded growth mechanism. This is because of the formation of spherical globular like nanostructure, as can be seen in Figure 8.6. Mean while, the CdSe nanoparticles with the molar ratio ([Cd^{2+}]: [Se^{2-}], in mM) of 10:20 are found to grow predominantly in the dumbbell like shape, as can be envisaged from the TEM (Figure 8.2d) and the SEM

images (Figure 8.4d). Although, it can be observed that the nanoparticles are having spherical shapes initially, which appeared to evolve into a dumbbell like shape and eventually merge with each other form a big sphere. Certainly, Ostwald ripening process which is basically the growth of larger particles from those of smaller size is responsible for this morphological evolution. Similar type of shape evolution of citrate capped gold nanoparticles from initial structure into dumbbell like morphologies have been reported by Wu *et al.*[409] and was ascribed due to Ostwald ripening mechanism.

Basically, the above obtained morphologies at different molar ratio of precursors can be explained on the basis of the nucleation and growth rates of the initially formed nuclei. And, which are further decided by the kinetic and thermodynamic aspects prevailing at those moments. For instance, the formation of nanorods (molar ratio ($[Cd^{2+}]$: $[Se^{2-}]$, in mM) of 20:10) eventually underwent segmented growth to give nanoring like structures. While, spherical globular like nanostructure are formed in the initial phase of the reaction, in case of (molar ratio ($[Cd^{2+}]$: $[Se^{2-}]$, in mM) of 10:20. It is to be emphasized here that the color evolution on mixing of precursors took place after ~ 2 hours in case of molar ratio ($[Cd^{2+}]$: $[Se^{2-}]$, in mM) of 20:10. Whereas, the color appearance took only 15-20 minutes (on mixing the precursors) in case of molar ratio ($[Cd^{2+}]$: $[Se^{2-}]$, in mM) of 10:20. The most probable reason for this observation can be explained as follows. Since, it is a well established fact that BSA has an inherent overall negative charge.[410,411] Further, it has been reported[150,151,390] that Cd^{2+} ions form a complex with BSA (Cd^{2+} -BSA). Taking this into account, and the low concentration of

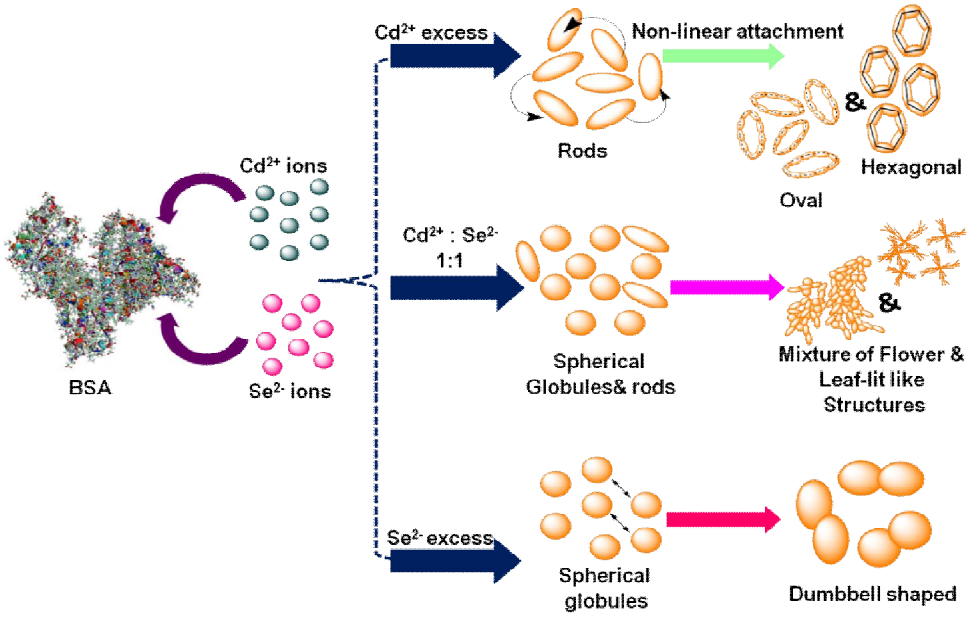

Scheme 8.1. *Diagrammatic representation of the formation of different morphologies of BSA-CdSe nanoparticles synthesized with their respective molar ratio of the precursors. [BSA] = 1 mg/ml.*

Se^{2-} ions in case of molar ratio ([Cd^{2+}]: [Se^{2-}], in mM) of 20:10, it can be realized that the concentration of precursor ions will be less freely available for the reaction to occur. In addition to that, the strong conjugated bonding mechanism (discussed earlier) of BSA is probably directing the growth of initially formed nuclei into rod shaped nanostructures.

In the case of molar ratio ([Cd^{2+}]: [Se^{2-}], in mM) of 10:20, the presence of excess Se^{2-} ions would lead to a much faster reaction with the Cd^{2+} ions to form spherical shaped nanostructures. In this case, the Se^{2-} ions having the similar charge (negative) as that of BSA appears to play an influential role in guiding the as obtained morphology. Similar observations have been reported by Teng *et al.*[412], where the high amount of Se lead to the formation of CdSe nanoparticles *via* the isotropic growth; while lower concentration of Se resulted in the formation of CdSe nanorods by facilitating the growth along c-axis.

All the three cases (at different molar ratios of Cd and Se precursors) leading to the different nanomorphologies (as discussed above) have been represented in Scheme 8.1. From these results and observations, it can be inferred that by simply varying the molar ratios of Cd and Se, diverse shape of CdSe nanocrystals could be synthesized in the host matrix of BSA of course by a facile and green methodology.

8.3.2. Optical absorption and photoluminescence studies

As mentioned earlier, the mixing of the precursor solutions lead to the evolution of color depending on the molar ratios of the Cd and the Se precursors. Figure 8.7 represents the trend in the evolution of color on varying the molar ratio of precursors i.e. $[Cd^{2+}]$: $[Se^{2-}]$ from 10:5 to 10:40, keeping concentration of Cd^{2+} precursor constant. As can be seen from the Figure 8.7, with the increase in the concentration of Se precursor, the color of the sols darkened and transformed from light green to bright red. The corresponding optical absorption spectra of the sols with various molar ratios of Cd^{2+} and Se^{2-} at an optimized BSA concentration of 1 mg/ml have been shown in Figure 8.8A. A clear

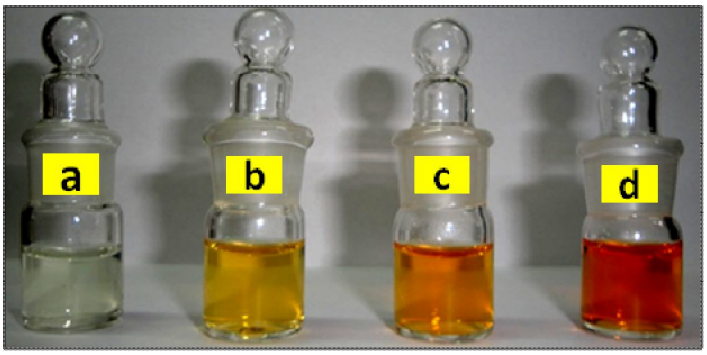

Figure 8.7. *Camera ready pictures of the BSA-CdSe nanoparticles synthesized with molar ratio ($[Cd^{2+}]$: $[Se^{2-}]$, in mM) of: (a) 10:5 (light green), (b) 10:10 (yellowish orange), (c) 10:20 (orange), (d) 10:40 (bright red). [BSA] = 1 mg/ml.*

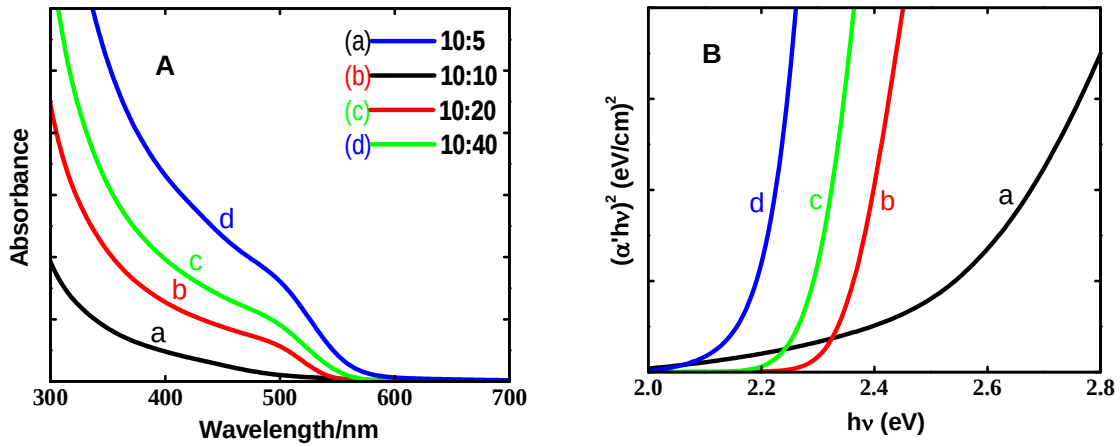

Figure 8.8. *(A) Optical absorption spectra of BSA-CdSe QDs synthesized with molar ratio ([Cd^{2+}]: [Se^{2-}], in mM) of:* ***(a)*** *10:5;* ***(b)*** *10:10;* ***(c)*** *10:20;* ***(d)*** *10:40. (B) Tauc plot of $(\alpha' h\nu)^2$ vs. $h\nu$ for the determination of energy band gap, E_g. [BSA] = 1 mg/ml.*

excitonic peak can be observed at ~ 420 nm for QDs with molar ratio ([Cd^{2+}]: [Se^{2-}], in mM) of 10:5, which subsequently shifted to red side with the increase in the concentration of Se. This clearly signifies the increase in the size of QDs. The sizes of the CdSe QDs were estimated from the absorption spectra by using modified Brus equation(8.2) and are listed in Table 8.1:

$$E_g = E_g\,(0) + \alpha/d^2 \qquad (8.2)$$

where, α = 3.7 eV nm^2, $E_g\,(0)$ = 1.75 eV, d = particle size (nm) and E_g = band gap value in eV. The band gap (E_g) values were determined from the Tauc plots of $(\alpha' h\nu)^2$ *vs* $h\nu$, as this is a direct band gap semiconductor (Figure 8.8B). The symbol 'α'' represents the absorption coefficient multiplied with the concentration of the CdSe nanoparticles, which is obtained from the relation (2.303A/*l*), where 'A' is the absorbance and '*l*' is the optical path length of the cell (10 mm). The term '$h\nu$' represents the photon energy. The

Table 8.1. ***The band gap values, E_g (eV), size (nm) and the PL yields of as synthesized BSA-CdSe QDs with their respective molar ratios of the precursors.***

Cd (mM) : Se(mM)	E_g (eV)	Size (nm)	PL $_{max.}$ (nm)	Quantum Efficiency (%)
10:5	2.52	2.19	527	1.08
10:10	2.36	2.46	555	1.00
10:20	2.27	2.66	585	0.38
10:40	2.20	2.86	610	0.17
2.5:10	2.52	2.19	595	0.17
5:10	2.44	2.31	570	0.44
10:10	2.36	2.46	555	1.00
20:10	2.39	2.40	540	2.00

Estimated values of the particle sizes are found to be between 2 to 3 nm, which are less than the exciton Bohr radius of CdSe (5.6 nm). An increase in the particle size has been observed with an overall increase in the concentrations of the precursors irrespective of their ratios.

In concurrence with the optical absorption spectral results, the room temperature PL spectra of as grown CdSe QDs shows a consistent red shift in the peak positions with increase in the Se concentration, while maintaining the other one ([Cd precursor]) constant (shown in Figure 8.9A). This observation further ascertains the increase in the size of QDs with the already discussed trend in the precursor concentrations.

Interestingly, the PL spectra appear to be a convolution of both intrinsic (band edge/gap, BGE) and surface state (trap state, TSE) emissions. However, the contribution of the later seems to be dominating with the increase in the Se concentration.

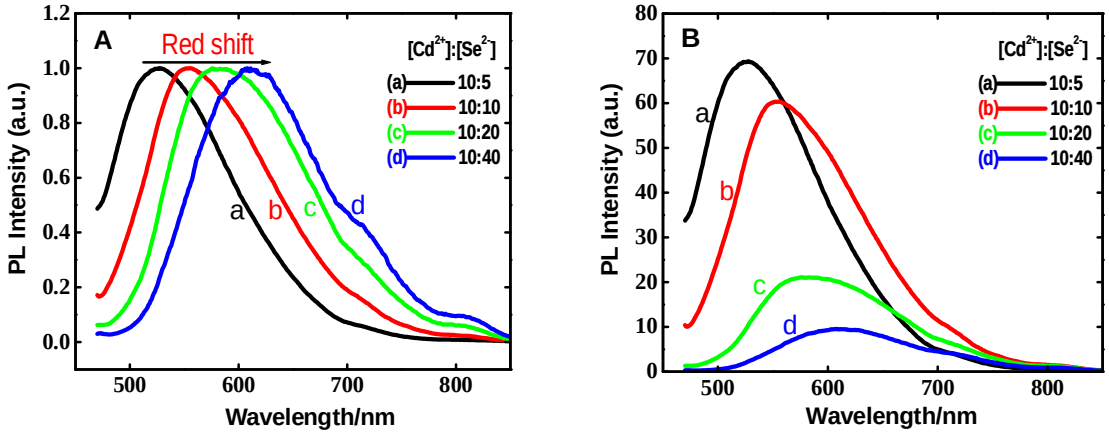

Figure 8.9. *Normalized room temperature PL spectra of BSA-CdSe QDs synthesized with molar ratio ([Cd^{2+}]: [Se^{2-}], in mM) of:* ***(a)*** *10:5;* ***(b)*** *10:10;* ***(c)*** *10:20;* ***(d)*** *10:40. (B) Corresponding room temperature PL spectra of BSA-CdSe QDs with their respective molar ratios (in mM).[BSA] = 1 mg/ml.*

Another noteworthy aspect is the strong PL dependence (exhibited by these QDs) on the concentration of the precursors and hence their luminescence could be conveniently tuned across the visible spectrum by varying molar ratios of the precursors. Indeed, a red-shift of about 100 nm in the PL peak position is observed when the molar ratio of the precursors ([Cd^{2+}]: [Se^{2-}], in mM) is varied from 10:5 to 10:40. Apparently, the broadening of the PL spectra of QDs with the increase in the Se concentration is a clear evidence of the substantial enhancement in the Se originated unsatisfied valencies (dangling bonds). This eventually resulted into the emergence of large number of trap/defects states on the surface of QDs. Obviously; it would further encourage the non-radiative recombination of the charge carriers, which can be seen from the decline in the trend of their quantum yields with the increase in the Se concentration relative to that of Cd (shown in Table 8.1).

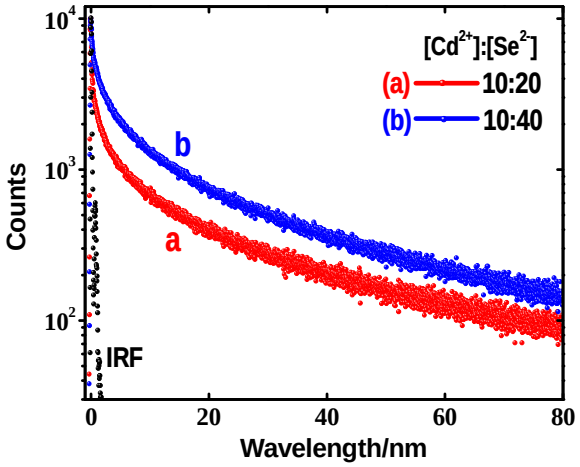

Figure 8.10. *Room temperature time resolved PL decay curve ($\lambda_{exc.}$ = 450 nm) of BSA-CdSe QDs with molar ratio ([Cd^{2+}]: [Se^{2-}], in mM) of:* ***(a)*** *10:20* ***(b)*** *10:40.[BSA] = 1 mg/ml.*

Moreover, the PL decay measurements also corroborate well with the trends and thereby substantiate the aforesaid statement. Figure 8.10 shows the time resolved PL decay trace of as grown QDs illustrating the influence of Se originated trap/defect states on the relaxation dynamics of charge carriers. In general, the presence of trap states inhibits the direct recombination of the charge carriers leading to longer life times for the excitons.[413] Taking cognizance of this and from the as observed PL decay trend (Figure 8.10), it can be inferred that the amount of trap states increases with the Se concentration. The time constant values along with their relative amplitudes (in %) and the average life time values at the respective molar ratios of the precursor concentrations has been provided in Table 8.2. The corresponding χ^2 values are also mentioned together in each case. It is further reflected in Table 8.2, which shows the rise in the average life time values with that of Se precursor concentration values i.e. from molar ratios ([Cd^{2+}]: [Se^{2-}], in mM) of 10 : 20 to 10 : 40.

Table 8.2: ***Emission lifetime values of the BSA-CdSe QDs; $\lambda_{exc.}$ = 450 nm***

[Cd Precursor] in mM	[Se Precursor] in mM	τ_1 (a_1), ns	τ_2 (a_2), ns	τ_3 (a_3), ns	Average lifetime (<τ>), ns	χ^2
10	20	2.7 (22 %)	21.0 (71 %)	0.018(7%)	15.5	1.4
10	40	4.0 (25%)	23.5(70 %)	0.045(6%)	17.4	1.3
5	10	4.0(16 %)	29.0(82%)	0.303(2%)	24.4	1.2
20	10	3.1(6%)	38.0(89%)	0.100(5%)	34.4	1.0

Furthermore, the PL decay curves of as synthesized CdSe QDs exhibited multi-exponential (tri-exponential) behavior, which were analyzed and fitted using equation (8.3):

$$I(t) = a_1 e^{-t/\tau_1} + a_2 e^{-t/\tau_2} + a_3 e^{-t/\tau_3} \quad (8.3)$$

Where, I (t) is the time-dependent emission intensity, 'a' is the amplitude, and τ is the lifetime. The average PL lifetime (<τ>) values were deduced using equation (8.4):

$$< \tau > = \frac{\tau_1 a_1 + \tau_2 a_2 + \tau_3 a_3}{a_1 + a_2 + a_3} \quad (8.4)$$

Such multi-exponential behavior of the CdSe nanoparticles is widely known and has been reported by various researchers earlier.[414-416] Although, most of these reports generally attribute such behavior to the diverse recombination pathways owing to the varying degree of size, shape, surface defects/energy traps between the individual nanocrystals. Still, the unambiguous origin and the explanation for this multi-exponential emission is currently a subject of debate. Nevertheless, the trend in the time constant values and their contributions seem to have a sort of correlation with the nature of the respective PL spectra in terms of peak positions and its width. This has been explained as follows.

It is a well known phenomenon that the photo-excitation of CdSe QDs lead to the promotion of an electron to the conduction band, and then the excited electron relaxes quickly to the bottom of the conduction band. The radiative relaxation of these electrons to the ground state gives rise to the BGE and contributes to the fastest decay of lifetime. Considering this and taking the case of molar ratio ($[Cd^{2+}]$: $[Se^{2-}]$, in mM) of 10:20, the time constant, τ_3 is the fastest component and thus attributed to the intrinsic recombination (band gap) of charge carriers. Further, the time constants, τ_1 and τ_2 are probably originated from the surface states/trap states. It signifies that the trap states might comprise both the shallow as well as the deep states. In fact, it has been reported that the shallow trap states exhibit lower lifetime than the deep trap states, depending on the chemical nature and crystal structure of QDs.[417,418] Therefore, the component, τ_1 having lower lifetime of 2.7 ns can be assigned to recombination time involving the shallow trap states, while the component, τ_2 with higher lifetime of 21.0 ns has been attributed to be originated from the deep trap states. On the similar note, the lifetime components obtained in case of molar ratio ($[Cd^{2+}]$: $[Se^{2-}]$, in mM) of 10:40 can also be rationalized in terms of their modes of origin. Now, it is to be noted that the sum contribution of the higher lifetimes constants (τ_1 and τ_2) rises, while that of fastest time constant (τ_3) declines with increase in the Se precursor concentration values i.e. from molar ratios ($[Cd^{2+}]$: $[Se^{2-}]$, in mM) of 10:20 to 10:40.

In another set of experiment, the concentration of selenium precursor is fixed at 10 mM, while the concentration of cadmium precursor is varied from 2.5 to 20 mM. The corresponding optical absorption spectra of as prepared sols with various molar ratios of

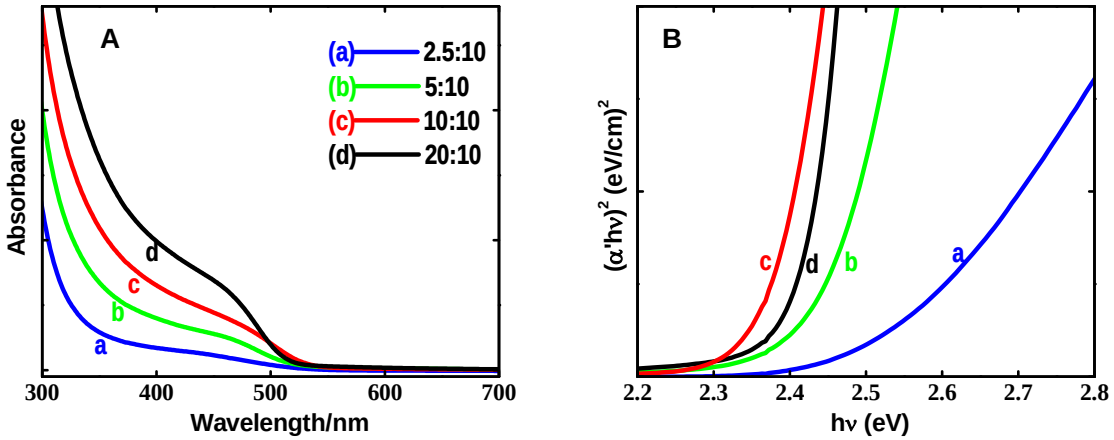

Figure 8.11. *(A) Optical absorption spectra of BSA-CdSe QDs synthesized with molar ratio ([Cd^{2+}]: [Se^{2-}], in mM) of:* ***(a)*** *2:5:10;* ***(b)*** *5:10;* ***(c)*** *10:10;* ***(d)*** *20:10. (B) Tauc plot of $(\alpha' h\nu)^2$ vs. $h\nu$ for the determination of energy band gap, E_g. [BSA] = 1 mg/ml.*

precursors ([Cd^{2+}]: [Se^{2-}]) have been shown in Figure 8.11. In this case also, there is an increase in the absorbance value with the increase in the cadmium precursor concentration along with a slight red-shift in the excitonic peak position. The concentration of BSA was maintained same as in case of first set of experiment i.e. 1 mg/ml. The size of the QDs is found to have predominantly increasing trend with the precursor concentration of Cd (Table 8.1). However, an interesting aspect in this case is the blue shift observed in the normalized room temperature PL spectra (Figure 8.12A) with the increase in Cd precursor concentration i.e. from molar ratios ([Cd^{2+}]: [Se^{2-}], in mM) of 2.5 : 10 to 20 : 10, unlike the red shift obtained in the earlier case.

It is to be mentioned here that the similar type of blue shift was observed earlier by Wuister *et al.*[419] in case of CdTe nanocrystals and the possible explanation was ascribed to the strength of the bond between the thiol (hexanthiol) groups and the Cd

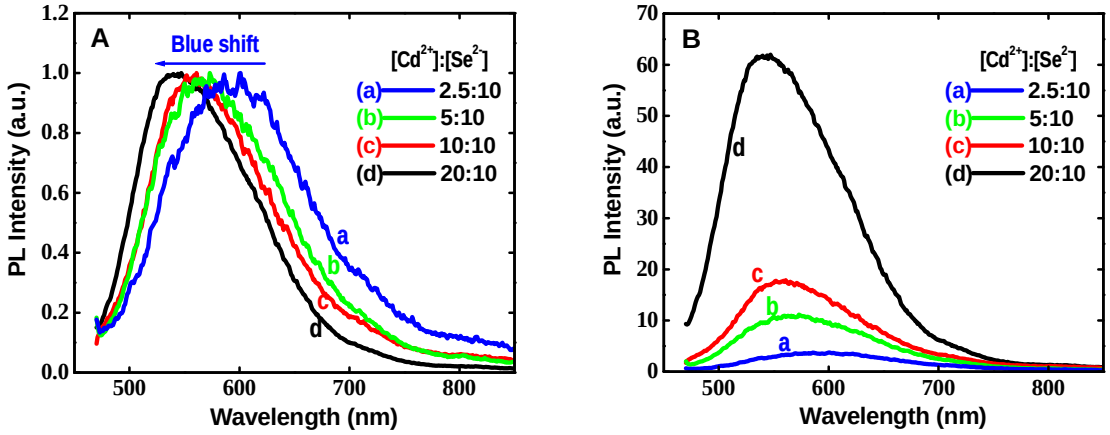

Figure 8.12. *Normalized room temperature PL spectra of BSA-CdSe QDs synthesized with molar ratio ([Cd^{2+}]: [Se^{2-}], in mM) of:* ***(a)*** *2.5:10;* ***(b)*** *5:10;* ***(c)*** *10:10;* ***(d)*** *20:10. Inset: Corresponding room temperature PL spectra of BSA-CdSe QDs with their respective molar ratios (in mM).[BSA] = 1 mg/ml*

atoms at the CdTe nanocrystal surface, which induces a redistribution of electron density and that eventually led to an increase in confinement of energy. Considering that, the bonding of Cd atoms and thiol groups is possible in the present case due to the presence of amino acid residues (such as cysteine containing thiol groups) in BSA and it would be further supplemented by the increase in the precursor concentration of Cd, while maintaining that of Se at constant level. This might be the reason for the blue shift in the absorption spectra as well as the comparatively high PL quantum yield exhibited by these QDs owing to the efficient passivation of their surface. Moreover, the blue shift in the PL peak positions is also accompanied by the increase in the contribution of BGE. It further signifies the drastic reduction in the number of trap/defect states on the surface of as grown CdSe QDs. This statement is further supported by the fact that the quantum yield also gets enhanced consecutively with the aforementioned trend of Cd precursor concentration (Table 8.1). As stated, can also be envisaged from the Figure 8.12B,

wherein the PL intensity is highest for the QDs synthesized with precursor molar ratio ($[Cd^{2+}]$: $[Se^{2-}]$, in mM) of 20 : 10 . Mean while, the PL decay measurements were performed taking into account of the enhancement in the quantum efficiencies of the QDs with the Cd precursor concentration (in proportion to that of Se). Here also, the PL decay traces were found to be multi-exponential in nature. The time constant values along with their respective contributions have been provided in Table 8.2.

As can be seen from Table 8.2 , the excitonic recombination lifetime rises from 24.4 ns to 34.4 ns, with the increase in the Cd precursor concentration i.e. on varying the molar ratio ($[Cd^{2+}]$: $[Se^{2-}]$, in mM) from 5:10 to 20:10. Subsequently, the contribution of the fastest time constant, τ_3 (related to BGE) increased and those of the sum contributions of time constants, $\tau_1 + \tau_2$ (related to TSE) decreased with the concentration of Cd relative to that of Se. Apart from this, there seems to be strong correlation between the lifetime and the PL quantum yields of the QDs (Table 8.1). In close agreement with these results, similar observations have been reported by various researchers[420-422], wherein the increase of the PL quantum efficiency of the QDs under photoactivation was found to be associated with an increase in the average PL lifetimes.

The achieved optical tunability (in terms of PL intensity as well as the emission peak position i.e. λ_{max}) of as grown CdSe QDs with the molar ratio of the precursors can be observed from Figure 8.13. From the steady state and the time resolved PL spectral measurements, it can be inferred that the contributions from the band gap, shallow trap and deep trap state emissions vary systematically with the molar ratio of the Cd and Se precursors. Further, the PL spectra of the QDs (shown in Figure 8.9 & 8.12) were fitted

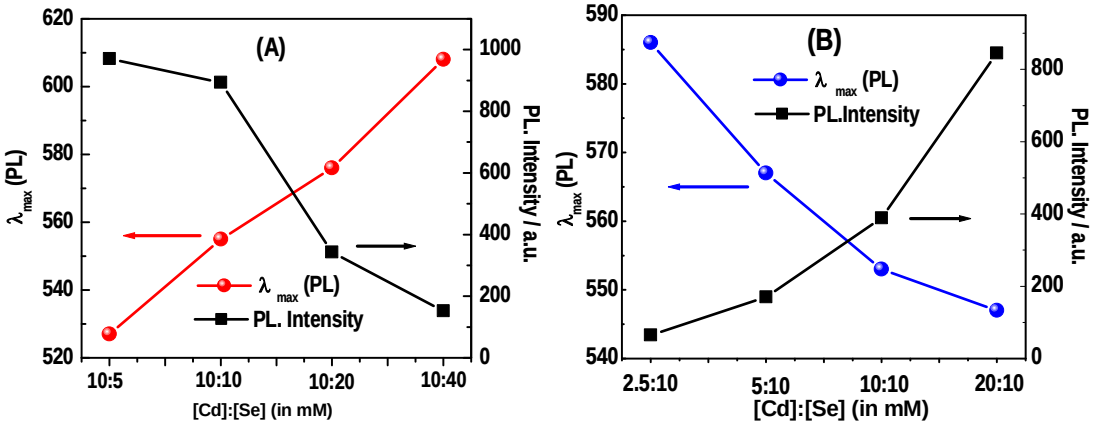

Figure 8.13. *Plots showing the trend in the variation of λ_{max} (PL) and PL intensity at different molar ratio of precursors, keeping concentration of Cd^{2+} (A) and Se^{2-} (B) constant, respectively.*

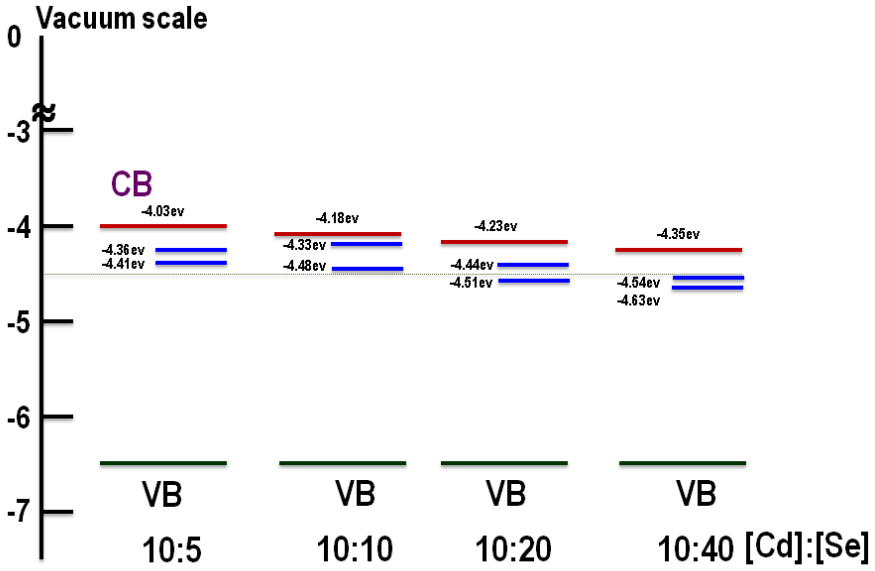

Figure 8.14. *Energy level diagram showing the band gap levels and the trap state levels in four different CdSe QDs formed in four different conditions with [Cd]:[Se] ratios (in mM) of 10:5,10:10, 10:20 and 10:40.*

with multiple peak fitting and three different peak positions are observed in all these cases. Assuming the valence band edge of the CdSe QDs to be at 6.5 eV with respect to the vacuum level, 0 eV, the conduction levels and the trap state levels are constructed

from these fitted peak values as shown in Figure 8.14. From this figure, a clear lowering in the conduction band as well as the trap states are evident with the increase in the Se composition, further supporting the results from PL decay measurements.

9.3.3. Proposed mechanism

On the basis of the discussed morphological and spectral studies, a mechanism has been proposed for the formation of CdSe QDs in the host matrix of BSA. It can be observed from Figure 8.15 that the pure BSA exhibit an intrinsic absorption at 280 nm due to the $\pi-\pi^*$ transition of the tyrosine, tryptophan, and phenyl alanine amino acid residues.[203] Consecutively, addition of $CdSO_4$ to the BSA solution lead to the disappearance of the characteristic peak of the later, thus indicating a sort of complex formation i.e. BSA-Cd^{2+}. This observation corroborate well with that reported by Haung *et al.*[423], wherein the analogous complex formation (BSA-Cu^{2+}) was found to take place accompanied by the similar spectral features. Further, it is a well established fact that BSA has multiple binding sites for metal ions.[424] Therefore, chelation of several Cd^{2+} ions with BSA may cause slight enhancement in the absorbance without displaying any shift. However, upon addition of Se precursor (Na_2SeSO_3) to the BSA-Cd^{2+} complex solution, there was an appearance of color (depending on the molar ratio of precursors), which indicates the formation of CdSe nanoparticles (Inset of Figure 8.15).

The absorption spectrum of BSA-CdSe nanoparticles clearly showed the excitonic peak in the 450-500 nm region indicating that the Se^{2-} ions released from Na_2SeSO_3 reacted with Cd^{2+}, thereby forming CdSe nanoparticles. The excitonic absorption peak gets saturated after about 24 hours (spectra not shown), which signifies the complete

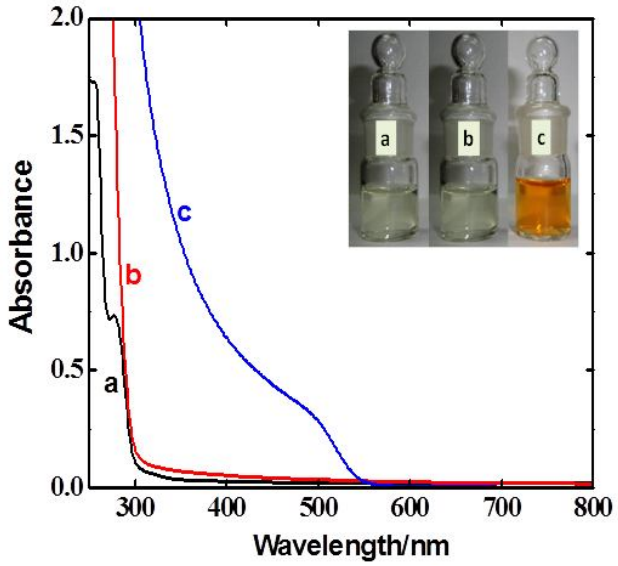

Figure 8.15. *Optical absorption spectra of (a) BSA, (b) BSA-Cd^{2+} and (c) BSA-CdSe. Inset: Camera-ready pictures of (a) BSA, (b) BSA-Cd^{2+} and (c) BSA-CdSe solutions.*

formation of CdSe nanoparticles. Since, no external reducing agent was employed in the present synthetic protocol; this confers the dual role of BSA as a reducing agent as well as a stabilizing agent.

The zeta potential of the as prepared CdSe nanoparticles (molar ratio ($[Cd^{2+}]$: $[Se^{2-}]$, in mM of 10:10) was measured to be -21.25 mV, which indicates the contribution of both the electrostatic and the steric repulsions being responsible for the stabilization of these nanoparticles, thus indicating the role of BSA as an efficient stabilizing agent. This can be further substantiated by the presence of large number of amino acid residues having side groups, including amine, carboxyl, sulfhydryl, and hydroxyl moieties and the ionization of the phenolic groups of tyrosine residues in the slight alkaline conditions.[425,426]

To clarify the conjugate bonding between the CdSe and functional groups of BSA, we recorded the FT-IR spectra of pure BSA and BSA/CdSe, as shown in Figure 8.16. The FT-IR peaks of pure BSA at ~ 3300, 3034, 1645, and 1514 cm^{-1} are assigned to the stretching vibrations of –OH, amide A′ (–NH stretching vibration), amide I (C=O stretching vibrations), and amide II (the coupling of the bending vibration of –NH and the stretching vibration of C–N bonds), respectively.[150,151,390] Comparing the IR spectra of BSA-CdSe QDs with that of pure BSA, the peak shift (~ 10 cm^{-1}) in the of –OH group is insignificant in comparison to the higher wave number shift of about 38 cm^{-1} for amide A′ 3072 cm^{-1}) peaks in the BSA-CdSe imply that the secondary structure of BSA in the coated layer on the surface of CdSe remains unaffected by the formation of CdSe QDs. In addition to that, possibility of thiolate linkages with the QDs surface cannot be ruled out, as thiol group containing amino acids are known for their strong chelating tendencies.[427]However, we have not observed any signatures of thiol related linkages in the present case. Nevertheless, the strong resemblance of the FT-IR spectra of pure BSA

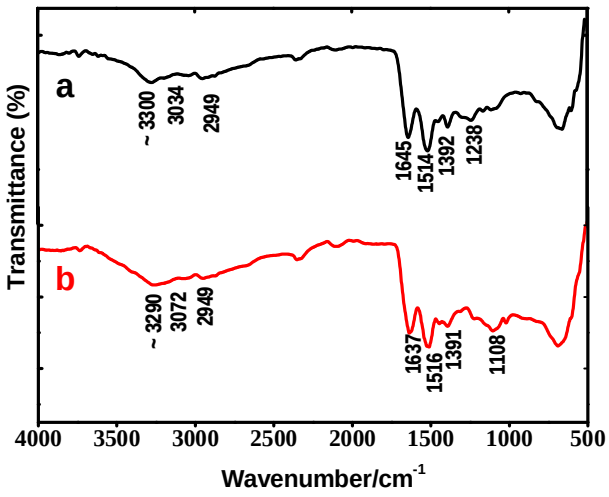

Figure 8.16. *FT-IR spectra of (a) pure BSA and (b) BSA-CdSe QDs.*

with the BSA-CdSe QDs categorically indicates towards the significant coating of the former on the surface of the QDs.

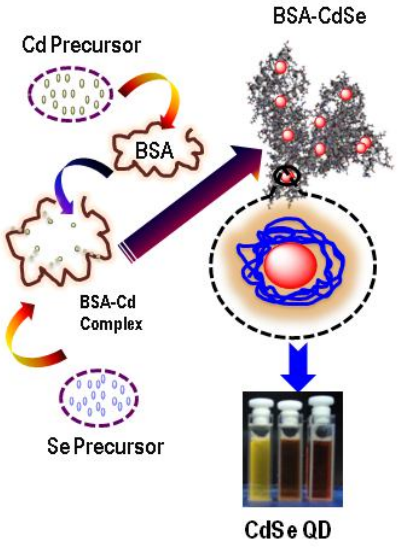

Scheme 8.2. *Proposed mechanism of formation of CdSe QDs in the host matrix of BSA*

It has already been mentioned that the pH of solution has found to be slight alkaline in nature (i.e. in the range of 7.0-8.0). Consequently, the release of Se^{2-} ions from the Se precursor (Na_2SeSO_3) is quite probable in such conditions.[428] Further, it may be possible that the amino acid residues of BSA such as tyrosine, can reduce Na_2SeSO_3 leading to the release of Se^{2-} ions. The probable reactions taking place in the present BSA assisted synthetic route, leading to the formation of CdSe nanoparticles, are summarized as follows:

$$Na_2SO_3 + Se \longrightarrow Na_2SeSO_3 \quad (8.5)$$

$$BSA + Cd^{2+} \longrightarrow BSA\text{-}Cd^{2+} \quad (8.6)$$

$$SeSO_3^{2-} + BSA \longrightarrow Se^{2-} \quad (8.7)$$

$$BSA\text{-}Cd^{2+} + Se^{2-} \longrightarrow BSA\text{-}CdSe \quad (8.8)$$

Therefore, it can be said that the BSA play a vital role in controlling the formation of CdSe QDs as well as providing them suitable microheterogeneous environments which act like capping agents.

8.4. Conclusions

In summary, this chapter demonstrates bovine serum albumin (BSA) assisted green chemical synthesis of CdSe QDs in aqueous solutions. The synthesized QDs are found to be fairly photoluminescent at room temperature in conjunction with quite good colloidal stability. BSA is found to play a dual role of a reducing agent as well as a stabilizing agent. The PL peak positions and the intensities are considerably dependent on the stoichiometric compositions of the precursors, thereby optical tuning covering most of the visible region is conveniently achieved. Apparently, the energy level structure is found to be considerably influenced by the variation in the molar ratio of the precursors as explained through the charge carrier relaxation dynamics involving the band edge and the trap states. Besides, the impact of the alteration in the stoichiometric compositions of the precursors is observed from the different morphologies (size as well as shape) of the CdSe nanoparticles, as evidenced from the electron based microscopic techniques. It is found that the fragments of initially formed nanostructures self-assembled to eventually give superstructures such as nanorings, nanoflowers and dumbbell like shaped nanostructures, depending on the molar ratio of the precursors. The probable mechanism for the as mentioned nanomorphologies has been proposed taking into account of the structural heterogeneity of the host matrix of the protein i.e. BSA. On the whole, the

present methodology of protein assisted synthesis of nanomaterials in water as a solvent medium aligns with the increasing emphasis on the topic of green chemistry and may provide some unique and interesting aspects to control and fine tune the morphology *vis-à-vis*, the optical properties of nanomaterials.

References

(1) Ball, P. *Chem. Rev.* **2008**, 108, 74.

(2) Ball, P. *ChemPhysChem* **2008**, 9, 2677.

(3) Chaplin, M. F. *http: //www.lsbu .ac.uk/water/.* **2007**.

(4) Chen, B.; I Ivanov; in, M. L K.; Parrinello, M. *Phys. Rev. Lett.* **2003**, 91, 215503.

(5) Cheung, M. S.; Garcia, A. E.; Onuchic, J. N. *Proc. Natl Acad. Sci. USA* **2002**, 99, 685.

(6) Papoian, G. A.; Ulander, J.; Eastwood, M. P.; Luthey-Schulten, Z.; Wolynes, P. G. *Proc. Natl Acad. Sci. USA* **2004**, 101, 3352.

(7) Zong, C.; Papoian, G. A.; Ulander, J.; Wolynes, P. G. *J. Am. Chem.Soc.* **2006**, 128, 5168.

(8) Levy, Y.; Onuchic., J. N. *Proc. Natl Acad. Sci. USA* **2004**, 101, 3325.

(9) Makarov, V.; Pettitt, B. M.; Feig, M. *Acc. Chem. Res.* **2002**, 35, 376.

(10) Ling, G. N. *Ann. N.Y. Acad. Sci.* **1965**, 125, 401.

(11) Hermann, T.; Patel, D. J. *J. Mo.l Biol.* **1999**, 294, 829.

(12) McConnell, K. J.; Beveridge, D. L. *J. Mol. Biol*. **2000**, 304, 803.

(13) Voet, D.; voet, J. G. *Biochemistry*; Wiley, New York, **1990**.

(14) McPhalen, C. A.; James, M. N. G. *Biochemistry* **1988**, 27, 6582.

(15) Clarke, C.; Woods, R. J.; Gluska, J.; Cooper, A.; Nutley, M. A.; Boons, G. J. *J. Am. Chem. Soc.* **2001**, 123, 12238.

(16) Tame, J. R.; Sleigh, S. H.; Wilkinson, A. J.; Ladbury, E. *Nat. Struct. Biol.* **1996**, 3, 998.

(17) Tezcan, F. A.; Crane, B. R.; Winkler, J. R.; Gray, H. B. *Proc. Natl.Acad. Sci. USA* **2001**, 98, 5002.

(18) Lin, J.; Balabin, I. A.; Beratan, D. N. *Science* **2005**, 310, 1311.

(19) Shui, X.; McFail-Isom, L.; Hu, G. G.; Williams, L. D. *Biochemistry* **1998**, 37, 8541.

(20) Levine, Y. K.; Wilkins, M. H. *Nat. New Biol.* **1971**, 230, 69.

(21) Zhang, Y.; Cremer, P. S. *Annu. Rev. Phys. Chem.***2010**, 61, 63.

(22) Marcus, Y. *Chem. Rev.* **2009**, 109, 1346.

(23) Bockris, J. O. M.; Reddy, A. K. N. *Modern Electrochemistry 2A: Fundamentals of Electronics*; 2 ed.; Plenum, New York, **2001**.

(24) Hofmeister, F. *Arch. Exp. Pathol. Pharmacol.* **1888**, 24, 247.

(25) Kunz, W.; Lo Nostro, P.; Ninham, B. W. *Curr. Opin. Colloid Interface Sci.* **2004**, 9, 1.

(26) Parsegian, V. A. *Nature* **1995**, 378, 335.

(27) Frank, H. S.; Wen, W.-Y. *Discussions of the Faraday Society* **1957**, 24, 133.

(28) Franks, F. *Water*; Royal Society of Chemistry: London, **1983**.

(29) Samoilov, O. Y. *Discussions of the Faraday Society* **1957**, 24, 141.

(30) Collins, K. D. *Biophys. J.***1997**, 72, 65.

(31) Washabaugh, M. W.; Collins, K. D. *J. Biol. Chem.* **1986**, 261, 12477.

(32) Cox, W. M.; Wolfenden, J. H. *Proc. R. Soc. London, A* **1934**, 145, 475.

(33) Collins, K. D.; Washabaugh, M. W. *Q. ReV. Biophys.* **1985**, 18, 323.

(34) Cox, W. M.; Wolfenden, J. H. *Proc. R. Soc. London, A* **1934**, 145, 475.

(35) Collins, K. D. *Biophys. Chem.* **2012**, 167, 43.

(36) Hribar, B.; Southall, N. T.; Vlachy, V.; Dill, K. A. *J. Am. Chem. Soc*. **2002**, 124, 12302.

(37) Chong, S.-H.; Hirata, F. *J. Phys. Chem. B* **1997**, 101, 3209.

(38) Heugen, U.; Schwaab, G.; Brundermann, E.; Heyden, M.; Yu, X.; Leitner, D. M.; Havenith, M. *Proc. Natl.Acad. Sci. USA* **2006**, 103, 12301.

(39) Mancinelli, R.; Botti, A.; Bruni, F.; Ricci, M. A.; Soper, A. K. *J. Phys. Chem. B* **2007**, 111, 13570.

(40) Mancinelli, R.; Botti, A.; Bruni, F.; Ricci, M. A.; Soper, A. K. *Phys. Chem. Chem. Phys.* **2007**, 9, 2959.

(41) Soper, A. K.; Weckstrom, K. *Biophys. Chem.* **2006**, 124, 180.

(42) Leberman, R.; Soper, A. K. *Nature* **1995**, 378, 364.

(43) Smith, J. D.; Saykally, R. J.; Geissler, P. L. *J. Am. Chem. Soc.* **2007**, 129, 13847.

(44) Winther, L. R.; Qvist, J.; Halle, B. *J. Phys. Chem. B* **2012**, 116, 9196.

(45) Halle, B. *J. Phys. Chem. B* **2014**, 118, 10806.

(46) Helm, L.; Merbach, A. E. *Coord. Chem. Rev.* **1999**, 187, 151.

(47) Kropman, M. F.; Bakker, H. J. *Science* **2001**, 291, 2118.

(48) Kropman, M. F.; Bakker, H. J. *J. Chem. Phys.* **2001**, 115, 8942.

(49) Ge, L.; Bernasconi, L.; Hunt, P. *Phys. Chem. Chem. Phys.* **2013**, 15, 13169.

(50) Kropman, M. F.; Bakker, H. J. *Chem. Phys. Lett.* **2003**, 370, 741.

(51) Park, S.; Fayer, M. D. *Proc. Natl.Acad. Sci. USA* **2007**, 104, 16731.

(52) Fayer, M. D.; Moilanen, D. E.; Wong, D.; Rosenfeld, D. E.; Fenn, E. E.; Park, S. *Acc. Chem. Res.* **2009**, 42, 1210.

(53) Ansell, S.; Barnes, A. C.; Mason, P. E.; Neilson, G. W.; Ramos, S. *Biophys. Chem.***2006**, 124, 171.

(54) Dixit, S.; Crain, J.; Poon, W. C. K.; Finney, J. L.; Soper, A. K. *Nature* **2002**, 416, 829.

(55) Mason, P. E.; Cruickshank, J. M.; Neilson, G. W.; Buchanan, P. *Phys. Chem. Chem. Phys.* **2003**, 5, 4686.

(56) Waluyo, I.; Huang, C.; Nordlund, D.; Bergmann, U.; Weiss, T. M.; Pettersson, L. G. M.; Nilsson, A. *J. Chem. Phys.* **2011**, 134, 064513.

(57) Laage, D.; Hynes, J. T. *Chem. Phys. Lett.***2006**, 433, 80.

(58) Laage, D.; Hynes, J. T. *Proc. Natl.Acad. Sci. USA* **2007**, 104, 11167.

(59) Ishiyama, T.; Morita, A. *Chem. Phys. Lett.* **2006**, 431, 78.

(60) Berkowitz, M. L.; Bostick, D. L.; Pandit, S. *Chem. Rev.* **2006**, 106, 1527.

(61) Sterpone, F.; Stirnemann, G.; Hynes, J. T.; Laage, D. *J. Phys. Chem. B* **2010**, 114, 2083.

(62) Collins, K. D.; Neilson, G. W.; Enderby, J. E. *Biophys. Chem.* **2007**, 128, 95.

(63) Petersen, J.; Moller, K. B.; Rey, R.; Hynes, J. T. *J. Phys. Chem. B* **2013**, 117, 4541.

(64) Tanford, C. *Science* **1978**, 200, 1012.

(65) Yamakata, A.; Osawa, M. *J. Am. Chem. Soc.***2009**, 131, 6892.

(66) Frank, H. S.; Evans, M. W. *J. Chem. Phys.* **1945**, 13, 507.

(67) Kauzmann, W. *Adv. Protein Chem.* **1969**, 14, 1.

(68) Blokzijl, W.; Engberts, J. B. F. N. *Angew. Chem., Int. Ed.* **1993**, 32, 1545.

(69) Soper, A. K.; Finney, J. L. *Phys. Rev. Lett.* **1993**, 71, 4346.

(70) Qvist, J.; Halle, B. *J. Am. Chem. Soc*. **2008**, 130, 10345.

(71) Petersen, C.; Bakulin, A. A.; Pavelyev, V. G.; Pshenichnikov, M. S.; Bakker, H. J. *J. Chem. Phys.* **2010**, 133, 164514.

(72) Bakulin, A. A.; Liang, C.; la Cour Jansen, T.; Wiersma, D. A.; Bakker, H. J.; Pshenichnikov, M. S. *Acc. Chem. Res*. **2009**, 42, 1229.

(73) Niehues, G.; Heyden, M.; Schmidt, D. A.; Havenith, M. *Faraday Discussions* **2011**, 150, 193.

(74) van der Post, S. T.; Scheidelaar, S.; Bakker, H. J. *J. Phys. Chem. B* **2013**, 117, 15101.

(75) Laage, D.; Stirnemann, G.; Hynes, J. T. *J. Phys. Chem. B* **2009**, 113, 2428.

(76) Laage, D.; Hynes, J. T. *Chem. Phys. Lett.* **2006**, 433, 80.

(77) Laage, D.; Hynes, J. T. *Science* **2006**, 311, 832.

(78) Perera, P. N.; Browder, B.; Ben-Amotz, D. *J. Phys. Chem. B* **2009**, 113, 1805.

(79) Mondal, J. A.; Nihonyanagi, S.; Yamaguchi, S.; Tahara, T. *J. Am. Chem. Soc*. **2010**, 132, 10656.

(80) Mondal, J. A.; Nihonyanagi, S.; Yamaguchi, S.; Tahara, T. *J. Am. Chem. Soc*. **2012**, 134, 7842.

(81) Tauber, M. J.; Mathies, R. A. *J. Am. Chem. Soc*. **2003**, 125, 1394.

(82) Eftekhari-Bafrooei, A.; Borguet, E. *J. Am. Chem. Soc*. **2010**, 132, 3756.

(83) Wernersson, E.; Jungwirth, P. *Journal of Chemical Theory and Computation* **2010**, 6, 3233.

(84) Bakker, H. J.; Skinner, J. L. *Chem. Rev.* **2010**, 110, 1498-1517.

(85) Sokolowska, A.; Kecki, Z. *J. Raman Spectrosc.* **1986**, 17, 29.

(86) Sovago, M.; Campen, R. K.; Wurpel, G. W. H.; Muller, M.; Bakker, H. J.; Bonn, M. Phys. Rev. Lett. **2008**, 100, 173901.

(87) Auer, B. M.; Skinner, J. L. *J. Chem. Phys.* **2008**, 128, 224511.

(88) Yang, M.; Skinner, J. L. *Phys. Chem. Chem. Phys.* **2010**, 12, 982.

(89) Wiafe-Akenten, J.; Bansil, R. *J. Chem. Phys.* **1983**, 78, 7132.

(90) Hare, D. E.; Sorensen, C. M. *J. Chem. Phys.* **1992**, 96, 13.

(91) Max, J. J.; Blois, S.; Veilleux, A.; Chapados, C. *Can. J. Chem.* **2001**, 79, 13.

(92) Nickolov, Z. S.; Miller, J. D. *J. Colloid Interface Sci.* **2005**, 287, 572.

(93) Stangret, J.; Gampe, T. *J. Phys. Chem. B* **1999**, 103, 3778.

(94) Stangret, J. *Spectrosc. Lett.* **1988**, 21, 369.

(95) Smiechowski, M.; Stangret, a. J. *Pure Appl. Chem.* **2010**, 82, 1869.

(96) Stenger, J.; Madsen, D.; Hamm, P.; Nibbering, E. T. J.; Elsaesser, T. *Phys. Rev. Lett.* **2001**, 87, 027401.

(97) Perera, P.; Wyche, M.; Loethen, Y.; Ben-Amotz, D. *J. Am. Chem. Soc*. **2008**, 130, 4576.

(98) Fega, K. R.; Wilcox, D. S.; Ben-Amotz, D. *Appl. Spectrosc.* **2012**, 66, 282.

(99) Dunn, M. F. *Protein-Ligand Interactions: General Description.* In Encyclopedia of Life Sciences; John Wiley & Sons, Ltd.: Chichester, **2010**.

(100) Finney, J. L.; Soper, A. K. *Chem.Soc. Rev.* **1994**, 23, 1.

(101) omans, S. W. *Drug Discovery Today* **2007**, 12, 534.

(102) Fisher, H. F. *Protein–Ligand Interactions: Molecular Basis.* In Encyclopedia of Life Sciences; John Wiley & Sons, Ltd.: Chichester, **2001**.

(103) Perozzo, R.; Folkers, G.; Scapozza, L. *J. Recept. Signal Transduction* **2004**, 24, 1.

(104) Freire, E. *Drug Discovery Today* **2008**, 13, 869.

(105) Gohlke, H.; Klebe, G. *Angew. Chem., Int. Ed.* **2002**, 41, 2645.

(106) Goodford, P. J. A. *J. Med. Chem.* **1985**, 28, 849.

(107) Dennis, S.; Kortvelyesi, T.; Vajda, S. *Proc. Natl.Acad. Sci. USA* **2002**, 99, 4290.

(108) Morris, G. M.; Goodsell, D. S.; Halliday, R. S.; Huey, R.; Hart, W. E.; Belew, R. K.; Olson, A. *J. J. Comput. Chem.* **1998**, 19, 1639.

(109) Dougherty, T. *J. Photochem Photobiol* **1993**, 58, 895.

(110) Bonnett, R. *Chem Soc Rev* **1995**, 24, 19.

(111) S N Emma, H. H. P. *J Photochem Photobiol B* **2004**, 73, 1.

(112) Motohiro, T.; U.Tadao; O.Tohru; Takuma, S. *Cancer Lett.* **1995**, 90, 163.

(113) Konrad, S.; Wojciech, M.; Agnieszka, D. M.; Małgorzata, B.; Grażyna, S. *Chem. Rev.* **2005**, 105, 2647.

(114) Honglian, X.; Changchun, Z.; Zhouyi, G.; Huiqing, Z.; Ruikang, W.; Songhao, L.; Yonghong, H. *Phys. Med. Biol.* **2008**, 53, 6767.

(115) Reddi, E.; Ricchelli, F.; Jori, G. *Int J Pept Protein Res* **1981**, 18, 402.

(116) Kratochwil N A, H. W., Muller F, Kansy M & Gerber P R *Biochem Pharmacol* **2002**, 64, 1355.

(117) Wunder A, M.-L. U., Stelzer E H, Funk J, Neumann E, Stehle G, Pap T, Sinn H, Gay S S & Fiehn C *J Immunol* **2003**, 170, 4793.

(118) Pardridge, W. M. *Am J Physiol Endocrinol Metab* **1987**, 252, 157.

(119) Dror, S. B.; Bronshtein, I.; Weitman, H.; Smith, K. M.; O'Neal, W. G.; Jacobi, P. A.; Ehrenberg, B. *Eur Biophys J* **2009**, 38, 847.

(120) Rinco, O.; Brenton, J.; Douglas, A.; Maxwell, A.; Henderson, M.; Indrelie, K.; Wessels, J.; Widin, J. *J Photochem Photobiol A* **2009**, 208, 91.

(121) Yu, X.; Liu, R.; Yi, R.; Yang, F.; Huang, H.; Chen, J.; Ji, D.; Yang, Y.; Li, X.; Yi, P. *Spectrochim Acta Part A* **2011**, 78, 1329.

(122) Feng, S.; Lin, J.; Li, Y.; Z, Z. H.; Chen, R. *http://ieeexplore.ieee.org/ stamp/stamp. jsp?tp=&arnumbe r=4781390*.

(123) Feng, X. Z.; Jin, R. X.; Qu, Y.; He, X. W. *Chem J Chin Univ* **1996**, 17, 866.

(124) Rosenberger, V.; Margalit, R. *Photochem Photobiol* **1993**, 58, 627.

(125) Alonso, H.; Bliznyuk, A. B.; Gready, J. E. *Med Res Rev* **2006**, 26, 531.

(126) Liu, H.; Bao, W.; Ding, H.; Jang, J.; Zou, G. *J Phys Chem B* **2010**, 114, 12938.

(127) El-Sayed, M. A. *Acc. Chem. Res.* **2004**, 37, 326.

(128) Coe, S.; Woo, W. K.; Bawendi, M.; Bulovic, V. *Nature* **2002**, 420, 800.

(129) Brus, L. E. *J. Chem. Phys.* **1983**, 79, 5566.

(130) Resch-Genger, U.; Grabolle, M.; Cavaliere-Jaricot, S.; Nitschke, R.; Nann, T. *Nature Methods* **2008**, 5, 763.

(131) Alivisatos, A. P. *Science* **1996**, 271, 933.

(132) Chan, W. C. W.; Nie, S. *Science* **1998**, 281, 2016.

(133) Mulder, W. J. M.; Koole, R.; Brandwijk, R. J.; Storm, G.; Chin, P. T. K.; Strijkers, G. J.; Donegá, C. D. M.; Nicolay, K.; Griffioen, A. W. *Nano Lett.* **2006**, 6, 1.

(134) Grieve, K.; Mulvaney, P.; Grieser, F. *Curr. Opin. Colloid Int.* **2000**, 5, 168.

(135) Burda, C.; Chen, X.; Narayanan, R.; El-Sayed, M. A. *Chem Rev.* **2005**, 105, 1025.

(136) Parak, W. J.; Gerion, D.; Zanchet, D.; Woerz, A. S.; Pellegrino, T.; Micheel, C.; Williams, S. C.; Seitz, M.; Bruehl, R. E.; Bryant, Z.; Bustamante, C.; Bertozzi, C. R.; Alivisatos, A. P. *Chem. Mater.* **2002**, 14, 2113.

(137) Michalet, X. *Science* **2005**, 307, 538.

(138) Burda, C.; Chen, X.; Narayanan, R.; El-Sayed, M. A. *Chem. Rev.* **2005**, 105, 1025.

(139) Love, J. C.; Estroff, L. A.; Kriebel, J. K.; Nuzzo, R. G.; Whitesides, G. M. *Chem. Rev.* **2005**, 105, 1103.

(140) Liu, W. *J. Am. Chem. Soc.* **2008**, 130, 1274.

(141) Kim, S. Nat. Biotechnol. **2004**, 22, 93.

(142) Chen, C.-L.; Rosi, N. L. *Angew. Chem. Int. Ed.* **2010**, 49, 1924.

(143) Palmer, L. C.; Newcomb, C. J.; Kaltz, S. R.; Spoerke, E. D.; I.Stupp, S. *Chem. Rev.* 2008, **108**, 4754.

(144) Meldrum, F. C. *Int. Mater. Rev.* **2003**, 48, 187.

(145) Weiner, S.; Addadi, L. *J. Mater. Chem.* **1997**, 7, 689.

(146) Lutolf, M. P.; Hubbell, J. A. *Nat. Biotechnol.* **2005**, 23, 47.

(147) Park, C.; Yoon, T. H. *Colloids Surf., B* **2010**, 75, 472.

(148) Xiang-Ying, S.; Bin, L.; Hui, L.; Yan-Hua, Y. *J. Nanosci. Nanotechnol.* 2011, 11, 6810.

(149) Yang, L.; Xing, R.; Shen, Q.; K. Jiang; Ye, F.; Wang, J.; Ren, Q. *J. Phys. Chem. B* **2006**, 110, 10534.

(150) Huang, P. P.; Bao, L.; Yang, D.; Gao, G.; Lin, J.; Li, Z.; Zhang, C.; Cui, D. *Chem. Asian J.* **2011**, 6, 1156.

(151) Ghosh, D.; Mondal, S.; Ghosh, S.; Saha, A. *J. Mater. Chem.* **2012**, 22, 699.

(152) Nithyaja, B.; Vishnu, K.; Mathew, S.; Radhakrishnan, P.; Nampoori, V. P. N. *J. Appl. phys.* **2012**, 112, 064704

(153) Yao, Y.; Song, Y.; Wang, L. *Nanotechnology* **2008**, 19, 405601.

(154) Bakshi, M. S.; Jaswal, V. S.; Kaur, G.; Simpson, T. W.; Banipal, P. K.; Banipal, T. S.; Possmayer, F.; Petersen, N. O. *J. Phys. Chem. C.* **2009**, 113, 9121.

(155) Raman, C. V. *Nature* **1928**, 123, 50.

(156) Raman, C. V. *Transactions of the Faraday Society* **1929**, 25, 0781.

(157) Krishnan, K. S. Nature **1928**, 122, 961.

(158) Atkins, P.; Paula, J. d. *Physical Chemistry*; 8 ed.; W. H. Freeman Company, New York, **2006**.

(159) R L McCreery *Raman Spectroscopy for Chemical Analysis*; John Wiley & Sons: New York, **2000**.

(160) Skoog, D. A.; Holler, F. J.; Nieman, T. A. *Principles of Instrumental Analysis* 5ed.; Thomson Learning, Inc., Philadelphia, **1998**.

(161) Pelletier, M. J. Analytical Applications of Raman Spectroscopy; Blackwell Science Ltd: Malden MA, USA, **1999**.

(162) Smith, E.; Dent, G. *Modern Raman Spectroscopy - A Practical Approach*; John Wiley & Sons, Inc.: England, **2005**.

(163) Turrell, G.; Corset, J. *Raman Microscopy: Developments and Applications*; Academic Press Ltd.: London, **1996**.

(164) Chen, Y.; Zhang, Y. H.; Zhao, L. J. *Phys. Chem. Chem. Phys.* **2004**, 6, 537.

(165) Xie, Y.; Zhang, D.; Ben-Arnotz, D. *Anal. Biochem.* **2008**, 373, 154.

(166) Bergstrom, P. A.; Lindgren, J.; Kristiansson, O. *J. Phys. Chem.* **1991**, 95, 8575.

(167) Wei, Z. F.; Zhang, Y. H.; Zhao, L. J.; Liu, J. H.; Li, X. H. *J. Phys. Chem. A.* **2005**, 109, 1337.

(168) Ikushima, Y.; Saito, Y. N.; Arai, M. *J. Phys. Chem. B.* **1998**, 102, 3029.

(169) Rull, F. *Pure Appl. Chem.* **2002**, 74, 1859.

(170) Li, R. H.; Jiang, Z. P.; Chen, F. G.; Yang, H. W.; Guan, Y. T. *J. Mol. Struct.* **2004**, 707, 83.

(171) Garrido, M.; Rius, F. X.; Larrechi, M. S. Anal. Bioanal. Chem. **2008**, 390, 2059.

(172) Ortiz, M. C.; Sarabia, L. *J. Chromatogr., A* **2007**, 1158, 94.

(173) Jaumot, J.; Vives, M.; Gargallo, R. *Anal. Biochem.* **2004**, 327, 1.

(174) Tauler, R.; Barcelo, D. *TrAC, Trends Anal. Chem.* **1993**, 12, 319.

(175) Bezemer, E.; Rutan, S. *Anal. Chim. Acta* **2002**, 459, 277.

(176) Tauler, R.; Izquierdo-Ridorsa, A.; E. Casassas *Chemom. Intell. Lab. Syst.* **1993**, 18, 293.

(177) Tauler, R. *Chemom. Intell. Lab. Syst.* **1995**, 30, 133.

(178) Juan, A. d.; Maeder, M.; Hancewicz, T.; Tauler, R. *J. Chemom.* **2008**, 22, 291.

(179) Navea, S.; Tauler, R.; Juan, A. d. *Anal. Chem.* **2006**, 78, 4768.

(180) Navea, S.; Juan, A. d.; Tauler, R. *Anal. Chem.* **2003**, 75, 5592.

(181) Jiang, J. H.; Ozaki, Y. *Appl. Spectrosc. Rev* **2002**, 37, 321.

(182) Juan, A. d.; Tauler, R. Crit. Rev. Anal. Chem. **2006**, 36, 163.

(183) Gabrielsson, J.; Trygg, J. Crit. Rev. Anal. Chem. **2006**, 36, 243.

(184) Schoonover, J. R.; Marx, R.; Zhang, S. L. L. *Appl. Spectrosc.* **2003**, 57, 154A.

(185) Garrido, M.; Rius, F. X.; Larrechi, M. S. *Anal. Biochem.* **2008**, 390, 2059.

(186) Uzunbajakava, N.; Lenferink, A.; Kraan, Y.; Volokhina, E.; Vrensen, G.; Greve, J.; Otto, C. *Biophys. J* **2003**, 84, 3968.

(187) Okuno, M.; Kano, H.; Leproux, P.; Couderc, V.; Day, J. P. R.; Bonn, M.; Hamaguchi, H. *Angew. Chem. Int. Ed.* **2010**, 49, 6773.

(188) Malinowski, E. R. *Factor Analysis in Chemistry*; Wiley, NewYork, **1991**.

(189) Juan, A. d.; Tauler, R. *Crit. Rev. Anal. Chem.* **2006**, 36, 163.

(190) Saurina, J.; Hernandezcassou, S.; Tauler, R. *Anal. Chem.* **1995**, 67, 3722.

(191)Saurina, J.; Hernandezcassou, S.; Tauler, R. *Anal. Chim. Acta* **1995**, 312, 189.

(192) Perera, P. N.; Fega, K. R.; Lawrence, C.; Sundstrom, E. J.; Tomlinson-Phillips, J.; Ben-Amotz, D. Proc. Natl. Acad. Sci. U. S. A. **2009**, 106, 12230.

(193) Ben-Amotz, D.; Rankin, B. M.; Hands, M. D.; Wilcox, D. S.; Fega, K. R.; Slipchenko, L. *Faraday Discussions* **2013**, 160, 255.

(194) Davis, J. G.; Gierszal, K. P.; Wang, P.; Ben-Amotz, D. *Nature* **2012**, 491, 582.

(195) Davis, J. G.; Rankin, B. M.; Gierszal, K. P.; Ben-Amotz, D. *Nature Chemistry* **2013**, 5, 796.

(196) Tomlinson-Phillips, J.; Davis, J.; Ben-Amotz, D.; Spangberg, D.; Pejov, L.; Hermansson, K. *J. Phys. Chem. A* **2011**, 115, 6177.

(197) Hollas, M. J. *Modern Spectroscopy*; 3 ed.; John Wiley and Sons., **1996**.

(198) Smith, B. C. *Quantitative Spectroscopy: Theory and Practice*; Academic Press, **2002**.

(199) Bernath, P. F. *Spectra of atoms and molecules*; Oxford University Press, **1995**.

(200) Birks, J. B. *Photophysics of Aromatic Molecules*; Wiley Interscience: New York, **1970**.

(201) Gilbert, A.; Baggott, J.; Wagner, P. J. *Essential of Molecular Photochemistry*; Blackwell science Inc.: Cambridge, USA, **1991**.

(202) Rohatgi-Mukherjee, K. K. *Fundamentals of Photochemistry*; Wiley Eastern Ltd.: India, **1986**.

(203) Lakowicz, J. R. *Principles of Fluorescence Spectroscopy*; 3 ed.; Springer Science Business Media, New York, **2006**.

(204) O'Connor, D. V.; Phillips, D. *Time-Correlated Single-Photon Counting*; Academic Press: London, **1984**.

(205) Zhang, Y.; Cremer, P. S. *Curr. Opin. Chem. Biol*. **2006**, 10, 658.

(206) Wang, X.; Hu, W.; Chou, I. M. *J. Geochem. Explor.* **2013**, 132, 111.

(207) Sovago, M.; Wurpel, G. W. H.; Smits, M.; Muller, M.; Bonn, M. *J. Am. Chem. Soc*. **2007**, 129, 11079.

(208) Halle, B.; Bellisent-Funel, M. C. *Hydration Processes in Biology: Theoretical and Experimental Approaches*, **1999**.

(209) Liu, D.; Ma, G.; Levering, L. M.; Allen, H. C. *J. Phys. Chem. B* **2004**, 108, 2252.

(210) Abe, N.; Ito, M. *J. Raman Spectrosc.* **1978**, 7, 161.

(211) Auer, B. M.; Skinner, J. L. *J. Chem. Phys.* **2007**, 127, 104105.

(212) Sokołowska, A. *J. Raman Spectrosc.* **1991**, 22, 31.

(213) Ratcliffe, C. I.; Irish, D. E. *J. Phys. Chem.* **1982**, 86, 4897.

(214) Xiong, K.; Asher, S. A. *J. Phys. Chem. B* **2011**, 115, 9345.

(215) Busing, W. R.; Hornig, D. F. *J. Phys. Chem.***1961**, 65, 284.

(216) Kropman, M. F.; Bakker, H. J. *Chem. Phys. Lett.* **2002**, 362, 349.

(217) Terpstra, P.; Combes, D.; Zwick, A. *J. Chem. Phys.* **1990**, 92, 65.

(218) Li, R.; Jiang, Z.; Guan, Y.; Yang, H.; Liu, B. *J. Raman Spectrosc.* **2009**, 40, 1200.

(219) Omta, A. W.; Kropman, M. F.; Woutersen, S.; Bakker, H. J. *Science* **2003**, 301, 347.

(220) Bakker, H. J.; Kropman, M. F.; Omta, A. W. *J. Phys. - Cond. Mat.* **2005**, 17, S3215.

(221) Brooker, M. H.; Hancock, G.; Rice, B. C.; Shapter, J. *J. Raman Spectrosc.* **1989**, 20, 683.

(222) Kanno, H.; Hiraishi, J. *J. Phys. Chem.***1983**, 87, 3664.

(223) Schultz, J. W.; Hornig, D. F. *J. Phys. Chem.***1961**, 65, 2131.

(224) Aoki, K.; Yamawaki, H.; Sakashita, M. *Science* **1995**, 268, 1322.

(225) Savatinova, I.; Anachkova, E.; Nikolaeva, R. *Spectrosc. Lett.* **1986**, 19, 167.

(226) Wick, C. D.; Xantheas, S. S. *J. Phys. Chem. B* **2009**, 113, 4141.

(227)Marielle, S.; Steven, W. R. *J. Chem. Phys.* **2012**, 137, 044511.

(228) Li, D.-F.; Gao, S.-Q.; Sun, C.-L.; Jiang, X.-L.; Li, Z.-W. *Spectrochim. Acta A: Mol. Biomol. Spec.* **2012**, 89, 155.

(229) Sharp, K. A.; Bhupinder, M.; Eric, M.; Jane, M. V. *J. Chem. Phys.* **2001**, 114, 1791.

(230) Seifert, G.; Graener, H. *J. Chem. Phys.* **2007**, 127, 224505.

(231) Ashihara, S.; Fujioka, S.; Shibuya, K. *Chem. Phys. Lett.* **2011**, 502, 57.

(232) Heuft, J. M.; Meijer, E. J. *J. Chem. Phys.* **2005**, 123, 094506.

(233) Heuft, J. M.; Meijer, E. J. *J. Chem. Phys.* **2005**, 122, 094501.

(234) Heuft, J. M.; Meijer, E. J. *J. Chem. Phys.* **2003**, 119, 11788.

(235) Albrecht, A. C.; Hutley, M. C. *J. Chem. Phys.* **1971**, 55, 4438.

(236) McCreery, R. L. **2006**. *Photometric Standards for Raman Spectroscopy. Handbook of Vibrational Spectroscopy*.

(237) Theodore, T. W.; Donald, F. H. *J. Chem. Phys.* **1967**, 47, 784.

(238) Wu, D.-Y.; Duan, S.; Liu, X.-M.; Xu, Y.-C.; Jiang, Y.-X.; Ren, B.; Xu, X.; Lin, S. H.; Tian, Z.-Q. *J. Phys. Chem. A* **2008**, 112, 1313.

(239) Williams, F.; Kerr, C. M. L. *J. Am. Chem. Soc.* **1971**, 93, 2805.

(240) Smith, M.; Symons, M. C. R. *Transactions of the Faraday Society* **1958**, 54, 346.

(241) Sharp, K. A.; Vanderkooi, J. M. *Acc. Chem. Res.* **2010**, 43, 231.

(242) Chen, Y.; Zhang, Y. H.; Zhao, L. J. *Phys. Chem. Chem. Phys.* **2004**, 6, 537.

(243) Heugen, U.; Schwaab, G.; BrÃndermann, E.; Heyden, M.; Yu, X.; Leitner, D. M.; Havenith, M. *Proc. Natl. Acad. Sci. U.S.A.* **2006**, 103, 12301.

(244) O'Brien, J. T.; Prell, J. S.; Bush, M. F.; Williams, E. R. *J. Am. Chem. Soc.* **2010**, 132, 8248.

(245) Kondoh, M.; Ohshima, Y.; Tsubouchi, M. *Chem. Phys. Lett.* **2014**, 591, 317.

(246) Heyden, M.; Schwaab, G.; Havenith, M. *J. Phys. Chem. B* **2014**, 108, 10802.

(247) Fenn, E. E.; Wong, D. B.; Fayer, M. D. *Proc. Natl. Acad. Sci. U.S.A.* **2009**, 106, 15243.

(248) Ahmed, M.; Singh, A. K.; Mondal, J. A.; Sarkar, S. K. *J. Phys. Chem. B* **2013**, 117, 9728.

(249) Watanabe, D.; Hamaguchi, H. *J. Chem. Phys.* **2005**, 123, 034508.

(250) Sun, Z.; Zhang, W.; Ji, M.; Hartsock, R.; Gaffney, K. J. *J. Phys. Chem. B* **2013**, 117, 15306.

(251) Tauler, R. *Chemom. Intell. Lab. Syst.* **1995**, 30, 133.

(252) Abdollahi, H.; Maeder, M.; Tauler, R. *Anal. Chem.* **2009**, 81, 2115.

(253) Cappa, C. D.; Smith, J. D.; Messer, B. M.; Cohen, R. C.; Saykally, R. J. *J. Phys. Chem. B* **2006**, 110, 5301.

(254) Walrafen, G. E. *J. Chem. Phys.* **1962**, 36, 1035.

(255) Waldron, R. D. *J. Chem. Phys.* **1957**, 26, 809.

(256) Kabisch, G. *J. Mol. Struct.* **1981**, 77, 219.

(257) Falk, M. *J. Raman Spectrosc.* **1990**, 21, 563.

(258) Kint, S.; Scherer, J. R. *J. Chem. Phys.* **1978**, 69, 1429.

(259) Bergstroem, P. A.; Lindgren, J.; Kristiansson, O. *J. Phys. Chem* **1991**, 95, 8575.

(260) Cannon, W. R.; Pettitt, B. M.; McCammon, J. A. *J. Phys. Chem* **1994**, 98, 6225.

(261) Gopalakrishnan, S.; Jungwirth, P.; Tobias, D. J.; Allen, H. C. *J. Phys. Chem B* **2005**, 109, 8861.

(262) Lund, M.; Cwiklik, J. B.; Woodward, C. E.; Vacha, R.; Jungwirth, P. *J. Phys. Chem. Lett.* **2010**, 1, 300.

(263) Stirnemann, G.; Wernersson, E.; Jungwirth, P.; Laage, D. *J. Am. Chem. Soc*. **2013**, 135, 11824.

(264) Ghosh, A.; Smits, M.; Bredenbeck, J.; Bonn, M. *J. Am. Chem. Soc*. **2007**, 129, 9608.

(265) Nihonyanagi, S.; Yamaguchi, S.; Tahara, T. *J. Chem. Phys.* **2009**, 130, 204704.

(266) Falk, M. *Spectrochim. Acta A* **1984**, 40, 43.

(267) O'Brien, J. T.; Williams, E. R. *J. Am. Chem. Soc*. **2012**, 134, 10228.

(268) Armishaw, R. F.; James, D. W. *J. Phys. Chem.* **1976**, 80, 501.

(269) Draegert, D. A.; Williams, D. *J. Chem. Phys.***1968**, 48, 401.

(270) Guo, F.; Friedman, J. M. *J. Am. Chem. Soc*. **2009**, 131, 11010.

(271) Wi, S.; Spano, J.; Ducker, W. A. *J. Phys. Chem C* **2010**, 114, 14986.

(272) Levinger, N. E.; Costard, R.; Nibbering, E. T. J.; Elsaesser, T. *J. Phys. Chem A* **2011**, 115, 11952.

(273) Costard, R.; Greve, C.; Heisler, I. A.; Elsaesser, T. *J. Phys. Chem. Lett.* **2012**, 3, 3646.

(274) Boulesbaa, A.; Borguet, E. *J. Phys. Chem. Lett.* **2014**, 5, 528.

(275) Cringus, D.; Yeremenko, S.; Pshenichnikov, M. S.; Wiersma, D. A. *J. Phys. Chem B* **2004**, 108, 10376.

(276) Chandler, D. *Nature* **2005**, 437, 640.

(277) K.A.Sharp *Curr. Opin. Struct. Biol*. **1991**, 1, 171.

(278) K.A.Dill *Biochemistry* **1990**, 29, 7133.

(279) P.L.Privalov *Crit.Rev.Biochem.Mol.Biol.* **1990**, 25, 281.

(280) Soda, K. *Adv. Biophys* **1993**, 29, 1.

(281) Tanford, C. *J. Mol. Biol.* **1972**, 67, 59.

(282) Kauzmann, W. *Some Factors in the Interpretation of Protein Denaturation*. **1959**, 14, 1-63.

(283) Chandler, D. *Nature* **2005**, 437, 640.

(284) Kauzmann, W. *In Advances in Protein Chemistry* **1959**; Vol. 14, p 1-63.

(285) Abraham, M. H. *J. Am. Chem. Soc.* **1982**, 104, 2085.

(286) Lee, B.; Graziano, G. *J. Am.Chem.Soc.* **1996**, 118, 5163.

(287) Naghibi, H.; Dec, S. F.; Gill, S. J. *J. Phys. Chem. B.* **1986**, 90, 4621.

(288) Frank, H. S.; Evans, M. W. J. *J. Phys. Chem. B.* **1945**, 13, 507.

(289) Soper, A. K.; Luzar, A. *J. Phys. Chem.* **1996**, 100, 1357.

(290) Blokzijl, W.; Engberts, J. B. F. N. *Angew. Chem., Intl. Ed. Engl.* **1993**, 32, 1545.

(291) Mayele, M.; Holz, M.; Sacco, A. *Phys. Chem. Chem. Phys.* **1999**, 1, 4615.

(292) Holz, M.; Haselmeier, R.; Mazitov, R.; Weingärtner, H. *J. Am. Chem. Soc.* **1994**, 116, 801.

(293) Nakahara, M.; Yoshimoto, Y. *J. Phys. Chem.* **1995**, 99, 10698.

(294) K. Fumino, K. Y., A. Shimizu, Y. Taniguchi *J. Mol. Liq.,* 75, 1.

(295) Buchner, R.; HÄolzl, C.; Stauber, J.; Barthel, J. *Phys. Chem. Chem. Phys*. **2002**, 4, 2169.

(296) Hallenga, K.; Grigera, J. R.; Berendsen, H. J. C. *J. Phys. Chem.* **1980**, 84, 2381.

(297) Kaatze, U.; Rupprecht, A. *J. Chem. Phys.* **2002**, 117, 4936.

(298) Mancera, R. L. *J. Chem. Soc., Faraday Trans.* **1996**, 92, 2547.

(299) Silverstein, K. A.; Haymet, A. D. J.; Dill, K. A. *J. Am. Chem. Soc.* **2000**, 122, 8037.

(300) Silverstein, K. A.; Haymet, A. D. J.; Dill, K. A. *J. Am. Chem. Soc.* **1998**, 120, 3166.

(301) Mancera, R. L.; Buckingham, A. D. *J. Phys. Chem.* **1995**, 99, 14632.

(302) Bagno, A. J. *J. Chem. Soc., Faraday Trans.* **1998**, 94, 2501.

(303) Laage, D.; Stirnemann, G.; Hynes, J. T. *J. Phys. Chem. B* **2009**, 113, 2428.

(304) Ma, G.; Chen, X.; Allen, H. C. *J. Am. Chem. Soc.* **2007**, 129, 14053.

(305) Ahmed, M.; Namboodiri, V.; Singh, A. K.; Mondal, J. A.; Sarkar, S. K. *J. Phys. Chem. B* **2013**, 117, 16479.

(306) Madan, B.; Sharp, K. *Biophys. Chem*. **1999**, 78, 33.

(307) Strazdaite, S.; Versluis, J.; Backus, E. H. G.; Bakker, H. J. *J. Chem. Phys*. **2014**, 140, 054711.

(308) Scatena, L. F.; Brown, M. G.; Richmond, G. L. *Science* **2001**, 292, 908.

(309) Yang, M. *J. Chem. Phys.* **2014**, 140, 144508.

(310) Stiopkin, I. V.; Weeraman, C.; Pieniazek, P. A.; Shalhout, F. Y.; Skinner, J. L.; Benderskii, A. V. *Nature* **2011**, 474, 192.

(311) Liu, J.; Andino, R. S.; Miller, C. M.; Chen, X.; Wilkins, D. M.; Ceriotti, M.; Manolopoulos, D. E. *J. Phys. Chem. C* **2013**, 117, 2944.

(312) Zhang, Z.; Piatkowski, L.; Bakker, H. J.; Bonn, M. *Nat Chem* **2011**, 3, 888.

(313) Hsieh, C. S.; Campen, R. K.; Okuno, M.; Backus, E. H. G.; Nagata, Y.; Bonn, M. *Proc. Natl. Acad. Sci. U. S. A.* **2013**, 110, 18780.

(314) Mrazkova, E.; Hobza, P.; Bohl, M.; Gauger, D. R.; Pohle, W. *J. Phys. Chem. B* 2005, 109, 15126.

(315) Joseph, J.; Jemmis, E. D. *J. Am. Chem. Soc.* **2007**, 129, 4620.

(316) Y. Koga, P. W., K. Nishikawa and S. Subramanian *J. Phys. Chem. B* **2011**, 115, 2995.

(317) Sagle, L. B.; Cimatu, K.; Litosh, V. A.; Liu, Y.; Flores, S. C.; Chen, X.; Yu, B.; Cremer, P. S. *J. Am. Chem. Soc*. **2011**, 133, 18707.

(318) Lopez, C. F.; Nielsen, S. O.; Klein, M. L.; Moore, P. B. *J. Phys. Chem. B* 2004, 108, 6603.

(319) Yoshimura, Y.; Kanno, H. *J. Raman Spec.* **1996**, 27, 671.

(320) Damodaran, K. V.; Merz, K. M. *Langmuir* **1993**, 9, 1179.

(321) Gu, Y.; Kar, T.; Scheiner, S. *J. Am. Chem. Soc*. **1999**, 121, 9411.

(322) Hermansson, K. *J. Phys. Chem. A* **2002**, 106, 4695.

(323) Barnes, A. J. *J. Mol. Struct.* **2004**, 704, 3.

(324) Alabugin, I. V.; Manoharan, M.; Peabody, S.; Weinhold, F. *J. Am. Chem. Soc*. **2003**, 125, 5973.

(325) Hermansson, K.; Gajewski, G.; Mitev, P. D. *J. Phys. Chem. A* **2008**, 112, 13487.

(326) Hobza, P.; Havlas, Z. k. *Chem. Rev* **2000**, 100, 4253.

(327) Li, X.; Liu, L.; Schlegel, H. B. *J. Am. Chem. Soc*. **2002**, 124, 9639.

(328) Masunov, A.; Dannenberg, J. J.; Contreras, R. *J. Phys. Chem. A* **2001**, 105, 4737.

(329) Mizuno, K.; Imafuji, S.; Fujiwara, T.; Ohta, T.; Tamiya, Y. *J. Phys. Chem. B* **2003**, 107, 3972.

(330) Scheiner, S.; Gu, Y.; Kar, T. *J. Mol. Struct.*: THEOCHEM **2000**, 500, 441.

(331) Di Michele, A.; Freda, M.; Onori, G.; Paolantoni, M.; Santucci, A.; Sassi, P. *J. Phys. Chem. B* **2006**, 110, 21077.

(332) Walrafen, G. E. *J. Chem. Phys.* **1970**, 52, 4176.

(333) Jungwirth, P.; Tobias, D. J. *Chem. Rev* **2006**, 106, 1259.

(334) Allen, H. C.; Casillas-Ituarte, N. N.; Sierra-Hernandez, M. R.; Chen, X.; Tang, C. Y. *Phys. Chem. Chem. Phys.***2009**, 11, 5538.

(335) Mizuno, K.; Imafuji, S.; Ochi, T.; Ohta, T.; Maeda, S. *J. Phys. Chem. B* **2000**, 104, 11001.

(336) Mizuno, K.; Imafuji, S.; Fujiwara, T.; Ohta, T.; Tamiya, Y. *J. Phys. Chem. B* **2003**, 107, 3972.

(337) Sil, S.; Kar, M.; Chakraborti, A. S. *J Photochem Photobiol B* **1997**, 41, 67.

(338) Sil, S.; Chakraborti, A. S. *Mol Cell Biochem* **2002**, 237, 103.

(339) ZFeng, X.; Jin, R. X.; Qu, Y.; He, X. W. *Chem J Chin Univ* **1996**, 17, 866.

(340) Silvester, J. A.; Timmins, G. S.; Davies, M. J. *Free Radic Biol Med* **1998**, 24, 754.

(341) Sudhamalla, B.; Gokara, M.; Ahalawat, N.; Amooru, D. G.; Subramanyam, R. *J Phys Chem B* **2010**, 114, 9054.

(342) Sengupta, A.; Sasikala, W. D.; Mukherjee, A.; Hazra, P. *Chem Phys Chem* **2012**, 13, 2142.

(343) Pace, C. N.; Vajdos, F.; Fee, L.; Grimsley, G.; Gray, T. *Protein Sci* **1995**, 4, 2411.

(344) Getoff, N.; Solar, S. *Int J Radiat Biol* **1995**, 67, 619.

(345) Bourassa, P.; Kanakis, C. D.; Tarantilis, P.; Pollissiou, M. G.; Tajmir-Riahi, H. A. *J Phys Chem B* **2010**, 114, 3348.

(346) Morris, G. M.; Goodsell, D. S.; Halliday, R. S.; R, R. H.; Hart, W. E.; Belew, R. K.; Olson, A. J. *J Comput Chem* **1998**, 19, 1639.

(347) Chen, E.; Cang, H. X.; Nymeyer, H. NOC 3.01. *http: //noch.sourceforge.net.*

(348) Cornell, W. D.; Cieplak, P.; Bayly, C. I.; Gould, I. R.; Merz, K. M.; Ferguson, D. M.; Spellmeyer, D. C.; Fox, T.; Caldwell, J. W.; Kollman, P. A. *J Am Chem Soc* **1995**, 117, 5179.

(349) Schmidt, M. W.; Baldridge, K. K.; Boatz, J. A.; Elbert, S. T.; Gordon, M. S.; Jensen, J. H.; Koseki, S.; Matsunaga, N.; Nguyen, K. A.; Su, S.; Windus, T. L.; Dupuis, M.; Montgomery, J. A. *J Comput Chem* **1993**, 14, 1347.

(350) Hess, B.; Kutzner, C.; der, S. D. v.; Lindahl, E. *J Chem Theory Comput* **2008**, 4, 435.

(351) Homak, V.; Abel, R.; Okur, A.; Strockbine, B.; Roitberg, A.; Simmerling, C. *Proteins: Struct Funct Bioinf* **2006**, 65, 712.

(352) Jorgensen, W. L.; Chandrasekhar, J.; Madura, J. D.; Impey, R. W.; Klein, M. L. *J Chem Phys* **1983**, 79, 926.

(353) Wolf, R. M. W.; Caldwell, J. W.; Kollman, P. A.; Case, D. A. *J Comput Chem* **2004**, 25, 1157.

(354) Jakalian, A.; Jack, D. B.; Bayly, C. I. *J Comput Chem* **2002**, 23, 1623.

(355) Hess, B.; Bekker, H.; Berendsen, H. J. C.; Fraaije, J. G. E. M. *J Comp Chem* **1997**, 18, 1463.

(356) Darden, T.; York, D.; Pedersen, L. *J Chem Phys* **1993**, 98, 10089.

(357) Pottier, R.; Truscott, T. G. *Int J Radiat Biol* **1986**, 50, 421.

(358) Lehrer, S. S. *Biochemistry* **1971**, 10, 3254.

(359) Paul, B. K.; Guchhait, N. *Photochem Photobiol Sci* **2011**, 10, 980.

(360) Hu, J.; Ou-Yang, Y.; Dai, C.; Liu, Y.; Xiao, X. *Biomacromolecules* **2010**, 11, 106.

(361) Anand, U.; Kurup, L.; Mukherjee, S. *Phys Chem Chem Phys* **2012**, 14, 4250.

(362) Anand, U.; Jash, C.; Boddepalli, R. K.; Shrivastava, A.; Mukherjee, S. *J Phys Chem B* 2011, **115**, 6312-6320.

(363) Förster, T. *Ann Phys* **1948**, 2, 55.

(364) Sahoo, H. *J Photochem Photobiol C: Photochem Rev* **2011**, 12, 20.

(365) Ross, P. D.; Subramanian, S. *Biochemistry* **1981**, 20, 3096.

(366) Klotz, I. M. *N Y Ann Acad Sci* **1973**, 126, 18.

(367) Naïm, M.; Bhat, S.; Rankin, K. N.; Dennis, S.; Chowdhury, S.; Siddiqi, I.; Drabik, P.; Sulea, T.; Bayly, C.; Jakalian, A.; Purisima, E. O. *J Chem Inf Model* **2007**, 47, 122.

(368) Cui, Q.; Sulea, T. T.; Schrag, J. D.; Munger, C.; Hung, M. N.; Naïm, M.; Cygler, M.; Purisima, E. O. *J Mol Biol* **2008**, 379, 787.

(369) Manyar, H. G.; Iliade, P.; Bertinetti, L.; Coluccia, S.; Berlier, G. *J. Colloid Interf Sci.* **2011**, 354, 511

(370) Chen, D.; Gao, L. *Solid State Commun.* **2005**, 133, 145

(371) Coe, S.; Woo, W. K.; Bawendi, M.; Bulovic, V. *Nature* **2002**, 420, 800.

(372) Niemeyer, C. M. *Angew. Chem., Int. Ed.* **2001**, 40, 4128.

(373) Gaponik, N.; Radtchenko, I. L.; Sukhorukov, G. B.; Weller, H.; Rogach, A. L. *Adv.Mater.* **2002**, 14, 879.

(374) Talapin, D. V.; Rogach, A. L.; Shevchenko, E. V.; Komowski, A.; Haase, M.; Weller, H. *J.Am. Chem. Soc.* **2002**, 124, 5782.

(375) Samia, A. C. S.; Chen, X.; Burda, C. *J. Am. Chem. Soc.* **2003**, 125, 15736.

(376) Samia, A. C. S.; Dayal, S.; Burda, C. *Photochem. Photobiol.* **2006**, 86, 617.

(377) Peng, P.; Milliron, D. J.; Hughes, S. M.; Alivisatos, A. P.; Saykally, R. *Nano Lett.* **2005**, 5, 1809.

(378) Xu, L.; Chen, K. L.; El-Khair, H. M.; Li, M. H.; Huang, X. F. *Appl. Surf. Sci*. **2001**, 172, 184.

(379) El-sadek, M. S. A.; Babu, S. M.; Nooralden, A. Y.; Palanisamy, P. K. *Nanosci. Nanotech. Lett.* **2011**, 3, 637.

(380) Hosokawa, H.; Fujiwara, H.; Murakoshi, K.; Wada, Y.; Yanagida, S.; Satoh, M. *J. Phys. Chem.* **1996**, 100, 6649.

(381) Nosaka, Y.; Shigeno, H.; Ikeuchi, T. *J. Phys. Chem.* **1995**, 99, 8317.

(382) Kortan, A. R.; Hull, R.; Opila, R. L.; Bawendi, M. G.; Steigerwald, M. L.; Carroll, P. J.; Brus, L. E. *J. Am. Chem. Soc.* **1990**, 112, 1327.

(383) Anderson, R. E.; Chan, W. C. *ACS Nano* **2008**, 2, 1341.

(384) Guleria, A.; Singh, S.; Rath, M. C.; Singh, A. K.; Adhikari, S.; Sarkar, S. K. *J. Lumin*. **2012**, 132, 652.

(385) Stephen, H. F.; Stacey, N. B.; Nakatsuka, N.; Banerjee, I. A. *Mater. Express* 2012, 2, 335.

(386) Bingkun, C.; Haizheng, Z.; Rui, L.; Yi, Z.; Yuqin, D.; Yongfang, L.; Bingsuo, Z. *Sci. Adv. Mat*. **2012**, 4, 342.

(387) Díaz, V.; Ramírez-Maureira, M.; Monrás, J. P.; Vargas, J.; Bravo, D.; Osorio-Román, I. O.; C.Vásquez, C.; Pérez-Donoso, J. M. *Sci. Adv. Mat.* **2012**, 4, 609.

(388) Yang, L.; Xing, R.; Shen, Q.; Jiang, K.; Ye, F.; Wang, J.; Ren, Q. *J. Phys. Chem. B* **2006**, 110, 10534.

(389) Yu, S. H. *Top.Curr.Chem.* **2007**, 271, 79.

(390) Wang, Q.; Ye, F.; Fang, T.; Niu, W.; Liu, P.; Min, X.; Li, X. *J. Colloid Interf Sci.* **2011**, 355, 9.

(391) Ma, N.; Dooley, C. J.; Kelley, S. O. *J. Am. Chem. Soc.* **2006**, 128, 12598.

(392) Curry, S.; Mandelkow, H.; Brick, P.; J. Franks, N. *J. Mol. Biol.* **1998**, 5, 827.

(393) Curry, S.; Brick, P.; Franks, N. P. *Biochem. Biophys. Acta.* **1999**, 1441, 131.

(394) Bhattacharya, A. A.; Grnne, T.; Curry, S. *J. Mol. Biol.* **2000**, 303, 721.

(395) Zhang, J.; Ma, X.; Guo, Y.; Yang, L.; Shen, Q.; Wang, H.; Ma, Z. *Mater. Chem. Phys.* **2010**, 119, 112.

(396) Rath, M. C.; Mondal, J. A.; Palit, D. K.; Mukherjee, T.; Ghosh, H. N. *J. Nanomaterials.* **2007**, 1, Art ID 36271.

(397) Michnik, A.; Michalik, K.; Drzazga, Z. *J. Therm. Anal. and Calorim.* **2005**, 80, 399.

(398) Wang, X.; Yang, D.; Huang, P.; Li, M.; Li, C.; Chen, D.; Cui, D. *Nanoscale* **2012**, 4, 7766.

(399) Yao, W. T.; Yu, S. H.; Liu, S. J.; Chen, J. P.; Liu, X. M.; Li, F. *J. Phys. Chem. B* **2006**, 110, 11704.

(400) Lee, J.; Govorov, A. O.; Kotov, N. A. *Nano Lett.* **2005**, 5, 2063.

(401) Mauro, E.; Eva, P.; Jordi, A.; Nicolas, S.; Thierry, P.; Joan, R. M. *Langmuir* **2008**, 24, 11182.

(402) Meulenberg, R. W.; Jennings, T.; Strouse, G. F. *Phys. Rev. B.* **2004**, 70, 235311.

(403) Tanaka, A.; Onari, S.; Arai, T. *Phys. Rev. B* **1992**, 45, 6587.

(404) Robert, W.; Meulenberg, J.; Lee, R. I.; Abraham, W.; Jin, Z.; Louis, J.; Tony, B. *ACS Nano* **2009**, 3, 325.

(405) JCPDS Cubic CdSe, File number 190191.

(406) Hu, P.; Jia, D.; Cao, Y.; Huang, Y.; Liu, L.; Luo, *J. Nanoscale Res. Lett.* **2009**, 4, 437.

(407) Liu, B.; Zeng, H. C. *J. Am. Chem. Soc.* **2005**, 127, 18262.

(408) Cho, K.; Talapin, D. V.; Gaschler, W.; Murray, C. B. *J. Am. Chem. Soc.* **2005**, 127, 7140.

(409) Wu, H.; Ji, X.; Zhao, L.; Yang, S.; Xie, R.; Yang, W. *Colloid Surf. A* **2012**, 415, 174.

(410) Bo¨hme, U.; Scheler, U. *Chem. Phys. Lett.* **2007**, 435, 342.

(411) Rezwan, K.; Meier, L. P.; Rezwan, M.; Voros, J.; Textor, M.; Gauckler, L. J. *Langmuir* **2004**, 20, 10055.

(412) Teng, X.; Jia, X. Cadmium Selenide-Gold (CdSe-Au) Hybrid Nanowires: Synthesis and Study of Charge Transfer, Nanowires - Recent Advances, 2012.

(413) Zhang, J. Z. *J. Phys. Chem. B* **2004**, 104, 7239.

(414) Fisher, B. R.; Eisler, H. J.; Stott, N. E.; Bawendi, M. G. *J. Phys. Chem. B* **2004**, 108, 143.

(415) Salman, A. A.; Tortschanoff, A.; Zwan, G. V.; Mourik, F. V.; Chergui, M. A. *Chem. Phys.* **2009**, 357, 96.

(416) Driel, A. F. V.; Nikolaev, I. S.; Vergeer, P.; Lodahl, P.; Vanmaekelbergh, D.; Vos, W. L. *Phys. Rev. B* **2007**, 75, 035329

(417) Karan, S.; Majumder, M.; Mallik, B. *Photochem. Photobiol. Sci.* **2012**, 11, 1220.

(418) Zhang, J. Z.; Grant, C. D. *Ann. Rev. Nano Res.* **2008**, 2, 1.

(419) Wuister, S. F.; Swart, I.; Driel, F.; Hickey, S. G.; Donegá, C. M. *Nano Lett.* **2003**, 3, 503.

(420) Wang, X.; Qu, L.; Zhang, J.; Peng, X.; Xiao, M. *Nano Lett.* **2003**, 3, 1103.

(421) Biju, V.; Kanemoto, R.; Matsumoto, Y.; Ishii, S.; Nakanishi, S.; Itoh, T.; Baba, Y.; Ishikawa, M. *J Phys. Chem. C* **2007**, 111, 7924.

(422) Hamada, M.; Shibu, E. S.; Itoh, T.; Kiran, M. S.; Nakanishi, S.; Ishikawa, M.; Biju, V. Nano Rev. **2011**, 2, 6366.

(423) Huang, P.; Kong, Y.; Li, Z.; Gao, F.; Cui, D. *Nanoscale Res. Lett.* **2010**, 5, 949.

(424) Sadler, P. J.; Viles, J. H. *Inorg. Chem.* **1996**, 35, 4490.

(425) Selvakannan, P. R.; Swami, A.; Srisathiyanarayanan, D.; Shirude, P. S.; Pasricha, R.; Mandale, A. B.; Sastry, M. *Langmuir* **2004**, 20, 7825.

(426) Liu, J.; Fu, S.; Yuan, B.; Li, Y.; Deng, Z. *J. Am.Chem.Soc.* **2010**, 132, 7279.

(427) Meziani, M. J.; Sun, Y. P. *J. Am.Chem.Soc.* **2003**, 125, 8015.

(428) Pathan, H. M.; Sankapal, B. R.; Desai, J. D.; Lokhande, C. D. *Mat. Chem. Phys.* **2002**, 78, 11.

List of Publications included in the present thesis

1 Deciphering the Binding modes of Hematoporphyrin to Bovine serum albumin
Mohammed Ahmed, Apurav Guleria, Ajay K Singh, Tusar Bandyopadhyay, and Sisir K Sarkar
Indian Journal of Biochemistry and Biophysics **2014**, *51(3)*, 175-182.

2 Facile and green synthesis of CdSe quantum dots in protein matrix: Tuning of morphology and optical properties,
Mohammed Ahmed, Apurav Guleria, Madhab C. Rath, Ajay K. Singh, Soumyakanti Adhikari and Sisir K. Sarkar
Journal of Nanoscience and Nanotechnology, **2014**, *14(8)*, 5730-5742.

3 Water in the Hydration Shell of Halide Ions Has Significantly Reduced Fermi Resonance and Moderately Enhanced Raman Cross-Section in the OH Stretch Regions
Mohammed Ahmed, Ajay K. Singh, Jahur A. Mondal, and Sisir K. Sarkar,
J. Phys. Chem. B, **2013**, *117*, 9728-9733.

4 How Ions Affect the Structure of Water: A Combined Raman Spectroscopy and Multivariate Curve Resolution Study
Mohammed Ahmed, Vinu V. Namboodiri, Ajay K. Singh, Jahur A. Mondal, and Sisir K. Sarkar
J. Phys. Chem. B, **2013**,*117*, 16479-16485.

5 On the intermolecular coupling and Librational freedom of water in the hydration shell of mono and bivalent ions
Mohammed Ahmed, Vinu V. Namboodiri, Ajay K. Singh, Jahur A. Mondal
J. Chem. Phys, **2014**,*141*, 164708-164715.

6 Vibrational Coupling and Hydrogen-bonding of Water at Charged and Neutral Molecular Hydrophobic Interfaces
Mohammed Ahmed, Ajay K. Singh, Jahur A. Mondal (communicated)

7 The Methyl groups Attached with Quaternary Nitrogen: Do They Behave Like a Polar Hydrophilic Group? *(Manuscript under preparation)*